Characterization of the inner regions of protoplanetary disks by spectro-interferometry

INAUGURAL-DISSERTATION

zur
Erlangung des Doktorgrades
der Mathematisch-Naturwissenschaftlichen Fakultät
der Universität zu Köln

vorgelegt von

Valerio Ganci
aus Palermo, Italy

Köln 2024

Berichterstatter: Univ.-Prof. Dr. Lucas Labadie
Univ.-Prof. Dr. Anton Zensus

Tag der letzten mündlichen Prüfung: 30.05.2023

Erklärung zur Dissertation

„Hiermit versichere ich an Eides statt, dass ich die vorliegende Dissertation selbstständig und ohne die Benutzung anderer als der angegebenen Hilfsmittel und Literatur angefertigt habe. Alle Stellen, die wörtlich oder sinngemäß aus veröffentlichten und nicht veröffentlichten Werken dem Wortlaut oder dem Sinn nach entnommen wurden, sind als solche kenntlich gemacht. Ich versichere an Eides statt, dass diese Dissertation noch keiner anderen Fakultät oder Universität zur Prüfung vorgelegen hat; dass sie - abgesehen von unten angegebenen Teilpublikationen und eingebundenen Artikeln und Manuskripten - noch nicht veröffentlicht worden ist sowie, dass ich eine Veröffentlichung der Dissertation vor Abschluss der Promotion nicht ohne Genehmigung des Promotionsausschusses vornehmen werde. Die Bestimmungen dieser Ordnung sind mir bekannt. Darüber hinaus erkläre ich hiermit, dass ich die Ordnung zur Sicherung guter wissenschaftlicher Praxis und zum Umgang mit wissenschaftlichem Fehlverhalten der Universität zu Köln gelesen und sie bei der Durchführung der Dissertation zugrundeliegenden Arbeiten und der schriftlich verfassten Dissertation beachtet habe und verpflichte mich hiermit, die dort genannten Vorgaben bei allen wissenschaftlichen Tätigkeiten zu beachten und umzusetzen. Ich versichere, dass die eingereichte elektronische Fassung der eingereichten Druckfassung vollständig entspricht."

Köln, 21/03/2024

Teilpublikationen

Gravity Collaboration: V. Ganci et al. (2024). "The GRAVITY young stellar object survey. XIII. Tracing the time-variable asymmetric disk structure in the inner AU of the Herbig star HD98922". In: arXiv:2401.17764 [astro-ph.SR].

Gravity Collaboration: V. Ganci et al. (2021). "The GRAVITY young stellar object survey. VIII. Gas and dust faint inner rings in the hybrid disk of HD141569". In: *A&Ap* 655, A112.

Gravity Collaboration: A. Wojtczak... V. Ganci et al. (2023). "The GRAVITY young stellar object survey. IX. Spatially resolved kinematics of hot hydrogen gas in the star-disk interaction region of T Tauri stars". In: *A&Ap* 669, A59.

Gravity Collaboration: F. Eupen... V. Ganci et al. (2021). "The GRAVITY young stellar object survey. V. The orbit of the T Tauri binary star WW Cha". In: *A&Ap* 648, A37.

Abstract (German)

Den protoplanetaren Scheiben, die um junge stellare Objekte herum beobachtet werden, wird eine Schlüsselrolle in dem noch immer unklaren Prozess der Planetenentstehung und -entwicklung zugeschrieben. In den letzten zehn Jahren hat sich unser Wissen über protoplanetare Scheiben dank der drastischen Verbesserung der Beobachtungsmöglichkeiten erheblich erweitert. Dennoch ist das Bild noch nicht vollständig, vor allem was die innersten Regionen betrifft, die mit Hilfe der langgestreckten Infrarot-Interferometrie beobachtet werden, die erforderlich ist, um Sub-AE-Skalen zu untersuchen. Offene Fragen werden immer noch diskutiert, z. B. über die Mechanismen zwischen Stern und Scheibe, die durch Emissionslinien wie die Wasserstoff-Brackett-γ-Linie und ihre Position aufgespürt werden, über das Vorhandensein von Staub innerhalb des Sublimationsradius der Systeme, über den Ursprung der Asymmetrien in der Helligkeitsverteilung der protoplanetaren Scheiben und ihre zeitliche Variabilität.
Besonders interessant sind die jungen stellaren Objekte, die zur Untergruppe der Herbig-Sterne gehören. Mit einer Sternmasse, die kanonisch zwischen ~ 2 and $\sim 12\,\mathrm{M}_\odot$ liegt, gelten sie in vielerlei Hinsicht als Brücke zwischen den relativ gut verstandenen massearmen Vorhauptreihensternen und den noch undurchsichtigen massereichen Sternen.

In dieser Arbeit untersuche ich drei verschiedene Herbig-Sterne, von denen jeder ein Maßstab für verschiedene offene Fragen zur Entwicklung junger stellarer Objekte und zu den physikalischen Prozessen in ihren innersten zirkumstellaren Regionen ist.
Das erste Objekt ist HD 141569, ein bekannter Herbig-Stern, der sich durch eine Übergangsscheibe auszeichnet. GRAVITY konnte eine sehr schwache Staubemission innerhalb der ersten AE des Systems nachweisen, von der man bisher annahm, dass sie, wie die meisten Übergangsscheiben, staubarm ist. Das System zeigt trotz seines hohen Alters eine Brγ-Linienemission, für die das GRAVITY-Spektrum und die differentiellen Phasen darauf hindeuten, dass das emittierende Gas in einer Keplerschen Scheibe um den Zentralstern liegt.
Anhand der Studie des zweiten Systems, HD 98922, wird eine einzigartige Untersuchung der Variabilität seines innersten Gas- und Staubmaterials vorgestellt. Ich stelle einen Weg vor, die schlechte Abdeckung der (u, v)-Ebene zu umgehen und die Variabilität durch geometrische Modellierung der interferometrischen Daten zu bewerten. Die Modellierung deutet auf eine umlaufende, sichelförmige, staubige Erscheinung hin, die auf ein Staubfallen-Szenario auf der Millibogensekunden-Skala in den ersten AE der zirkumstellaren Umgebung von HD 98922 hindeutet. Es wird auch eine stark zeitvariable Brackett-γ-Linienemission beobachtet, die in erster Ordnung der Orbitalbewegung des staubigen Merkmals folgt.
Schließlich wird das vierfache Herbig-Sternsystem HD 52721 untersucht und auf interferometrische Binarität in AE-Skalen geprüft. Ein neuer Begleiter wird entdeckt, ebenso wie eine komplexe und stark zeitvariable Brackett-γ-Linienemission.

Abstract (English)

The protoplanetary disks observed around young stellar objects are recognized as having a key role in the still unclear processes of planet formation and evolution. In the last decade our knowledge on protoplanetary disks has grown considerably thanks to the drastic improvement of the observing facilities. However, their picture is not yet complete, especially with regards to their innermost regions, observed through long-baseline infrared interferometry, required to probe sub-au scales. Open questions are still debated, for example, on the star–disk mechanisms traced by emission lines like the hydrogen Brackett-γ and its location, on the presence of dust inside the systems' sublimation radius, on the origin of the protoplanetary disks brightness distribution asymmetries, and their time-variability.
Particularly interesting are the young stellar objects belonging to the Herbig stars sub-group. With a stellar mass canonically set to range between ~ 2 and $\sim 12\,\mathrm{M}_\odot$, they are thought to be, in many aspects, the bridge between the relatively well understood low mass pre-main-sequence stars and the still obscure high mass ones.

In this work I study three different Herbig stars, each one of them being a benchmark for various open-ended questions on young stellar objects evolution and on the physical processes happening in their innermost circumstellar regions.
The first object is HD 141569, a well-known Herbig star characterized by a transitional disk. GRAVITY was able to detect a very faint dust emission in the first au of the system, previously thought, as the majority of transitional disks, to be dust-depleted. The system, despite his old age, shows a Brγ-line emission, for which the GRAVITY spectrum and differential phases suggest the emitting gas to lie in a Keplerian disk around the central star.
Through the study of the second system, HD 98922, a unique variability investigation of its innermost gas and dust material is presented. I suggest a way to bypass poor (u, v)-plane coverage and to assess variability through interferometric data geometrical modeling. The modeling suggests an orbiting, crescent, dusty feature, hinting to a dust-trap scenario at milli-arcsec scale in the first au of the HD 98922 circumstellar environment. A strongly time-variable Brackett-γ-line emission is also observed, which follows at first order the orbital motion of the dusty feature.
Lastly, the quadruple Herbig stars system HD 52721 is studied and tested for interferometric binarity in au scales. A new companion is detected, as well as a complex and strongly time-variable Brackett-γ-line emission.

Contents

Chapter 1

Introduction

A relatively lucky kid living in a rural area, by looking up at the sky during a clear night, would get amused by the numerous bright dots that constellate what it seems a dark and empty void. The space between the stars in the Milky Way is however far from being vacant. These regions are indeed inhabited inhomogeneously by a tenuous matter component, the interstellar medium, mainly composed of hydrogen, and which was observed in many ways, from its obscuration and reddening effects on starlight, to its various emission mechanisms (see e.g., Ferrière 2001, and references therein). If we do not consider dark matter, an hypothetical form of matter unaffected by electromagnetic radiation which interact with its "normal" counterpart only through gravity and thought to account for $\sim 90\,\%$ of the Milky Way total mass (e.g., Watkins et al. 2019), about $95\,\%$ of the galactic volume is occupied by hot ($\gtrsim 6000\,\mathrm{K}$), neutral, ionised hydrogen, with densities ranging between 10^{-4} and 1 particles/cm^3. In the remaining $5\,\%$, the gas is cold ($\sim$ 10-100 K), neutral, and characterized by a density of $\sim$ 20–50 particles/cm^3 (see e.g., Ferrière 2001, and references therein). This gas is concentrated in the galactic plane, and, from this cold component, high density ($10^2 - 10^6$ particles/cm^3) gas sub-regions form, in which consequent formation of ionized hydrogen and molecules occur (e.g., Valdivia et al. 2016). These sub-regions, called giant molecular clouds, account for less than 1 % of the galactic volume, and are the nursery of star formation.

The work I am about to present, focuses on the early life stage of intermediate mass stars. Even though they represent a very small portion of the total matter in the Milky Way, being the total stars mass (for stars of any ages and masses) $\sim 4\,\%$ of the total galaxy mass (McMillan 2011), young stars are of prime interest. Their formation and evolution are directly linked to the ones of their circumstellar accreting disk, and sequentially to the ones of planets. Understanding planetary systems formation may ultimately answer the questions around our origins, quenching one of our inherent inclination. Our curiosity. Which should be in astronomy, more or less, what it is all about.

Figure 1.1: Star-forming region NGC 3324 as seen in infrared by NASA's James Webb Space Telescope. Image credit: NASA, ESA, CSA, and STScI.

1.1 Young Stellar Objects

1.1.1 From Molecular Clouds to Stars

Giant molecular clouds extend from hundred to thousands of parsecs (pc), and are observed to show over-dense filamentary sub-structures. The filaments are not uniform, but are characterized by faint areas and more dense ones, the latter resembling spherical cores with a typical size of ~ 0.1 pc (see e.g., Smith et al. 2016, and references therein). The origin of these sub-structures is still debated, with one of the scenarios being turbulence produced by interactions with other molecular clouds or by supernova shock-waves, leading to gravitational collapse, with formation and consequent fragmentation of the filaments into cores (e.g., Habe et al. 1992). Star formation and evolution theory suggests that if a core is massive and compact enough, with critical values set simplistically by the Jeans mass ($M_J \propto T^{3/2}\rho^{-1/2}$) and the Jeans length ($R_J \propto T^{1/2}\rho^{-1/2}$), it will continue to collapse, following the virial theorem, meaning that half the gravitational potential energy is radiated away and half is converted into thermal energy (Jeans 1928; Prialnik 2009). A collapsing core is considered the first stage of the stars' life, and it is labeled as a young stellar object (YSO) of Class 0, following the classification of Lada (1987) and Andre et al. (1993), based on the spectral energy distribution (SED) slope between 2 and 25 μm. These objects are characterized by a SED produced only by a cold black body function in the sub-millimeter range, since the star is yet not formed.

The collapse of the gaseous core is thought to be not spatially uniform in its velocity, but it is

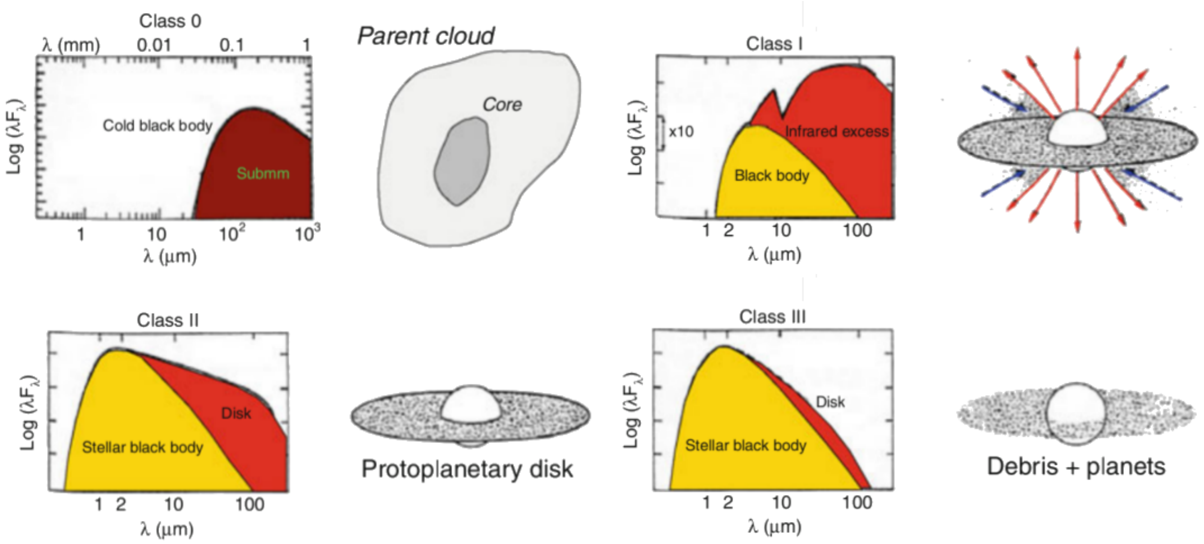

Figure 1.2: Depiction of the different star formation stages, their SED, and their Lada (1987) classification. In the SED plots, the star is marked in yellow and the circumstellar material in red. Figure adapted from (Gargaud et al. 2015).

faster the closer to the core center of mass, leading to the formation of a proto-star embedded in an infalling envelope that still accounts for most of the system mass (e.g., Larson 2003). Additionally, due to the conservation of angular momentum, quantity calculated to be high in the solar system (Armitage 2007), the envelope will flatten his shape into a disk, as the size of the core decreases and the gas angular velocity increases. This evolutionary scenario interprets the origin of the observed YSOs labeled as Class I, characterized by a SED produced by a relatively weak stellar black-body, by the envelope cold black body, and by an additional strong infrared (IR) flux excess, arising from stellar light re-radiation by the material surrounding the star. In this phase the proto-star is not optically visible due to the optically thick envelope. Common to this class is the presence of ionized material outflows, in the form of jets and stellar/disk winds (e.g., Tafalla et al. 2017, and references therein).

The proto-star is expected to continue its collapse, accreting material from its circumstellar disk and dissipating the envelope, until it is hot enough to burn deuterium (e.g., Larson 2003). The proto-star reaches the so-called pre-main-sequence (PMS) phase, where YSOs are labeled as Class II. Envelopes and outflows (if present), as well as the IR excess emission seen in the SED, are fainter with respect to the ones of Class I objects. As the star collapses and accretes more and more circumstellar material, in conjunction with the dissipating effects of stellar radiation and winds, the system reaches the end stage of the PMS phase, marking the Class III YSOs. These objects show a very faint IR emission excess, arising from an almost depleted disk, referred to as “debris disk” (see Chapter 2 for a more detailed summary of their properties). In Fig. 1.2 a depiction of the star formation and evolution phases is shown, as well as their characteristic SED. Once the nuclear reactions in the star interior counterbalance gravity, the star stops collapsing, reaching the so-called main-sequence (MS), a long-lived stable phase characterized by hydrogen burning (e.g., Larson 2003). The star formation process is completed.

1.1.2 Herbig Stars

Herbig Ae/Be stars are optically visible PMS stars characterized by a relatively high mass, canonically ranging between ~ 2 and $\sim 12\,\mathrm{M}_{\odot}$. They belong to the YSOs Class II or III of Lada (1987) classification. Historically, Herbig Ae/Be stars were classified as such on the base of three criteria set by Herbig (1960): emission line objects with a spectral type A or earlier, located in an obscured region, and that illuminate nearby and bright nebulosities. Additional criteria were added through the years, like the presence of IR excess and photometric variability (The et al. 1994), but nowadays none of them is a necessary requirement to classify a star as Herbig Ae/Be, since this group encloses objects with a relatively wide range of ages (e.g., Vioque et al. 2018). One common characteristic that these early spectral type stars nonetheless share is the fact that they show prominent IR excess due to thermal re-radiation by their dusty circumstellar accretion disks (e.g., Garufi et al. 2022), sign of their PMS nature.

1.1.3 Herbig Stars SEDs Classifications

The SEDs of Herbig Ae/Be stars show different slopes and a wide range in the amount of IR excess, reflecting the different properties of the stars and their circumstellar environment (Garufi et al. 2017a, and references therein). Based on their SEDs, these stars have been classified in subgroups following diverse criteria. The most famous and first of such classifications was done by Meeus et al. (2001), who defined two families, Group I and Group II. Sources are classified as Group II if they show a continuous spectrum that can be described by a single power law, from the IR to the sub-millimeter range, which would be produced by thermal emission from $\sim 10\,\mathrm{K}$ to $\sim 1500\,\mathrm{K}$. Sources are classified as Group I if the continuum fit needs an additional strong black-body component in the far-IR.

Later, the classification in the two groups was defined quantitatively through the slope of the mid-IR SED, given by the ratio between the flux at $30\,\mu$m and the one at $13.5\,\mu$m, $\mathrm{F}_{[30/13]}$, which gives an estimate of the warm dust continuum (Acke et al. 2009). Sources showing a flux ratio smaller than 2.2, show also a far-IR excess larger than 10% of the star luminosity, and are classified as Group I sources. Sources showing a larger flux ratio, show instead a far-IR excess smaller than 10%, and are classified as Group II (Garufi et al. 2017a). Finally, the most recent classification was proposed by Banzatti et al. (2018) based on the near-IR and far-IR excess plane shown in Fig. 1.3. Indeed, the authors found that all the Group II stars of their sample, i.e. with $\mathrm{F}_{[30/13]} < 2.2$, are characterized by a near-IR excess ranging between 14% and 19%, while for their Group I sample, i.e. sources with $\mathrm{F}_{[30/13]} > 2.2$, they found two subgroups, one characterized by a low ($\lesssim 10\%$) near-IR excess, and a second characterized by a high ($> 20\%$)

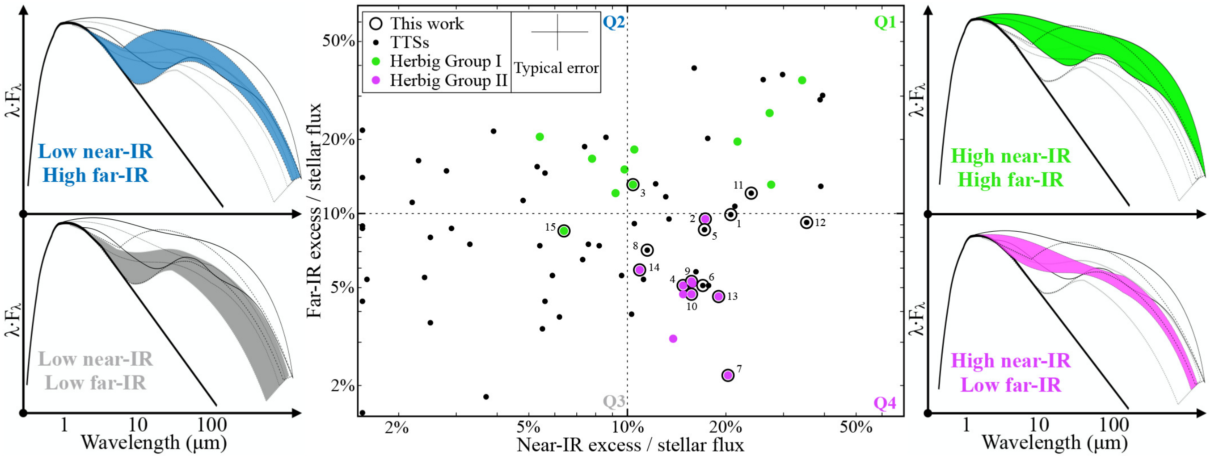

Figure 1.3: Near-IR versus far-IR excess as fraction of the stellar luminosity for the sample of stars studied in Garufi et al. (2022). The dashed lines represent the suggested separation between low and high excesses. Laterally, the SEDs for each quadrant is shown. Figure from Garufi et al. (2022).

one. The 10% value was then used to split the near-IR and far-IR excess plane in four quadrants, in which the Herbig stars locate in three clusters.

1.1.4 Meeus Groups Disks Properties

The two Meeus groups are thought to be associated to different star and disk properties, like photometric variability (e.g., Dullemond et al. 2003), the presence of organic molecules (e.g., Acke et al. 2004), and disk geometry (e.g., Dullemond et al. 2004a). The idea of an evolutionary link between the two groups seemed reasonable, in which the younger Group I sources would evolve through dust settling and grain growth to Group II ones (e.g., Dullemond et al. 2004a,b). Recent observations have shown the presence of gaps in the disks of a significant portion of the Group I sources, while for Group II ones, no or only very small (~ 1 au) interferometric cavities have been observed (e.g., Fedele et al. 2018; Gravity Collaboration et al. 2019; Honda et al. 2015; Maaskant et al. 2013; Menu et al. 2015). In the latter sources, the innermost region of the disk, being so close to the star, is directly exposed to the stellar radiation, it reaches very high temperatures and increases its volume, getting "puffed-up". A shadow effect is created that shields the outer part of the disk, characterized by a flattened surface (Dong 2015; Dullemond et al. 2004a). This picture would explain why Group II sources don't show the additional SED far-IR black-body component, seen instead in Group I ones. The presence of the cavity in these latter sources would make so that the star radiation reaches the outer parts of the disk, characterized by a flared surface instead (see Fig. 1.4), creating the far-IR excess (Dullemond et al. 2004a, 2001). Moreover, the scenario would explain the contrasting scattered light intensity observed in the two groups, with the Group II sources showing faint emission and Group I sources showing a strong one (e.g., Garufi et al. 2017a, 2022).

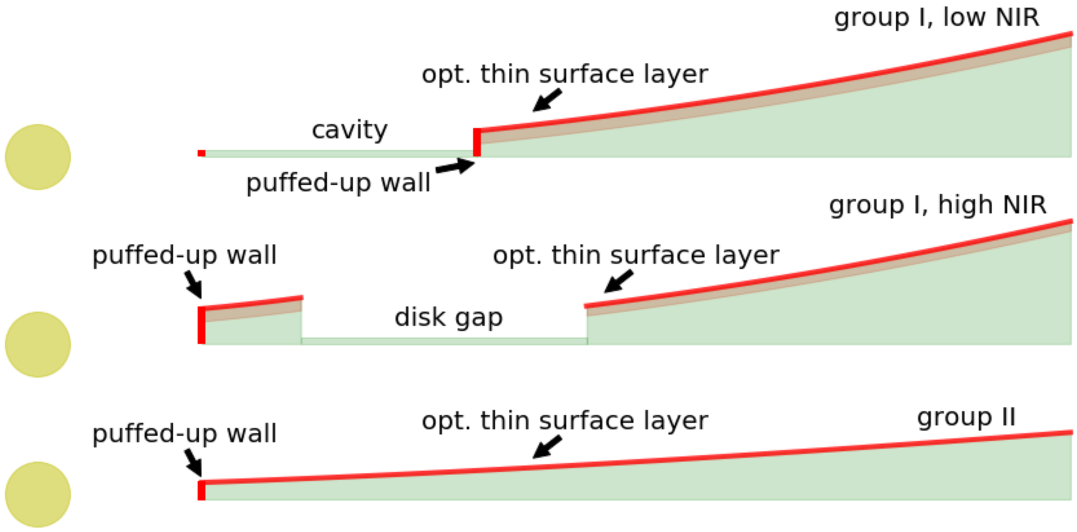

Figure 1.4: Herbig Ae/Be stars' disks depiction proposed by Banzatti et al. (2018) on the base of their SEDs. Figure from Bosman et al. (2019) adapted by Brittain et al. (2023).

Various mechanisms are thought to produce the inner gaps, like the clearing effect of a low-mass companion (Papaloizou et al. 1984), magneto-rotational instability (Flock et al. 2015), or photo-evaporation (Ercolano et al. 2017); gaps that will last throughout the disk life. The supposedly more evolved Group II sources, characterized by the absence of gaps, make so that the evolutionary link between the two groups is put into question. Moreover, the fact that several ALMA observations showed high frequency of small size disks ($\lesssim 30\,\mathrm{au}$) in star-forming regions (e.g., Cieza et al. 2019), may explain the faint scattered light emission in Group II sources without relying on the evolution scenario. The instruments used so far to observe these objects might not have the high angular resolution needed to resolve such small disks (Garufi et al. 2017a). This is why authors have suggested the two groups being two distinct disk evolutionary paths, depicted in Fig. 1.5, which have a "common ancestor" characterized by a continuous flared density distribution (e.g., Garufi et al. 2017a; Maaskant et al. 2013).

1.1.5 Star Accretion in PMS stars

Star formation and evolution theory depict Herbig Ae/Be stars having a convective core and a radiative envelope once they reach the MS phase after the fully convective PMS stage. In contrast, T Tauri stars, the less massive ($M \lesssim 2\,M_\odot$) counterpart of Herbig Ae/Be stars, reach the MS phase with a radiative core and a large convective envelope. Stars with a mass higher than $\sim 10\,M_\odot$, due to their fast evolution, are not optically visible during their PMS phase (Lumsden et al. 2013), and reach the MS stage with a fully radiative structure. The different stars' interior physics translate in different star properties, like temperature, radius, surface gravity, magnetic field strength, and therefore accretion mechanism. Material accretion from the circumstellar

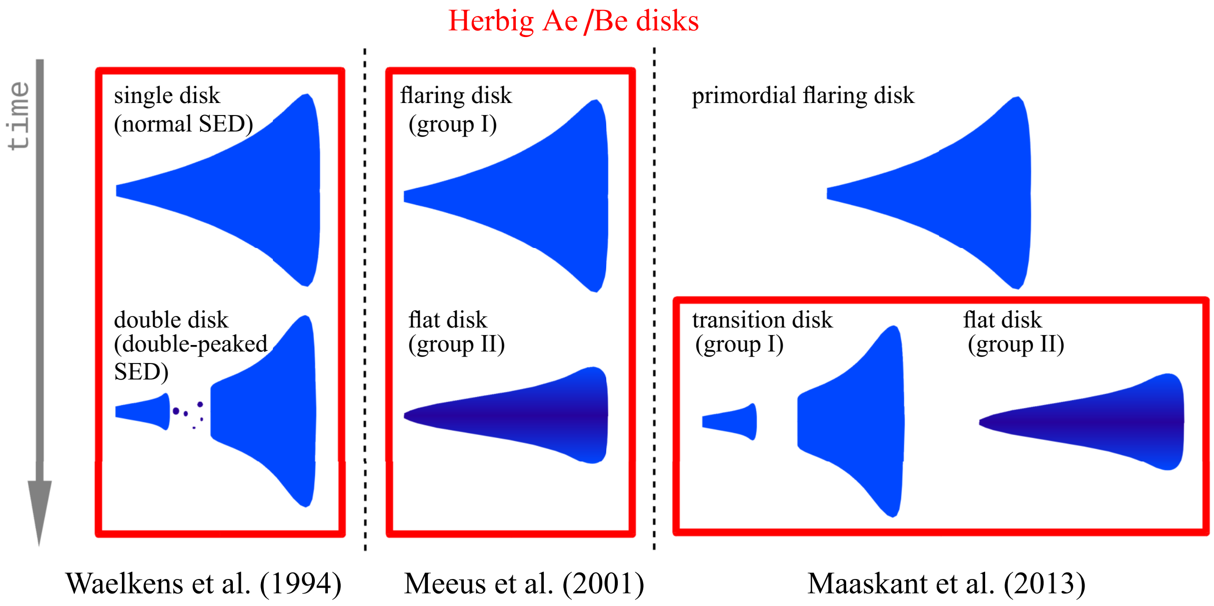

Figure 1.5: Herbig Ae/Be stars' disks evolution scenarios proposed in the past. The red boxes pinpoint the Herbig Ae/Be phase. Figure from Menu et al. (2015).

environment onto the central star is one of the fundamental processes in the life and death of the circumstellar disk itself. Figuring out the different mechanisms of such phenomenon and in which conditions they manifest, will help us comprehend the evolution of such objects, still not clear, especially for the higher mass ones.

For low mass Class II stars, i.e. T Tauri stars, the accretion process is generally recognized as driven by their strong dynamo-generated magnetic field, i.e. generated by internal convection and rotation of charged particles (e.g., Donati et al. 2011; Gregory et al. 2012; Johns-Krull 2007; Villebrun et al. 2019). The field truncates the circumstellar disk at a radius of a few stellar radii, where the ram pressure of the material spiraling inward is counterbalanced by the magnetic pressure exerted perpendicular to the field lines (Bessolaz et al. 2008). Here the material is forced to flow through the magnetic field lines onto the star at free fall velocity, close to its magnetic poles, creating heated shock regions of a few percent of the stellar surface and producing X-ray radiation. The radiation is absorbed by the surrounding gas which then re-radiates at ultra-violet (UV) wavelengths, producing an UV excess, observed in some cases (Curran et al. 2011). For a more detailed treatment of magnetospheric accretion, I refer the reader to Bouvier et al. (2007a) and references therein.

In higher mass stars, due to their radiative structure, the dynamo process is weaker. This translates in a significantly weaker magnetic field, which is rarely detected (e.g., Alecian et al. 2013; Villebrun et al. 2019), and therefore in a smaller disk's truncation radius. Moreover, the higher the mass, the higher is the radiation pressure, which hinders the infalling material up to a point of zero accretion (e.g., Kuiper et al. 2018). In such objects, the puzzling situation of how the disk is dissipated, is yet to be clarified. Herbig Ae/Be stars, with their intermediate mass, could be in this context one of the key objects to study, since they may display the shift from magnetospheric accretion to the thus far unidentified accretion mechanism experienced by high mass PMS stars.

1.1.6 Accretion Diagnostics

Before presenting the latest results and the accreting scenarios proposed for the massive PMS stars, it is important to remind that to date no direct observations of the accretion process were made due to the small size (~ 0.1 au) of the region where these processes take place. This is why the science community relies on measurements of observables that trace accretion. One of the most reliable tracer is the UV excess. Through accretion shock modeling of an object's SED in the Balmer region, an estimate of its mass accretion rate ($\dot{\mathrm{M}}_{\mathrm{acc}}$) can be derived (e.g., Ingleby et al. 2013; Mendigutia et al. 2011a). If the stellar mass ($\mathrm{M}_\star$) and radius ($\mathrm{R}_\star$) are known, the accretion luminosity ($\mathrm{L}_{\mathrm{acc}}$), i.e. the amount of gravitational potential energy converted into UV radiation, can be as well deduced (e.g., Herczeg et al. 2008):

$$\mathrm{L}_{\mathrm{acc}} \approx \frac{\mathrm{G}\mathrm{M}_\star \dot{\mathrm{M}}_{\mathrm{acc}}}{\mathrm{R}_\star}\left(1 - \frac{\mathrm{R}_\star}{\mathrm{R}_{\mathrm{tr}}}\right), \tag{1.1}$$

where R_{tr} is the truncation radius, assumed to be $\sim 5\,\mathrm{R}_\star$ for T Tauri stars (Gullbring et al. 1998), and $\sim 2.5\,\mathrm{R}_\star$ for Herbig Ae stars (Muzerolle et al. 2004). Unfortunately, it is not easy to attain UV observations. One way around to estimate the accretion rate is the use of empirical correlations, which were found to relate the luminosity of a quite vast group of gas emission lines ($\mathrm{L}_{\mathrm{line}}$), that would be produced during the accretion flows from the disk onto the star, with the accretion luminosity (e.g., Mendigutia et al. 2011a):

$$\log\left(\frac{\mathrm{L}_{\mathrm{acc}}}{\mathrm{L}_\odot}\right) = A + B \times \log\left(\frac{\mathrm{L}_{\mathrm{line}}}{\mathrm{L}_\odot}\right), \tag{1.2}$$

where A and B are given by the intercept and the slope of the line fitting the observational data in the $\log(\mathrm{L}_{\mathrm{acc}}/\mathrm{L}_\odot) - \log(\mathrm{L}_{\mathrm{line}}/\mathrm{L}_\odot)$ plane (see Fig. 1.6). Example of these spectral tracers are the Hα-line and the Brγ-line. These correlations were then shown to stem from the more fundamental correlation between the accretion luminosity and the star luminosity, which is also used (e.g., Mendigutia et al. 2015).

However, some caution is required when these correlations are adopted. Firstly, one assumes that all the line emission stems from accretion, which is not the only process that can produce emission lines, other processes being for examples stellar winds (e.g., Strafella et al. 1998) or disk-field driven wind (e.g., Ferreira 1997). Secondly, the mass accretion rate estimate through accretion shock modeling and the estimate of the accretion luminosity, are less reliable the less

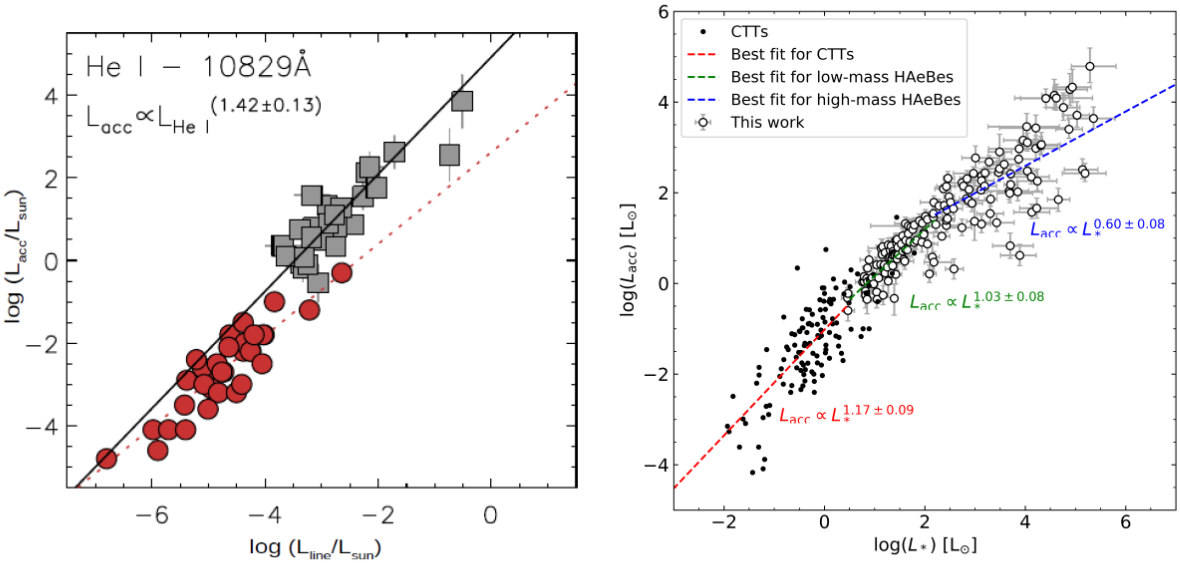

Figure 1.6: Left – UV excess accretion luminosity versus He I 10829 Å line luminosity for Herbig Ae/Be (gray markers) and T Tauri stars (red markers). The samples used are listed in Fairlamb et al. (2017). Figure from Fairlamb et al. (2017). Right – Hα-line accretion luminosity versus stellar luminosity for Herbig Ae/Be (white makers) and T Tauri stars (black markers). The samples used are listed in Wichittanakom et al. (2020). Figure from Wichittanakom et al. (2020).

reliable are the estimates of the stellar mass, radius, temperature, and distance. Additionally, for the case of high mass stars, the determination of the UV excess gets more complex, since these stars intrinsically have a significant UV emission due to their high temperature (e.g., Jiménez-Donaire et al. 2017). Lastly, the correlations found could be biased. This could be especially true for the Herbig Ae/Be stars, that are known in small number ~ 270, in contrast with the thousands of T Tauri stars. The Herbig Ae/Be stars group is also greatly heterogeneous, since the sources on the higher end of the mass range are scarse and easily mistaken for MS classical Be stars (Vioque et al. 2018).

1.1.7 T Tauri and Herbig Ae stars similarities

Returning on the question of the accretion mechanism for high mass PMS stars, in the recent years more indications have been found on the fact that Herbig Ae stars could experience magnetospheric accretion comparable to the one experienced by T Tauri stars. For example, the correlations found for Herbig Ae stars between the accretion luminosity and the Hα-line (e.g., Wichittanakom et al. 2020), the Brγ-line (e.g., Grant et al. 2022), and many other lines (e.g., Fairlamb et al. 2017), have comparable slope within the error bars with the ones found for T Tauri stars. The scatter of the data points in the $\log(L_{acc}/L_\odot) - \log(L_{line}/L_\odot)$ plane is also comparable between the two groups. This is not true for Herbig Be stars, the more massive ones, as shown in Fig. 1.6 for the He I 10829 Å line and the Hα-line. The breakpoint is found to be at ~ 4 M⊙ (Wichittanakom et al. 2020). For higher mass sources, indeed, the mechanism of magnetospheric accretion was shown to be not compatible (e.g., Fairlamb et al. 2015).

Additional evidences on the similarity between T Tauri stars and Herbig Ae come, for example from magnetospheric accretion modeling, spectroscopic variability, and linear spectropolarimetry studies. Regarding the first method, Muzerolle et al. (2004) showed that their model can reproduce the profiles of the emission lines observed in the Herbig Ae star UX Ori. Through variability studies, T Tauri and Herbig Ae stars were observed to share similar variability timescales and amplitude in the Hα-line strength and equivalent width (Costigan et al. 2014), variability that can be reproduced by more complex non-axsymmetric magnetospheric accretion models (see e.g., Bouvier et al. (2007a), and references therein). The variability is found to be significantly different in Herbig Be stars with respect to the Herbig Ae ones. For the former, the Hα-line is more stable, with smaller, or in some cases close to null, variations amplitude (Mendigutia et al. 2011b). Lastly, similarity were noticed between T Tauri and Herbig Ae stars in their Hα-line linear spectropolarmetric properties, while Herbig Be stars show distinctive ones (Ababakr et al. 2017; Vink et al. 2005).

1.1.8 Accretion in Massive YSOs

All the diverse behaviours observed in the Herbig Be stars suggest that a different accretion mechanism in high mass stars is occurring. However, no clear scenario has emerged up to now. The most credited one is the so-called "boundary layer" accretion scenario (Lynden-Bell et al. 1974). Concisely and qualitatively, in this accretion scenario the circumstellar material extends up to a close distance from the star, where the particles start to release their kinetic energy by decreasing their velocity from Keplerian to the rotational velocity of the star, until they are accreted by the latter. The boundary layer scenario was firstly proposed for T Tauri stars, but it cannot explain some of the properties seen in these objects, like the redshifted self-absorption and the inverse P Cygni line profiles, reproduced instead by magnetospheric accretion models (Muzerolle et al. 2001). The boundary layer scenario is instead compatible with some of the Herbig Be stars properties, like the Hα-line depolarization (Ababakr et al. 2017) and the undersized near-IR continuum emission (e.g., Gravity Collaboration et al. 2019), both explainable in theory by the fact that the disk basically reaches the star. A conclusion however cannot be made, since no boundary layer model has been tested in Herbig Be or more massive stars.

1.2 The Circumstellar Environment of YSOs

The processes of star formation and evolution, and especially the ones of planets, is still a matter of debate, but it is acknowledged that the circumstellar material plays a major role in them. Planet formation theories cannot be comprehensive if they do not account for the phenomena

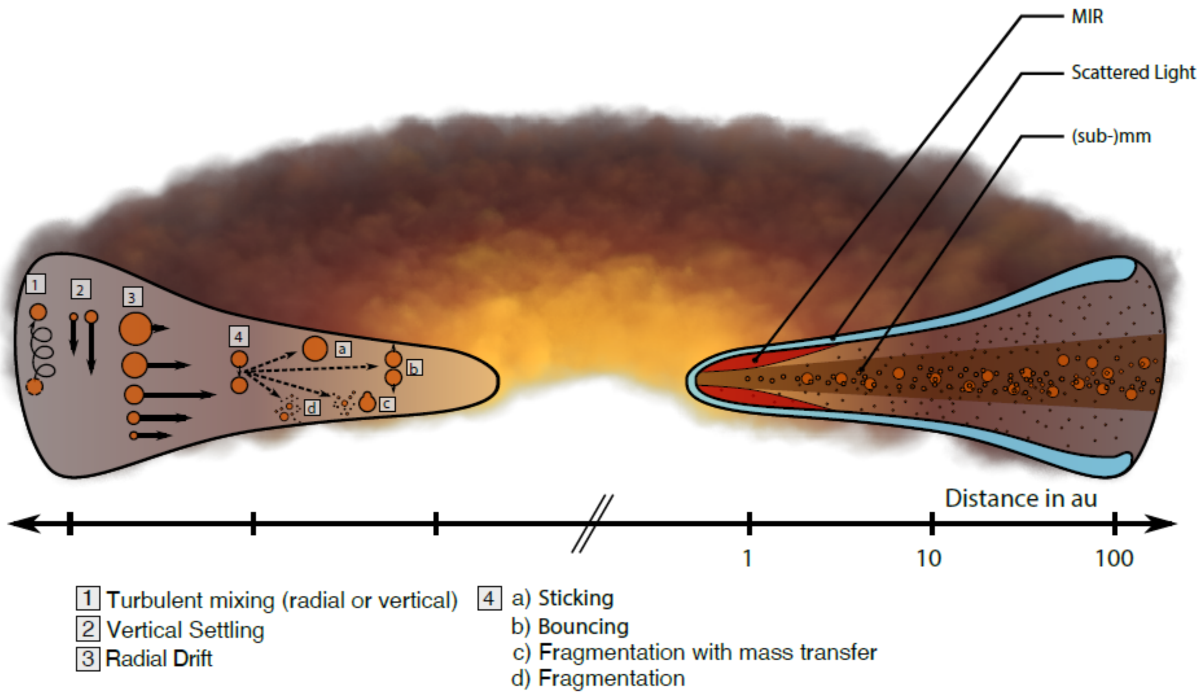

Figure 1.7: PMS star's disk structure depiction. The main grain transport and collision mechanism properties are shown on the left. The different lengths of the arrows represent the different grain velocities. On the right, the different disk regions probed by various wavelengths are highlighted by the different colors. Figure adapted from Testi et al. (2014) by Brittain et al. (2023).

giving birth to and happening in protoplanetary disks. This is why the science community has been motivated in studying these environments, leading to a major theoretical and observational effort, and improving our knowledge about them.

1.2.1 The Dust and Gas Interplay

The life of dust particles in a protoplanetary disk is directly linked to the gas component in many different ways. The dynamical properties of the dust grains, for example, are deeply affected by their more massive gaseous counterpart. Indeed, they do not orbit freely in a Keplerian motion around the star, but their movement is countered by the gas; a friction effect that under certain conditions can be quite significant (Whipple 1972). This phenomenon is due to the fact that while the dust particles are affected by centrifugal and gravitational forces only, which would result in Keplerian orbits, the gas is affected also by pressure forces that usually point outwards. These additional forces lead the gas to move in sub-Keplerian velocity orbits, creating a velocity mismatch between the two components.

The mismatch translates in a deceleration of the dust particles, which lose angular momentum and spiral towards the disk's inner regions, phenomenon called "radial drift" (Weidenschilling 1977; Whipple 1972). The intensity of the force exerted on the dust depends on the relative motion between gas and dust, on the dust particle size, and on the local gas surface density (e.g., Birnstiel et al. 2010; Brauer et al. 2008). The force's intensity, and therefore how efficiently the gas and the dust are coupled, can be described by the Stokes number:

$$\mathrm{St} = \tau_s \, \Omega_K = \frac{\pi a \rho_\bullet}{2\Sigma_\mathrm{g}}, \tag{1.3}$$

where $\tau_s = m\,v/F$ is the friction time, i.e. the characteristic time scale for acceleration or deceleration of the dust particles, with m the particle mass, v the particle velocity, and F the drag force, Ω_K is the particle orbital period, a the size of the grain, $\rho_\bullet$ its internal density, and Σ_g the local vertically integrated gas density. When $\mathrm{St} \lesssim 10^{-4}$, the particles are said to be well coupled to the gas, while, when $\mathrm{St} \gtrsim 1$ the coupling is weak. The smaller the particle, the stronger is the coupling. This means that the radial drift effect is stronger on larger grains. Quantitatively, for particles smaller than $\sim 1\,\mathrm{mm}$, the inward drift velocity is not significant, while it is of the order of $\gtrsim 50\,\mathrm{m\,s^{-1}}$ for mm-sized particles and above (Testi et al. 2014). In about 100 years, large dust grains migrate towards region close to the star to finally be accreted by the latter (Weidenschilling 1977). Additionally to this inward movement, the drag force mixes radially and vertically the dust particles due to the gas turbulence (Whipple 1972).

1.2.2 Dust Growth and Destruction

The gas-dust interaction and its consequences presented above, increase the chances of collision between the dust particles. Depending on the physical and dynamical properties of the latter, like for example their shape, porosity, chemical composition, charge state, and collisional velocity, the kinetic energy of two colliding particles can be dissipated efficiently. This can lead to hysteresis effects at the contact point, which cause a direct hit-and-stick coagulation of the two particles (Chokshi et al. 1993). The more particles coagulate with time, the more the resulting body becomes compact, as part of the kinetic energy of the colliding particles is absorbed, rearranging its internal structure. The hit-and-stick coagulation process starts to become less efficient as larger grains form ($\approx$ cm size range). The kinetic energy is not dissipated well enough and the particles bounce upon collision, stage called "bouncing barrier" (Zsom et al. 2010). Moreover, if the kinetic energy of the colliding particles is too high, the collision can lead to the fragmentation of the two bodies (e.g., Birnstiel et al. 2010; Windmark et al. 2012; Zsom et al. 2010). The dust in the disk reaches therefore a stage in which growth and destruction balance each other, and the largest pebbles are accreted by the star, stage called the "meter-size barrier". Particles larger than the meter threshold could originate through the "growth by mass-transfer" process, in which a larger body grows by collision with other smaller low-velocity particles (e.g., Kothe et al. 2010; Windmark et al. 2012; Zsom et al. 2010). However, it is not clear yet if planetesimals could form solely by this process. A depiction of the processes taking place in YSO's disks is shown in Fig. 1.7. In Fig. 1.8 are shown the different dust collisions results and the required physical conditions for them to happen.

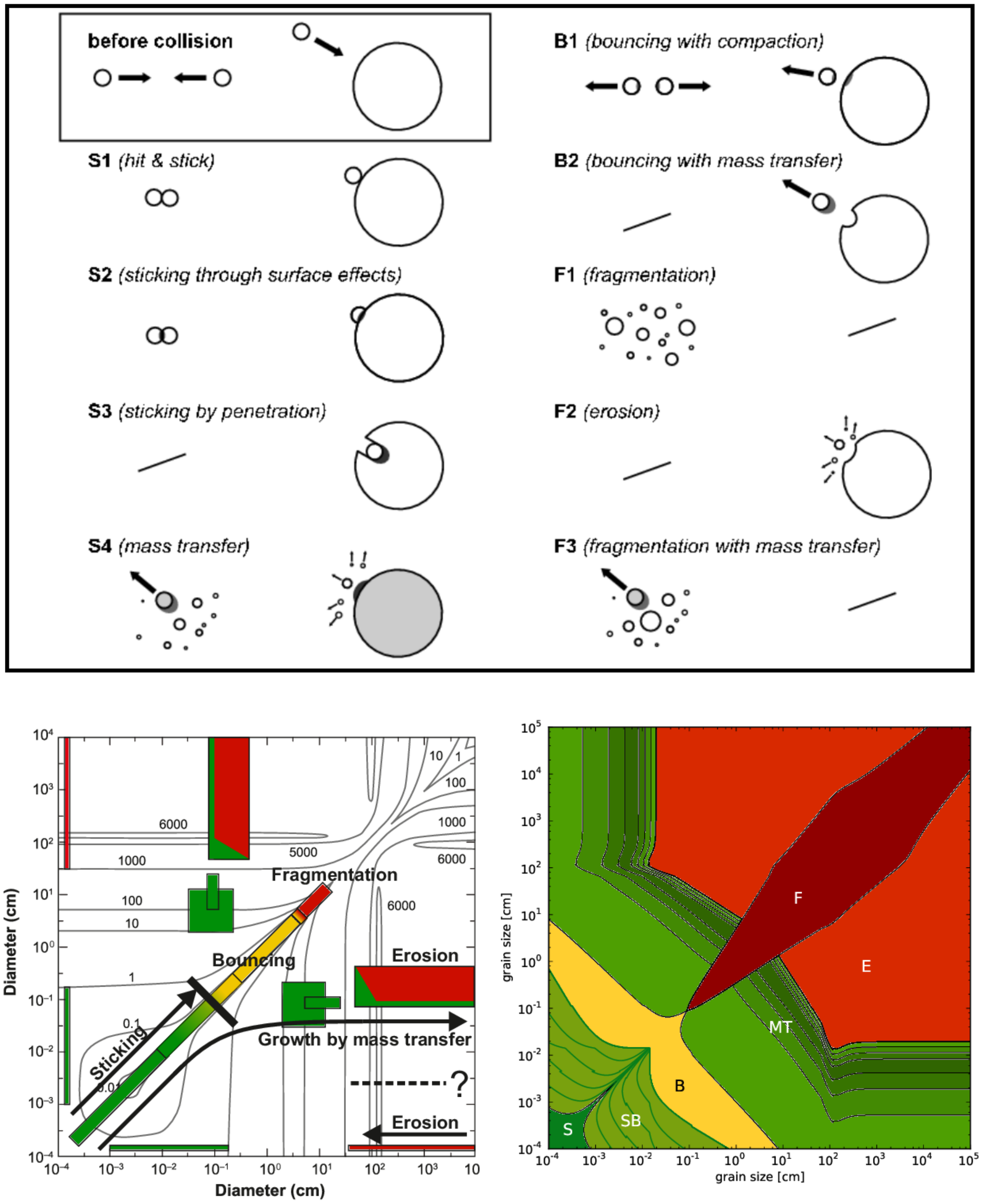

Figure 1.8: Top – Collision scenarios between similar-sized and different-sized particles. The gray color refer to a compact mass. Figure from Zsom et al. (2010). Bottom – silicates collisions outcomes for different particles sizes and velocities. Left – The collision velocities (in units of cm/s) are shown in the background. The colored boxes represent the explored parameter space and results of laboratory experiments by Weidenschilling et al. (1993). Right – results of laboratory experiments by Windmark et al. (2012). Figure from Testi et al. (2014).

Surprisingly, since the beginning of the 21st century, numerous observations have indicated that the outer regions of protoplanetary disks are populated also by mm- and cm-sized dust particles (e.g., Ricci et al. 2010; van Boekel et al. 2003), as if the radial drift is in some way counteracted. The best supported explanation for this supposedly inconsistency is the so-called "dust trap" scenario, in which a region of the disk is characterized by the presence of a pressure bump, restraining the dust particles (e.g., Klahr et al. 1997). In these regions, the increased concentration of dust particles, coupled with the low collisional velocities, pushes the standard gas-to-dust ratio value of 100 close to unity (e.g., Yang et al. 2017), favouring further growth of the particles into planetesimals through streaming instability (Johansen et al. 2007; Youdin et al. 2005) or direct gravitational collapse (Goldreich et al. 1973; Youdin et al. 2002). When the dust trap scenario was proposed in the first decade of the century, the only support on the theory were observations of disks which showed the presence of gaps and asymmetries (e.g., Isella et al. 2010). However, the low angular resolution and the low signal-to-noise ratio of the images did not allow to recognize the scenario as trustworthy by the science community.

1.2.3 Observations of the Circumstellar Environment

Different methods were used through the years to observe the circumstellar environments of T Tauri and Herbig stars. Each method is sensitive to distinct emissions and therefore to the various chemical composition of the materials and the different locations of the emission itself with respect to the star and the disk midplane. The main three methods are:

- observations of optical and near-IR scattered light emission by $\sim\mu$m size dust particles located in the disk surface.

- observations of continuum emission in the wavelength range from $\sim 1\,\mu$m to ~ 1 cm by $\sim\mu$m or millimeter size dust grains located respectively in the disk surface and in the midplane.

- observations of the gas component, that makes the bulk of the disk itself, through spectral lines emission in the wavelength range from $\sim 1\,\mu$m to the millimeter.

Even though one does not get a complete picture of the circumstellar environment, the diverse properties of the tracers allow to gain useful information on different regions of the disks. In Fig. 1.9, the three emissions are shown for the disk of the T Tauri star TW Hya. I underline the various sizes of the emitting components, the distinct locations of the emissions' peak (due to the different temperature needed to emit at a particular wavelength), the different degree of resolution, and the fact that observations through scattered light do not allow to examine the innermost region of the circumstellar environment ($\lesssim 10$ au) due to the contamination of the disk emission by the central star.

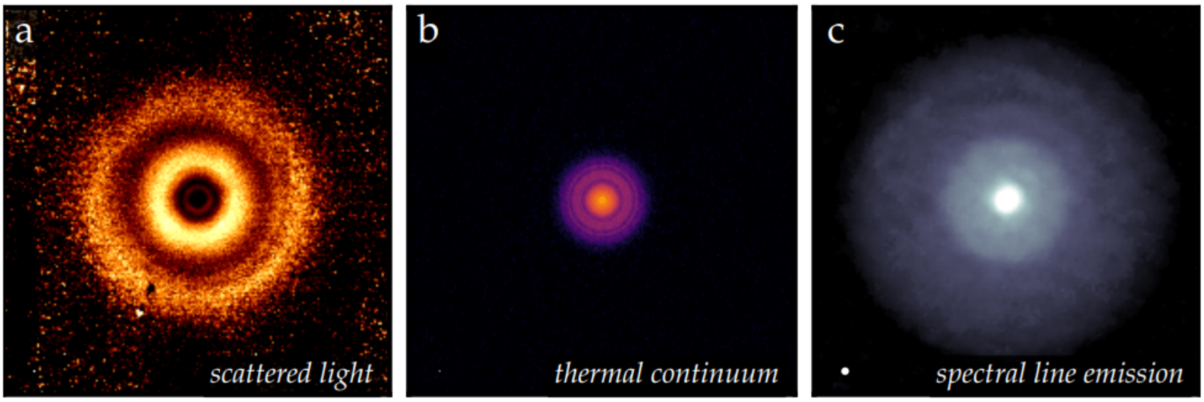

Figure 1.9: TW Hya disk from three different tracers. Left – scattered light at $\lambda = 1.6\,\mu$m (van Boekel et al. 2017); center – 0.9 mm continuum (Andrews et al. 2016); right – CO $J = 3-2$ spectral line emission (Huang et al. 2018). The white ellipses in the left corner of each panel represent the resolutions. Each panel spans 500 au on each side. Figure from Andrews (2020).

1.2.4 Observing "Dust Traps"

To observe such overdense disk regions however, angular resolution of the order of ~ 0.1" is needed, considering the small size of these features (on the order of 1 to tens of au) with respect to the size of the disks (hundreds of au), and the distance of the objects ~ 100-200 pc (even larger for Herbig Be stars, $d \gtrsim 500$ pc). It was only with the advent of ALMA (ALMA Partnership et al. 2015) operations in 2011 that the first indications of dust traps were directly observed. Remarkable images were obtained for the circumstellar disk around the Herbig star Oph IRS 48 with an angular resolution of ~ 0.25", in which a highly asymmetric millimeter continuum emission is clearly seen (van der Marel et al. 2013). The turning point was not only the asymmetry, but the fact that the latter is coupled with a CO emission evenly distributed in a gapped axisymmetric disk, and with an axisymmetric mid-IR continuum disk imaged by VLT/VISIR (Geers et al. 2007), suggesting the presence of a companion.

Various phenomena are thought to originate radial or azimuthal dust traps, for example the tidal effects of a sub-stellar companion (Pinilla et al. 2012; Zhu et al. 2012), the capturing effect of a long-lived vortex (e.g., Klahr et al. 1997), or gravitational instability (e.g., Goldreich et al. 1965; Toomre 1964). The sub-stellar companion scenario was the one proposed for Oph IRS 48. The gap seen in the CO and in the mid-IR continuum disks would have been created by the clearing effect of the companion, which would generate a pressure bump in the inner rim of the gap. The bump becomes Rossby unstable, translating in a vortex (e.g., Regaly et al. 2012). The vortex would trap the particles, more efficiently the bigger they are (e.g., Zhu et al. 2012), backing-up the asymmetric continuum emission detected by ALMA in the millimeter wavelength range in Oph IRS 48. The only caveat is the pre-assumption of the companion presence as cause of the dust trap, and not the other way around, leaving the questions on planet formation still a matter of debate.

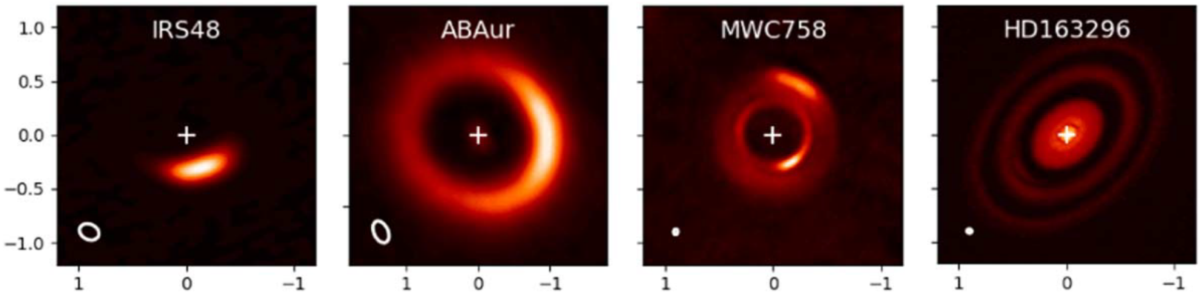

Figure 1.10: ALMA continuum images of a selection of sources of the sample studied by van der Marel et al. (2021). The white ellipses show the resolutions.

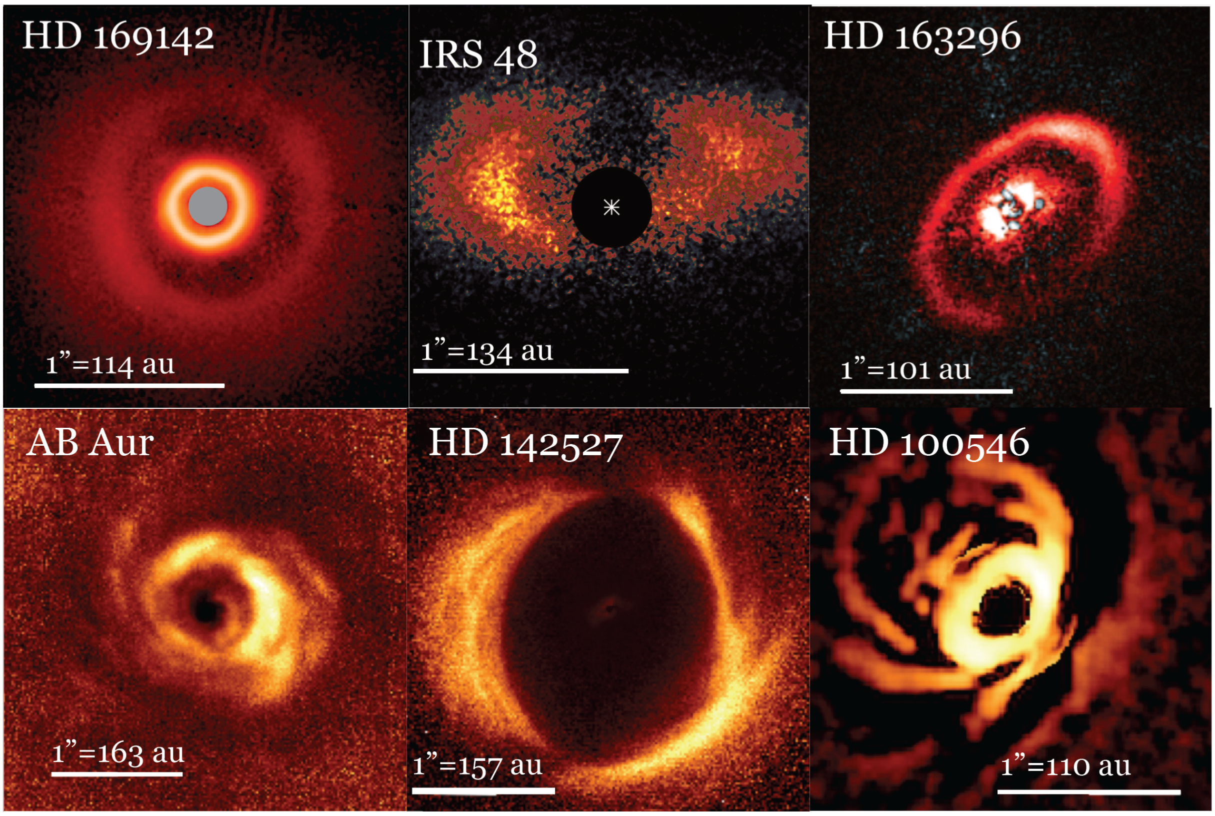

Figure 1.11: Near-IR scattered-light images of Herbig Ae/Be disks from literature. From left to right, from top to bottom: Pohl et al. (2017), van der Marel et al. (2021), Muro-Arena et al. (2018), Hashimoto et al. (2011), Avenhaus et al. (2017), Follette et al. (2017). Figure from Brittain et al. (2023).

More and more circumstellar disks were observed to be characterized by asymmetries in their dust millimeter continuum emission by ALMA (e.g., Long et al. 2018), with varying shapes ranging from peanut-shaped blobs, horseshoe-like features, bright spots in gapped disks, multiple rings, and a mixture of the above (few cases shown in Fig. 1.10). Similar asymmetries were also detected in scattered light near-IR emission, for example with VLTI/SPHERE (see Fig. 1.11, e.g., Beuzit et al. 2019; Garufi et al. 2017b). These instruments biasedly identify features located at radii of tens of au with respect to the star, due to a resolution obstacle, since the disks' scale-height decreases going towards regions closer to the star, translating in asymmetries smaller in size and weaker in emission. Observations of the first few au in circumstellar disks, where terrestrial proto-planet may form, are of prime interest, and only available through near-IR interferometry, which can reach milli-arcsec (mas) resolution.

1.2.5 The Innermost Regions of YSOs Disks

At the beginning of near-IR interferometric observations with instruments like the Infrared Optical Telescope Array interferometer (Millan-Gabet et al. 1999), the Palomar Testbed Interferometer (Colavita et al. 1999), and the Keck interferometer (Colavita et al. 2003), only information on the extent of the inner thermal emitting regions ($\sim 0.05 - 4\,\mathrm{au}$) were obtainable (e.g., Eisner et al. 2004; Millan-Gabet et al. 2001; Monnier et al. 2005). An important result nonetheless was derived. From the literature data of inner region sizes measured in the H- or K-band, Monnier et al. (2002) found a positive correlation between the latter and the star luminosity, correlation shown in Fig. 1.12 for an extended sample of T Tauri and Herbig stars (GRAVITY Collaboration et al. 2021c). The authors suggested this behaviour being due to the presence of a directly illuminated rim located at the dust sublimation radius (Natta et al. 2001), that can be expressed as (Kama et al. 2009):

$$\mathrm{R_{subl}} = \sqrt{\frac{\mathrm{L_\star C_{bw}}}{16\pi\epsilon\sigma \mathrm{T_{subl}^4}}}, \tag{1.4}$$

where $\mathrm{L_\star}$ is the stellar luminosity, $\mathrm{C_{bw}}$ is the "backwarming" factor, to account for re-emission of photons by nearby matter after the first interaction between star's photons and the disk material, ϵ is the cooling efficiency factor, that depends on the chemical and geometrical properties of the dust grains, σ is the Stefan-Boltzmann constant, and $\mathrm{T_{subl}}$ the sublimation temperature of the dusty material, $\sim 1500\,\mathrm{K}$ for silicates dust grains (Pollack et al. 1994). Some luminous objects however do not follow the relationship (e.g., Kluska et al. 2020), and show thermal emission inside the dust sublimation radius. Scenarios proposed to explain the survival of dust grains in regions so close to the star are the shielding effect of an optically thick inner gas region (e.g., Kraus et al. 2008; Monnier et al. 2005) or the presence of refractory dust species that can survive temperatures of $\sim 2100 - 2300\,\mathrm{K}$ (Benisty et al. 2010; Kama et al. 2009).

With the most advanced long-baseline interferometers, like PIONIER (Le Bouquin et al. 2011) and GRAVITY (Gravity Collaboration et al. 2017), asymmetries were finally seen also at sub-au scales in the innermost regions of many circumstellar disks (e.g., Gravity Collaboration et al. 2019; Lazareff et al. 2017), with some of them reminding the dust traps seen in the outer disks' regions. Imaging of a few sources with PIONIER data done by Kluska et al. (2020) are shown in Fig. 1.13. I underline the arc-shaped feature in HD 45677 and R CrA, and the detected emission inside the sublimation radius for most of the sources. Although the presence of overdense

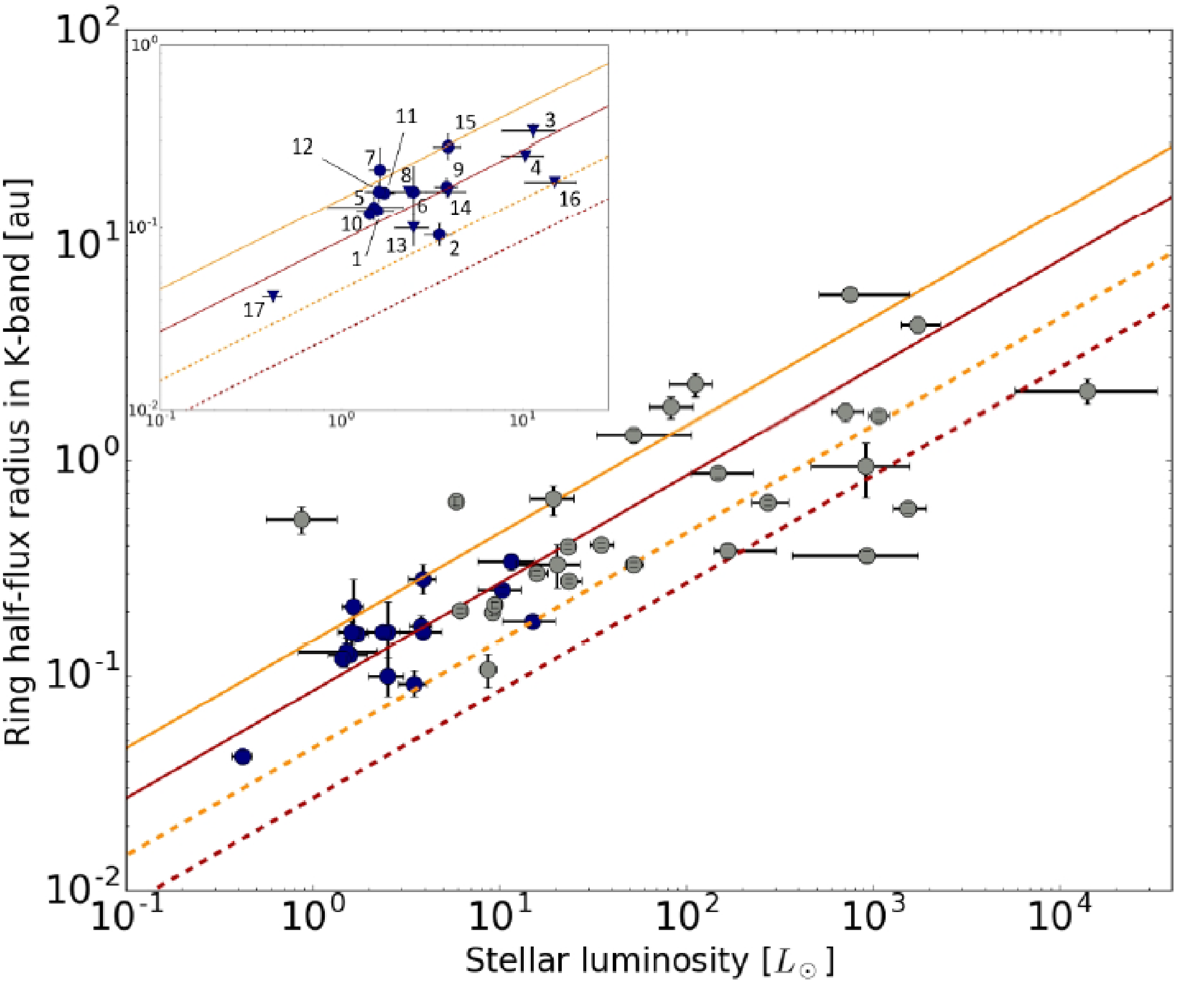

Figure 1.12: R_{Disk} - $L_\star$ correlation for the T Tauri (blue markers) and Herbig Ae/Be (gray markers) samples of Gravity Collaboration et al. (2019) and GRAVITY Collaboration et al. (2021c). The lines represent different disk models with an optically thin inner cavity. The orange color represent models with dust temperature of 1300 K, while the red a temperature of 1700 K. Full lines represent models with a dust cooling efficiency of 0.1, dashed lines an efficiency of 1. Figure from GRAVITY Collaboration et al. (2021c).

regions in protoplanetary disks were observed at all radial extents, their origin still remains an open question. To discriminate between different hypothesis and models, one approach could be to spatially resolve these systems at different wavelength and characterize even better the disks' asymmetries. In this sense, VLTI/MATISSE (Lopez et al. 2014), VLTI/GRAVITY+ (GRAVITY+ Collaboration et al. 2022), and the Next Generation Very Large Array (Di Francesco et al. 2019) could shed light on the matter.

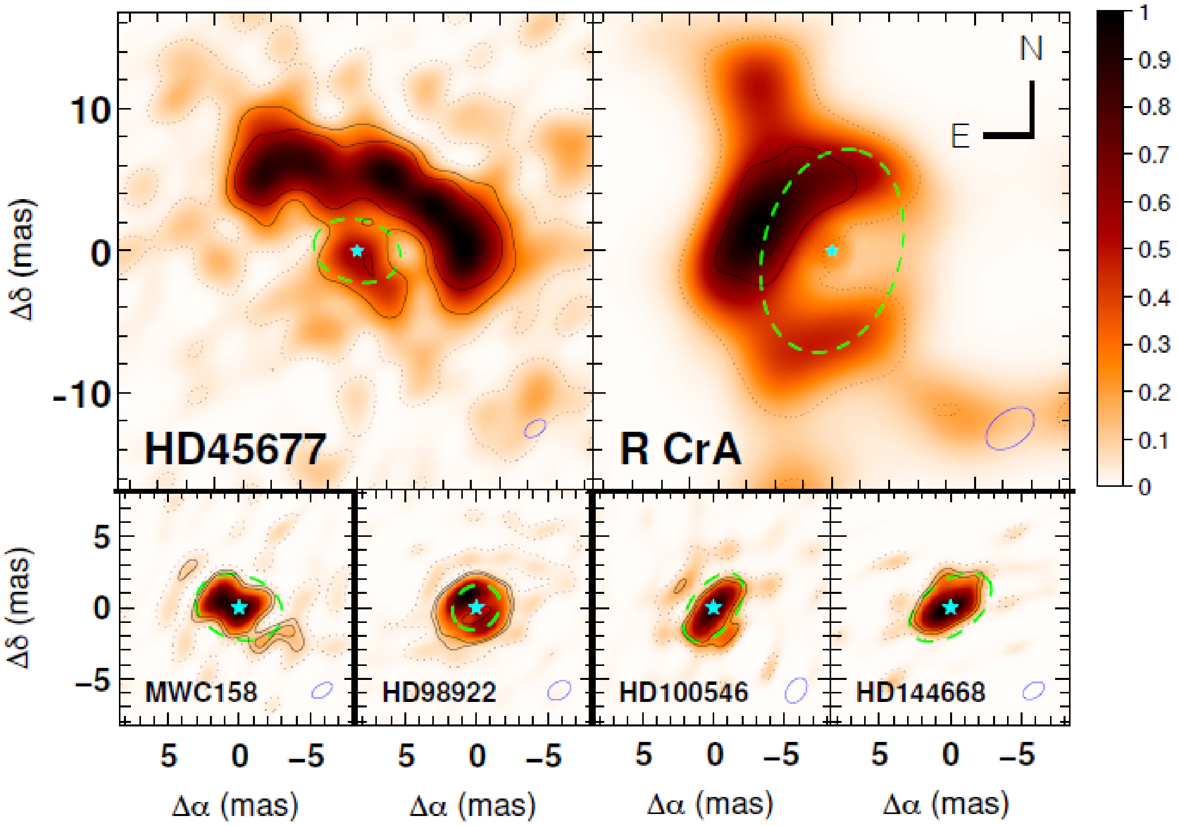

Figure 1.13: Herbig stars PIONIER reconstructed images. Top: centrally depressed objects; bottom: centrally peaked objects. The central star (cyan star marker) has been subtracted to enhance the circumstellar emission. The black contours represent the significance at 1 (dashed line), 3, and 5σ (solid lines). The blue ellipse shows the size of the beam. The dust sublimation radius is indicated by the green dashed ellipses. Figure from Kluska et al. (2020).

1.2.6 The Brγ-line Emitting Gas

A generally accepted picture of YSOs is that the bulk of the total mass of these systems comes from the gaseous component, mainly hydrogen, with a gas to dust ratio of the order of 100. As mentioned previously, the gas in YSOs is overall observed through the spectral lines arising from its emission. In the innermost ($\lesssim 1$ au) region of YSOs circumstellar disks, the gas can reach sufficiently high temperature for hydrogen to emit. Relevant for this thesis is the Brγ-line emission at 2.16612 μm, which requires a gas temperature between 8000 and 10 000 K (Muzerolle et al. 1998; Tambovtseva et al. 2016), and which arises when the hydrogen electron transits from the upper energy level characterized by the principal quantum number $n = 7$, to the lower energy level with principal quantum number $n' = 4$ (Brackett 1922). Useful information on the kinematics of the gas and hints on the physical processes happening in the emitting region can be obtained through spectral lines analysis (e.g., Tambovtseva et al. 2016), but such analysis alone cannot fully determine the origin mechanism of the emission, which is still a matter of debate. The main scenarios proposed are the following:

- Heating by stellar radiation of a gaseous disk located inside the dust sublimation radius (e.g., Gravity Collaboration et al. 2021; Kraus et al. 2008; Tambovtseva et al. 2016). A double-peaked emission line may be hinting such mechanism, since it reflects a gas disk in Keplerian rotation (e.g., Gravity Collaboration et al. 2021). This scenario is mainly relevant for Herbig stars, for which effective temperatures and mass accretion rates are significantly high to heat the gas (Tambovtseva et al. 2016; Wichittanakom et al. 2020). T Tauri stars, having lower effective temperatures and mass accretion rates, are not able to heat the gas at the temperature needed (Bertout et al. 1988).

- Heating by gas accretion onto the star through magnetospheric accretion columns, occurring inside the magnetospheric truncation radius (Muzerolle et al. 1998). This scenario is thought to be the main contributor of the Brγ-line emission in T Tauri stars, which show a strong magnetosphere (e.g., Gravity Collaboration et al. 2023; Johns-Krull 2007). It is instead thought to be marginal in Herbig stars, which show weak or no magnetic field (e.g., Gravity Collaboration et al. 2023; Järvinen et al. 2019). Asymmetric lines and/or inverse P Cygni profile may be a hints of this scenario (e.g., Bouvier et al. 2007a; Gravity Collaboration et al. 2023).

- Heating by magnetically driven stellar or disk wind, which can extend from the co-rotation radius out to several au (e.g., Ferreira 1997; Mestel 1968). This scenario has been proposed and tested for both T Tauri and Herbig stars, and it is thought for the latter to be the main contributor of the Brγ-line emission (e.g., Ferreira et al. 2006; Garcia Lopez et al. 2015). P Cygni line profile may be a hint of this scenario (e.g., Mestel 1968).

Since the different scenarios can produce similar emitting line profile (e.g., Catala et al. 1999), and since all the above mentioned processes may occur at the same time but in different spatial regions, it is crucial to spatially resolve the innermost circumstellar environment. Such observations would be able to help in discriminating between the competing models (e.g., Gravity Collaboration et al. 2021, 2023).

1.3 YSOs Variability

Variability in YSOs is a common property. Observed through photometry, spectroscopy, and interferometry, is associated to variations of both the star and the circumstellar environment. The variations are seen on disparate time-scales, periodic and non, and with diverse levels of intensity. Variability is one of the key aspects of any stellar objects, and in the case of YSOs, it is important to investigate, in order to get information on their birth and evolution processes.

1.3.1 Photometric Variability

Brightness variations have been detected for a multitude of PMS stars in the visible and in the near-IR wavelength range (Herbst et al. 1994). One of the most common variations seen are short-time optical fading events (e.g., Capistrant et al. 2022; Cody et al. 2014). These episodes are observed in both T Tauri and early-type Herbig Ae/Be stars, for which the obtained light curves show drops in brightness on the order of 10% to 50%, translating in a magnitude variability of $\Delta V \sim 0.1 - 3$ mag. The dimming events can be periodic, quasiperiodic (variable dips' shape and amplitude), or aperiodic, and last hours, days, or weeks. The causes of the variations are thought to be due to variable partial occultations of the central star by opaque dust cloud intersecting our line of sight (e.g., Alencar et al. 2010). This idea is supported by the fact that similar variable events were observed in the near- and mid-IR, even though characterized by more modest intensities of the order of $\Delta V \sim 0.1$ mag, and the fact that they are correlated with the optical ones (Ansdell et al. 2016; Cody et al. 2014). While some objects follow the correlation, some do not. A possible scenario to explain this behaviour is the presence of cool spot on the star photosphere and their rotational modulation (e.g., Vrba et al. 1993).

These scenarios described above are consistent with the periodic variations, but not with the quasiperiodic and aperiodic ones. For the former, an asymmetric magnetically-warped inner disk edge would obscure the star when crossing our line-of-sight, which would create dips in the light-curve characterized by variable amplitude due to the star variable accretion rate (e.g., Bouvier et al. 2007b). For the aperiodic events, the most up-to-date speculative scenario is stellar photosphere stochastic occultations due to accretion tongues that generate from an unstable accretion regime (McGinnis et al. 2015). Aperiodic variations are also observed as short and strong increase in the sources brightness, the so-called "burst" events, which are thought to be related to accretion shocks (e.g., Stauffer et al. 2014). These are mostly seen in younger systems, but an analysis of a large sample of PMS stars is needed before making a conclusion (e.g., Capistrant et al. 2022). Finally, variation events with moderate brightness increase are also observed as periodic episodes (e.g., Herbst et al. 1994). In this case, the variability is explained by long-lived hot spots in the stellar photosphere generated by accreting gas flows (e.g., Kulkarni et al. 2008).

1.3.2 Spectroscopic Variability

Likewise photometric variability, variations of spectral lines have been observed for many PMS stars. As mentioned earlier, spectral lines are a common accretion tracer of the circumstellar material into the star. Additionally, they can give information on the kinematics of the gas closest to the star, like infall accretion or outward wind (e.g., Muzerolle et al. 2004). The variations can be drastic and are seen on all scales from minutes to years. The lines not only show changes in their intensity, but they are also seen to turn their profile shape, for example from double-peaked to single-peaked, or from double-peaked to a P Cygni profile, and viceversa (e.g., Catala 1994, and references therein). The cause of the variability are not clear and different scenarios have been proposed, from variable accretion due to a rotating magnetosphere (e.g., Muzerolle et al. 2004), to a combination of magnetospheric accretion and a disk wind or a bipolar outflow (e.g., Garcia Lopez et al. 2016).

1.3.3 Interferometric Variability

By interferometric variability, I refer in this section to the YSOs photometric variability observed through interferometry. Indeed, the multi-year operations of PIONIER and GRAVITY revealed that, for a few sources, the innermost circumstellar material shows an emission characterized by a time-variable brightness distribution (e.g., GRAVITY Collaboration et al. 2021b; Kobus et al. 2020). The variability was detected in the squared visibility, up to $\Delta V = 0.5$, translating in variations of the flux contribution ratio between the central star and the circumstellar environment (Kobus et al. 2020), and in the closure phase signals, up to $\phi_{\rm CP} \sim 20°$, reflecting asymmetric variations of the disk's emission brightness distribution (GRAVITY Collaboration et al. 2021b). Finally, as I will show in Chapter 3, variations were also seen in the differential phases, up to $\phi_{\rm line} \sim 20°$, indicating variability of the emitting gas component photocenter with respect to the continuum one. The small number of sources in which interferometric variability was detected is likely a bias. Interferometric observations are usually taken months or years apart, and with different (u, v)-plane coverage. Long-period, high-cadence observations of the same object with similar (u, v)-plane coverage, that are needed to assess variability and periodicity, are rarely available, preventing the study of such phenomenon on such small scales. An effort is being made by the GRAVITY community and more studies will be possible in the near future. One of such study is presented in this thesis and constitutes Chapter 3.

1.4 Interferometry

As we grasped in the previous sections, the innermost au of YSOs circumstellar disks are crowded of fundamental processes, which affect both the dust and gas components. However, high angular resolution on the order of milli-arcsec is needed to observe such regions, as the distance of the closest star forming regions are on the order of $\sim 100 - 150\,$pc. Nowadays, only long-baseline interferometry manages to reach such resolutions. The following sections present briefly the basics of interferometry, based on the work of Monnier (2007) and Monnier et al. (2013), as well as the VLTI instrument GRAVITY with information gathered from GRAVITY Collaboration et al. (2017).

1.4.1 Basics of Interferometry

When observing a celestial object with any single telescope, diffraction introduces a limit on the quality of the obtained images, and limits the angular resolution (Θ) to the Raylegh-criterion, $\Theta = 1.22\,\lambda/\mathrm{D}$, where D is the diameter of the telescope. An interferometer can bypass this limitation by combining the light collected by two telescopes separated by a distance B, called baseline. In this way, the resolution achievable is $\Theta = \lambda/2\mathrm{B}$, reaching in the IR values of the order of milli-arcsec, an order-of-magnitude better than even the Hubble Space Telescope. Simplistically, the two telescopes act like a Michelson interferometer. The photons are therefore gathered to the so-called "combiner" to produce interference. The latter produces a fringe pattern from which useful information about the observed system can be derived. In Fig. 1.14 the patterns derived from observations of a point-like star at infinity and the case of two separate stars with equal brightness are depicted. The latter case is used to define the angular resolution of an interferometer, in the way that the system is resolved when the fringe contrast goes to zero at the longest baseline. For the simple case described here, the fringe contrast, commonly called visibility $\mathcal{V}$, is given by:

$$\mathcal{V} = \frac{I_{\mathrm{max}} - I_{\mathrm{min}}}{I_{\mathrm{max}} + I_{\mathrm{min}}}, \tag{1.5}$$

where I_{max} and I_{min} are the maximum and minimum fringes intensity. The fringe spacing is given by $\Delta\Phi = \lambda/\mathrm{B}$, and to have destructive interference one needs the two signals to be out of phase with one another by 180°, i.e. $\Delta\Phi = \lambda/2\mathrm{B}$.

The core of interferometry lies in the van Cittert–Zernike theorem (van Cittert 1934; Zernike 1938). The theorem states that the fringe pattern (amplitude and phase), expressed as the frequency-dependent complex visibility $\tilde{\mathcal{V}}_\nu(u,v)$, observed by an interferometer for a certain object, is equal to the normalized Fourier transform of the brightness distribution $I_\nu(\alpha,\beta)$ of the object:

$$\tilde{\mathcal{V}}_\nu(u,v) = |\tilde{\mathcal{V}}_\nu(u,v)|\mathrm{e}^{-\mathrm{i}\phi_{\tilde{\mathcal{V}}}} = \frac{\int_{\delta\Omega} \mathrm{d}\alpha\,\mathrm{d}\beta\, I_\nu(\alpha,\beta)\mathrm{e}^{-2\pi\mathrm{i}(u\alpha+v\beta)}}{\int_{\delta\Omega} \mathrm{d}\alpha\,\mathrm{d}\beta\, I_\nu(\alpha,\beta)}, \tag{1.6}$$

where $|\tilde{\mathcal{V}}_\nu(u,v)|$ is the modulus of the complex visibility, $\phi_{\tilde{\mathcal{V}}}$ is the argument of the complex visibility, referred to as the fringe phase, (u,v) are the projections of the baseline vector onto the sky plane in units of wavelength, which describe the spatial frequencies of the brightness distribution, and (α,β) the angular coordinates on the sky in units of radians. The spatial frequencies plane is referred to as the Fourier plane, or the (u,v)-plane, from the coordinates previously defined. If enough Fourier components of the observed system are collected, one can retrieve its brightness distribution through an inverse Fourier Transform. Image reconstruction through interferometry is however only occasionally done, due to the long time needed to fill up the (u,v)-plane, and, as I will show in this thesis for a particular case, during this time the system may vary. This is why it is frequent to use observations with relatively poor (u,v)-plane coverage by fitting the data with parametric geometrical models, from which important quantities can be estimated, like the flux contributions of the different components building the model, usually a point like source representing the star (or more for multiple stars systems) and a ring/ellipsoid for the circumstellar environment.

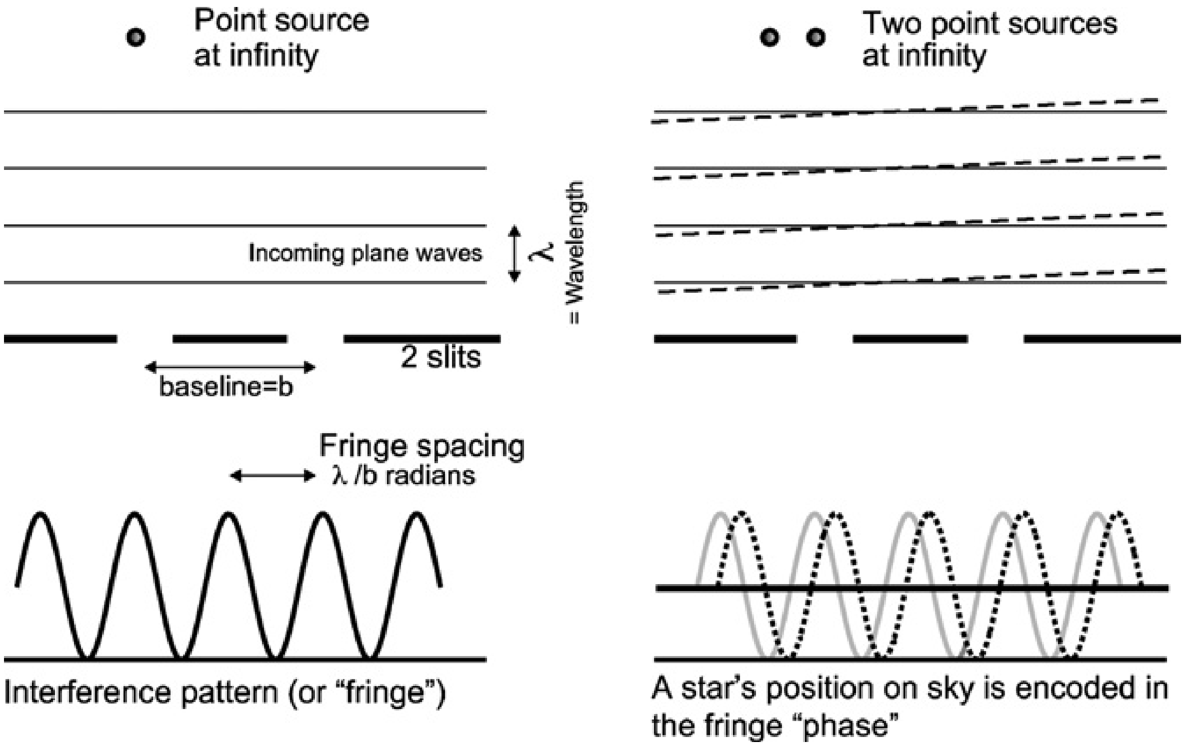

Figure 1.14: Young's two-slit interferometer ideal response to a single point source (left), and to a double point source system (right). Figure from Monnier (2007).

If the object observed is characterized by an asymmetric brightness distribution, one can obtained most of the information about it only by analysing the fringe phase. However, atmospheric effects blur the fringes, decreasing the interferometer sensitivity and spoiling the phase information, by affecting the light-paths to the telescopes. If three telescopes are available, the problem can be avoided by calculating the so-called "closure-phase":

$$\Phi_{ijk} = \phi_{ij}^{\mathrm{obs}} + \phi_{jk}^{\mathrm{obs}} + \phi_{ki}^{\mathrm{obs}} = \phi_{ij}^{\mathrm{obj}} + \phi_{jk}^{\mathrm{obj}} + \phi_{ki}^{\mathrm{obj}} \tag{1.7}$$

where ϕ_{ij}^{obs} is the observed fringe phase affected by the atmosphere for the baseline connecting the telescopes i and j, and ϕ_{ij}^{obj} is the pure object fringe phase. The closure-phase is indeed insensitive of telescope-specific phase shifts induced by atmospheric effects, as the atmospheric-induced phase delay detected above telescope j, referred as ϕ_j^{atm}, is detected as equal but opposite for baselines (i, j) and (j, k):

$$\phi_{ij}^{\mathrm{obs}} = \phi_{ij}^{\mathrm{obj}} + \phi_{j}^{\mathrm{atm}} - \phi_{i}^{\mathrm{atm}} \tag{1.8}$$

$$\phi_{jk}^{\mathrm{obs}} = \phi_{jk}^{\mathrm{obj}} + \phi_{k}^{\mathrm{atm}} - \phi_{j}^{\mathrm{atm}} \tag{1.9}$$

$$\phi_{ki}^{\mathrm{obs}} = \phi_{ki}^{\mathrm{obj}} + \phi_{i}^{\mathrm{atm}} - \phi_{k}^{\mathrm{atm}} \tag{1.10}$$

Modern interferometers use multiple telescopes not only to calculate the closure-phases, but also because the more telescopes used, the larger the number of baselines, making easier to fill-up the (u, v)-plane. Given N telescopes, the number of baselines is $N(N-1)/2$, and the number of independent closure phases is $(N-1)(N-2)/2$.

Finally, the last two interferometric observables relevant for this thesis are the so-called “differential” visibility and phase. The difference between the differential quantities and the non-differential ones is the fact that the former are retrieved across many spectral channels simultaneously. The differential quantities are usually retrieved to obtain information on gas emission lines. Since the width of the spectral lines $(\Delta\nu)$ is narrow compared to the emission frequency (e.g., $\nu/\Delta\nu > 1000$), one can assume the atmospheric-induced phase delay to be constant across the line. The atmospheric-induced phase delay can be therefore avoided by measuring the line visibility phase relative to the continuum, by subtracting the continuum phase measured on either side of the line.

1.4.2 VLTI GRAVITY

The Very Large Telescope Interferometer (VLTI) is operated by the European Southern Observatory and located on Cerro Paranal in the Atacama Desert, north of Chile. The interferometer uses the light collected in the near and mid-IR wavelength range by four 8.2 m Ritchey-Chretien Cassegrain telescopes set on fixed locations, called the “Unit Telescopes” (UTs), or by four movable 1.8 m telescopes, called the “Auxiliary Telescopes” (ATs), that can be relocated on more than 10 different stations, creating different baselines in length and position angle.

GRAVITY is one of the second generation instruments mounted in the VLTI. It interferometrically combines the light collected by the four telescopes (UTs or ATs) in the K-band, between 1.98 and 2.40 μm, and delivers spectrally dispersed interferometric observables in low (R ~ 20), medium (R ~ 500), and high spectral resolution (R ~ 4000). The instrument can observe stars as faint as $\mathrm{m_K} = 10$ through the UTs, and $\mathrm{m_K} = 7$ through the ATs, in ideal seeing conditions. One of the key feature of GRAVITY is the possibility of observing two distinct sources simultaneously (dual-field mode or off-axis). The light of the primary star is funneled to the so-called “Science Channel” (SC), while the light of the secondary is funneled to the so-called “Fringe Tracker” (FT) channel. The fringe position detected by the FT is analysed at a frequency of approximately a kHz, allowing for atmospheric effects correction. In this way, the fringe phase of the primary star observed by the SC can be calibrated to that of the secondary, usually selected to be similar in spectral type to the primary, bright, isolated, and unresolved, increasing the possible integration time up to 60 seconds. Observations in single-field mode are also possible, in which the FT and SC are funneled by 50% each of the light from the same object. Commissioned particularly for observations of the Milky Way galactic center, GRAVITY is used also to study active galactic nuclei, circumstellar disks and jets around YSOs, binarity assessment, orbits and masses of substellar companions in multiple star systems, and microlensing, setting a new standard for IR interferometry.

1.5 Thesis Outline and Goals

Since the start of GRAVITY operations in 2016, a multitude of YSOs has been observed. In this work I will focus on three different PMS stars, each one of them being a benchmark for various open-ended questions on YSOs evolution and on the physical processes happening in their innermost circumstellar regions. In Chapter 2, the attention is put on the Herbig star HD 141569 and his complex multiple rings circumstellar "hybrid" disk. The full power of GRAVITY is shown as it was able to detect a very faint dust emission in the first au of the system, previously thought being dust-depleted. In Chapter 3, a unique variability study of the innermost gas and dust material around HD 98922 is presented. I suggest a way to bypass poor (u, v)-plane coverage and to assess variability through interferometry with the GRAVITY data already available. An orbiting, crescent, dusty feature is suggested by the continuum data modeling, hinting to a dust-trap scenario at mas scale in the first au of the system circumstellar environment. In Chapter 4, the quadruple stars system HD 52721 is studied and tested for interferometric binarity in au scales. A new companion is detected, as well as a complex time-variable Brγ-line emission. In Chapter 5 I conclude the monograph by summarizing the main findings and the still open questions, and by posing newly arisen ones.

Chapter 2

The Hybrid Disk of HD 141569

In this chapter I present a study on HD 141569, which led to the publication of an open-access peer-reviewed article in the international journal Astronomy & Astrophysics (A&A) in November 2021 (Gravity Collaboration et al. 2021).

2.1 Science Case Overview

All the processes experienced by the gas and dust in the circumstellar environment of a YSO, like star accretion, star and disk winds, dust sublimation, and planetesimal growth, which were described in the Introduction Section, will lead to the depletion of the disk itself in a time scale of $\sim 10\,\mathrm{Myr}$ (e.g., Ercolano et al. 2017). Examples of systems considered prototypes of old, almost depleted disks, which are referred as "debris disks", are the ones around Vega and β Pictoris (e.g., Lagrange et al. 2020; Sibthorpe et al. 2010). In contrast to a young protoplanetary disk, like the one around AB Aur (e.g., Rivière-Marichalar et al. 2020), in which their large dust content translates in an optically thick disk at most wavelength ranges, debris disks are optically thin at all wavelengths. This is reflected by their low integrated fractional luminosity $f = \mathrm{L_{disk}}/\mathrm{L}_\star$, or, also often used, by the IR fractional luminosity $\tau = \mathrm{L_{IR}}/\mathrm{L}_\star$ (e.g., Liu 2021; Sibthorpe et al. 2018). The fractional luminosity is indeed used to classify disks as protoplanetary or debris ones, with a boundary value between $\tau = 10^{-3} - 10^{-2}$ (e.g., Wyatt et al. 2015). The difference in IR excess between the debris and the protoplanetary disks is better seen in the near-IR versus mid-IR colours plane, shown in Fig. 2.1. We note two separate groups. One, the debris disk group, with low colours values consistent with stellar photosphere emission, i.e. no or very small μm-size dust particles presence; and one with high colours values reflecting strong excess emission, the protoplanetary disks group.

The dust component in debris disks is thought to be not a remnant of the primordial disks, but a product of ongoing collisional processes (e.g., Wyatt 2008, and references therein), since they show, even if in a smaller amount, IR excess emission attributed to short-lived μm-size dust

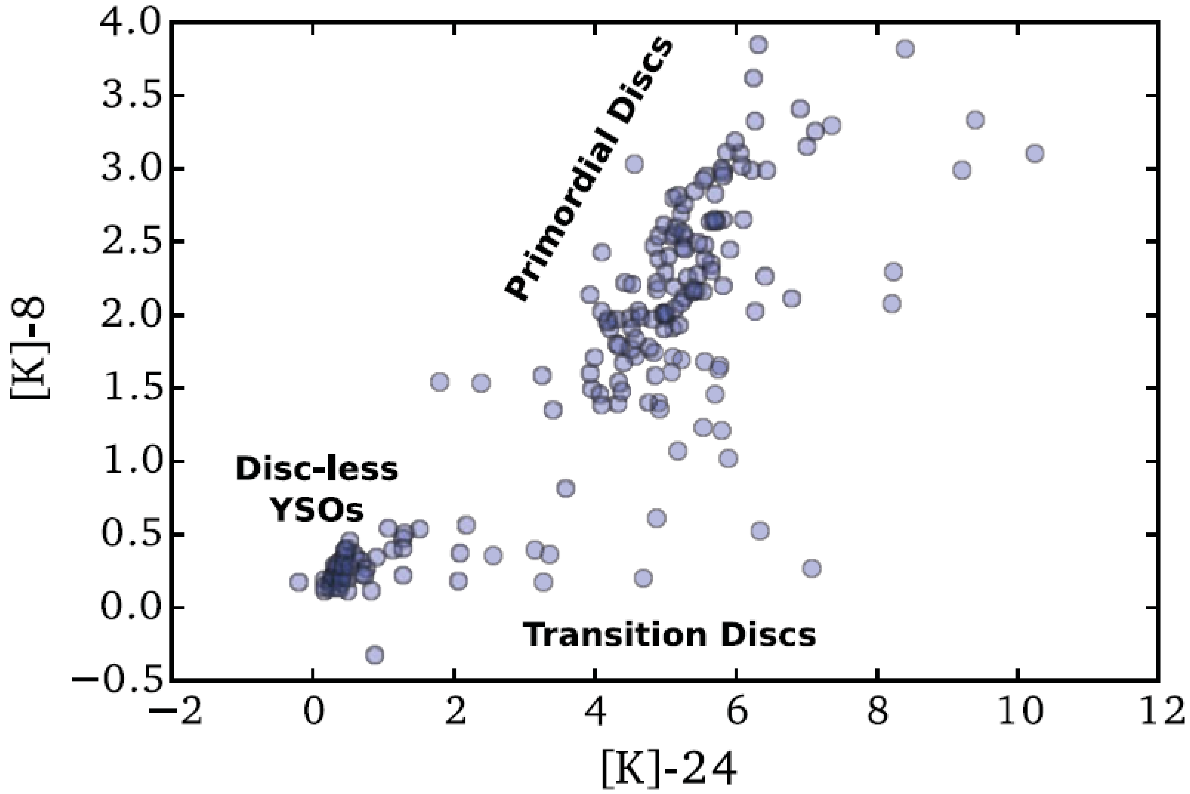

Figure 2.1: Spitzer near-IR versus mid-IR colours plane for YSOs. Data from Luhman et al. (2010) and Koepferl et al. (2013). Image from Owen (2016).

particles, despite the old age of the systems (e.g., Decin et al. 2003). As determined from SEDs analysis, the bulk of the dust is characterized by relatively low temperatures of $\lesssim 150\,\mathrm{K}$ (e.g., Liu 2021; Sibthorpe et al. 2018), with few extreme cases in which $T \gtrsim 300\,\mathrm{K}$ (e.g., Moór et al. 2021). The lack of hot dust is interpreted in their dust radial distribution as a large inner hole. The distribution continues quite discontinuously, with multiple narrow rings and gaps located at tens to hundreds of au from the central star (e.g., Sibthorpe et al. 2018), resembling the Kupier belt of our Solar System but orders of magnitude brighter (Hughes et al. 2018). Debris disks are dust-dominated, being their gas component even poorer. The latter was previously thought to be completely vacant, but recently its low intensity emission has been detected in more systems thanks to the sensitivity of ALMA (e.g., Nilsson et al. 2012). The gas origin in debris disks is still a matter of debate, being proposed to be a remnant of the primordial disk, or having a second generation nature from collisional vaporization of icy dust grains or sublimation of comets (e.g., Beust et al. 1990; Czechowski et al. 2007).

Transitional disks are circumstellar environments with characteristics in between the protoplanetary and the debris disks ones, having a significant amount of gas and being poor in near-IR excess (e.g., Moór et al. 2017, and references therein). Based on their position in the near-IR versus mid-IR colours plane of Fig. 2.1, they have been hypothesised to fill the theoretical evolutionary gap between the two disk stages, and to be in an active disk dispersal phase (e.g.,

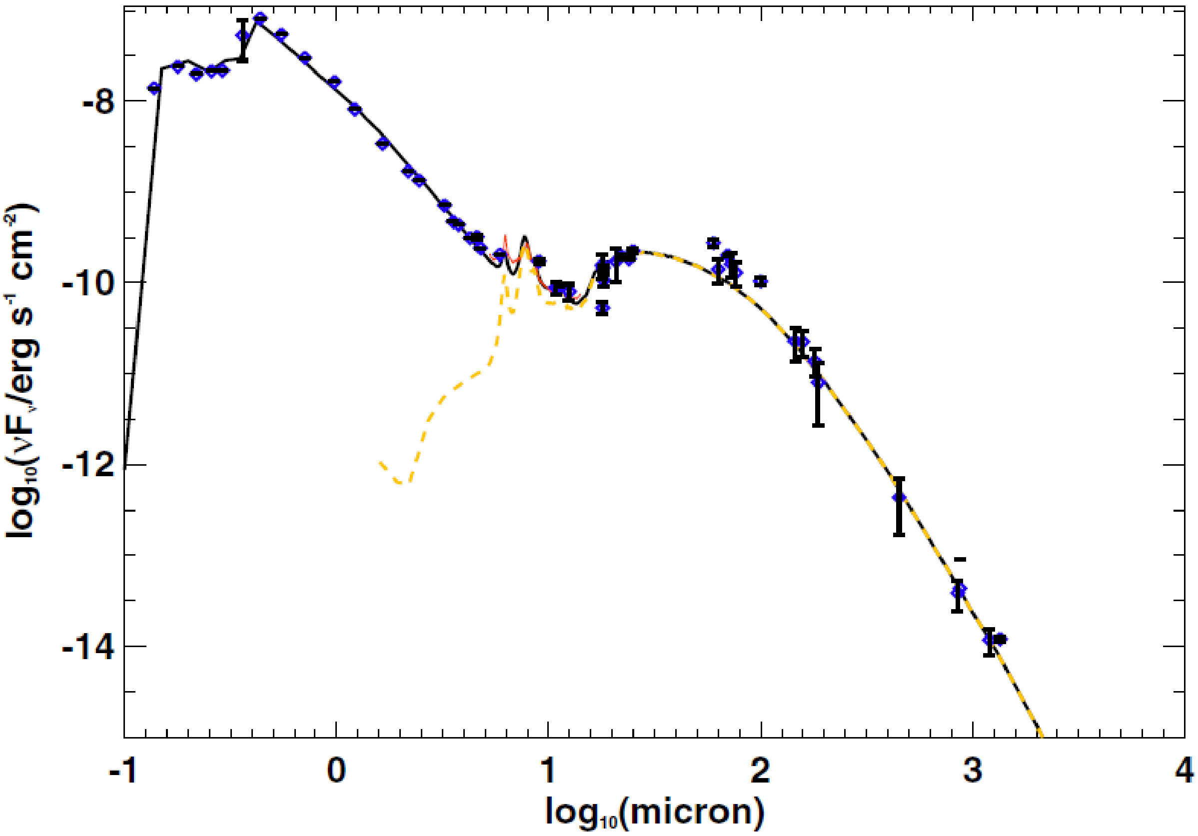

Figure 2.2: HD 141569 SED and Spitzer-IRS spectrum fit by Thi et al. (2014).

Kenyon et al. 1995). The fact that they are located in a region of the plane characterized by a high mid-IR excess and an almost null near-IR one, suggests that the disks' dispersal process proceeds from the inside out (Owen 2016). HD 141569 is the benchmark of such systems. Its fractional luminosity $\tau_0 = 8 \times 10^{-3}$ was indeed used as boundary value to separate debris disks ($\tau < \tau_0$) from protoplanetary ones (Hughes et al. 2018; Sylvester et al. 1996). From analysis of its SED, shown in Fig. 2.2, the disk of the source has been depicted having a total dust mass of $5 \times 10^{-6}\,M_\odot$ and a dust-depleted inner hole, up to 5 au from the central star (Thi et al. 2014). The inner hole scenario stems from the featureless SED in the near-IR wavelength range, consistent with pure stellar photosphere emission, relating the system more to debris disks than protoplanetary ones. However, it is known that SED modeling is highly degenerate, giving loose constraints on the disk parameters (Thamm et al. 1994). Moreover, a significant amount of gas has been detected in both atomic (H) and molecular form (CO) (e.g., Di Folco et al. 2020; Eisner et al. 2009; Mendigutia et al. 2017), with a total mass estimated to be $5 \times 10^{-4}\,M_\odot$ (Di Folco et al. 2020), leading to a gas-to-dust ratio of 100, canonical value for protoplanetary disks. HD 141569 Brγ-line and Hα-line emission show signatures of a Keplerian-rotating gas disk, as hinted by the double-peaked lines shape. Interferometric spatially unresolved observations constrained the gas inside the first ~ 0.15 au of the system (Eisner et al. 2009; Mendigutia et al. 2017), raising questions on the gas origin and survivability mechanisms. On the base of HD 141569 peculiar nature, the object was observed with GRAVITY, to assess the presence of hot dust inside the supposedly dust-depleted inner region.

2.2 Goals of the Study

As my first work of my PhD project, the goals of this study were to gain a general understanding of interferometric data, and to acquire the competence and know-how to analyse them. Specifically for the case of HD 141569, the goal of the paper was to get information on the innermost au regions of the system, like the geometry of the K-band continuum, the dust properties, and the dynamics of the Brγ-line emission. Being HD 141569 a benchmark for transitional disks, the study will help on improving the vague picture of such systems.

2.3 Approach, Steps, and Article

The study is based mainly on GRAVITY data. The data were taken within the framework of the Guaranteed Time Observations (GTO) YSO program. They came in my possession already reduced and calibrated, processes done with the GRAVITY data reduction software (Lapeyrere et al. 2014). As first author of a large cooperation article, and as my first work of my PhD project, here I list the actions done from my side:

(i) Literature study on the state-of-the-art of YSOs general science case, with particular attention on Herbig Ae/Be stars, their circumstellar dusty and gaseous environment, and the observational techniques used.

(ii) In depth literature study on HD 141569. Steps (i) and (ii) allowed me to write the Introduction Section of the article.

(iii) Literature study on interferometry, on the VLTI/GRAVITY instrument, and on its output data files format (OIFits file). This allowed me to understand and work with the interferometric data, and to write the Observation Section and the Data Description Section of the article.

(iv) Literature study on interferometric data fitting procedures through parametric geometrical models, and on the `emcee` python package, an MIT licensed pure-Python implementation of Goodman & Weare's Affine Invariant Markov chain Monte Carlo (MCMC) Ensemble sampler (Foreman-Mackey et al. 2013), used for data fitting process.

(v) Regarding the FT data, a Python code was written to clean the data of outliers, and to fit them with `emcee` through parametric geometrical models based on the ones of Berger et al. (2007) and Lazareff et al. (2017), in order to get information on the shape of the K-band continuum emission and the flux contribution of the circumstellar environment. I present more details in the Methodology Section of the article. A Gaussian-ellipsoid model and a ring one representing the circumstellar environment were tested for the GRAVITY data of HD 141569, with the fit procedure favouring the latter.

(vi) A Python code was written to check for degenerate fitting solutions by looking for possible local minima in the parameters' χ^2 maps.

(vii) Regarding the SC data, a Python code was written to: 1) clean the data of outliers; 2) apply a wavelength calibration based on the atmospheric telluric lines position, radial velocity of the star, and the local standard of rest velocity; 3) correct the Brγ-line spectrum for the telluric lines absorption; 4) account for the star Brγ-line photospheric absorption feature; 5) fit the visibilities with parametric geometrical models in order to get an estimate of the emitting gas region size; 6) calculate the pure-line differential phases and the pure-line photocenters shifts. I present more details in the Methodology Section of the article. The analysis led to the confirmation of the Keplerian-rotating disk geometry for the Brγ-line emitting gas.

(viii) I remark here that the Keplerian-rotating axisymmetric disk geometrical model presented in Section 5.3 was produced by Alois de Valon (De Valon 2021). I used the model to test this scenario on the Brγ-line emission of HD 141569. The emission of the object follows at first order the model. Deviations from Keplerian velocity were detected and are addressed in Section 2.4.

(ix) Literature study of the radiative transfer (RT) code MCMAx (Min et al. 2009). Learned how to use the code with the tutoring of Dr. Lucia Klarmann. The goal was to produce SEDs from physical models, and fit the photometric data of HD 141569 in order to get information on the dust properties of the newly detected innermost component. Three different dust chemical compositions were tested, namely, pure silicate grains, carbonaceous silicate grains, and quantum-heated particles. Only the latter were able to reproduce the near-IR flux excess estimated by GRAVITY and at the same time being consistent with the photometric data, featureless in the $10\,\mu$m silicate emission.

(x) In combination of a literature study on topics relevant to the results obtained, the work done in the steps above allowed me to write the Results and the Discussion Section of the article, as well as the Abstract and the Summary.

(xi) All the images and Tables were produced by myself with Python and the `matplotlib` package (Hunter 2007), except for Fig. 8 of the article, which was adapted from Di Folco et al. (2020).

The approach, tools, equations, models, and additional data used to carry out the work are properly referenced in the article.

A&A 655, A112 (2021)
https://doi.org/10.1051/0004-6361/202141103
© GRAVITY Collaboration 2021

Astronomy & Astrophysics

The GRAVITY young stellar object survey

VIII. Gas and dust faint inner rings in the hybrid disk of HD141569

GRAVITY Collaboration⋆: V. Ganci[1,2], L. Labadie[1], L. Klarmann[3], A. de Valon[4], K. Perraut[4], M. Benisty[4,5], W. Brandner[3], A. Caratti o Garatti[3,6,7,16], C. Dougados[4], F. Eupen[1], R. Garcia Lopez[3,6,7], R. Grellmann[1], J. Sanchez-Bermudez[3,8], A. Wojtczak[1], P. Garcia[9,10], A. Amorim[9,11], M. Bauböck[12], J.-P. Berger[4], P. Caselli[12], Y. Clénet[13], V. Coudé du Foresto[13], P. T. de Zeeuw[12,14], A. Drescher[12], G. Duvert[4], A. Eckart[1,2], F. Eisenhauer[12], M. Filho[9,10], F. Gao[12], E. Gendron[13], R. Genzel[12], S. Gillessen[12], G. Heissel[13], T. Henning[3], S. Hippler[3], M. Horrobin[1], Z. Hubert[4], A. Jiménez-Rosales[12], L. Jocou[4], P. Kervella[13], S. Lacour[13], V. Lapeyrère[13], J.-B. Le Bouquin[4], P. Léna[13], T. Ott[12], T. Paumard[13], G. Perrin[13], O. Pfuhl[15], G. Heißel[13], G. Rousset[13], S. Scheithauer[3], J. Shangguan[12], T. Shimizu[12], J. Stadler[12], O. Straub[12], C. Straubmeier[1], E. Sturm[12], E. van Dishoeck[12,14], F. Vincent[13], S. D. von Fellenberg[12], F. Widmann[12], and J. Woillez[15]

(Affiliations can be found after the references)

Received 15 April 2021 / Accepted 8 September 2021

ABSTRACT

Context. The formation and evolution of planetary systems impact the evolution of the primordial accretion disk in its dust and gas content. HD 141569 is a peculiar object in this context as it is the only known pre-main sequence star characterized by a hybrid disk. Observations with 8 m class telescopes probed the outer-disk structure showing a complex system of multiple rings and outer spirals. Furthermore, interferometric observations attempted to characterize its inner 5 au region, but derived limited constraints.

Aims. The goal of this work was to explore with new high-resolution interferometric observations the geometry, properties, and dynamics of the dust and gas in the internal regions of HD 141569.

Methods. We observed HD 141569 on milliarcsecond scales with GRAVITY/VLTI in the near-infrared (IR) at low ($R \sim 20$) and high ($R \sim 4000$) spectral resolution. We interpreted the interferometric visibilities and spectral energy distribution with geometrical models and through radiative transfer techniques using the code MCMax to constrain the dust emission. We analyzed the high spectral resolution quantities (visibilities and differential phases) to investigate the properties of the Brackett-γ (Brγ) line emitting region.

Results. Thanks to the combination of three different epochs, GRAVITY resolves the inner dusty disk in the K band with squared visibilities down to $V^2 \sim 0.8$. A differential phase signal is also detected in the region of the Brγ line along most of the six baselines. Data modeling shows that an IR excess of about 6% is spatially resolved and that the origin of this emission is confined in a ring of material located at a radius of ~1 au from the star with a width $\lesssim$0.3 au. The MCMax modeling suggests that this emission could originate from a small amount ($1.4 \times 10^{-8}\ M_{\oplus}$) of quantum-heated particles, while large silicate grain models cannot reproduce at the same time the observational constraints on the properties of near-IR and mid-IR fluxes. The high spectral resolution differential phases in the Brγ line clearly show an S-shape that can be best reproduced with a gaseous disk in Keplerian rotation, confined within 0.09 au (or 12.9 $R_{\star}$). This is also hinted at by the double-peaked Brγ emission line shape, known from previous observations and confirmed by GRAVITY. The modeling of the continuum and gas emission shows that the inclination and position angle of these two components are consistent with a system showing relatively coplanar rings on all scales.

Conclusions. With a new and unique observational dataset on HD 141569, we show that the complex disk of this source is composed of a multitude of rings on all scales. This aspect makes HD 141569 a potentially unique source to investigate planet formation and disk evolution in intermediate-mass pre-main sequence stars.

Key words. protoplanetary disks – infrared: planetary systems – techniques: interferometric – stars: individual: HD 141569

1. Introduction

The formation and evolution of protoplanetary disks are directly linked to planet formation. The outer disk features of young stellar objects (YSOs) have been thoroughly studied in the past through scattered light imaging (e.g., with SPHERE/VLT, Beuzit et al. 2019) and with ALMA in the (sub-)millimeter range (ALMA Partnership 2015). With both techniques, disk observations have shown rings, gaps, and asymmetric structures up to a few hundred au (e.g., Lodato et al. 2019; Benisty et al. 2017). The inner regions (at ~au scale) of such disks are also of prime interest since key processes like gas accretion flows, winds, outflows, and dust sublimation take place. All these processes affect the dynamics and evolution of the first few au regions where terrestrial planets may form and/or migrate over few million years. Constraints on these processes can be derived indirectly through spectroscopic studies, but at typical distances of a few hundred parsecs only observations with milliarcsecond (mas) resolution, which are required to probe sub-au scales,

---

⋆ GRAVITY is developed in a collaboration by the Max Planck Institute for Extraterrestrial Physics, LESIA of Paris Observatory and IPAG of Université Grenoble Alpes/CNRS, the Max Planck Institute for Astronomy, the University of Cologne, the Centro de Astrofísica e Gravitação and the European Southern Observatory.

Open Access article, published by EDP Sciences, under the terms of the Creative Commons Attribution License (https://creativecommons.org/licenses/by/4.0), which permits unrestricted use, distribution, and reproduction in any medium, provided the original work is properly cited.
Open Access funding provided by Max Planck Society.

can discriminate between competing models. Numerous interferometric studies have been conducted in the past in the near- and the mid-infrared (IR), for instance with IOTA (Millan-Gabet et al. 2001), the Palomar Testbed Interferometer (PTI; Eisner et al. 2004), the Keck Interferometer (Monnier et al. 2005; Eisner et al. 2014), and the VLTI (Menu et al. 2015; Lazareff et al. 2017; GRAVITY Collaboration 2019). To date, the new generation of four-telescope instruments including GRAVITY, operating in the K band (GRAVITY Collaboration 2017), and MATISSE, operating in L to N band (Lopez et al. 2014), are pushing further the achievable spectral coverage, the sensitivity, and precision of interferometric measurements. Even though statistical studies of large YSO samples are of high relevance (Lazareff et al. 2017; GRAVITY Collaboration 2019), some of these objects require a more in-depth study enabled by the improved data quality of recent interferometric observations. Some objects, like HD 141569, are unusual in their evolutionary sequence and require dedicated studies. For such systems the exact nature and properties of the very inner regions are still a matter of debate and can be solved in part by modeling the distribution of the warm dust traced in the K band. Furthermore, it is still unclear how to characterize the star–disk mechanisms traced by emission lines like the hydrogen Brackett-γ (Brγ $\sim$8000–10 000 K) and CO ($T \sim 2000$–3000 K) bandheads, and where this emission occurs. The high-quality spectroscopic capabilities of the GRAVITY instrument allows us to study in detail the gas phase and its spatial morphology thanks to the interferometric visibilities and differential phase signals (GRAVITY Collaboration 2020a,b, 2021).

HD 141569 is a Herbig star classified as a B9-A0 spectral type (Augereau & Papaloizou 2004), with an effective temperature of 9750 ± 250 K, an estimated age of 7.2 ± 0.02 Myr, a luminosity between $16.60 \pm 1.07\,L_\odot$ (Vioque et al. 2018) and $27.0 \pm 3.6\,L_\odot$ (Di Folco et al. 2020), a mass of $2.14 \pm 0.01\,M_\odot$, and a *Gaia* distance of 110 ± 1 pc (Arun et al. 2019)[1]. It is a non-flaring disk system with little mid-IR excess classified as a group-II source (Meeus et al. 2001). It is the only known pre-main sequence star characterized by a hybrid disk (Wyatt et al. 2015; Péricaud et al. 2017; Di Folco et al. 2020), an evolutionary disk state between the protoplanetary and debris-disk regimes. Near-IR imaging spatially resolved an optically thin disk consisting of two rings located at about ~280 and ~455 au from the star Augereau et al. (1999); Weinberger et al. (1999); Biller et al. (2015). A more complex system is shown in the visible, consisting of multiple rings and outer spirals that could be explained through perturbations by two nearby (~7.5 arcsec) M dwarfs, or by planetary perturbations (Augereau & Papaloizou 2004; Wyatt 2005; Reche et al. 2009). Fisher et al. (2000) found a warm disk component up to 110 au at 10.8 and 18.2 µm, later confirmed by Marsh et al. (2002). The short-wavelength counterpart of this component was detected by Mawet et al. (2017) through L′ imaging and ranging between 20 and 85 au. Emission at 8.6 µm was detected by Thi et al. (2014), and was interpreted as emission from polycyclic aromatic hydrocarbons (PAHs). NOEMA and ALMA observations in the millimeter range showed continuum emission equally shared between a compact ($\lesssim$50 au) and a smooth extended dust component (~350 au), with large millimeter grains dominating the inner regions and smaller grains in the outer ones (Di Folco et al. 2020). Finally, inner disk features were detected by SPHERE in the *Y, J, H,* and *K* bands (Perrot et al. 2016) and by Keck/NIRC2 in the L' band (Currie et al. 2016) at physical separations of 45, 61, and 88 au. These results point out the high morphological complexity of the outer disk in the HD 141569 system.

Little is known about the central astronomical units of the system. The spectral energy distribution (SED) of HD 141569 alone does not help us in this sense since the IR excess is very small (see Fig. 9 of Thi et al. 2014). The majority of the K-band measurements listed in Table G.1 reflect a featureless SED in the near-IR. Moreover, pure SED fits obtained by different authors (Li & Lunine 2003; Merín et al. 2004; Thi et al. 2014) may suggest at first that the near-IR emission is exclusively photospheric in nature and that the disk contributes only at longer wavelengths. The object was observed at milliarcsecond resolution in the K band with the PTI and the Keck interferometer, but it was spatially unresolved (Eisner et al. 2004, 2009). Monnier et al. (2005) derived a 10 mas upper limit in radius for the spatial extension of the K-band emission. Therefore, trustworthy information on the first 5 au of the system are scarce, and the question arises of whether the inner region of the disk could be already in a debris disk stage, where the SED fits in the near-IR are not accurate enough to detect such a faint excess.

The circumstellar gas has been observed in both atomic and molecular form, which suggests the system has not yet reached the gas-depleted stage characteristic of a debris disk system. Mendigutía et al. (2017) set an upper limit of ~0.11 au for the gas region responsible for the spatially unresolved double-peaked Hα emission. A comparable upper limit of ~0.13 au for the Brγ line emitting region is suggested by Eisner et al. (2009). Both lines are observed to be not variable over timescales of days and years (Eisner et al. 2015; Mendigutía et al. 2011b). In addition to hydrogen, CO ro-vibrational emission ($\upsilon \geq 1$, $\Delta\upsilon = 1$) was observed by many authors extending from 10 to 275 au (Dent et al. 2005; Goto et al. 2006; Brittain et al. 2007; Flaherty et al. 2016; White et al. 2016; Miley et al. 2018; Di Folco et al. 2020).

We present here the first GRAVITY interferometric observations of this disk, with the goal of revealing the geometry and dynamics of the internal structure of HD 141569, and of gaining insights about the dust and gas properties. Section 2 describes the observations; Sects. 3 and 4 present the observational data and the adopted methodology; Sect. 5 describes the results of the possible scenarios along with the corresponding modeling; a discussion is developed in Sect. 6.

2. Observations

HD 141569 was observed with VLTI/GRAVITY (GRAVITY Collaboration 2017) using the four 1.8 m Auxiliary Telescopes (ATs), on March 18 and July 12, 2019, in the intermediate D0-G2-J3-K0 configuration, and on May 23, 2019, in the large A0-G1-J2-J3 configuration. The observations span a spatial frequency range between about 15 and 65 Mλ (see Fig. 1, left panel) with a maximum angular resolution of $\lambda/2B$, about 1.7 mas for the longest baseline (B) of 130 m, which corresponds to about 0.19 au at a distance of 110 pc. The data consist in high spectral resolution ($R \sim 4000$) observables recorded by the science channel (SC) detector over the whole K band with individual integration times of 30 s and in low spectral resolution ($R \sim 20$) observables recorded by the fringe tracker (FT) detector (five spectral channels over the K band at 1.908, 2.058, 2.153, 2.256, 2.336 µm) at frame rates of ≈300 and ≈900 Hz (Lacour et al. 2019). Each observation block corresponds to 5 min on the object. In total, three files were acquired in March 2019, one in May 2019, and eight in July 2019. HD 141569 observations were

---

[1] The recent distance estimate in the new EDR3 of *Gaia* suggests 111.6 ± 0.4 pc. Considering the very close value to DR2, we decided to keep the former distance throughout the paper.

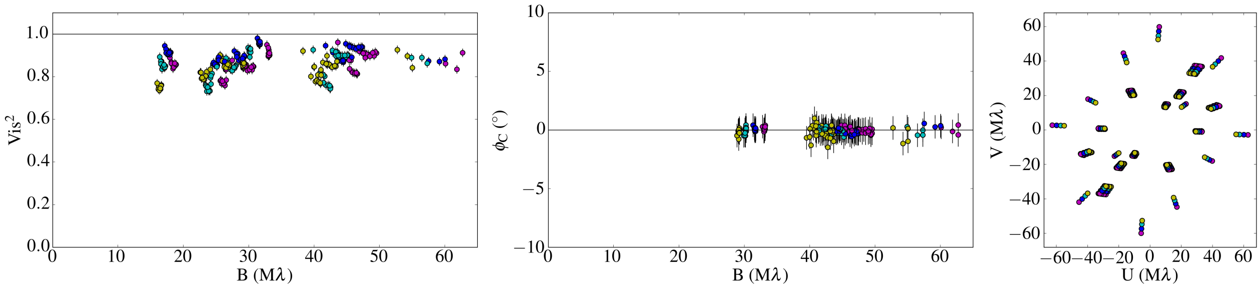

Fig. 1. HD 141569 FT data; squared visibilities (*left panel*), closure phases (*central panel*), and U-V plane coverage (*right panel*), from all the observation epochs. Colors refer to the different GRAVITY spectral channels.

preceded by the observation of a point-source calibration star, close to our object on the sky, and of similar spectral type and brightness in order to calibrate the atmospheric and instrumental transfer function. We observed the calibrator HD 137006 in March and July 2019, and the calibrator HD 141977 in May 2019. Further details on the executed runs and observing conditions are given in Table A.1.

3. Data

All the data were reduced and calibrated using the GRAVITY data reduction software (Lapeyrere et al. 2014). For the low-resolution FT data we discarded the first spectral channel, which can typically be affected by the metrology laser operating at 1.908 µm. Figure 1 shows the U-V plane coverage and the FT calibrated squared visibilities and closure phases (right, left, and center panel, respectively). Following GRAVITY Collaboration (2019), we applied a floor value on the error bars of 2% for the squared visibilities and 1° on the closure phases as the error bars computed by the pipeline might be underestimated or correlated. We observe that GRAVITY partially resolved the near-IR emission in HD 141569 with squared visibilities between 0.8 and 1.0. Therefore, the data can be used to estimate the characteristic size of the dust environment (see Sect. 5.1). Moreover, with the inclusion of the May 2019 large configuration data, we observe that the visibility reaches a plateau at almost all spatial frequencies, allowing us to constrain near-IR flux contributions of the star and environment.

Since the closure phases are consistent with 0° at all baselines and for all the epochs, we can confidently consider the emission to be centro-symmetric on the spatial scale of our observations, and we therefore discard the hypothesis of a close companion as the origin of the resolved emission, at least within the 250 mas (~28 au) field of view of GRAVITY with the ATs.

For the high-resolution SC data, we concentrated on the July 2019 dataset only since this is the epoch where we gathered the highest number of files. In order to optimally exploit the SC dataset, the eight files from July 2019 have been merged in order to increase the signal-to-noise ratio per spectral channel. Considering that the maximum span in position angle between the two extreme positions of the UV coverage is only ~4 °, we do not expect any visibility smearing of the data due to differences in hour angles. The error bars were computed as the standard deviation between the eight files of the corresponding differential quantity (visibility or differential phase) in each spectral channel. For instance, we derived the absolute error on the visibility to about 1.8%. Figure 2 shows the visibility amplitude (left panels) and the differential phase (right panels) for the six baselines in the region of interest of the Brγ line, between 2.15 and 2.18 µm. The top panels show the object spectrum normalized to the continuum, corrected for telluric lines (left plot), and corrected for both telluric lines and photospheric absorption (right plot). The visibilities appear to be spectrally flat with no clear signature at 2.16612 µm. They are measured to vary between 0.9 and 0.96 as a function of the baseline, which is indicative of a compact region well inside the dusty disk. Interestingly, the differential phase signal is more marked at the position of the Brγ line. We observe a clear S-shaped signal through baselines J3-D0 (100.1 m, 220°)

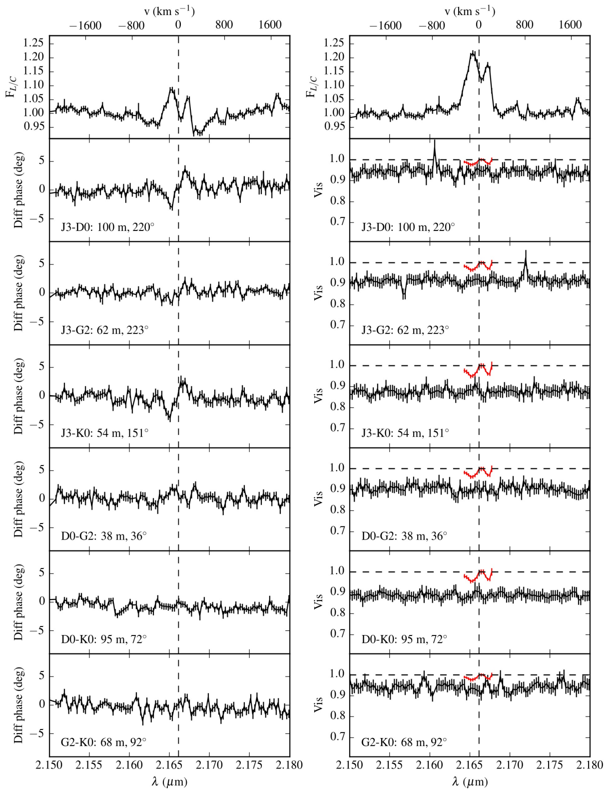

Fig. 2. Science channel data of July 2019. *Top left*: wavelength-calibrated continuum-normalized spectrum, corrected for telluric lines. *Top right*: same as top left, but corrected for the Brγ photospheric absorption. Differential phases (*left column*) and visibilities (*right column*) along the six GRAVITY baselines. The red lines in the visibility plots show the pure-line visibilities.

and J3-K0 (53.6 m, 152°), and a weaker signal through baselines J3-G2 (62.1 m, 223°) and D0-G2 (38.2 m, 36°). No clear signal is detected within the error bars through the baselines D0-K0 (95.1 m, 72°) and G2-K0 (68.1 m, 92°).

In order to study the Brγ line gas region using the SC high spectral resolution data, we need precise measurements for the line-to-continuum flux ratio. It is essential to perform a proper wavelength calibration of the spectrum and to take out the contribution by the telluric lines. We describe the whole procedure in Appendix C. Errors are from the original data, reduced and calibrated through the GRAVITY data reduction software.

The high-resolution GRAVITY spectrum of HD 141569 (see top panels of Fig. 2) shows a double-peaked Brγ emission line. Since the error associated with the GRAVITY wavelength calibration is ~3 Å, the two peak positions can be considered to be symmetric with respect to the Brγ wavelength rest position. Both the double-peaked emission line and the S-shaped feature in the differential phase suggest a scenario where the gas emitting in the Brγ line could be in Keplerian rotation. We explore this hypothesis further in the following sections.

4. Methodology

The properties of the spatially resolved continuum emission were first investigated with the help of low spectral resolution FT data (see Sects. 4.1 and 5.1). The squared visibility curve was modeled through chromatic geometrical models accounting for a point-like central star, and simple geometrical shapes (Gaussian geometrically thin rings, Gaussian-convolved infinitesimally thin rings) representing the circumstellar environment. Useful information was obtained such as the star-to-dust flux ratio, the dust spectral index, and the spatial distribution of the dust. To gain further information on the dust emission properties, we investigated through radiative transfer (RT) modeling the impact of such a component on the SED (see Sect. 5.2). We used the RT code MCMax (Min et al. 2009), which solves 2D RT (e.g., Bjorkman & Wood 2001) to calculate the dust density and temperature structure of a given disk setup. In Sects. 4.2 and 5.3 we discuss the high-spectral resolution SC data in the Brγ region used to constrain the spatial scale of the hot gas emitting component through modeling of the visibility curves, and through the analysis of the Brγ spectrum under the assumption of a gas disk in Keplerian rotation. Further information on the gas region size and its dynamical properties were derived through the analysis of the differential phases and the resulting photocenters shifts. Finally, an analytical axisymmetric Keplerian disk model is compared to our observations.

4.1. Dust continuum: low spectral resolution data

Following the work of Lazareff et al. (2017) and GRAVITY Collaboration (2019), we used geometric models that consist of a point-like central star, assumed to be unresolved at all observed baselines, and a circumstellar environment in order to fit the observed visibilities. The complex visibility of the system at spatial frequencies (u, v) and at wavelength λ is therefore described by a linear combination of the two components as

$$V(u, v, \lambda) = \frac{F_\mathrm{s}(\lambda)\, V_\mathrm{s}(u, v, \lambda) + F_\mathrm{c}(\lambda)\, V_\mathrm{c}(u, v, \lambda)}{F_\mathrm{s}(\lambda) + F_\mathrm{c}(\lambda)}, \tag{1}$$

where V_c is the visibility of the circumstellar environment, and F_s and F_c the specific fractional flux contributions of the star and of the circumstellar environment, respectively. The visibility of the star V_s is equal to 1 since we assume it to be unresolved. Since our GRAVITY FT data contains six visibility measurements and four closure phases for each of the four spectral channels and for each file, we can derive the spectral dependence of the circumstellar environment by modeling it as a power law, defined by its spectral index k_c, where $k = \mathrm{d} \log F_\lambda / \mathrm{d} \log \lambda$, and by describing the complex visibility of the system as

$$V(u, v, \lambda) = \frac{F_\mathrm{s}\, (\lambda/\lambda_0)^{k_\mathrm{s}} + F_\mathrm{c}\, (\lambda/\lambda_0)^{k_\mathrm{c}}\, V_\mathrm{c}(u, v)}{F_\mathrm{s}\, (\lambda/\lambda_0)^{k_\mathrm{s}} + F_\mathrm{c}\, (\lambda/\lambda_0)^{k_\mathrm{c}}}, \tag{2}$$

where $\lambda_0 = 2.15\ \mu\mathrm{m}$ is the wavelength of the central spectral channel of the FT, and k_s the spectral index of the star derived assuming that it radiates as a black body at the star effective temperature $T_\mathrm{eff} = 9750\ \mathrm{K}$, which translates into s spectral index $k_\mathrm{s} = -3.62$ at λ_0 for the central star.

We chose to fit our visibility data with three different geometric models that differ only by the V_c term in Eq. (2). Since the closure phases are basically zero for every baseline, as shown in the central panel of Fig. 1, we do not consider any azimuthal modulation in our models. Therefore, the resulting brightness distributions are centro-symmetric.

The first model consists of a Gaussian disk whose visibility is described, from Berger & Segransan (2007), as

$$V_\mathrm{c}(u, v) = V_\mathrm{gauss}(u, v) = \exp\left(-\frac{(\pi\Theta r)^2}{4 \ln 2}\right), \tag{3}$$

where Θ is the Gaussian full width at half maximum (FWHM) and $r = \sqrt{u^2 + v^2} = B/\lambda$, with u and v the spatial frequency coordinates, and B the projected baseline.

The second model consists of a geometrically thin ring whose visibility is described by subtracting an inner smaller uniform disk from a larger one:

$$V_\mathrm{c}(u, v) = V_\mathrm{ring}(u, v) = \frac{F_\mathrm{outer}\, V_\mathrm{outer} - F_\mathrm{inner}\, V_\mathrm{inner}}{F_\mathrm{outer} - F_\mathrm{inner}}. \tag{4}$$

Here the subscript outer refers to the larger disk and the subscript inner refers to the inner hole. After normalization and knowing that $F_\mathrm{disk} = \pi D^2/4$, where D is the diameter of the disk, we can express Eq. (4) as

$$V_\mathrm{ring}(u, v) = \frac{D_\mathrm{outer}\, 2\, \frac{J_1(\pi D_\mathrm{outer}\, r)}{\pi r} - D_\mathrm{inner}\, 2\, \frac{J_1(\pi D_\mathrm{inner}\, r)}{\pi r}}{D^2_\mathrm{outer} - D^2_\mathrm{inner}}, \tag{5}$$

where J_1 is the first-order Bessel function. Finally, our last model consists of an infinitesimally thin ring convolved by a Gaussian whose visibility is described as the product between $V_\mathrm{gauss}(u, v)$ and

$$V_\mathrm{inf-ring}(u, v) = J_0(2\pi a r), \tag{6}$$

where J_0 is the zero-order Bessel function and a is the radius of the infinitesimally thin ring (Berger & Segransan 2007). Since in the Fourier space the convolution of two functions is simply their multiplication, we have

$$V_\mathrm{c}(u, v) = V_\mathrm{gauss-ring}(u, v) = V_\mathrm{gauss}(u, v) \cdot V_\mathrm{inf-ring}(u, v). \tag{7}$$

The inner hole radius and ring width are defined as $r_i = D_\mathrm{inner}/2$ and $w = (D_\mathrm{outer} - D_\mathrm{inner})/2$, respectively, for the geometrically thin ring model while they are defined as $r_i = a - \Theta/2$ and $w = \Theta$, respectively, for the Gaussian-convolved infinitesimally thin ring. Inclination and position angle of the circumstellar environment are taken into account through the parameter $r = \sqrt{u^2 + v^2}$ following Berger & Segransan (2007). The model fitting is based on a Markov chain Monte Carlo (MCMC, Foreman-Mackey et al. 2013) numerical approach and was implemented on the combined dataset of all three epochs in order to maximize the number of experimental points against the number of free parameters. This assumes that the near-IR emission and the disk structures are not variable over a five-month period, which is strengthened by the fact that the star is not variable, either spectroscopically in the optical (Mendigutía et al. 2011a) or photometrically in the mid-IR (Kóspál et al. 2012). Once a global solution was identified, we further checked how well the parameters are indeed constrained by the data. For this purpose, we performed a series of squared visibility fits to the model by fixing the tested parameter to different values and left the other parameters free in the subsequent minimization. In this way we obtain a χ^2 curve as a function of the tested parameter value.

Finally, the error on the χ^2 was estimated by treating the quantity T_i as a stochastic variable with

$$T_i = N \left(\frac{y_i - y_{\rm model}}{\sigma_{\rm i}} \right)^2, \tag{8}$$

where N is the number of points in the dataset, y_i the individual measurement, $y_{\rm model}$ the value of the model, and σ_i the error associated to the measurement. The χ^2 value is given by the mean of T_i,

$$\chi^2 = \frac{1}{N} \sum_{i=1}^{N} T_i = \sum_{i=1}^{N} \left(\frac{y_i - y_{\rm model}}{\sigma_i} \right)^2, \tag{9}$$

and the χ^2 error is given by the error on the mean of T_i,

$$\sigma_{\chi^2} = \sqrt{\frac{\sum_{i=1}^{N} T_i^2}{N(N-1)} - \frac{(\chi^2)^2}{N-1}}. \tag{10}$$

This applies to the reduced χ^2 as well.

4.2. Gas: high spectral resolution data

To estimate the gas region size from the SC visibility we extrapolated the pure-line contribution from the total visibility (line+continuum) displayed in Fig. 2. To do this we modeled the total visibility with a three-component model that accounts for the contributions from the star, the circumstellar dust, and the line emitting gas. The total visibility is given therefore by

$$V_{\rm tot}(u, v, \lambda) = \frac{\alpha(\lambda)\, F_{\rm s}(\lambda)\, V_{\rm s}(u, v, \lambda) + F_{\rm c}(\lambda)\, V_{\rm c}(u, v, \lambda) + F_{\rm L}(\lambda)\, V_{\rm L}(u, v, \lambda)}{\alpha(\lambda)\, F_{\rm s}(\lambda) + F_{\rm c}(\lambda) + F_{\rm L}(\lambda)}, \tag{11}$$

where $\alpha(\lambda)$ is the science star continuum-normalized photospheric absorption (see Appendix C for more details), the subscript c refers to the dust component, and the subscript L refers to the Brγ line gas. From Eq. (11) it can be proven (see Appendix D) that the pure-line visibility is given by

$$V_{\rm L}(u, v, \lambda) = \frac{V_{\rm tot}(u, v, \lambda)\, \{[1 + \beta(\lambda)]\, F_{\rm L/C} - 1 - \beta(\lambda)\} - \alpha(\lambda) + 1}{[1 + \beta(\lambda)]\, F_{\rm L/C} - \alpha(\lambda) - \beta(\lambda)}, \tag{12}$$

where $F_{\rm L/C}$ is the line-to-continuum flux ratio

$$F_{\rm L/C} = \frac{\alpha(\lambda)\, F_{\rm s}(\lambda) + F_{\rm c}(\lambda) + F_{\rm L}(\lambda)}{F_{\rm s}(\lambda) + F_{\rm c}(\lambda)} \tag{13}$$

and $\beta(\lambda)$ is the disk-to-star flux ratio outside the line

$$\beta(\lambda) = \frac{F_{\rm c}}{F_{\rm s}}(\lambda) = \frac{F_{\rm c}}{F_{\rm s}} \left(\frac{\lambda}{\lambda_0} \right)^{k_{\rm c} - k_{\rm s}}. \tag{14}$$

For clarity, we note that, outside the line emitting region, $\alpha(\lambda)$ and $F_{\rm L}(\lambda)$ tend toward 1 and 0, respectively. Equation (13) corresponds to the line-to-continuum ratio including the photospheric absorption. Finally, we estimated the gas region size by modeling it with an infinitesimal ring model given by Eq. (6).

In the same way, we needed to take out the continuum contribution from the total differential phases (Fig. 2). Following Weigelt et al. (2011), the pure-line differential phase is given by

$$\sin \phi_{\rm L} = \sin \phi\, \frac{F_{\rm tot}\, V_{\rm tot}}{F_{\rm L}\, V_{\rm L}} = \sin \phi\, \frac{V_{\rm tot}}{V_{\rm L}}\, \frac{F_{\rm L/C}}{F_{\rm L/C} - \left(\frac{\alpha + \beta}{1 + \beta} \right)}, \tag{15}$$

where $\phi_{\rm L}$ is the pure-line differential phase, ϕ the total differential phase, $F_{\rm tot}$ the total flux (star, dust, and gas), and we write the ratio $F_{\rm tot}/F_{\rm L}$ through Eq. (D.5). Following Le Bouquin et al. (2009), we can derive wavelength-dependent photocenter displacements along each baseline from the pure-line differential phases by

$$\mathbf{p} = \frac{-\phi_{\rm L}}{2\pi} \cdot \frac{\lambda}{\mathbf{B}}, \tag{16}$$

where $\mathbf{p}$ is the projection on the baseline $\mathbf{B}$ of the 2D photocenter vector with origin on the central star. The error bars on the pure-line differential quantities are computed through error propagation in Eqs. (12) and (15).

5. Results

5.1. Disk component inside 2 au

Of the three models discussed in Sect. 4.1, the fit of the squared visibilities to the Gaussian disk model (Eq. (3)) did not converge to a solution (i.e., the marginal posterior distributions for the Gaussian width, inclination, and position angle are flat). Therefore, we discarded this model in the rest of the work. Solutions were found for the geometrically thin ring model (Eq. (5)) and the Gaussian-convolved ring model (Eq. (7)). The two models converge basically toward the same solution, with a reduced $\chi_r^2 = 4.7$ for both models.

We performed a wide scan range of the fitted parameters to find convergence toward a global solution. The results of the minimization are presented in Fig. B.1 and Table 1 for the ring model along with the parameter scan range and the 1σ uncertainties. The resulting MCMC posterior distribution is presented in Fig. B.1 (top plots) and allows us to identify an optimal global solution for the six parameters. The fitting process leads to a photospheric near-IR flux contribution of ~93.8%, and therefore to a dust ring flux contribution of ~6.2% for both models. Interestingly, the degeneracy typically found between the disk's flux and the characteristic size in V^2 is broken here because the constant plateau as a function of spatial frequencies unambiguously determines the level of the disk's flux contribution. Both models predict a spectral index $k_{\rm c}$ for the dust ring with a value

Table 1. FT squared visibility best-fit solution for the geometrically thin ring model and the Gaussian-convolved ring model.

Geometrically thin ring			Gaussian-convolved ring			
Parameter	Unit	Fit solution	Parameter	Unit	Fit solution	Scan range
F_s	[%]	93.81 ± 0.07	F_s	[%]	93.81 ± 0.07	[0 ; 100%]
F_c	[%]	6.19 ± 0.07	F_c	[%]	6.19 ± 0.07	1 - F_s
k_c		-0.35 ± 0.21	k_c		-0.35 ± 0.21	[−4 ; 4]
r_i	[mas (au)]	7.40 ± 0.21 (0.81)	r_i	[mas (au)]	7.35 ± 0.21 (0.81)	[0 ; 60]
w	[mas (au)]	0.35 ± 0.35 (0.04)	w	[mas (au)]	0.24 ± 0.24 (0.03)	[0 ; 100]
i	[deg]	58.47 ± 1.55	i	[deg]	58.45 ± 1.55	[30 ; 80]
PA	[deg]	-1.77 ± 1.11	PA	[deg]	-1.78 ± 1.11	[−40 ; 40]
χ^2_r		4.67 ± 0.33	χ^2_r		4.67 ± 0.33	

Notes. F_s is the stellar flux contribution, F_c the dusty circumstellar environment flux contribution, k_c the dust spectral index at 2.15 µm, r_i the ring inner hole radius, w the ring width (r_i and w defined in different ways for the two models, see Sect. 4.1), i the ring inclination from face-on, PA the northeast position angle, and χ^2_r the reduced chi-square. The uncertainties on the fitted parameter correspond to the 1σ error. Scan ranges refer to both models.

of -0.35 ± 0.2. To better illustrate the visibility plateau and the expected modulation due to the modeled thin ring, we show in the bottom plots of Fig. B.1 three visibility curves corresponding to the best model for three selected baseline orientations and for a fixed wavelength value of 2.15 µm. Regarding the geometrical shape of the circumstellar environment, both models lead to a ring inclined from face-on by 58.5°, with a northeast position angle PA ~ 0°. The inner hole radius is estimated to be $r_i \approx 7.4$ mas (0.8 au) from both models, while the ring width is estimated to be ~0.24−0.35 mas (0.03−0.04 au, for the Gaussian-convolved ring model and the geometrically thin ring model, respectively).

Importantly, Fig. B.2 shows the χ^2_r curves of each parameter for the geometrically thin ring model, which helps us to evaluate how well each parameter is constrained by our data. The star near-IR flux contribution is very well constrained as we expected from the plateau seen in the squared visibility curve. The ring spectral index is more loosely constrained, since the best value is consistent with values ranging between −2 and 2. The ring inclination is constrained between ~ 45° and ~75°, while the position angle is less well constrained with two possible minima at ~ 0° and 120°, the former considered to be the absolute minimum. The inner hole radius is constrained to be inside the first 2 au of the system, with a global minimum found around 0.8 au (7.4 mas) and a second (almost equally possible) solution, at ~1.7 au (15.4 mas). Taking into account the upper limit of 10 mas for the radius of the *K*-band emission found by Monnier et al. (2005), we decided to adopt $r_i = 0.8$ au. According to Fig. B.2, the ring width w tends toward small values, not larger than ~ 0.3 au. This is discussed further in Sect. 6.1.

5.2. Dust properties through radiative transfer modeling

To strengthen the obtained results and to assess the scenario of an inner ring as close as 0.8 au, gaining further information on the emission properties, we investigated through RT modeling the impact of such a component on the SED. We note here that our aim was not to perform a detailed mineralogy study of the system, but rather to understand how the detected inner dust is consistent with both the near-IR flux and overall SED of the system.

We modeled the multiple and complex outer rings with only three rings based on the results from Thi et al. (2014). In their model, the lower limit particle size was set at 0.5 µm and the upper one at 0.5-1 cm for the two outermost rings and the innermost one, respectively. The grain size follows a distribution $\propto a^{-3.5}$, the surface density profile is a modified version from Li & Lunine (2003), and the flaring index is $\gamma = 1$. The three rings peak at ~15, 185, and 300 au, with the first two rings separated by a 75 au gap.

Our initial disk setup consists of a disk structure similar to Thi et al. (2014), but with updated stellar parameters (see Sect. 1) and a grain population based on DIANA standard dust grains (Woitke et al. 2016) containing 75% amorphous silicates (e.g., $Mg_{0.7}Fe_{0.3}SiO_3$), 25% porosity, and no amorphous carbon. Our modified grain size distribution and surface density is described in next paragraph. The computed SEDs account for both thermal emission and scattered light contributions.

A silicate dust ring. First, we attempted to reproduce the near-IR excess detected by GRAVITY by including dust grains close to the star, but also taking into account the fact that HD 141569 does not show a silicate emission feature at 10 µm (Seok & Li 2017), which is in part connected to the grain size distribution. We tested several models of the inner ring with the following properties: a varying lower-limit dust grain size of 0.6, 1.2, 2.5, 5.0, 10, 20, 40, 80, 158, and 316 µm; an equal upper-limit grain size of 1 cm, with a size distribution $\propto a^{-3.5}$; a surface density $\propto r^{-1}$; and an inner ring radius fixed at 0.8 au with a width of 0.04 au according to our best-fit model.

All models with grains smaller than ~20 µm in the inner ~1 au region can be tuned to reproduce the ~6% near-IR excess, but at the same time they still exhibit a clear 10 µm silicate feature, which is not in adequacy with the observations.

Models accounting only for grains larger than 40 µm result in an almost complete quenching of the 10 µm silicate feature. When testing the mass at ~1 au required not to exceed the mid-IR flux, we find that $10^{-10}\,M_\odot$ (or $3.3 \times 10^{-5}\,M_\oplus$) would be compliant with this condition, but only a ~1% near-IR excess is generated. On the other hand, the dust mass required to reach a ~6% near-IR excess is well beyond $8.5 \times 10^{-10} M_\odot$ (or $2.8 \times 10^{-4}\,M_\oplus$), but this then produces a too large mid-IR emission inconsistent with the known SED.

Finally, decreasing the percentage of silicates and increasing the carbon percentage in the dust grains up to 25% did not improve the SED fit. Obtaining a more precise fit to the global SED would require further analysis and tuning of the outer ring contribution in the mid-IR, which is beyond the immediate goal

Table 2. Parameters relevant to the RT modeling of the HD 141569 disk.

Star parameters					
Distance	[pc]	110			
Temperature	[K]	9750			
Luminosity	[$L_\odot$]	19	(see table notes)		
A_V	[mag]	0.095			
Rings parameters					
Parameter	Unit	1st	2nd	3rd	4th
Inner rim	[au]	0.8	5	185	300
Outer rim	[au]	0.84	110	500	500
Particle type		QHP	Silicate	Silicate	Silicate
Dust mass	[$M_\oplus$]	1.4×10^{-8}	0.020	1.665	0.233
Smallest particle size	[µm]	0.006	1.26	0.63	20
Biggest particle size	[µm]	0.006	10 000	10 000	10 000
Inner surface density power law		–1	–1	–1	–1
Size distribution power law		–3.5	–3.5	–3.5	–3.5
Scale-height at 100 au	[au]	1.4	1.4	7.5	7.5
Ring inclination	[degree]	59	59	59	59

Notes. This model only describes the case of a QHP-dominated inner ring. The stellar luminosity has been revisited in this work as follows. We determined a lower and upper limit of that value by matching in the K band the photospheric flux plus the near-IR excess with the 2 MASS photometry within its 5% uncertainty (see Table G.1). This provided a stellar luminosity between 18 and 19 $L_\odot$, in agreement with the revised value by Vioque et al. (2018).

of the paper. However, our modeling seems to point out that it is difficult to reconcile the level of near- and mid-IR excess reported with a model of solely silicate dust in the disk ring at ~1 au. Three representative cases of our modeling are presented in Fig. E.1.

A ring of quantum heated particles. Another way to produce near-IR emission consistent with the absence of the prominent 10 µm silicate feature and with the presence of the mid-IR PAH bands is to consider quantum heated particles (QHPs, Purcell 1976; Draine & Li 2001). In the context of interferometric observations, this scenario was invoked for HD 100453 where QHPs were detected in the disk gap (Klarmann et al. 2017), and for HD 179218 with the presence of hot QHPs inside the disk cavity (Kluska et al. 2018).

We tested different amounts of QHPs (from 10^{-13} to 10^{-15} $M_\odot$), and two different QHP particles sizes (10^5 and 5×10^5 carbon atoms), based on the results obtained by Klarmann et al. (2017).

The highest masses (~10^{-13} $M_\odot$) produce an inner rim emission which results in a near-IR excess that is too large and inconsistent with the GRAVITY measurement. The smallest value (~10^{-15} $M_\odot$) corresponds instead to an optically thin disk with negligible excess at 2 µm. For a ring geometry in agreement with our best fit of the GRAVITY data, a sweet spot is found for a mass of 4.3×10^{-14} $M_\odot$ (or 1.4×10^{-8} $M_\oplus$) for which the resulting disk produces a near-IR excess of ~7 %. Smaller particle sizes (e.g., 10^2 carbon atoms) would require a larger mass reservoir of QHPs to reach a near-IR excess of ~6%. As a consequence, a higher mass would result in stronger mid-IR PAH features overestimating the HD 141569 SED observed in the *Spitzer* IRS spectrum (Sloan et al. 2005). The order of magnitude of ~10^5 carbon atoms per particle appears consistent with the SED profile estimated by GRAVITY and IRS/*Spitzer*.

The resulting disk SED shows a spectral index ($d\log F_\lambda / d\log\lambda$) of −1.4 at 2.15 µm which is consistent with the minimization curve of the spectral index in Fig. B.2. The details of the QHP model parameters is shown in Table 2. In Fig. F.1 we show the density and temperature structure of the full-disk model. For the silicate dust in the outer second (~15 au), third (~185 au), and fourth ring (~300 au), the equilibrium temperature varies between 125 K at ~5 au to 20 K in the outermost disk regions. The QHPs used to model the innermost optically thin ring are not in thermal equilibrium. Their temperature distribution depends on their size (the smaller, the hotter) and on the strength of the local ultraviolet (UV) radiation field as they absorb UV photons to quickly re-emit in the near-IR, changing their temperature drastically and very fast. The dark red color in Fig. F.1 shows the location of the QHPs, and according to our RT simulations their temperatures are in the range between 1865 and 95 K.

We find that the strongest constraint on the ring width is set by our interferometric measurement. When considering widths from 0.04 to 0.3 au in our RT modeling, the observed tendency remains the same: the population of silicate dust grains does not satisfactorily reproduce the near- and mid-IR excess, contrary to a population of a stochastically heated small grains.

Beside the ring's width, the important result of this analysis suggests that a tenuous, QHP-dominated, optically thin inner ring may provide a suitable description of the close circumstellar environment of HD 141569 in agreement with existing detailed modeling of the outer disks. On the contrary, a silicate-dominated dusty inner ring, heavier by about four orders of magnitude and composed of large grains, fails to provide a satisfying description of the system, in particular in terms of flux contribution in the mid-IR spectral range. Figure 3 presents the final result of our MCMax modeling with the parameters of Table 2. We note that the strong PAH feature at 7.8 µm in HD 141569 is not seen in this model because the corresponding opacity has not been added to our models of the outer rings, unlike the models of Thi et al. (2014).

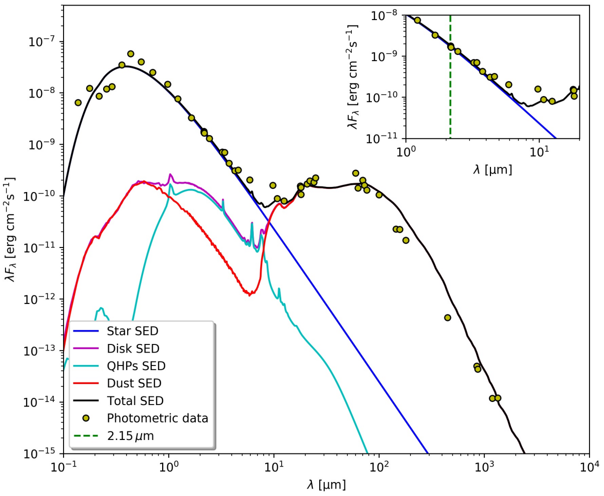

Fig. 3. MCMax SED (black line) of the model described in Table 2. The yellow circles are HD 141569 photometric data listed in Table G.1. The blue line represents the star SED modeled as a black body. The cyan line represents the QHPs SED and the red line the silicates SED. The magenta line is the total disk SED accounting for both QHP and silicate emission. The *top right plot* focuses on the first 10 μm wavelength range of the SED.

5.3. Spatial scale of the Brγ-line emitting region

We exploited the high-spectral resolution data of GRAVITY in the Brγ region to constrain the spatial scale of the hot gas emitting component, following the formalism in Sect. 4.2. Conservatively, the resulting pure-line visibilities plotted in red in Fig. 2 are very close to 1 for all the baselines. Considering the error bars we can say that the gas region is at the limit of spatially unresolved emission. We therefore propose to constrain the size of the gas emitting region by considering the gas emitting at the Brγ line wavelength peaks (i.e., 2.1654 and 2.1672 μm) using an infinitesimally thin ring model and estimating the upper-limit size that would exceed the error bar of ∼2% on the pure-line visibilities. In this way, we estimated a maximum radius of ∼0.35 mas (0.0385 au) for the gas emitting region.

While the analysis of the visibility amplitudes only provides us an estimate of the size scale of the gas emitting region, further information on the spatial and kinematic properties of the gas component is found in the differential phase signal. Typically, differential phases provide information on photocenter displacements along the baselines on angular scales that can surpass the nominal resolution of the interferometer. Figure 4 shows the GRAVITY pure-line differential phases. After removal of the continuum contribution (cf. Sect. 4.2), the S-shape becomes clearly visible for the baselines J3-D0 (100 m, 220°) and J3-K0 (54 m, 151°) around the Brγ line, while a weaker trend is seen for the baselines J3-G2 (62 m, 223°) and D0-G2 (38 m, 36°). The strongest signature shows an amplitude in the differential phase exceeding ∼20° for J3-K0. Since the differential phase signals for the baselines D0-K0 (95 m, 72°) and G2-K0 (68 m, 92°) are consistent with zero at all wavelengths, we fixed the pure-line differential phases to 0°. The typical uncertainties after correcting for the continuum subtraction are ∼4°. The resulting deprojected photocenter shifts per spectral channel, with reference frame fixed to the star location, are shown in Fig. 5. We clearly observe that all points are aligned along the same direction with an angle of $-10° \pm 7°$. The redshifted points are located along northwest, while the blueshifted points are located toward the southeast. Based on the redshifted maximum extent of the photocenter shifts, we estimated the radius of the gas region from the differential phases to be 0.333 ± 0.039 mas or 0.037 ± 0.004 au. This appears consistent with the less precise upper-limit size set through the analysis of the visibility amplitudes. We recall however that the size estimate derived through the photocenter shift does not correspond to the physical outer radius of the gas region, but to the size where the gas emission is more intense for a given wavelength.

The distribution of the 2D photocenter solution can be interpreted to the first order as being caused by a gas disk in Keplerian rotation orbiting HD 141569. Under this assumption the analysis of the Brγ emission line's shape provides further clues to the gas kinematics. We can indeed derive an estimate of the gaseous disk's radius from the separation between the two peaks of the line and the rest position. From Beckwith & Sargent (1993) we use

$$R_{\rm g} = \frac{G\,M_\star}{v_{\rm obs}^2}\sin^2 i, \tag{17}$$

where $R_{\rm g}$ is the radius, G is the gravitational constant, $M_\star$ the mass of the star, $v_{\rm obs}$ the projected velocity at the line peaks, and i the disk inclination. The $128 \pm 42\,{\rm km\,s^{-1}}$ average peaks shift of the Brγ line with respect to the line rest position leads to an outer limit for the gas region of 0.766 ± 0.554 mas in radius, or 0.084 ± 0.061 au. The resulting error accounts for the uncertainty on the stellar mass ($0.01\,M_\odot$), on the distance (1 pc), on the disk inclination (15°), and on the peak position (3 Å), the last being the dominant one.

The three approaches presented above and based on the analysis of the visibility amplitudes, differential phases, and the spectrum all seem consistent with a gas component in Keplerian rotation confined within ∼0.8 mas (∼0.09 au, $\sim 12.9\,R_\star$) in radius. We compared our differential phase signals, our strongest measurable quantity, to a simple geometrical model of an axisymmetric disk in Keplerian rotation built with two thin layers that account for the top and bottom sides of the disk, parameterized by an inner radius $r_{\rm in}$ (varying from 0.008 to 0.03 au), an outer radius $r_{\rm out}$ (varying from 0.033 to 0.8 au), and a power-law exponent α (varying from 0 to 4.0) for the disk's intensity radial profile following $I(r) \propto r^{-\alpha}$. The inclination of the disk was fixed to 58.5°, based on the results of the FT data analysis and under the assumption of coplanar dust-gas rings, and its position angle was fixed to −10°, based on the photocenter shift analysis. The hypothesis of an optically thin disk is made, which implies that the disk intensity does not strongly depend on the disk scale height, which is then fixed to H/R = 0.1 throughout the ring, but only on the surface area of the disk: $I \propto {\rm d}S$ where ${\rm d}S$ is an area element (for a complete description of the model, see de Valon et al., in prep.). The model delivers a spectral profile that is eventually normalized and fitted to our experimental double-peaked spectrum in Fig. 6. A grid of 2700 models has been explored, and a best-fit model is found for $r_{\rm in} = 0.011$ au, $r_{\rm out} = 0.09$ au, and $\alpha = 0.5$. From this best-fit model, we produced 2D velocity maps (Fig. 7) and retrieved the theoretical pure-line differential phase signal (see Fig. 4). Our Keplerian disk model reproduces qualitatively well the observed pure-line differential phases both in the orientation of the sine wave relative to the wavelength and in amplitude reinforcing the Keplerian gas disk scenario. We also observe that the weakest signals indeed correspond to the baselines D0-K0 and G2-K0 for which the peak

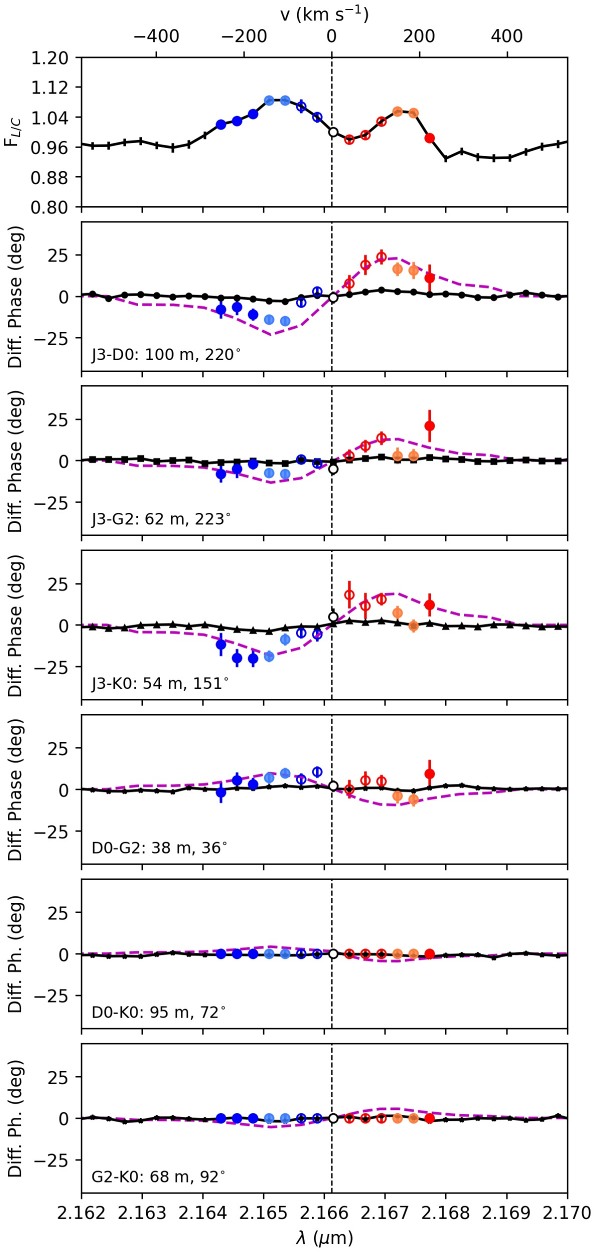

Fig. 4. HD 141569 spectrum (*top*), total (black circles and line), and pure-line differential phases (colored signs) along the different baselines. D0-K0 and G2-K0 baseline pure-line differential phases are set to zero. The colors refer to the different spectral channels. Dashed magenta lines represent the pure-line differential phases of the analytical Keplerian disk model described in Sect. 5.3.

amplitudes are ~3–5°. On a final note, for the best-fit solution model we tested the optically thick hypothesis by accounting for projection effects on the emissivity law, $I \propto \mathbf{dS} \cdot \mathbf{e_y} = \mathrm{d}S \cdot (\mathbf{n} \cdot \mathbf{e_y})$, where $\mathbf{e_y}$ is the line-of-sight unit vector and $\mathbf{n}$ the normal unit vector of the area element considered (see de Valon et al., in prep.). The resulting model leads to a spectrum that is similar to that derived from the optically thin model (a small difference is seen at the lowest velocities), and to pure-line differential phases and photocenters shifts consistent with those of the optically thin model.

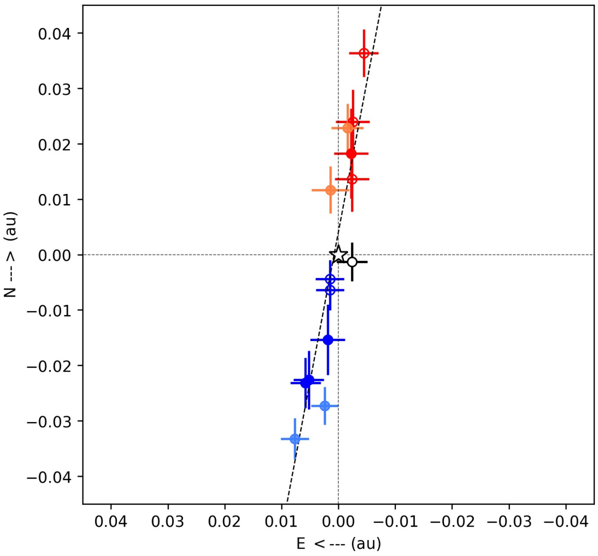

Fig. 5. Deprojected photocenter shifts. The colors refer to the different spectral channels and velocities, as shown in Fig. 4. The dashed black line, derived through a linear fit of the photocenter shifts, represents the gas region position angle.

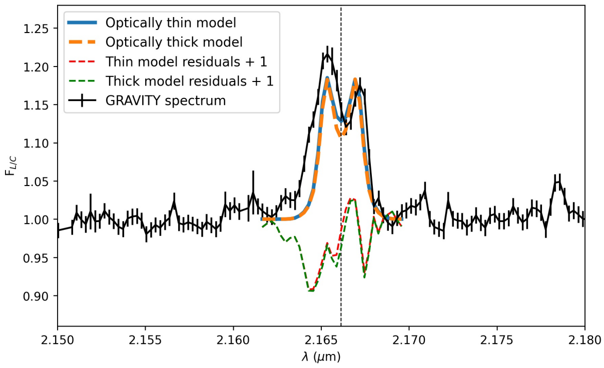

Fig. 6. HD 141569 GRAVITY spectrum (black line), and the spectra of the Keplerian disk models described in Sect. 5.3. The blue line represents the model in the optically thin scenario with residuals given by the red dashed line, while the orange line represents the model in the optically thick scenario with residuals given by the green dashed line.

6. Discussion

6.1. A newly detected inner dust ring

Thanks to GRAVITY, an additional inner ring component at ~1 au from the star, narrower than ~ 0.3 au, has been discovered, which adds to the multi-ring picture identified for HD 141569. A schematic visualization of the dust and gas distribution obtained from multi-epoch and multi-instrument observations is depicted in Fig. 8. The low level of near-IR excess (~6%) is comparable to the typical 5% accuracy of *K*-band photometric data

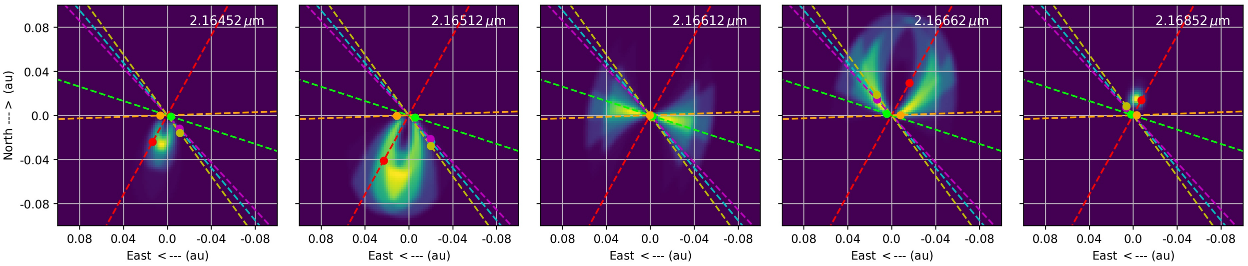

Fig. 7. Monochromatic images (from 2.16452 to 2.16852 μm, i.e., from 221 to 332 km s^{-1}) of the Keplerian ring model described in Sect. 5.3. The colored dashed lines refer to the different GRAVITY baselines. Circles represent the 2D photocenter shift for each baseline.

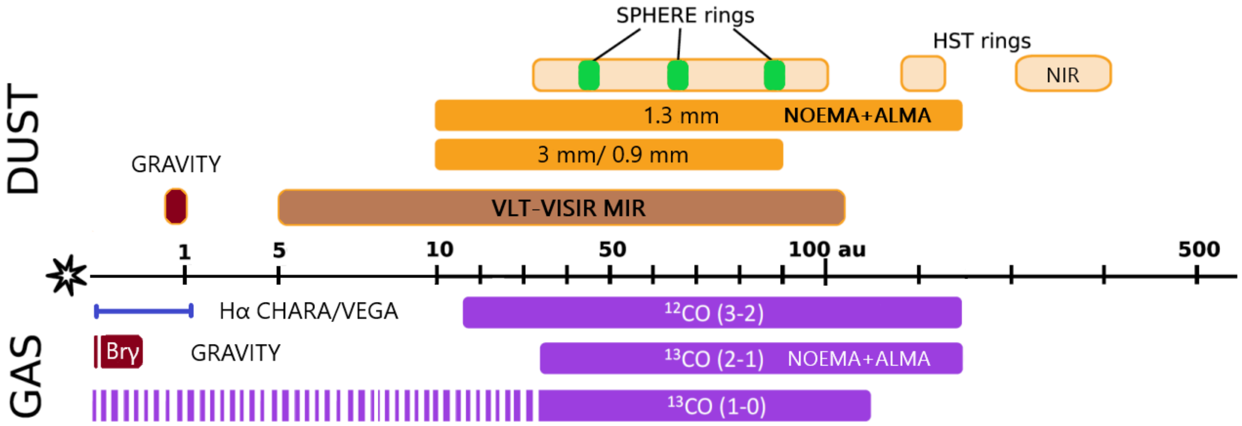

Fig. 8. Visualization of dust and gas distribution in HD 141569 (adapted from Di Folco et al. 2020). Shown in light orange are the optical–IR dust rings detected in scattered light by HTS (e.g., Augereau et al. 1999; Clampin et al. 2003; Konishi et al. 2016). Overplotted in green are the three near-IR dust ringlets detected by VLT/SPHERE (Perrot et al. 2016). The extended millimeter continuum emission detected by ALMA (Miley et al. 2018) and NOEMA (Di Folco et al. 2020) is shown in orange. The large brown ring represents the mid-IR continuum emission detected by VLT-VISIR and modeled by Thi et al. (2014). In dark red is shown the near-IR dust emission detected by GRAVITY and studied in this work. In the same color is the Brγ line emitting gas region detected by GRAVITY, also analyzed in this work. In blue is depicted the Hα line region based on the upper-limit size estimated by Mendigutía et al. (2017). Finally, in purple is shown the CO gas region whose emissions were detected by ALMA (e.g., White et al. 2016; Miley et al. 2018) and NOEMA (Di Folco et al. 2020).

(e.g., 2 MASS), which led to considering the near-IR flux of HD 141569 as essentially photospheric in earlier studies. With this result, the presence of dust as close as 1 au from the star, but well beyond the sublimation radius $R_{\rm sub}$ ~0.25 au is a more robust piece of evidence. The disk inclination and position angle estimated through the GRAVITY FT data analysis are consistent within the error bars with the values found for the outer rings that make up the circumstellar environment of the system (see Table H.1), suggesting an almost coplanar system of circumstellar rings. Considering how many constraints can effectively be set on the position angle (see Fig. B.2), it does not appear that any clear misalignment between the inner and outer disks could be claimed.

The inclination and position angle could be the reason why PTI and the Keck interferometer were not able to spatially resolve the near-IR emission of HD 141569 in earlier measurements, since the alignment of their single baseline was around 42° from north to east, hence not far from the semi-minor axis of the disk. However, the upper limit of 10 mas in radius for the location of the dust proposed by Monnier et al. (2005) is in agreement with our results. They also report a fractional excess of ~5%, but compatible within the error bars with pure photospheric flux in the *K* band.

Our results are substantially different from those obtained by Lazareff et al. (2017) with PIONIER in the *H* band. The reported flux excess is ~ 50% larger than in our case and their half-flux radius for the dust emission is only 0.03 au, well inside the sublimation radius of the system expected to be at ~0.21-0.26 au (for $L_\star = 16.6 - 27.0\,L_\odot$, $T_{\rm subl} \sim 1470$ K and a cooling efficiency ϵ ~0.5). Lazareff et al. (2017) modeled the *H*-band excess emission using an ellipsoid distribution and not a ring (see their Table B.2 and B.3). The choice of the model and the low-quality PIONIER data could potentially explain this unexpected result.

The values derived for the radius and width of this new innermost dusty component allows us to compare the system with other YSOs. The analysis made by GRAVITY Collaboration (2019) for a sample of 27 Herbig Ae/Be stars revealed dusty circumstellar environments with half-flux radii that range between 0.1 and 6 au depending on the stellar luminosity with a median of 0.6 au, and a width-to-radius ratio w ranging from 0.1 to 1 with a median of 0.83, which is interpreted as smooth and wide rings, even though with large error bars.

Our radius estimate for HD 141569 (~0.8 au) is within the range found by these authors, but its peculiarity is also reflected in the fact that its position in the size-luminosity diagram does not coincide with the bulk of the Herbig stars, reinforcing the idea that HD 141569 is a unique system in terms of evolution. From Table B.2, the width-to-size ratio is estimated to 0.05 ± 0.05 for the best-fit model, but it is also noticeable from Fig. B.2 that the ring's width is difficult to clearly constrain in the region below 0.3 au. This implies that the width-to-size ratio could be seven times larger. Therefore, our estimate of the width-to-size ratio goes on the lower end of the range found in GRAVITY Collaboration (2019), but remains comparable to systems such as HD 114981 (0.10 ± 0.03) or HD 190073 (0.14 ± 0.03).

In addition to the disk's well-known flux-size degeneracy, which in our case is broken thanks to the constant plateau in the squared visibilities curve as a function of spatial frequencies, Lazareff et al. (2017) found a negative correlation between the ring width and its half-flux radius, meaning that it gets more difficult to detect with the VLTI baseline small-radius ring-like structures than small-radius ellipsoid structures for angular sizes of the K-band emission of ~1 mas or smaller. In our case the size is well constrained being beyond the suggested limit, which is one argument favoring the robustness of our modeling as opposed to the model of a Gaussian brightness distribution that did not converge to a solution.

To further test our model findings, first we tried to add the contribution of a fully resolved emission (also known as a halo) to our geometrically thin ring model following Eq. (4) of Lazareff et al. (2017). Our best-fit solution ($\chi^2_{\rm red} = 4.69 \pm 0.32$) led to results similar to our geometrically thin ring model with a halo contribution that actually converges toward zero ($0.103^{+0.144}_{-0.075}$ %). Interestingly, this is in full agreement with Lazareff et al. (2017) who found null halo flux contribution as well. Second, we also tried a Lorentzian-convolved infinitesimally thin ring (see Table 5 of Lazareff et al. 2017), which leads to practically the same solution ($\chi^2_r = 4.68 \pm 0.32$). We conclude from this detailed analysis that the narrow ring-like shape with a width smaller than 0.3 au is a good description of our observations.

6.2. Nature and origin of the detected ring

We advance in Sect. 5.2 the scenario of a population of stochastically heated particles (e.g., PAH-like very small grains) as the cause for the near-IR excess. A number of arguments can be discussed in this context.

Our best-fit chromatic model shows a spectral index $k_{\rm c} = -0.35 \pm 0.21$ for the circumstellar emission. Following Lazareff et al. (2017) and GRAVITY Collaboration (2019), we estimate from the parameter $k_{\rm c}$ a temperature of the radiating dust under the gray body hypothesis (i.e., wavelength-independent emissivity) and find $T_{\rm c} = 1460 \pm 70$ K. In the case of a silicate dust ring in thermal equilibrium at ~0.8 au, we would expect a cooler temperature[2] of $T_{\rm c}$ ~650–850 K using the stellar parameter of Table 2 and a cooling efficiency ϵ between 0.3 and 1. Therefore, we argue that the near-IR emission is not dominated by emission of dust in thermal equilibrium, which can be explained by the presence of these small particles that are quantum heated by the stellar UV radiation. Even though the spectral index is found to be not very well constrained (see Fig. B.2), the spectral index corresponding to dust in thermal equilibrium at 800 K would be around +3.4 at λ_0, relatively far from the our best-fit model.

Maaskant et al. (2014) interpret the high intensity ratio between the PAH band at 6.2 μm to the band at 11.3 μm as a tracer of predominantly ionized PAH species located in a disk's gap and exposed to the intense ionizing UV radiation field of the central star. For instance, with a $I_{6.2}/I_{11.3}$ feature peak ratio of ~3−4 (Seok & Li 2017) the PAH sources IRS 48 and HD 179218 present emission from such predominantly ionized PAHs located in part inside the gap or disk cavity (Maaskant et al. 2014; Klarmann et al. 2017; Kluska et al. 2018; Taha et al. 2018). Interestingly, the $I_{6.2}/I_{11.3}$ peak ratio of HD 141569 derived from Seok & Li (2017) is high as well, estimated to ~5−6. This may indicate the presence of PAH species close to the star, with a predominantly ionized state due to the direct irradiation by UV stellar flux, bringing further support to our QHP-dominated inner ring model.

Comparing the IRS spectrum to our model, we find that the our model accounts for 28, 25, and 4% of the observed PAH peak emission for the features at 6, 8, and 11 μm, respectively. The remaining emission would come from PAHs located in the outer rings. Comparing the outer ring PAH mass reservoir estimated by Thi et al. (2014) to that of our innermost ring model, we find that our estimate ($4.3 \times 10^{-14}\,M_\odot$) is smaller than their ~15 au and ~300 au rings by three orders of magnitude ($2.0 \times 10^{-11}\,M_\odot$ and $2.1 \times 10^{-11}\,M_\odot$, respectively), and by four orders of magnitude for their ~185 au ring ($1.2 \times 10^{-10}\,M_\odot$) and the entire outer disk environment ($1.6 \times 10^{-10}\,M_\odot$). We recall however that in their model Thi et al. (2014) do not account for any dust located at ~1 au and suggest a 5 au dust-free inner gap, which could result in overestimated values on their side.

Regarding the origin of the ring structure, the case of HD 141569 is particularly interesting under the aspect of our proposed QHP-dominated inner component: one could question the presence of QHPs in an inner narrow ring since this kind of particle is expected to be coupled to the gas component and to date have been mostly invoked in more extended emission (e.g., Klarmann et al. 2017; Kluska et al. 2018).

Several authors have detected CO emission beyond ~10 au (see Introduction), whereas little information is available on the presence of CO within the first 10 au. It is likely however that this inner region is not gas depleted. The [O I] λ6300 emission detected by Acke et al. (2005), and suggested by these authors as a dissociation product of OH in the circumstellar disk, would originate between ~0.05 and 0.8 au under the assumption of a gas disk in Keplerian motion (Brittain et al. 2007). Hydrogen recombination and sodium lines were also detected (van der Plas et al. 2015). Both Mendigutía et al. (2017) and our results (see Sect. 6.3) find excited atomic hydrogen in the dust-free cavity, which implies the existence of a replenishment mechanism from the outer regions. Moreover, Brittain et al. (2007) set an upper limit on the column density of CO inside 6 au of N(CO) < 10^{15} cm^{-2}, which translates into a gas mass $<5.9 \times 10^{-13}\,M_\odot$. Considering our QHPs mass ($4.3 \times 10^{-14}\,M_\odot$), a gas-to-dust ratio of 100, and a [CO/H$_2$] ratio of 10^{-4}, this would translate in a CO mass of $4.3 \times 10^{-16}\,M_\odot$, which is well below the upper limit and therefore not detected yet. These arguments suggest that a gaseous component may exist and coincide with the proposed QHP component to which it would be coupled.

Furthermore, even though QHPs have been invoked in more extended emission in past works, we cannot exclude the possibility of more compact or narrow components. For example, Khalafinejad et al. (2016) modeled its inner circumstellar region through an optically thin spherical halo extending from 0.1 to

---

[2] Equation (14) in Lazareff et al. (2017).

1.7 au in order to explain the near-IR flux of HD 100453 and to fit simultaneously its Q-band flux. The choice of the spherical halo was based on the fact that their data poorly constrained the structure of the inner disk (and so it is the halo extension estimate) and the optically thin hypothesis was set in order to not affect the Q-band flux modeling. This component was also suggested by Klarmann et al. (2017). Their QHP model for HD 100453 underestimates the observed flux in the 1-5 μm wavelength range by up to 30%, and slightly overestimates the long-baseline visibility data, indicating that the missing flux is emitted on short spatial scales. Closer results to those we obtained for HD 141569 were found by Maaskant et al. (2013). These authors suggest a compact optically thin spherical halo for HD 169142 (0.1–0.2 au), HD 135344 B, and Oph IRS 48 (0.1–0.3 au) to reproduce the observed near-IR flux. Several scenarios have been proposed to explain the different structures that protoplanetary disks exhibit, such as gaps, spirals, or rings. Fragmentation of wide rings into narrow ones by secular gravitational instability (e.g., Tominaga et al. 2020), self-induced pileup of particles by aerodynamical feedback (e.g., Gonzalez et al. 2017), and dust traps at local maxima in the gas density due to a reversal of the pressure gradient by dynamical clearing from a companion (e.g., Pinilla et al. 2012) could explain a structured nature of the disk. Our observations leave this matter as an open question since GRAVITY informs us solely on the spatial properties of the detected K-band continuum emission.

6.3. HD 141569 Brγ-line emitting gas region

Our analysis of the kinematic and spatial distribution (via the differential phase) of the hot hydrogen gas is in line with a scenario of a Keplerian disk inside the dust-free cavity. The distribution of the photocenter shifts shown in Fig. 5 agrees well with the behavior expected from a Keplerian disk (Mendigutía et al. 2015). The position angle of the photocenter shifts distribution ($-10° \pm 7°$ north to east) is also found to be in overall agreement with the position angle of the inner ring responsible for the near-IR excess, and of the outer rings. Moreover, the photocenters of the Brγ line emitting gas region are located as the photocenters of the outer CO regions, blueshifted ones along the southeast and redshifted ones along the northwest (White et al. 2016). The profiles of pure-line differential phase signals depart a bit from the perfect S-shaped signal expected for a pure Keplerian disk. We believe that it is also limited ultimately by our spectral calibration. In this sense, more accurate measurement of the differential phases in HD 141569 using GRAVITY with the 8 m Unit Telescopes could certainly improve the accuracy of this analysis. In order to evaluate the quality of our spectral data, we chose to compare the GRAVITY profile measured with the ATs to other high-quality spectra obtained with the ISAAC spectrograph at the VLT (Garcia Lopez et al. 2006), the NIRSPEC echelle spectrograph at the Keck Observatory (Brittain et al. 2007), and with SINFONI/VLT from archival data. The comparison is shown in Fig. 9 and we observe that the GRAVITY spectrum exhibits a mild asymmetry between the blue and red peaks. This would suggest that our spectrum could be still affected by some calibration effects, either telluric or instrumental. We then further explored how far our resulting differential phases might be impacted by the slight spectrum asymmetry and tested the derivation of the pure-line differential phases using the SINFONI spectrum, which has a very similar spectral resolution, instead of the GRAVITY spectrum. We found that the 2D distribution of the photocenter shifts remains unchanged within the error bars reported in Fig. 5.

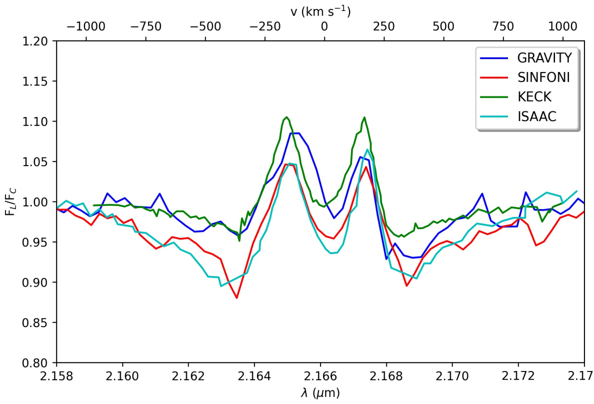

Fig. 9. HD 141569 continuum-normalized spectrum taken at different epochs and with different instruments. In blue is depicted the data taken on July 12, 2019, by GRAVITY; in red data taken in June 2019 by SINFONI; in green data taken in 2002 by the KECK NIRSPEC (Brittain et al. 2007); and in cyan data taken in 2004 by the VLT/ISAAC (Garcia Lopez et al. 2006).

The star is known to be a fast rotator ($222.0 \pm 7.0\,\mathrm{km\,s^{-1}}$, Folsom et al. 2012), which results in a small co-rotation radius around $2.38 \pm 0.53\,R_\odot$ (0.011 ± 0.002 au), assuming $R_\star = 1.5 \pm 0.5\,R_\odot$ (Fairlamb et al. 2015). We cannot exclude that part of the Brγ line emission comes from magnetospheric accretion flows, but the small co-rotation radius compared to the size of the Brγ line emitting region estimated from the SC data analysis (~0.09 au) would not favor this scenario, as opposed to what has been recently found for TW Hya (GRAVITY Collaboration 2020b). Interestingly, the scenario of magnetospheric accretion was also tested by Mendigutía et al. (2017) to explain the Hα double-peaked emission line, but they were not able to reproduce the observed profile with any set of input parameters. Comparing the extent of the Brγ emission to the continuum emission ($R_{\mathrm{Br}\gamma}/R_{\mathrm{cont}} \approx 0.1$), we find that the case of HD 141569 is in contrast with the findings of Kraus et al. (2008). These authors found for a small sample (5 objects) of Herbig Ae/Be stars that those showing a P Cygni Hα line profile and a high mass-accretion rate ($>10^{-7}\,M_\odot\,\mathrm{yr}^{-1}$) seem to show compact Brγ-emitting regions ($R_{\mathrm{Br}\gamma}/R_{\mathrm{cont}} < 0.2$), from which the emission stems from magnetospheric accretion or recombination line from ionized hydrogen, while stars showing a double-peaked or single-peaked Hα line profile show a more extended Brγ-emitting region ($0.6 \leq R_{\mathrm{Br}\gamma}/R_{\mathrm{cont}} \leq 1.4$), which would trace a stellar or disk wind. Our system shows mixed features, a Brγ and Hα double-peaked emission line that originates from compact disks in Keplerian rotation where magnetospheric accretion is not the most likely main emission mechanism. Therefore, recombination line emission from ionized hydrogen in an inner gaseous accretion disk as hinted by GRAVITY is a more supported scenario. If that is the case, considering the age of the system and the reported accretion rates between 10^{-7} and $10^{-11}\,M_\odot\,\mathrm{yr}^{-1}$ (Merín et al. 2004; Garcia Lopez et al. 2006; Mendigutía et al. 2011a; Thi et al. 2014; Fairlamb et al. 2015), the inner gaseous disk requires some sort of replenishment mechanism to explain its presence and for it to survive. Replenishment flows, planet-boosted or not (Mendigutía et al. 2017), connecting the inner and outer disk as already observed in other Herbig stars like HD 142527 (Casassus et al. 2013) could be investigated in the future.

6.4. Hybrid or debris disk?

As mentioned in the introduction, HD 141569 is the only known pre-main sequence star characterized by a hybrid disk. The main characteristic of a hybrid disk is the weak fractional excess of IR emission (8.4×10^{-3} for HD 141569, Sylvester et al. 1996), that stems from the optically thin second-generation grains dust component, coupled with the presence of a significant gaseous component, believed to be primordial. Unfortunately the other known best hybrid disk system candidates, which are 49 Cet, HD 21997 (Moór et al. 2011), HD 131835 (Moór et al. 2015), HD 121617, HD 131488 (Moór et al. 2017), and HD 32297 (Moór et al. 2019), have not been studied in their hot dust content. As HD 141569 does, they show a featureless SED in the near-IR suggesting systems depleted of material inside the first 5 au. However, as we saw in this work, interferometric observations could reveal as-yet-undetected dust, so this scenario should not be excluded for the other mentioned objects. The potential of long-baseline interferometry to detect small levels of hot circumstellar dust emission in supposedly dust-free systems has been indeed exploited for older main sequence stars (Ertel et al. 2014).

In this context it is interesting to compare our results for HD 141569 with Vega, the most iconic debris disk system with a similar spectral type (A0V), but that is significantly older than our source (400–700 Myr). Near-IR excess from Vega was detected and constrained to $\sim 1.29 \pm 0.19\%$ by interferometric observations with CHARA/FLUOR in the K band (Absil et al. 2006). These authors suggest by SED modeling that the excess comes from hot small grains starting at ∼0.2–0.3 au with a total dust mass of $8 \times 10^{-8}\,M_\oplus$. Knowing the age of Vega, it is clear that its circumstellar dust is of second generation, a characteristic of debris disks. In the scenario of a silicate-dominated inner ring for HD 141569, the total mass required to induce a larger near-IR excess is, as expected, significantly larger ($>10^{-4}\,M_\oplus$). Considering the younger age of HD 141569 (∼7.2 Myr), a more massive inner disk is compatible with a system at an earlier stage of disk evolution. Since the timescale for disk dissipation is known to be about 5−10 Myr (Wyatt 2008), it is plausible that part of the dust in the inner region of HD 141569 is of first generation and a remnant of the primordial circumstellar environment. This would confirm that HD 141569 is closer to a system in the final stage of the protoplanetary disk phase than a debris disk system.

The fact that gas, both H and CO, is detected in HD 141569 is an factor in favor of a system in the (late) protoplanetary disk stage rather than in the debris disk stage. The system, similarly to other hybrid disks, does not follow the correlation between the CO flux density and the millimeter continuum emission followed by T Tauri, Herbig Ae, and debris disks, but lies systematically above the correlation line (Péricaud et al. 2017). The authors suggest that the dust and gas evolution are decoupled, with the dust evolving faster than the gas, leading to an unusual high gas-to-dust ratio (between 135 and 2370 for HD 141569, Di Folco et al. 2020). Other than the primordial origin scenario, a secondary origin of CO was proposed (Kral et al. 2019) in which the gas is self-shielded and shielded by accumulated neutral carbon produced through photodissociation of molecular gas released by planetesimals. This model is able to explain the estimated CO masses in all the hybrid disk candidates (Kral et al. 2019; Moór et al. 2019) except for HD 141569, for which it was not tested. Since CO molecule photodissociation occurs at UV wavelengths, we note that C^0 could shield these molecules, and also QHPs (Woitke et al. 2016), which are known to absorb UV photons and cool down very quickly by emitting photons in the near-IR. The new detected innermost ring, which we propose in this work to be dominated by a small amount of QHPs, could contribute to the shielding process.

7. Summary

We presented the first GRAVITY interferometric observations of HD 141569. Here we summarize the main conclusions of our work:

- The system was resolved by GRAVITY with squared visibilities down to $V^2 \sim 0.8$. If before these observations the near-IR flux contribution of a dust disk was considered absent because no feature was seen in the SED of the object, now, thanks to interferometry, the presence of dust in the first au of the system is a more robust piece of evidence and the flux excess is clearly detected and constrained to be ∼6.2% of the total flux.
- Data modeling suggests that the dust is located in a thin ring ($\lesssim$0.3 au in width) at a radius of ∼1 au from the star. The ring shares, within the errors of Fig. B.2, the same inclination (∼58°) and position angle (∼0°) as the outer rings observed in the past.
- MCMax SED modeling suggests that this innermost ring could be made of a small amount ($1.4 \times 10^{-8}\,M_\oplus$) of QHPs. Large silicate grain models, with and without carbon, can reproduce the 6% flux excess at 2.15 μm, but at the same time they show a significant emission in the mid-IR not consistent with the SED of the system.
- The SC data analysis confirms the significant amount of Brγ line emitting gas already observed in the past. The gas region is spectrally resolved, but spatially unresolved.
- The pure-line differential phases constrain the gas to be in a Keplerian disk-like structure, as hinted by the double-peaked line shape, confined within ∼0.09 au (∼12.9 $R_\star$) and oriented in the same was as the outer rings ($\mathrm{PA_{NE}} \sim -10°$).

These results confirm the complexity of the HD 141569 circumstellar environment also at milliarcsecond scale, making the system a unique astronomical laboratory to investigate the missing steps of disk evolution and planet formation theories.

Acknowledgements. We thank the anonymous referee for reviewing this work in detail and for providing useful comments that have improved the quality of the paper. This work is based on observations made with ESO Telescopes at the La Silla Paranal Observatory under program IDs 0102.C-0408(D), 0103.C-0347(C), and 0103.C-0347(A). V.G. was supported for this research through a stipend from the International Max Planck Research School (IMPRS) for Astronomy and Astrophysics at the Universities of Bonn and Cologne, and from the Bonn-Cologne Graduate School of Physics and Astronomy (BCGS). A.C.G. received fundings from the European Research Council (ERC) under the European Union's Horizon 2020 research and innovation programme (grant agreement No. 743 029). L.K. acknowledges the helpful discussions that took place during the ISSI meeting "Zooming In On Rocky Planet Formation" (team 482). We thank Michiel Min for allowing us to use his MCMax code and for his help on understanding the code itself. We thank Anne-Marie Lagrange, Mickaël Bonnefoy and Florian Peissker for providing the SINFONI spectrum of HD 141569. We acknowledge the Gemini Observatory for the use of the IR spectrum model of the atmospheric transmission above Cerro Pachon. This research has made use of the model atmosphere grid NeMo, provided by the Department of Astronomy of the University of Vienna, Austria (`http://www.univie.ac.at/nemo/`). NeMo was funded by the Austrian Science Fonds.

References

Absil, O., di Folco, E., Mérand, A., et al. 2006, A&A, 452, 237
Acke, B., van den Ancker, M. E., & Dullemond, C. P. 2005, A&A, 436, 209
Allard, F., Hauschildt, P. H., Alexander, D. R., & Starrfield, S. 1997, ARA&A, 35, 137
ALMA Partnership (Fomalont, E. B., et al.) 2015, ApJ, 808, L1
Arun, R., Mathew, B., Manoj, P., et al. 2019, AJ, 157, 159

Augereau, J. C., & Papaloizou, J. C. B. 2004, A&A, 414, 1153
Augereau, J. C., Lagrange, A. M., Mouillet, D., & Ménard, F. 1999, A&A, 350, L51
Beckwith, S. V. W., & Sargent, A. I. 1993, ApJ, 402, 280
Benisty, M., Stolker, T., Pohl, A., et al. 2017, A&A, 597, A42
Berger, J. P., & Segransan, D. 2007, New Astron. Rev., 51, 576
Beuzit, J. L., Vigan, A., Mouillet, D., et al. 2019, A&A, 631, A155
Biller, B. A., Liu, M. C., Rice, K., et al. 2015, MNRAS, 450, 4446
Bjorkman, J. E., & Wood, K. 2001, ApJ, 554, 615
Brittain, S. D., Simon, T., Najita, J. R., & Rettig, T. W. 2007, ApJ, 659, 685
Casassus, S., van der Plas, G. M., Perez, S., et al. 2013, Nature, 493, 191
Clampin, M., Krist, J. E., Ardila, D. R., et al. 2003, AJ, 126, 385
Currie, T., Grady, C. A., Cloutier, R., et al. 2016, ApJ, 819, L26
Dent, W. R. F., Greaves, J. S., & Coulson, I. M. 2005, MNRAS, 359, 663
Di Folco, E., Péricaud, J., Dutrey, A., et al. 2020, A&A, 635, A94
Draine, B. T., & Li, A. 2001, ApJ, 551, 807
Eisner, J. A., Lane, B. F., Hillenbrand, L. A., Akeson, R. L., & Sargent, A. I. 2004, ApJ, 613, 1049
Eisner, J. A., Graham, J. R., Akeson, R. L., & Najita, J. 2009, ApJ, 692, 309
Eisner, J. A., Hillenbrand, L. A., & Stone, J. M. 2014, MNRAS, 443, 1916
Eisner, J. A., Rieke, G. H., Rieke, M. J., et al. 2015, MNRAS, 447, 202
Ertel, S., Absil, O., Defrère, D., et al. 2014, A&A, 570, A128
Fairlamb, J. R., Oudmaijer, R. D., Mendigutía, I., Ilee, J. D., & van den Ancker, M. E. 2015, MNRAS, 453, 976
Fisher, R. S., Telesco, C. M., Piña, R. K., Knacke, R. F., & Wyatt, M. C. 2000, ApJ, 532, L141
Flaherty, K. M., Hughes, A. M., Andrews, S. M., et al. 2016, ApJ, 818, 97
Folsom, C. P., Bagnulo, S., Wade, G. A., et al. 2012, MNRAS, 422, 2072
Foreman-Mackey, D., Hogg, D. W., Lang, D., & Goodman, J. 2013, PASP, 125, 306
Garcia Lopez, R., Natta, A., Testi, L., & Habart, E. 2006, A&A, 459, 837
Gonzalez, J. F., Laibe, G., & Maddison, S. T. 2017, MNRAS, 467, 1984
Goto, M., Usuda, T., Dullemond, C. P., et al. 2006, ApJ, 652, 758
GRAVITY Collaboration (Abuter, R., et al.) 2017, A&A, 602, A94
GRAVITY Collaboration (Perraut, K., et al.) 2019, A&A, 632, A53
GRAVITY Collaboration (Caratti o Garatti, A., et al.) 2020a, A&A, 635, L12
GRAVITY Collaboration (Garcia Lopez, R., et al.) 2020b, Nature, 584, 547
GRAVITY Collaboration (Koutoulaki, M., et al.) 2021, A&A, 645, A50
Gray, R. O., & Corbally, C. J. 1994, AJ, 107, 742
Hauschildt, P. H., Allard, F., & Baron, E. 1999, ApJ, 512, 377
Heiter, U., Kupka, F., van't Veer-Menneret, C., et al. 2002, A&A, 392, 619
Khalafinejad, S., Maaskant, K. M., Mariñas, N., & Tielens, A. G. G. M. 2016, A&A, 587, A62
Klarmann, L., Benisty, M., Min, M., et al. 2017, A&A, 599, A80
Kluska, J., Kraus, S., Davies, C. L., et al. 2018, ApJ, 855, 44
Konishi, M., Grady, C. A., Schneider, G., et al. 2016, ApJ, 818, L23
Kóspál, Á., Ábrahám, P., Acosta-Pulido, J. A., et al. 2012, ApJS, 201, 11
Kral, Q., Marino, S., Wyatt, M. C., Kama, M., & Matrà, L. 2019, MNRAS, 489, 3670
Kraus, S., Hofmann, K. H., Benisty, M., et al. 2008, A&A, 489, 1157
Lacour, S., Dembet, R., Abuter, R., et al. 2019, A&A, 624, A99
Lapeyrere, V., Kervella, P., Lacour, S., et al. 2014, SPIE Conf. Ser., 9146, 91462D
Lazareff, B., Berger, J. P., Kluska, J., et al. 2017, A&A, 599, A85
Le Bouquin, J. B., Absil, O., Benisty, M., et al. 2009, A&A, 498, L41
Li, A., & Lunine, J. I. 2003, ApJ, 594, 987
Lodato, G., Dipierro, G., Ragusa, E., et al. 2019, MNRAS, 486, 453
Lopez, B., Lagarde, S., Jaffe, W., et al. 2014, The Messenger, 157, 5
Lord, S. D. 1992, A new software tool for computing Earth's atmospheric transmission of near- and far-infrared radiation, NASA Technical Memorandum 103957
Maaskant, K. M., Honda, M., Waters, L. B. F. M., et al. 2013, A&A, 555, A64
Maaskant, K. M., Min, M., Waters, L. B. F. M., & Tielens, A. G. G. M. 2014, A&A, 563, A78
Malfait, K., Waelkens, C., Waters, L. B. F. M., et al. 1998, A&A, 332, L25
Marsh, K. A., Silverstone, M. D., Becklin, E. E., et al. 2002, ApJ, 573, 425
Mawet, D., Choquet, É., Absil, O., et al. 2017, AJ, 153, 44
Meeus, G., Waters, L. B. F. M., Bouwman, J., et al. 2001, A&A, 365, 476
Meeus, G., Montesinos, B., Mendigutía, I., et al. 2012, A&A, 544, A78
Mendigutía, I., Calvet, N., Montesinos, B., et al. 2011a, A&A, 535, A99
Mendigutía, I., Eiroa, C., Montesinos, B., et al. 2011b, A&A, 529, A34
Mendigutía, I., de Wit, W. J., Oudmaijer, R. D., et al. 2015, MNRAS, 453, 2126
Mendigutía, I., Oudmaijer, R. D., Mourard, D., & Muzerolle, J. 2017, MNRAS, 464, 1984
Menu, J., van Boekel, R., Henning, T., et al. 2015, A&A, 581, A107
Merín, B., Montesinos, B., Eiroa, C., et al. 2004, A&A, 419, 301
Miley, J. M., Panić, O., Wyatt, M., & Kennedy, G. M. 2018, A&A, 615, L10
Millan-Gabet, R., Schloerb, F. P., & Traub, W. A. 2001, ApJ, 546, 358
Min, M., Dullemond, C. P., Dominik, C., de Koter, A., & Hovenier, J. W. 2009, A&A, 497, 155
Moerchen, M. M., Telesco, C. M., & Packham, C. 2010, ApJ, 723, 1418
Monnier, J. D., Millan-Gabet, R., Billmeier, R., et al. 2005, ApJ, 624, 832
Moór, A., Ábrahám, P., Juhász, A., et al. 2011, ApJ, 740, L7
Moór, A., Henning, T., Juhász, A., et al. 2015, ApJ, 814, 42
Moór, A., Curé, M., Kóspál, Á., et al. 2017, ApJ, 849, 123
Moór, A., Kral, Q., Ábrahám, P., et al. 2019, ApJ, 884, 108
Nilsson, R., Liseau, R., Brandeker, A., et al. 2010, A&A, 518, A40
Penprase, B. E. 1992, ApJS, 83, 273
Péricaud, J., Di Folco, E., Dutrey, A., Guilloteau, S., & Piétu, V. 2017, A&A, 600, A62
Perrot, C., Boccaletti, A., Pantin, E., et al. 2016, A&A, 590, L7
Pinilla, P., Benisty, M., & Birnstiel, T. 2012, A&A, 545, A81
Purcell, E. M. 1976, ApJ, 206, 685
Reche, R., Beust, H., & Augereau, J. C. 2009, A&A, 493, 661
Sandell, G., Weintraub, D. A., & Hamidouche, M. 2011, ApJ, 727, 26
Seok, J. Y., & Li, A. 2017, ApJ, 835, 291
Sloan, G. C., Keller, L. D., Forrest, W. J., et al. 2005, ApJ, 632, 956
Sylvester, R. J., Skinner, C. J., Barlow, M. J., & Mannings, V. 1996, MNRAS, 279, 915
Sylvester, R. J., Dunkin, S. K., & Barlow, M. J. 2001, MNRAS, 327, 133
Taha, A. S., Labadie, L., Pantin, E., et al. 2018, A&A, 612, A15
Thi, W. F., Pinte, C., Pantin, E., et al. 2014, A&A, 561, A50
Tominaga, R. T., Takahashi, S. Z., & Inutsuka, S.-i. 2020, ApJ, 900, 182
van der Plas, G., van den Ancker, M. E., Waters, L. B. F. M., & Dominik, C. 2015, A&A, 574, A75
Vioque, M., Oudmaijer, R. D., Baines, D., Mendigutía, I., & Pérez-Martínez, R. 2018, A&A, 620, A128
Weigelt, M., Baur, O., Reubelt, T., Sneeuw, N., & Roth, M. 2011, ESA SP, 696, 36
Weinberger, A. J., Becklin, E. E., Schneider, G., et al. 1999, ApJ, 525, L53
White, J. A., Boley, A. C., Hughes, A. M., et al. 2016, ApJ, 829, 6
Woitke, P., Min, M., Pinte, C., et al. 2016, A&A, 586, A103
Wyatt, M. C. 2005, A&A, 440, 937
Wyatt, M. C. 2008, ARA&A, 46, 339
Wyatt, M. C., Panić, O., Kennedy, G. M., & Matrà, L. 2015, Ap&SS, 357, 103

---

[1] I. Physikalisches Institut, Universität zu Köln, Zülpicher Str. 77, 50937 Köln, Germany
e-mail: `ganci@ph1.uni-koeln.de`

[2] Max-Planck-Institute for Radio Astronomy, Auf dem Hügel 69, 53121 Bonn, Germany

[3] Max Planck Institute for Astronomy, Königstuhl 17, 69117 Heidelberg, Germany

[4] Univ. Grenoble Alpes, CNRS, IPAG, 38000 Grenoble, France

[5] Unidad Mixta Internacional Franco-Chilena de Astronomía (CNRS, UMI 3386), Departamento de Astronomía, Universidad de Chile, Camino El Observatorio 1515, Las Condes, Santiago, Chile

[6] Dublin Institute for Advanced Studies, 31 Fitzwilliam Place, D02 XF86 Dublin, Ireland

[7] School of Physics, University College Dublin, Belfield, Dublin 4, Ireland

[8] Instituto de Astronomía, Universidad Nacional Autónoma de México, Apdo. Postal 70264, Ciudad de México 04510, Mexico

[9] CENTRA, Centro de Astrofísica e Gravitação, Instituto Superior Técnico, Avenida Rovisco Pais 1, 1049 Lisboa, Portugal

[10] Universidade do Porto, Faculdade de Engenharia, Rua Dr. Roberto Frias, 4200-465 Porto, Portugal

[11] Universidade de Lisboa - Faculdade de Ciências, Campo Grande, 1749-016 Lisboa, Portugal

[12] Max Planck Institute for Extraterrestrial Physics, Giessenbachstrasse, 85741 Garching bei München, Germany

[13] LESIA, Observatoire de Paris, PSL Research University, CNRS, Sorbonne Universités, UPMC Univ. Paris 06, Univ. Paris Diderot, Sorbonne Paris Cité, France

[14] Sterrewacht Leiden, Leiden University, Postbus 9513, 2300 RA Leiden, The Netherlands

[15] European Southern Observatory, Karl-Schwarzschild-Str. 2, 85748 Garching bei München, Germany

[16] INAF – Osservatorio Astronomico di Capodimonte, via Moiariello 16, 80131 Napoli, Italy

Appendix A: GRAVITY observations

Table A.1. Observation logs of the VLTI/GRAVITY HD141569 observations.

Date	UT	Configuration	N	Calibrator (diam. [mas], SpT †)	Seeing [″]	Airmass	τ_0 [ms]	Frame rate [Hz]
2019-03-18	08:08	D0-G2-J3-K0	3	HD 137006 (0.291±0.008, A5 II/III)	0.4	1.1	14	909
2019-05-24	04:15	A0-G1-J2-J3	1	HD 141977 (0.251±0.006, K3 III)	1.4	1.1	3	303
2019-07-12	00:44	D0-G2-J3-K0	8	HD 137006 (0.291±0.008, A5 II/III)	0.6 – 1.1	1.1	3	909

Notes. The date format is year-month-day. N denotes the number of 5-minute files that have been recorded on the target. Reference †: uniform disk diameter and SpT derived from the software package SearchCal from the Jean-Marie Mariotti Center (JMMC).

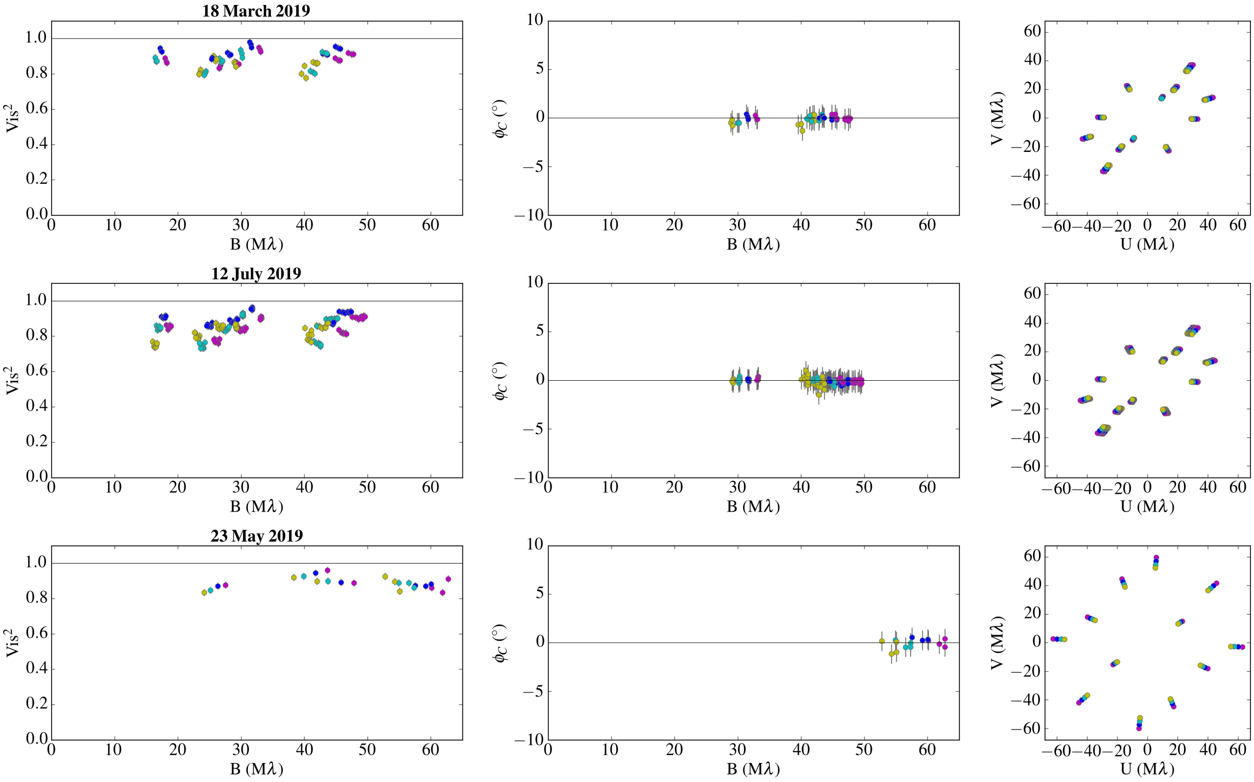

Fig. A.1. HD 141569 FT data, squared visibilities, closure phases, and U-V plane coverage, from the three different observation epochs. The colors refer to the different GRAVITY spectral channels.

Appendix B: MCMC posterior distribution functions and visibility modeling

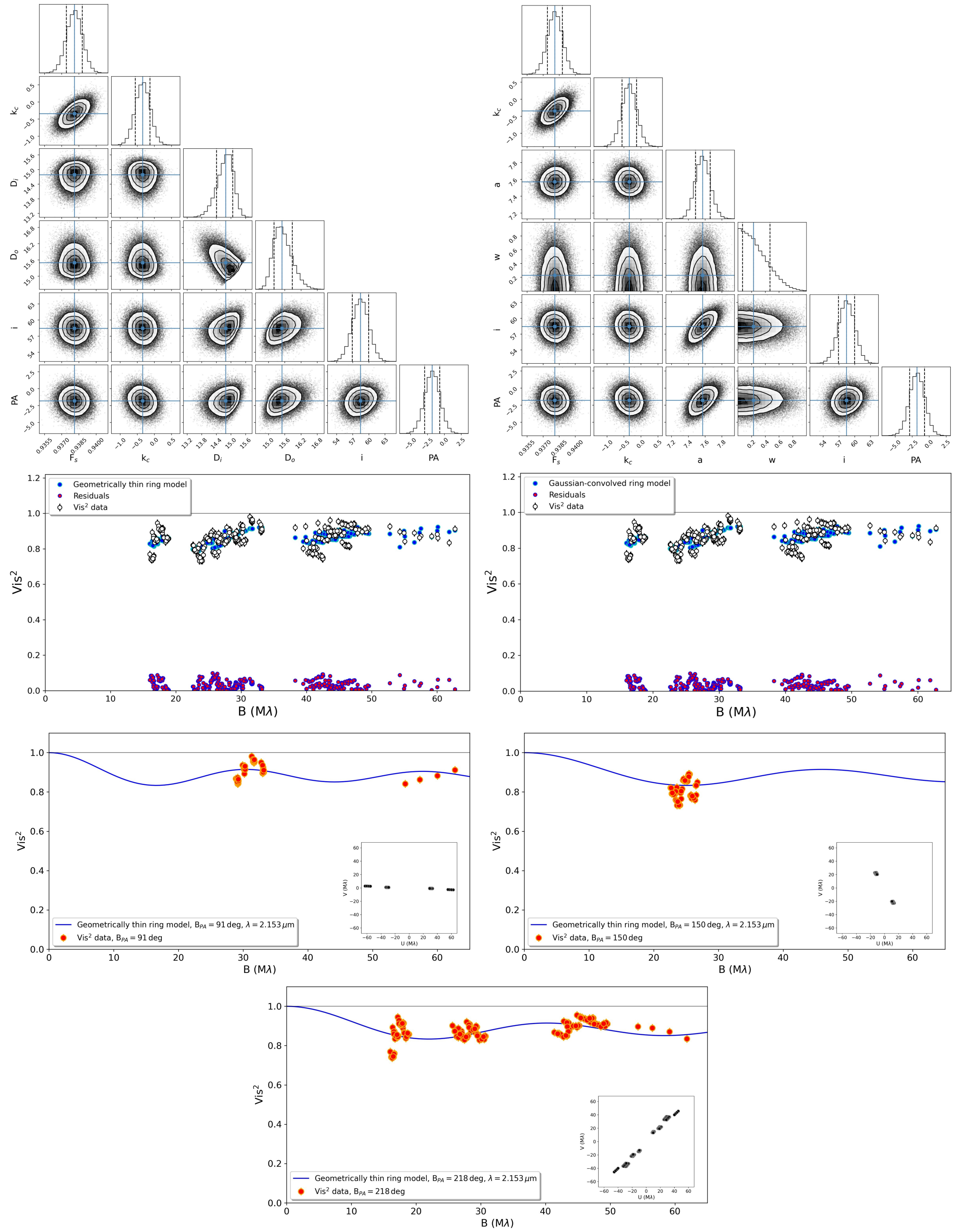

Fig. B.1. Results of the FT data fit. Top: MCMC marginal posterior distributions of the fitted parameters. The blue lines identify the median of the distributions for the geometrically thin ring model (left) and for the Gaussian-convolved infinitesimally thin ring model (right). Center: Comparison between the model squared visibilities (blue dots) and the observational data (white–black dots). The red dots represent the absolute residuals. Bottom: Vis^2 best fit to the geometrically thin ring model (blue continuous line) at λ=2.153 μm for three different position angles identified in the insets. The visibility data are shown for all spectral channels by the red circles.

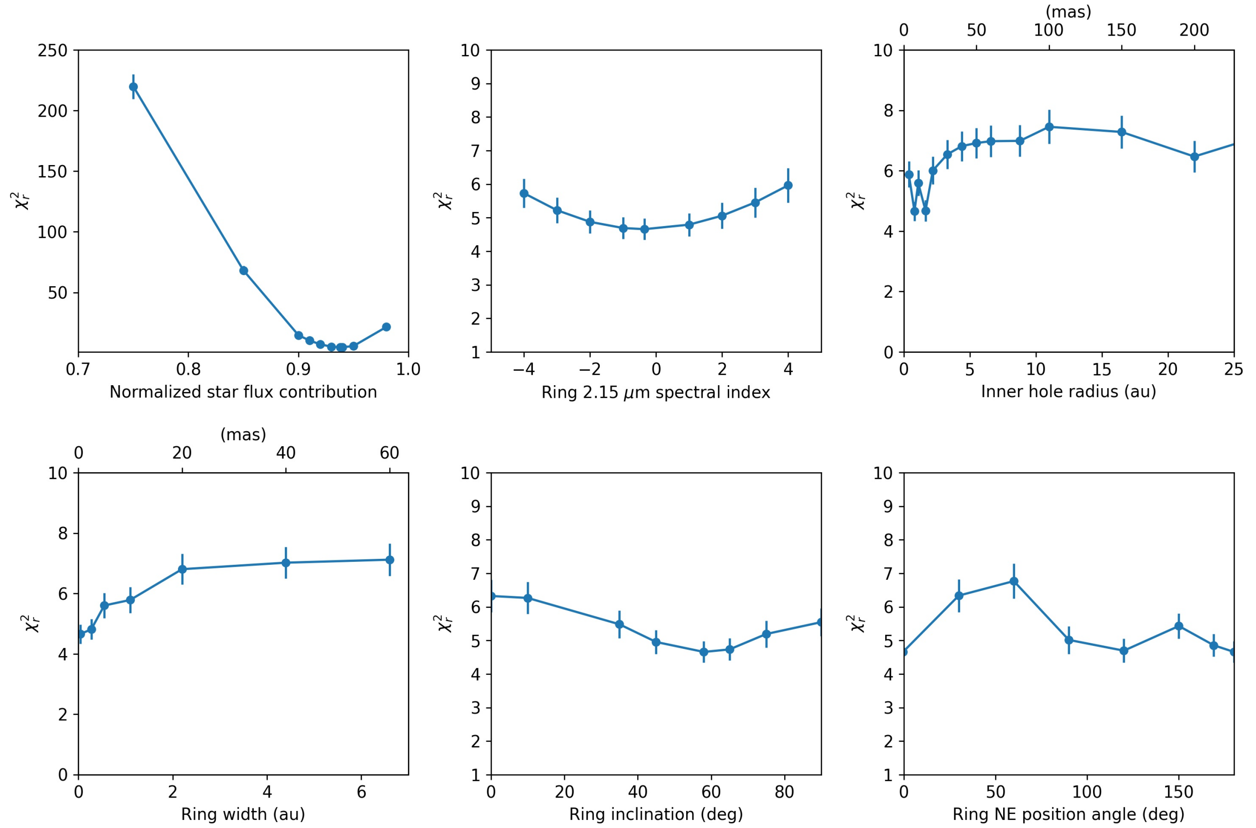

Fig. B.2. Reduced chi-squared χ_r^2 from the geometrically thin ring model squared visibility fit as a function of the different model parameters. Each point represents a squared visibility fit with the respective parameter fixed to that value while the other parameters are set free.

Appendix C: Spectrum wavelength calibration, telluric line correction, and photospheric absorption correction

The 2.15-2.18 μm part of the HD 141569 spectrum is shown in Fig. 2 after continuum-normalization, wavelength calibration, telluric line correction (left panel), and photospheric absorption correction (right panel). The continuum-normalization was done in both the science object spectrum and in our inteferometric calibrator HD 137006 spectrum ($\alpha = 230.932°$, $\delta = -01.022°$, A5II/III SpT) by fitting the slope of each raw spectrum and dividing the raw spectrum by the resulting fit. The first step of the wavelength calibration was done by comparing the observed wavelength positions of the telluric lines in the HD 141569 spectrum with respect to the positions of the telluric lines present in the IR spectrum of the atmospheric transmission above Cerro Pachon, generated using the ATRAN modeling software (Lord 1992) accounting for a 4.3 mm water vapor column and a 1.5 mm airmass column, available on the Gemini Observatory website. The atmospheric transmission spectrum was convolved by a Gaussian with FHWM of 6 Å to have the same resolution as GRAVITY. The same correction, which results in a 5 Å blueshift, was also applied on the SC visibilities and differential phases, and on the HD 137006 spectrum, our calibrator star. The calibrator was also used as a telluric spectroscopic standard. It shows a photospheric absorption feature at 2.16612 μm that was taken out before the telluric correction on the science object through a NextGen spectrum model (Allard et al. 1997; Hauschildt et al. 1999), available on the GAIA archive, with the following parameters: 7600 K effective temperature, 6.0 surface gravity logarithm, and a −2.0 solar metallicity. Moreover, the spectrum shows an absorption feature at around 2.16712 μm that is not observed in the spectrum of the other calibrators observed that night and that significantly affects the shape and the intensity of the HD 141569 Brγ red peak. For this reason we chose to calculate the atmospheric transmission function of the night by taking the average of three calibrator spectra, HD 137006, HD 149789, and HD 157029, shown in Fig. C1. The HD 141569 spectrum was then corrected for its radial velocity (−6.4 km/s) and its proper motion with respect to the local standard of rest, resulting in a correction of −8.7 km/s. Finally, the HD 141569 spectrum was corrected for atmospheric absorption through a spectrum model from the Vienna New Model Grid of Stellar Atmospheres (Heiter et al. 2002)[3]. The model accounts for a star effective temperature of 9800 K, a surface gravity logarithm of 4.4 (Fairlamb et al. 2015), solar metallicity, and microturbulence of 2.0 km/s (Folsom et al. 2012). Since the star is a fast rotator having a projected linear velocity of $v \sin i = 222.0 \pm 7.0$ km/s (Folsom et al. 2012), we included the rotation broadening effect on the spectrum model using SPECTRUM (Gray & Corbally 1994). We decreased the intensity of the absorption model by 3 % to better fit our spectrum.

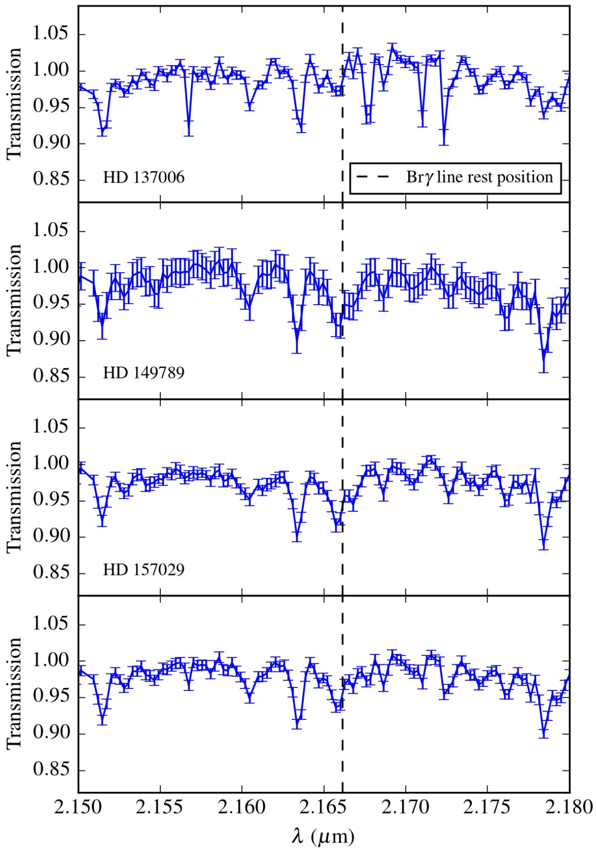

Fig. C.1. Atmospheric transmission functions derived from calibrator spectra: HD 137006 (top), HD 149789 (center), and HD 157029 (bottom). The last plot is the average transmission function of the three spectra.

---

[3] available on the NeMo webpage (Ch. Stütz and E. Paunzen, `http://www.univie.ac.at/nemo/`)

Appendix D: Pure-line visibility in presence of photospheric absorption

The total visibility three-component model used to fit the SC visibilities accounts for the contributions from the star, the circumstellar dust, and the line emitting gas. The total visibility as a function of the wavelength is given by

$$V_{\mathrm{Tot}}(u,v,\lambda) = \frac{\alpha(\lambda)\,F_{\mathrm{s}}(\lambda)\,V_{\mathrm{s}}(u,v,\lambda) + F_{\mathrm{c}}(\lambda)\,V_{\mathrm{c}}(u,v,\lambda) + F_{\mathrm{L}}(\lambda)\,V_{\mathrm{L}}(u,v,\lambda)}{\alpha(\lambda)\,F_{\mathrm{s}}(\lambda) + F_{\mathrm{c}}(\lambda) + F_{\mathrm{L}}(\lambda)}. \tag{D.1}$$

The parameter $\alpha(\lambda)$ is the star continuum-normalized photospheric absorption, which implies that $\alpha(\lambda) = 1$ outside the Brγ line and $\alpha(\lambda) < 1$ inside the line. This parameter is estimated from the Vienna New Model Grid of Stellar Atmospheres fitting the stellar parameters of HD 141569, as described in Section C. $F_{\mathrm{s}}(\lambda)$, $F_{\mathrm{c}}(\lambda)$, and $F_{\mathrm{L}}(\lambda)$ are the wavelength-dependent fluxes of, respectively, the stellar continuum (i.e., outside the line and temperature-dependent), the dust ring continuum, and the Brγ line emitting gas. $F_{\mathrm{L}}(\lambda)$ varies across the line and vanishes to zero outside the line. $V_{\mathrm{s}}(\lambda)$, $V_{\mathrm{c}}(\lambda)$, and $V_{\mathrm{L}}(\lambda)$ are the intrinsic visibility functions of each of the three components taken individually. From now on, the star is considered unresolved; therefore, V_{s} is equal to 1, and we drop the explicit parameter dependencies for convenience.

Outside the Brγ line (i.e., in the continuum region) the total visibility is given by

$$V_{\mathrm{Tot}}^{\mathrm{Cont}} = \frac{F_{\mathrm{s}} + F_{\mathrm{c}}\,V_{\mathrm{c}}}{F_{\mathrm{s}} + F_{\mathrm{c}}}. \tag{D.2}$$

Using Eq. D.2 to replace V_{c}, we can rewrite Eq. D.1 as

$$V_{\mathrm{Tot}} = \frac{\alpha\,F_{\mathrm{s}} + V_{\mathrm{Tot}}^{\mathrm{Cont}}\,(F_{\mathrm{s}} + F_{\mathrm{c}}) - F_{\mathrm{s}} + F_{\mathrm{L}}\,V_{\mathrm{L}}}{\alpha\,F_{\mathrm{s}} + F_{\mathrm{c}} + F_{\mathrm{L}}}, \tag{D.3}$$

and using the definition of the line-to-continuum flux ratio (Eq. 13), Eq. D.3 becomes

$$V_{\mathrm{Tot}} = \frac{F_{\mathrm{s}}\,(\alpha - 1)}{F_{\mathrm{Tot}}} + \frac{V_{\mathrm{Tot}}^{\mathrm{Cont}}}{F_{\mathrm{L/C}}} + \frac{F_{\mathrm{L}}\,V_{\mathrm{L}}}{F_{\mathrm{Tot}}}, \tag{D.4}$$

where $F_{\mathrm{Tot}} = \alpha\,F_{\mathrm{s}} + F_{\mathrm{c}} + F_{\mathrm{L}}$. We note once again that $F_{\mathrm{L/C}}$ is the raw line-to-continuum ratio including the photospheric absorption. This quantity corresponds to the top left spectrum in Fig. 2. We also note that outside the line (i.e., α=1 and F_{L}=0), Eq. D.4 simplifies to Eq. D.2. Now, making use of the parameter β of Eq. 14, we can write

$$\frac{F_{\mathrm{L}}}{F_{\mathrm{Tot}}} = 1 - \frac{\alpha + \beta}{1 + \beta}\,\frac{1}{F_{\mathrm{L/C}}}, \tag{D.5}$$

and finally Eq. D.4 becomes

$$V_{\mathrm{Tot}} = \frac{\alpha - 1}{1 + \beta}\,\frac{1}{F_{\mathrm{L/C}}} + \frac{V_{\mathrm{Tot}}^{\mathrm{Cont}}}{F_{\mathrm{L/C}}} + V_{\mathrm{L}}\,(1 - \frac{\alpha + \beta}{1 + \beta}\,\frac{1}{F_{\mathrm{L/C}}}). \tag{D.6}$$

Solving Eq. D.6 for V_{L}, and noting that from our data $V_{\mathrm{Tot}} = V_{\mathrm{Tot}}^{\mathrm{Cont}}$ since the SC visibilities are spectrally flat for all wavelengths and baselines, we obtain Eq. 12:

$$V_{\mathrm{L}} = \frac{V_{\mathrm{Tot}}\,[(1 + \beta)\,F_{\mathrm{L/C}} - 1 - \beta] - \alpha + 1}{(1 + \beta)\,F_{\mathrm{L/C}} - \alpha - \beta}. \tag{D.7}$$

This equation tells us that the pure-line visbility can be estimated from the total visibility in the line (which in our case is comparable to the total visibility in the continuum) if the photospheric absorption profile can be estimated, the continuum disk-to-star flux ratio β is known and the continuum-normalized spectrum of the line is accessible. We note, in the case where $V_{\mathrm{Tot}} = V_{\mathrm{Tot}}^{\mathrm{Cont}}$, that the absence of photospheric absorption (i.e., α=1) leads simply to $V_{\mathrm{L}} = V_{\mathrm{Tot}}^{\mathrm{Cont}} = V_{\mathrm{Tot}}$.

Finally, we see that the pure-line visibility V_{L} is lower than 1 only when $F_{\mathrm{L/C}}$ is greater than 1, which is equivalent to detecting the line above the continuum.

Appendix E: MCMax silicate model

Here are shown three representative cases of our SED modeling through a silicate dust ring, as described in Section 5.2. The first model accounts for particles with a lower-limit size of 1.26 μm, a dust mass of 10^{-5} $M_\oplus$, and 0 % carbon with a resulting temperature distribution in the range 570 – 1070 K. The second model accounts for particles with a lower-limit size of 40 μm, a mass of 1.17×10^{-4} $M_\oplus$, and 0 % carbon with a resulting temperature distribution in the range 620 – 840 K. The last model accounts for particles with a lower-limit size of 40 μm, a mass of 3.33×10^{-4} $M_\oplus$, and 25 % carbon with a resulting temperature distribution in the range 440 – 770 K. We note that in all three cases the near-IR excess is smaller than that obtained through the GRAVITY data analysis, while the mid-IR emission exceeds the photometry data. Decreasing the mid-IR excess would at the same time decrease further the near-IR value, suggesting that a pure silicate innermost ring model is not compatible with the nature of the HD 141569 system.

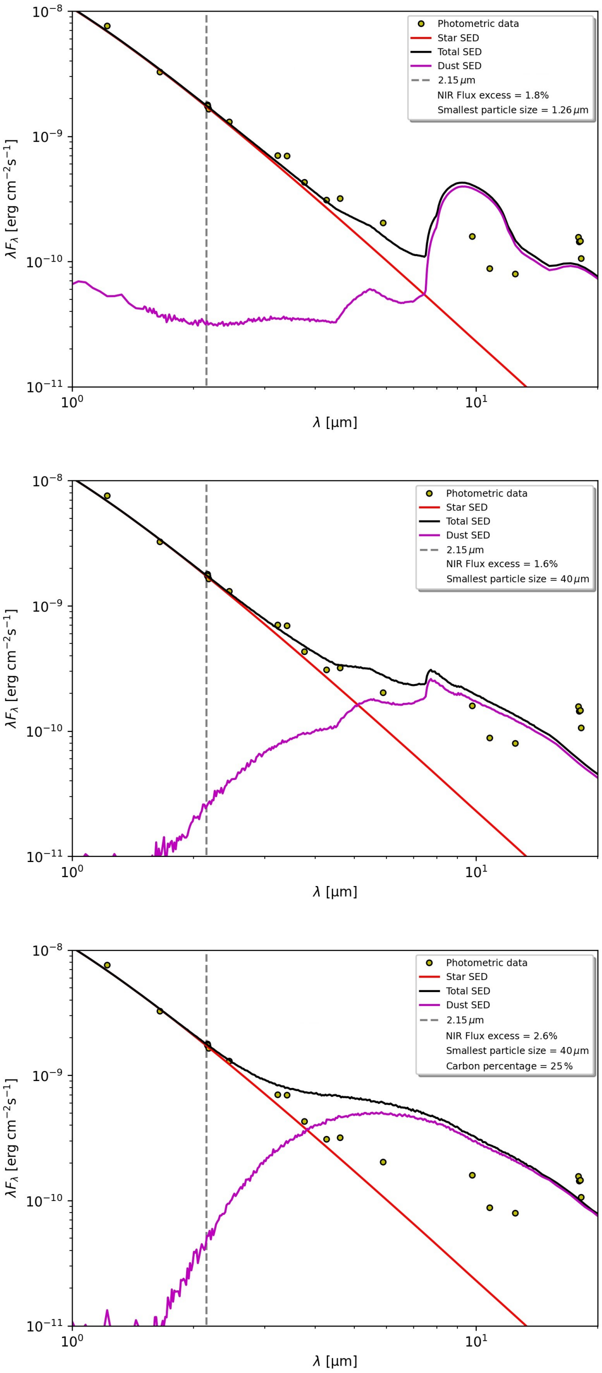

Fig. E.1. MCMax models that account for the emission of the star and only the first innermost silicate ring located at 0.8 au and 0.04 au in width. The models differ for the particle size lower limit, dust mass, and carbon percentage. The top plot model accounts for a dust mass of 10^{-5} $M_\oplus$ and no carbon; the center plot model accounts for a mass of 1.17×10^{-4} $M_\oplus$ and no carbon; the bottom plot model accounts for a mass of 3.33×10^{-4} $M_\oplus$ and 25 % carbon.

Appendix F: MCMax model density and temperature structure for the QHP model

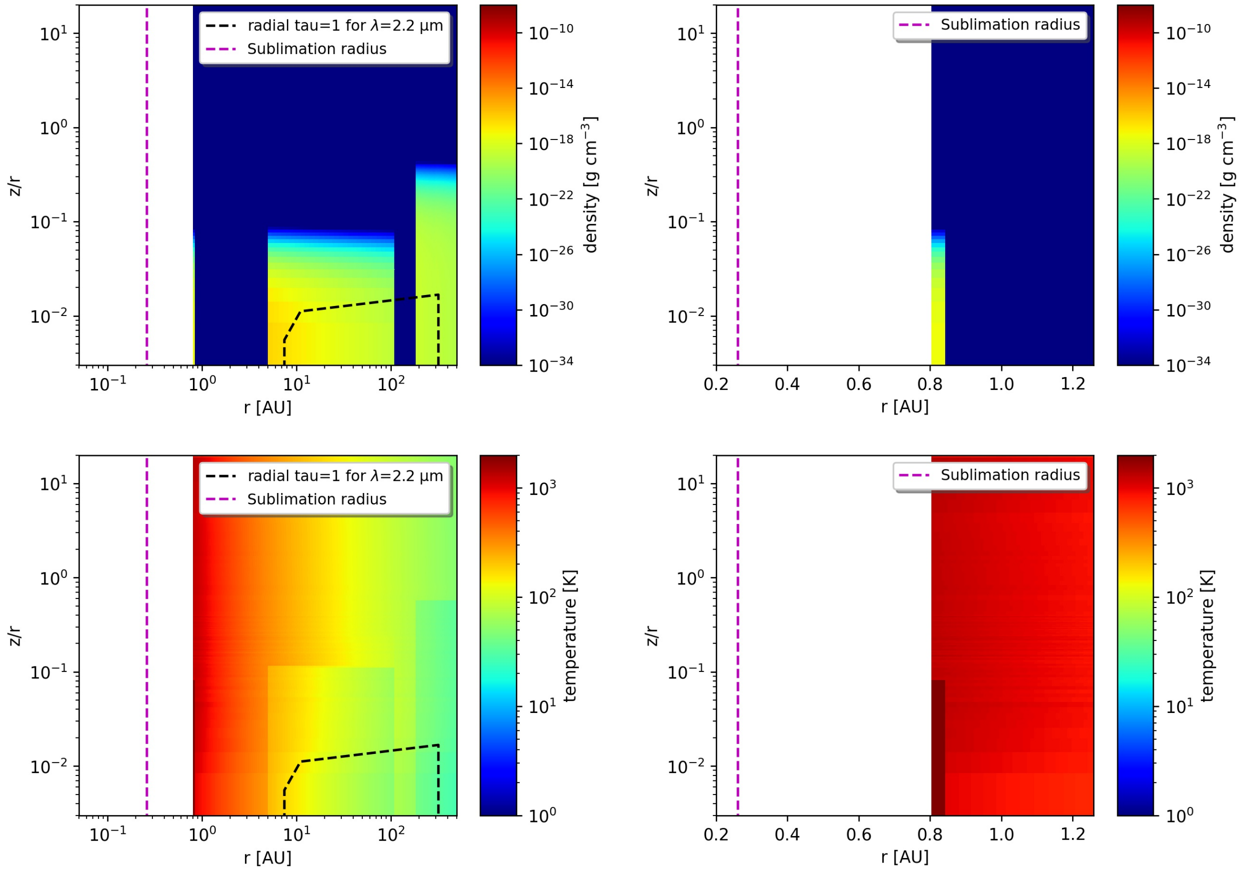

Fig. F.1. Density and temperature structure of the QHP model described in Section 5.2 and Table 2. The x-axis shows the radius in au, the y-axis the height divided by the radius. The colors of the top plots indicate the mass density, the colors of the bottom plot the temperature. QHPs are located at 0.8 au in a very narrow (0.04 au) ring. The optical depth at the observation wavelength is indicated by the radial (dotted line) $\tau = 1$ surface. The magenta dashed line represents the sublimation radius of the system. The dark red color in the temperature plot refers only to the location of the QHPs and not their temperature, since QHPs do not have an equilibrium temperature value.

Appendix G: Photometric data

Table G.1. HD 141569 photometric data.

Band	λ [μm]	Flux [Jy]	Beam size and reference
IUE	0.138	0.30	archival data
IUE	0.178	0.73	archival data
IUE	0.218	0.628	archival data
IUE	0.257	1.023	archival data
IUE	0.29	1.274	archival data
U	0.36	4.19	Sylvester et al. (1996)
B	0.436	8.37	Sylvester et al. (1996)
V	0.55	7.36	Sylvester et al. (1996)
R	0.708	5.92	Sylvester et al. (1996)
I	0.977	4.81	Sylvester et al. (1996)
J	1.22	3.1	2Mass
H	1.65	1.8	2Mass
K	2.16	1.29	2Mass
K	2.16	1.26±0.03	2Mass
K	2.16	1.25	2Mass
K	2.18	1.2	2Mass
K	2.19	1.22±0.02	2Mass
K	2.19	1.23	Penprase (1992)
K	2.24	1.3±0.04	Malfait et al. (1998)
ISO	2.45	1.07	ESA archive
ISO	3.23	0.76	ESA archive
WISE	3.4	0.79 ± 0.025	6.1" NASA archive
UKIRT	3.76	0.54	Sylvester et al. (1996)
ISO	4.26	0.44	ESA archive
WISE	4.6	0.49 ± 0.01	6.4"
ISO	5.89	0.40	ESA archive
ISO	6.76	0.43	ESA archive
ISO	7.76	0.82	ESA archive
ISO	8.70	0.62	ESA archive
AKARI	9.0	0.5178 ± 0.0104	NASA archive
ISO	9.77	0.52	ESA archive
ISO	10.7	0.58	ESA archive
OSCIR	10.8	0.318 ± 0.016	Fisher et al. (2000)
Michelle	11.2	0.338 ± 0.034	Moerchen et al. (2010)
ISO	11.48	0.635	14’×20’ ESA archive
IRAS	12.0	0.55 ± 0.04	1’×5’ NASA archive
WISE	12.0	0.38 ± 0.006	6.5’ NASA archive
MIRLIN	12.5	0.333 ± 0.022	Marsh et al. (2002)
MIRLIN	17.9	0.936 ± 0.094	Marsh et al. (2002)
AKARI	18	0.8655 ± 0.0168	NASA archive
Michelle	18.1	0.883 ± 0.147	Moerchen et al. (2010)
OSCIR	18.2	0.646 ± 0.035	Fisher et al. (2000)
MIRLIN	20.8	1.19 ± 0.16	Marsh et al. (2002)
WISE	22	1.44 ± 0.027	12" NASA archive
MIPS	24.0	1.47 ± 0.01	6" Spitzer archive
IRAS	25	1.87 ± 0.13	1’×5’ NASA archive
IRAS	60	5.54 ± 0.49	2’×5’ NASA archive
PACS-Spec	63.2	2.98 ± 0.01	Thi et al. (2014)
MIPS	70	4.70 ± 0.02	18" Spitzer archive
PACS-Spec	72.8	3.91 ± 0.03	Thi et al. (2014)
PACS-Spec	76.4	3.30 ± 0.03	Thi et al. (2014)
PACS-Spec	90	2.80 ± 0.03	Thi et al. (2014)
IRAS	100	3.48 ± 0.35	4’×5’ NASA archive
PACS-Spec	145	1.1 ± 0.1	Thi et al. (2014)
PACS-Spec	158	1.18 ± 0.02	Thi et al. (2014)
PACS-Spec	180	0.83 ± 0.04	Thi et al. (2014)
SCUBA	450	0.0649 ± 0.0133	Sandell et al. (2011)
SCUBA	850	0.0140 ± 0.0020	Sandell et al. (2011)
LABOCA	870	0.0126 ± 0.0046	Nilsson et al. (2010)
MAMBO	1200	0.0047 ± 0.0005	Meeus et al. (2012)
SCUBA	1350	0.0054 ± 0.0001	Sylvester et al. (2001)

Notes. Data without references are from Merín et al. (2004).

Appendix H: Inclination and position angle of outer disks from the literature

Table H.1. Inclination and position angle of the HD 141569 outer rings.

Reference	Radius [au]	i [deg]	PA$_{NE}$ [deg]
Dust components			
Augereau et al. (1999)	361 ± 10	52.5 ± 4.5	−4.6 ± 1.0
Weinberger et al. (1999)	206	51 ± 3	−4.0 ± 5.0
Biller et al. (2015)	232 ± 3	44.9 ± 0.5	−8.9 ± 1.3
	385 ± 13	47.3 ± 3.3	−11.3 ± 6.1
Perrot et al. (2016)	185 ± 1	56.9 ± 1.0	−3.9 ± 0.4
	88 ± 2	57.6 ± 1.3	−4.0 ± 2.0
	61 ± 1	56.0 ± 2.2	−5.5 ± 1.0
	45 ± 1	57.9 ± 1.3	−6.3 ± 1.1
Currie et al. (2016)	37 ± 2	56.0 ± 4.0	−1.2 ± 2.4
White et al. (2016)	81	55	−8.8
Mawet et al. (2017)	37 ± 4	53.0 ± 6.0	−11.0 ± 8.0
This work	~ 1	58.5 ± 1.6	−1.8 ± 1.1
Gas components			
White et al. (2016)	81 − 199	53.4 ± 1.0	−3.4 ± 0.6
Di Folco et al. (2020)	17 − 277	56 − 58	−4 ± 1
	35 − 232	53 ± 2	0 ± 2
This work	0.01 − 0.09	58.5	−10 ± 7

2.4 Comments

From the previous work, we saw the exceptional power of GRAVITY, capable of detecting a very faint K-band emission in the first au of HD 141569, previously thought to be dust-depleted. Moreover, thanks to the resolution achievable through the differential phases, we were able to study the kinematics of the Brγ-line emitting gas, confirming at first order the scenario of a Keplerian disk inside ~0.1 au, already hinted by the double-peaked emission line.

2.4.1 On the Brγ-line Gas Keplerian Velocity Deviations

It is interesting to note that the derived Brγ-line emitting gas photocenters shifts show some deviations from Keplerian velocity. This is better seen in Fig. 2.3. In the top plot we see the HD 141569 gas photocenters shifts derived from the GRAVITY data, while in the bottom plot, the gas photocenters shifts derived from the images of the Keplerian-rotating axisymmetric disk model are shown. I remember here that the goal of the geometrical model was not to recreate perfectly the observations, but to check if the observational data were consistent with a Keplerian-rotating disk. This is true, as for both plots we note that the photocenters are all aligned with a PA ~ -10°, and that the blue-shifted photocenters are all located in the SE region while the red-shifted photocenters in the NW one. However, two differences are clear. Firstly, the GRAVITY photocenters are located closer to the star with respect to the ones of the ideal case; secondly some GRAVITY photocenters that should reflect low velocity gas (empty markers) are instead located close to the star, closer than photocenters reflecting high velocity gas (red and blue full markers), suggesting super-Keplerian velocities. The deviations seem to be asymmetric, with the blue empty markers being closer to the star than the red empty markers. The first discrepancy may be attributed on the fact that the model does not reflect in perfect details the gas region of HD 141569, as we can see also in the differences between the GRAVITY spectrum and the model spectrum in Fig. 6 of the paper. However, these differences cannot explain the Keplerian-velocity deviations observed in the GRAVITY data.

Perturbations on the gas particles' velocity may be caused by the presence of an embedded planet, that would launch spiral waves both inside and outside its orbit (e.g., Ogilvie et al. 2002). ALMA line observations were used in this context with the goal of spotting possible planets, by detecting perturbations in the velocity pattern of the gas disks surrounding HD 163296 and HD 97048 (see Fig. 2.4, Pinte et al. 2018, 2019). The authors show through hydrodynamical simulations that a two-Jupiter mass planet located at hundreds of au can explain the deviations seen by ALMA for both systems. This scenario is consistent when the planet is embedded in a region of the disk where both the dust and gas components are present.

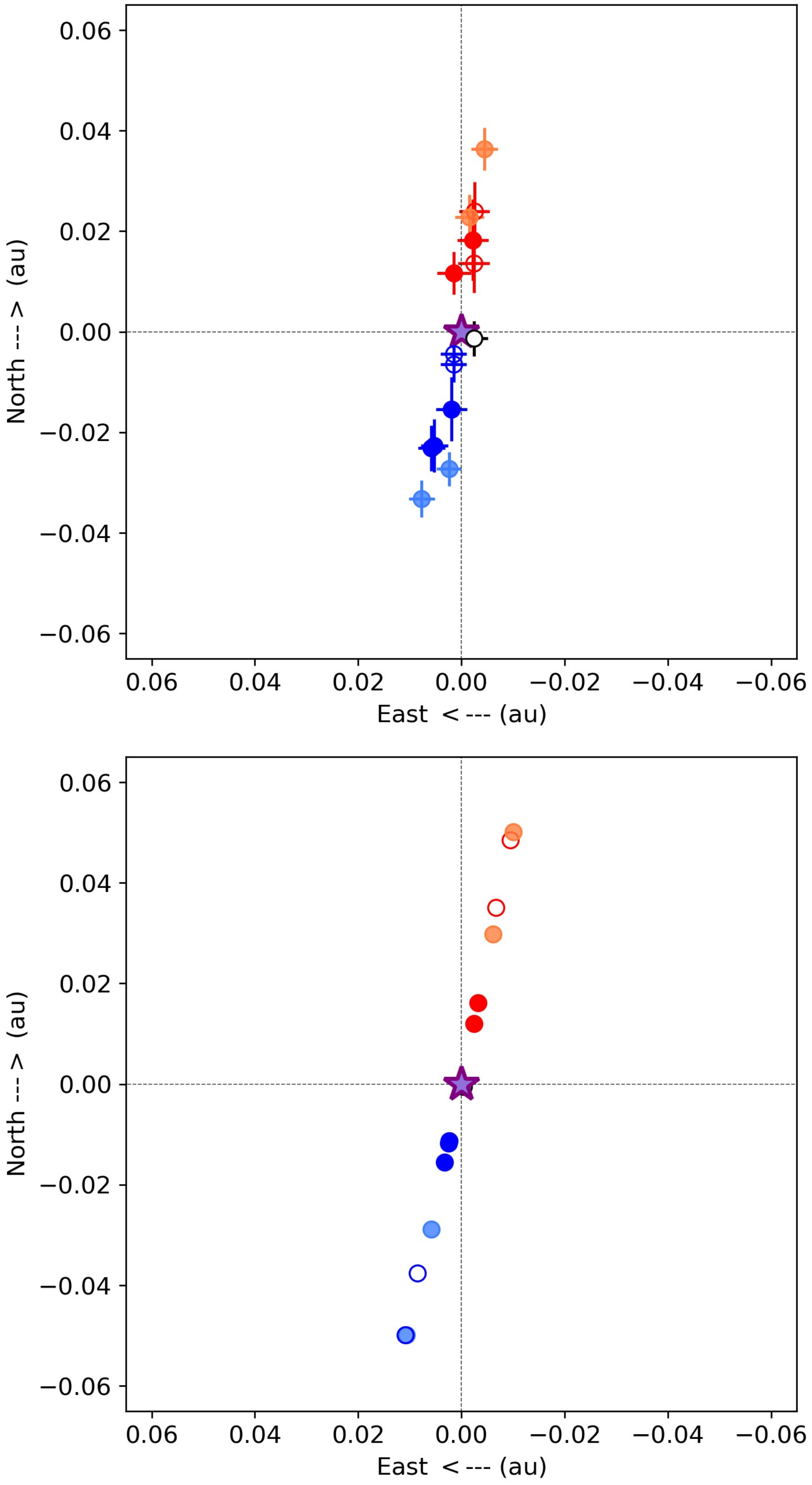

Figure 2.3: Top: gas photocenters shifts derived from HD 141560 GRAVITY data. Bottom: gas photocenters shifts derived from the Keplerian-rotating axisymmetric disk model described in the paper. Colors refer to the different spectral channels.

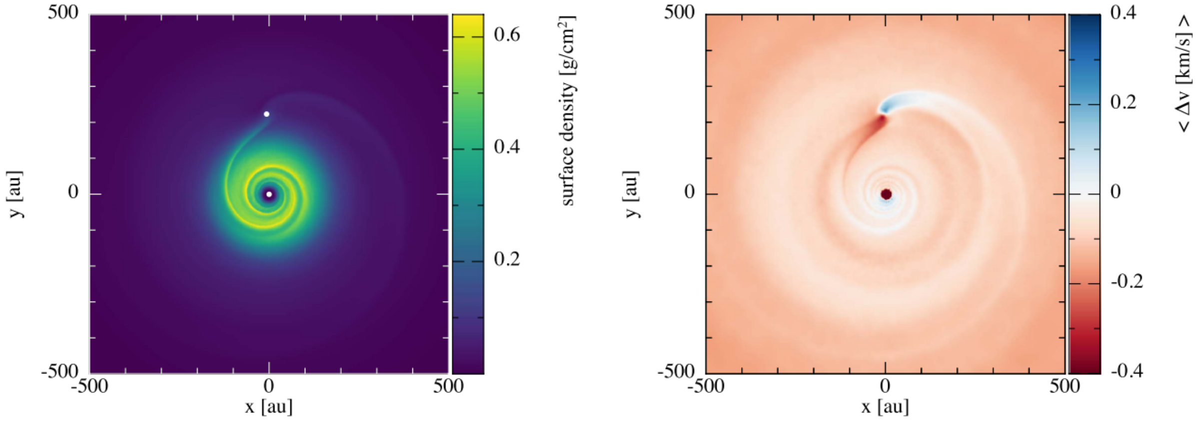

Figure 2.4: Left: 3D hydrodynamics simulation of the HD 163296 disk surface density in the presence of a planet. Right: Keplerian velocity deviations of the azimuthal velocity. Figure from Pinte et al. (2018).

In the case of HD 141569, we allegedly see velocity deviations in gas located at most ~ 0.1 au from the star, in a region well inside the dust sublimation radius and the newly detected dust ring. Ultra-short-period planets, which are known to settle inside the system truncation radius, may be a possible solution (Becker et al. 2021, and referecens therein). However, for planets to move to ultra-short-period orbits, the star needs to have a strong magnetic field (~ 1 kG, Becker et al. 2021), which is not the case for HD 141569, being its magnetic field never detected, probably due to its weakness (e.g., Alecian et al. 2013; Wade et al. 2007). Lastly, we cannot rule out the fact that the Keplerian-velocity deviations could be due to a limit of our spectral resolution (R = 4000), or due to a limitation from the use of the ATs, used to make the GRAVITY observations. The ATs are indeed less sensitive than the UTs, due to their smaller diameter, 1.8 m for the ATs versus 8.2 m for the UTs. This could explain why the deviations are only seen in the spectral channels close to the Brγ-line wavelength rest position, which correspond to the region of the spectrum between the two peaks, and therefore a fainter emission. Higher sensitivity and spectral resolution observations may be useful to confirm or discredit the deviations.

2.4.2 On the Asymmetry of the Brγ-line Emission

The Keplerian disk configuration of the Brγ-line emitting gas tested in the article would favour a scenario for HD 141569 in which the bulk of the emission stems from recombination line emission from ionized hydrogen by stellar radiation. As mentioned in the introduction however, a certain line profile shape is not uniquely reproduced by a specific scenario, but different scenarios can reproduce the same line profile. Additionally, different physical processes can contribute at the same time to the gas emission of a given system. Even though the pure-line photocenters shifts are consistent at first order with a Keplerian gas disk scenario, we saw the presence of Keplerian velocity deviations which may hint at the presence of an ongoing additional physical process. This may also be hinted by the HD 141569 Brγ-line spectrum. As

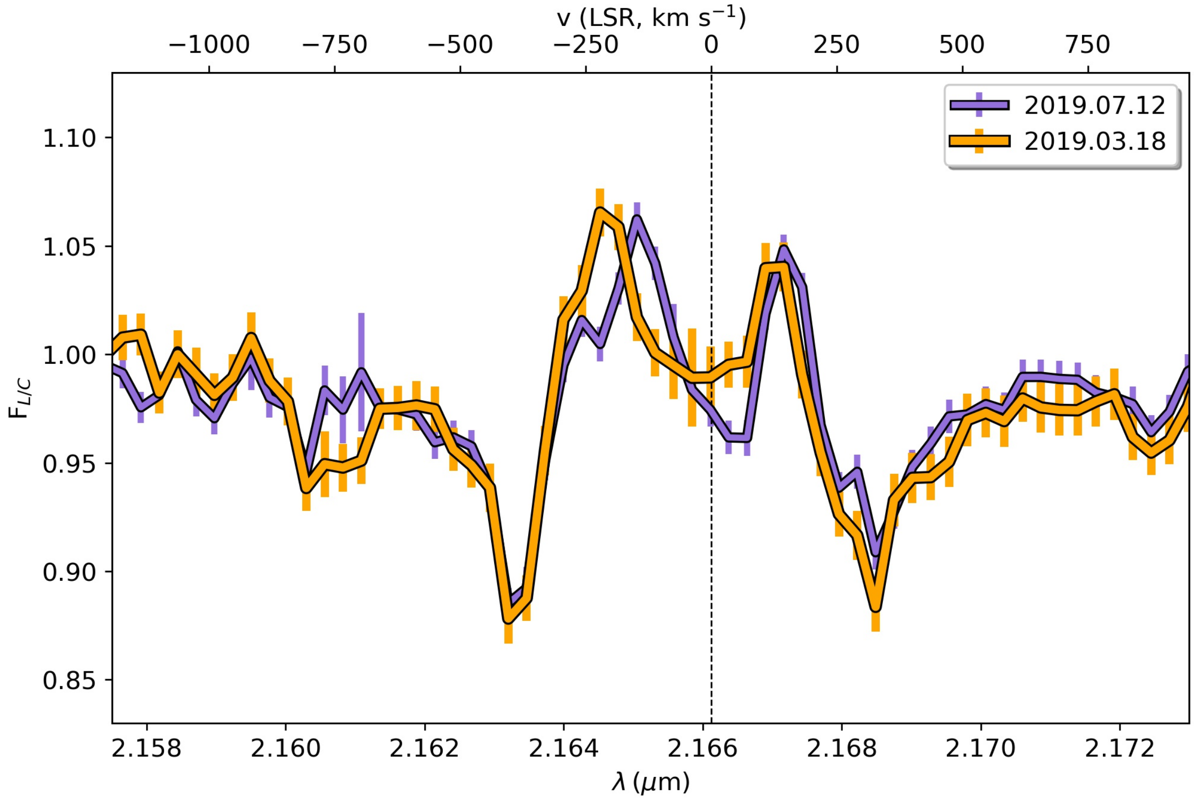

Figure 2.5: HD 141569 continuum-normalized Brγ-line average spectrum from the GRAVITY data sets of 18 March 2019 (orange) and 12 July 2019 (purple). Both spectra are wavelength calibrated with respect to the telluric lines positions, the radial velocity of the system, and the local standard of rest velocity. No telluric lines correction is applied.

discussed in the article, the GRAVITY spectrum shows a mild asymmetry between the blue and red peaks, asymmetry not seen with other instruments at different epochs (see Fig. 9 of the article). In the article I suggested that such asymmetry could be caused by some telluric or instrumental calibration effects. To check if this is true, I plotted in Fig. 2.5 the HD 141569 continuum-normalized Brγ-line average spectrum from the GRAVITY data sets of 18 March 2019 (orange) and 12 July 2019 (purple, same SC data set analysed in the article). The spectra are wavelength calibrated with respect to the telluric lines positions, the radial velocity of the system, and the local standard of rest velocity, but the telluric absorption lines are not corrected, unlike the July 2019 GRAVITY spectrum shown in Fig. 9 of the article. Firstly, I note that the asymmetry is already present in the spectrum even before the telluric lines correction. Secondly, I note that in the March spectrum the asymmetry is less marked; the blue peak is more blue-shifted, resembling the shape seen by the other instruments, and the emission between the two peaks is more intense and more symmetric with respect to the July spectrum. Nonetheless, the red peak is still less intense and more narrow in shape than the blue peak. Therefore, I disfavour the telluric lines correction as the artificial cause of the asymmetry.

The asymmetry could be the result of outliers data propagated through the spectrum averaging

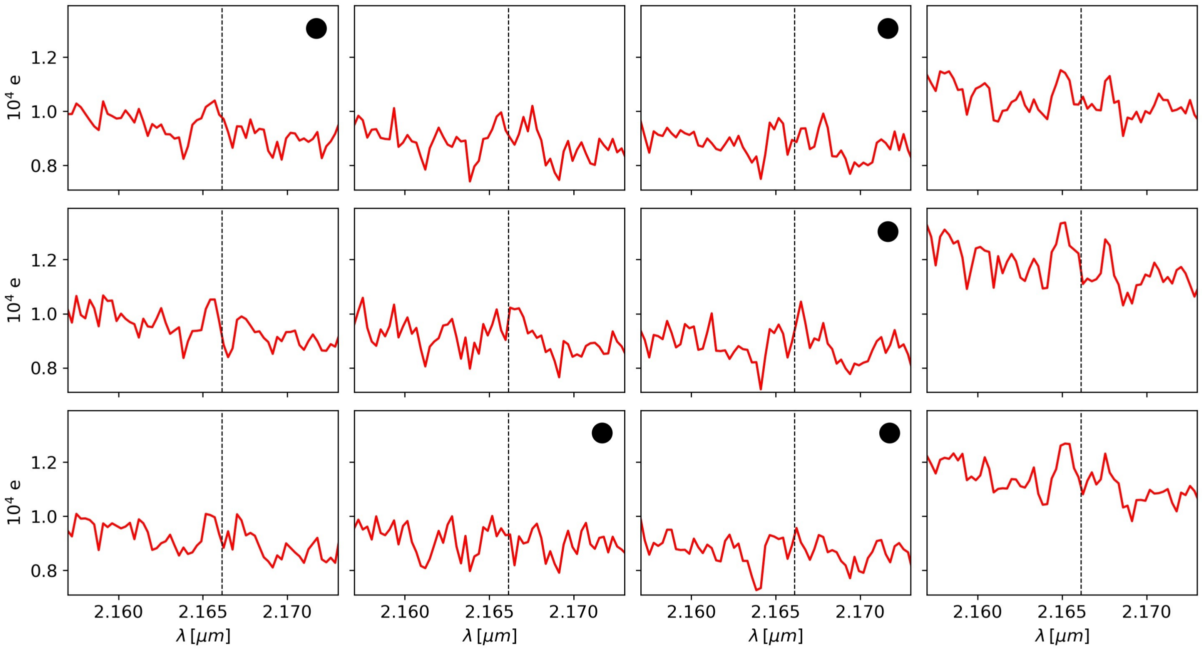

Figure 2.6: HD 141569 raw Brγ-line spectra from the GRAVITY data set of 18 March 2019. The dashed-black line represent the Brγ-line wavelength rest position. The dark circles refer to data classified subjectively as non-reliable if taken independently.

process. To check if this is the case, in Fig. 2.6 and Fig. 2.7, I show the HD 141569 raw GRAVITY spectra for the March 2019 and July 2019 data set, respectively. As one can see, the data are not of the highest quality, as in some files the Brγ-line shape is difficult to relate to a double-peaked one. It is indeed the main goal of the averaging process itself to smooth out outliers data and to improve the signal-to-noise-ratio. For the March data set, I subjectively classify by eye 5 files out of 12 as non-reliable if taken independently (marked by the dark circles). In the remaining files, a symmetric spectrum is only seen in 2 of them. For the July data set, 14 files out of 32 are classified as non-reliable if taken independently. In the remaining files, a symmetric spectrum is only seen in 4 of them. This is of course reflected by the average spectra shown in Fig. 2.5. Since the asymmetric spectra are not the exception, I disfavour the presence of outliers data as the artificial cause of the asymmetry.

Two last explanations are left: limitations due to the use of the ATs, and, as mentioned, additional real physical processes occurring in the circumstellar environment of the system. For the former, observations with the UTs could confirm or deny the asymmetry with more reliability, as for the Keplerian velocity deviations. For the latter only conjectures can be made. Recently, Gravity Collaboration et al. (2023) tested a radiative transfer model of magnetospheric accretion to several T Tauri stars by comparing the observed spectra and gas photocenters shifts to the ones derived through the model. I note that the quantities they derived through models with magnetosphere inclination of $\gtrsim 60^\circ$ resemble the ones HD 141569, i.e. a double-peaked spectrum with a weaker red-peak and aligned Keplerian-looking photocenters shifts. However, the

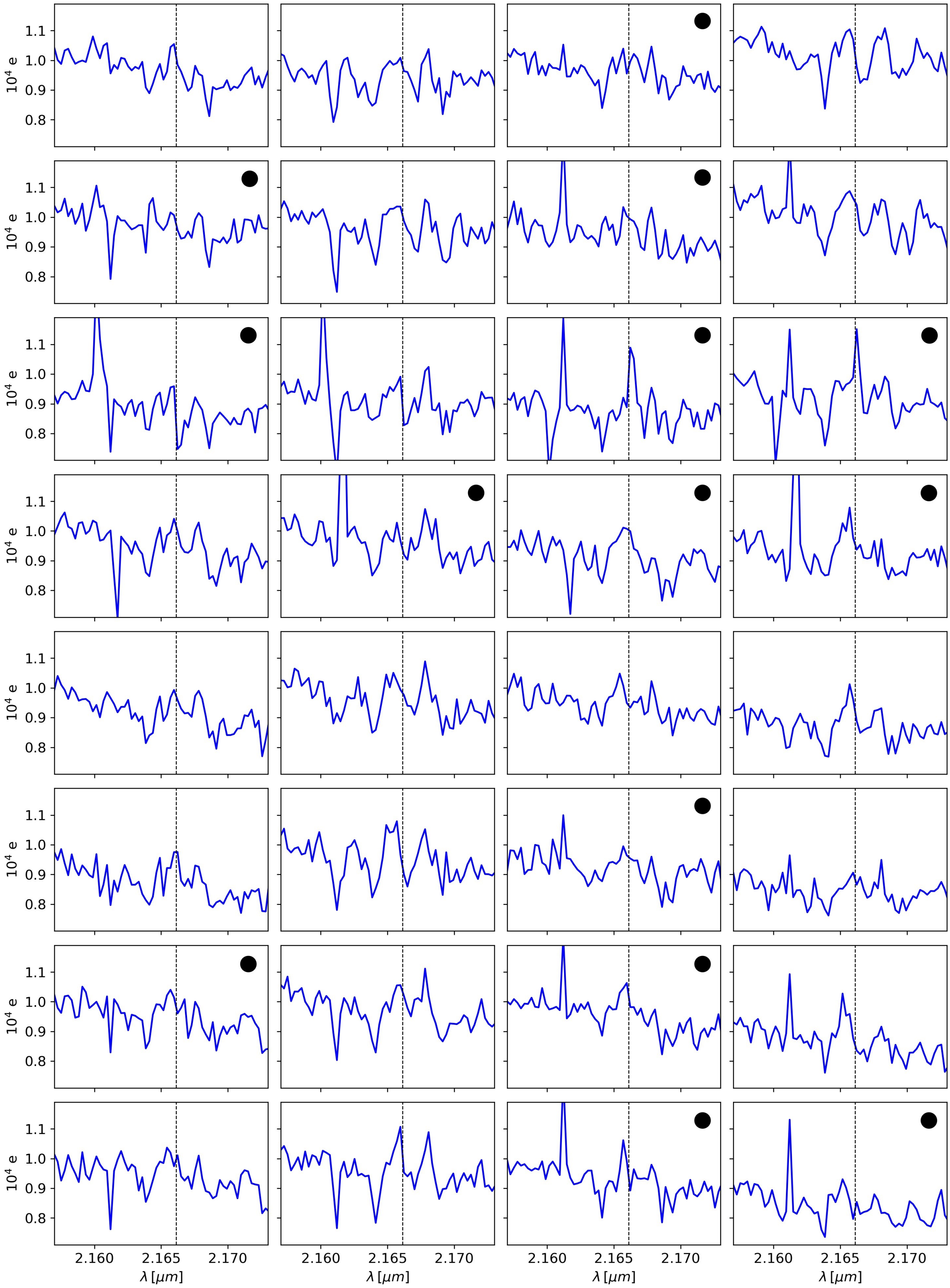

Figure 2.7: HD 141569 raw Brγ-line spectra from the GRAVITY data set of 12 July 2019. The dashed-black line represent the Brγ-line wavelength rest position. The dark circles refer to data classified subjectively as non-reliable if taken independently.

HD 141569 magnetic field has never been detected, probably due to its weakness (e.g., Alecian et al. 2013; Wade et al. 2007), therefore one should expect this scenario to play a minor role, if not null. Tambovtseva et al. (2014) suggested through non-LTE modeling that a weaker red-shifted emission would be produced in the scenario of a disk or X-wind affected by screening and extinction effects due to an opaque gas and/or dust disk. Beside explaining the asymmetry as an emission decrement on the red side of the spectrum due to accretion/extinction, the scenario of an emission increment on the blue side due to the presence of an outflow/jet towards our line-of-sight is likewise a possibility, where the Brγ-line emission would trace the hot gas at the base of the jet (e.g., Tambovtseva et al. 2016). Additional modeling are required to discriminate between the models, but more accurate and higher quality data would be the priority.

2.4.3 On the Transitional Disks Candidates

HD 141569 is not the only transitional disk ever discovered. Thanks to ALMA, rotational transitions of CO have been detected in a few systems, which show debris disk-like properties in their dust component (e.g., Moór et al. 2017, and references therein). As HD 141569, these sources show a seeming featureless SED in the near-IR, shown in Fig. 2.8, suggesting a dust-depleted inner hole. However, GRAVITY thought us that such conclusion is too simplistic and precipitous. Analysis of these transitional systems at mas spatial scales would be therefore of prime interest, since a systematic detection of dust particles in terrestrial planets formation regions of relatively young stars, would put some constraints on the unfamiliar disk evolution and planet formation processes. Unfortunately, near-IR mas scale observations of the known hybrid disk candidates are available only for three of them. Here I shortly summarize what we already know about these candidates, advocating for future observations for a few of them. All the star parameters can be found in Rebollido et al. (2018) and references therein.

– *HD 9672 (49 Ceti).* Herbig A1V 40 Myr old star located at a distance of 59.4 pc. With a total fractional luminosity of 8.5×10^{-4} (Holland et al. 2017), its SED excess can be described by a low temperature (60 K) component and a warm one (165 K, Roberge et al. 2013). Axisymmetric CO emission was detected extending from ~ 20 to 220 au through ALMA observations (Hughes et al. 2017), with an estimated significant gas mass of $1 - 35 \times 10^{-2}\,M_\oplus$ (Higuchi et al. 2020; Moór et al. 2019). The asymmetry was also seen in the SPHERE near-IR scattered light emission, that extends from ~ 65 to 250 au (Choquet et al. 2017), and in the mm dust emission, extending between ~ 60 and 300 au. The dust is estimated to have a mass of $5 - 150 \times 10^{-3}\,M_\oplus$ (Hughes et al. 2017; Moór et al. 2019). The disk mass and geometry suggest the presence of a sculpting planet/s (Pearce et al. 2022). The low H_2/CO ratio and the small scale height of the disk suggest that the gas may be of secondary origin (Higuchi et al. 2020; Hughes et al. 2017). However, the fact that the gas reaches a distance of 20 au from the star while the dust stops at 60 au, favours the primordial gas scenario (e.g., Kóspál et al. 2013). The system was observed with PIONIER through the small and medium baseline configurations in 2014 and 2017 (see Fig. 2.9). The squared visibilities are consistent with unity at all wavelength and baselines, with no signals in the closure phases, reinforcing the scenario of a dust-depleted inner region. Nonetheless, Ca II and Na I non-photospheric absorptions lines were detected, which are interpreted as a tracer of hot gas released by comets or small grains close to the star (Rebollido et al. 2018).

– *HD 21997.* Herbig A3IV/V 42 Myr old star located at a distance of 68.3 pc. With a total fractional luminosity of 5.9×10^{-4}, its SED excess can be described by a single cold component (65 K, Moór et al. 2011). ALMA observations detected mm dust emission extending from ~ 55 to 150 au, dust having a mass of 9×10^{-2} $M_\oplus$ (Moór et al. 2013). CO emission was also detected, extending from ~ 25 to 140 au, with an estimated gas mass of $4 - 85 \times 10^{-2}$ $M_\oplus$ (Higuchi et al. 2020; Kóspál et al. 2013). The dislocation of the gas and dust components, as in 49 Ceti, favours a primordial gas scenario (Kóspál et al. 2013). No near-IR interferometric observations are available.

– *HD 32297.* Herbig A0V <30 Myr old star located at a distance of 136.2 pc. With a total fractional luminosity of 5.4×10^{-3} (Kral et al. 2017), its SED excess can be described by a low temperature (80 K) component and a warm one (240 K, Donaldson et al. 2013). A mm halo emission extending up to 440 au was detected by ALMA (e.g., MacGregor et al. 2018; Olofsson et al. 2022), sharing the same geometry of the smaller particles counterpart seen in SPHERE near-IR scattered light images. The latter emission is distributed in an edge-on (~ 87°) disk extending up to 130 au (Olofsson et al. 2022). The dust mass is estimated to be 0.6 $M_\oplus$ (Moór et al. 2019). The inner rim of the dust disk is estimated to be at ~ 20 au from H-band scattered light images (Duchêne et al. 2020). CO gas emission is detected, with a total mass estimate of 7×10^{-2} $M_\oplus$, and co-located with the dust (Moór et al. 2019). Supposedly second generation hot gas (Ca II and Na I) is detected as in 49 Ceti (Rebollido et al. 2018). The system was observed with PIONIER through the small baseline configuration in 2018 (see Fig. 2.9). The data are quite noisy but it is clear that the squared visibilities reach values down to ~ 0.6, hinting at the presence of hot dust in the first few au of the system. The small baseline configuration is sensitive to the total light fraction distributed in a large-scale halo and/or to the presence of a substellar companion (Setterholm et al. 2018). The closure phases signals, consistent with zero at all baselines and wavelength within the error bars, hint to a symmetric emission at the spatial resolution of PIONIER, suggesting a hot-counterpart of the halo seen by ALMA. Moreover, no direct evidence of a substellar companion was found in the H-band scattered light images by Duchêne et al. (2020). Interferometric observations with medium and large baseline configurations are highly recommended.

– *HD 110058.* Herbig A0V 15 Myr old star located at a distance of 188.7 pc. With a IR fractional luminosity of 2×10^{-3}, its SED excess can be described by a warm temperature component

(105 K, Hales et al. 2017). ALMA observations detected mm dust emission in an almost edge-on disk (~ 82°) extending from ~ 25 to 70 au, as well as CO emission extending from ~ 7 to 20 au, with an estimated dust mass of 8×10^{-2} $M_\oplus$ and a gas mass of 7×10^{-2} $M_\oplus$ (Hales et al. 2022). Also in this object, the gas and dust components are not co-located. The edge-on geometry was also seen through SPHERE near-IR imaging, extending from ~ 20 to 65 au (Kasper et al. 2015). The latter images show a pair of symmetrically placed knots at ~ 35 au and a pair of symmetric, hooklike features in both disk's wings, which the authors interpret with the presence of an inner and an outer planetesimal belt. Atomic lines (Ca II and Na I) were detected (Hales et al. 2017; Rebollido et al. 2018). No near-IR interferometric observations are available.

– *HD 121191.* Herbig A5IV/V 16 Myr old star located at a distance of 135.9 pc. With a total fractional luminosity of 2.7×10^{-3} (Kral et al. 2017), its SED excess can be described by a warm temperature (120 K) component and a hot one (555 K, Vican et al. 2016). Good fit results were also obtained by Melis et al. (2013) with colder dust components (95 and 450 K), highlighting the degeneracy of SED fit solutions mentioned before. ALMA observations detected mm dust emission from ~ 20 up to 80 au with a dust mass of 9.5×10^{-3} $M_\oplus$ (Moór et al. 2017). CO emission was also detected, extending from ~ 15 to 30 au, with a gas mass estimate of 3×10^{-3} $M_\oplus$ (Kral et al. 2020; Moór et al. 2017). No near-IR interferometric observations are available. However, the hot dust presence suggested by the clear mid-IR excess, makes this object a prime candidate for such observations in the context of hybrid disk systems.

– *HD 121617.* Herbig A1V 16 Myr old star located at a distance of 128.2 pc. With a total fractional luminosity of 4.8×10^{-3} (Moór et al. 2017), its SED excess can be described by a single warm component (105 K, Moór et al. 2011). ALMA observations detected mm dust emission extending from ~ 50 to 105 au (Pearce et al. 2022) with a dust mass estimate of 0.14 $M_\oplus$ (Moór et al. 2017). CO emission was also detected, co-located with the dust, with an estimated gas mass of 2×10^{-2} $M_\oplus$ (Moór et al. 2017). As for 49 Ceti, the disk mass and geometry suggest the presence of a sculpting planet/s (Pearce et al. 2022). No near-IR interferometric observations are available; based on the SED, this object should raise interest for such observations.

– *HD 131488.* Herbig A1V 16 Myr old star located at a distance of 150.0 pc. With a total fractional luminosity of 5.5×10^{-3} (Moór et al. 2017), its SED excess can be described by a low temperature (95 K) component and a hot one (570 K, Vican et al. 2016). Good fit results were also obtained by Melis et al. (2013) with two components having temperature of 100 and 750 K. ALMA observations detected mm dust emission up to ~ 170 au in a almost edge one disk (~ 82°) characterized by a central depression and a dust mass of 0.32 $M_\oplus$ (Moór et al. 2017). CO emission was also detected, co-located with the dust, with an estimated gas mass of 9×10^{-2} $M_\oplus$ (Moór et al. 2017). Ca II and Na I were also detected (Rebollido et al. 2018). No near-IR interferometric observations are available. As HD 121191, based on the SED, this object is a prime candidate for mas observations of its innermost regions.

– *HD 131835.* Herbig A2IV 16 Myr old star located at a distance of 145.6 pc. With a total fractional luminosity of 3×10^{-3} (Moór et al. 2017), its SED excess can be described by a cold (70 K) component and a warm one (175 K, Moór et al. 2015). ALMA observations detected mm dust emission extending in a highly inclined axisymmetric disk (~ 80°) from ~ 50 up to 140 au, with a total mass of 0.7 $M_\oplus$ (Kral et al. 2019). Mid-IR observations have shown the presence of a small particles dust halo up to ~ 350 au (Hung et al. 2015). SPHERE revealed three concentric rings in scattered light at ~ 40, 65, and 100 au (Feldt et al. 2017). The disk mass and geometry suggest the presence of a sculpting planet/s (Pearce et al. 2022). CO emission was also detected, co-located with the dust, with an estimated gas mass of $5 - 600 \times 10^{-4}\,M_\oplus$ (Hales et al. 2019; Kral et al. 2019; Moór et al. 2015; Moór et al. 2017). Thermochemical modeling favours a secondary nature gas scenario (Hales et al. 2019), as the detection of Ca II and Na I non-photospheric absorption lines (Rebollido et al. 2018). The dust collisional model of Kral et al. (2016) suggests instead a primordial nature (Kral et al. 2017). No near-IR interferometric observations are available.

– *HD 138813.* Herbig A0V 10 Myr old star located at a distance of 134.4 pc. With a total fractional luminosity of 9×10^{-4}, its SED excess can be described by a cold (95 K) component and a warm one (195 K, Chen et al. 2014). ALMA observations detected mm dust emission in a ring extending from ~ 70 up to 130 au, with a total mass of $8 - 1100 \times 10^{-3}\,M_\oplus$ (Lieman-Sifry et al. 2016; Mathews et al. 2012). The disk mass and geometry suggest the presence of a sculpting planet/s (Pearce et al. 2022). CO emission was also detected, co-located with the dust, with an estimated gas mass of $10^{-3}\,M_\oplus$ (Hales et al. 2019). The dust collisional model of Kral et al. (2016) suggests a primordial nature for the CO (Kral et al. 2017). No near-IR interferometric observations are available.

– *HD 156623.* Herbig A0V 16 Myr old star located at a distance of 118.3 pc. With a total fractional luminosity of 5×10^{-3}, its SED excess can be described by a warm (125 K) component and a hot one (625 K, Moór et al. 2017). ALMA observations detected mm dust emission in a disk extending up to ~ 150 au, with no resolved inner hole (Lieman-Sifry et al. 2016), and with a total mass of $3 \times 10^{-2}\,M_\oplus$ (Moór et al. 2017). The same geometry is seen through H-band scattered light images (Esposito et al. 2020). CO emission was also detected, co-located with the dust, with an estimated gas mass of $10^{-3}\,M_\oplus$ (Hales et al. 2019). The latter authours suggest secondary a nature for the gas. No near-IR interferometric observations are available; based on the SED, this object should raise interest for such observations.

– *HD 172555.* Herbig A7V 23 Myr old star located at a distance of 28.6 pc. With a total fractional luminosity of 5×10^{-4}, its SED excess can be described by a warm component (190 K, Absil et al. 2021). No ALMA observations are available. CO emission was not detected above the 5σ level by the APEX telescope (Güsten et al. 2006), translating in a gas mass of $< 4 \times 10^{-5}\,M_\oplus$ (Moór et al. 2011). The system was observed with PIONIER through the small baseline configuration in few occasions. In Fig. 2.9, data of the earliest and latest observations are shown. The PIONIER data were studied by Ertel et al. (2014, 2016). The authors considered the object as marginally resolved (we can see the squared visibilities reaching ~ 0.9 for the 2017 epoch) suggesting the presence of a hot halo as in HD 32997. Mid-IR interferometric MIDI observations have detected dust as close as ~1 au, up to 8 au (Smith et al. 2012). SPHERE polarized light images confirm the outer radius but cannot resolve the inner one (Engler et al. 2018). The total dust mass was estimated from the 160 μm flux to be $5\times10^{-4}\,\mathrm{M}_{\oplus}$. Transient absorption Ca II and H doublet lines are detected, suggesting exocomets (Kiefer et al. 2014; Rebollido et al. 2018). This object is a prime example of the capability and the need of interferometric observations to assess more confidently the presence of dust in the innermost regions of protoplanetary disks, advocating for such observations for all the systems previously described.

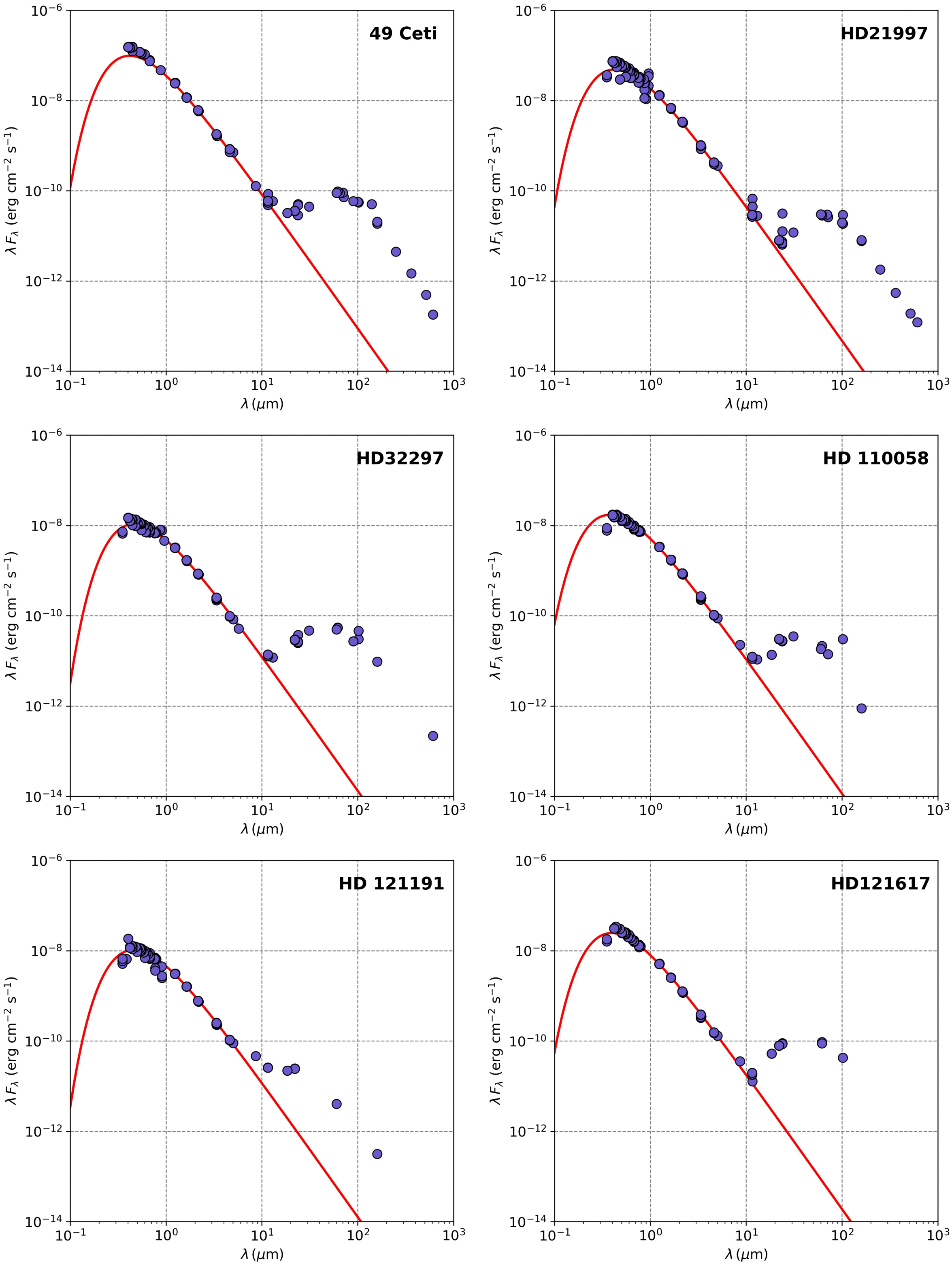

Figure 2.8: SEDs of YSOs hybrid disk candidates. Blue marks represent the photometric data listed in the VizieR Photometry tool (`http://vizier.cds.unistra.fr/vizier/sed/`), detected around 1 arcsec from the star. The red lines represent a black-body function with star parameters values from Rebollido et al. (2018).

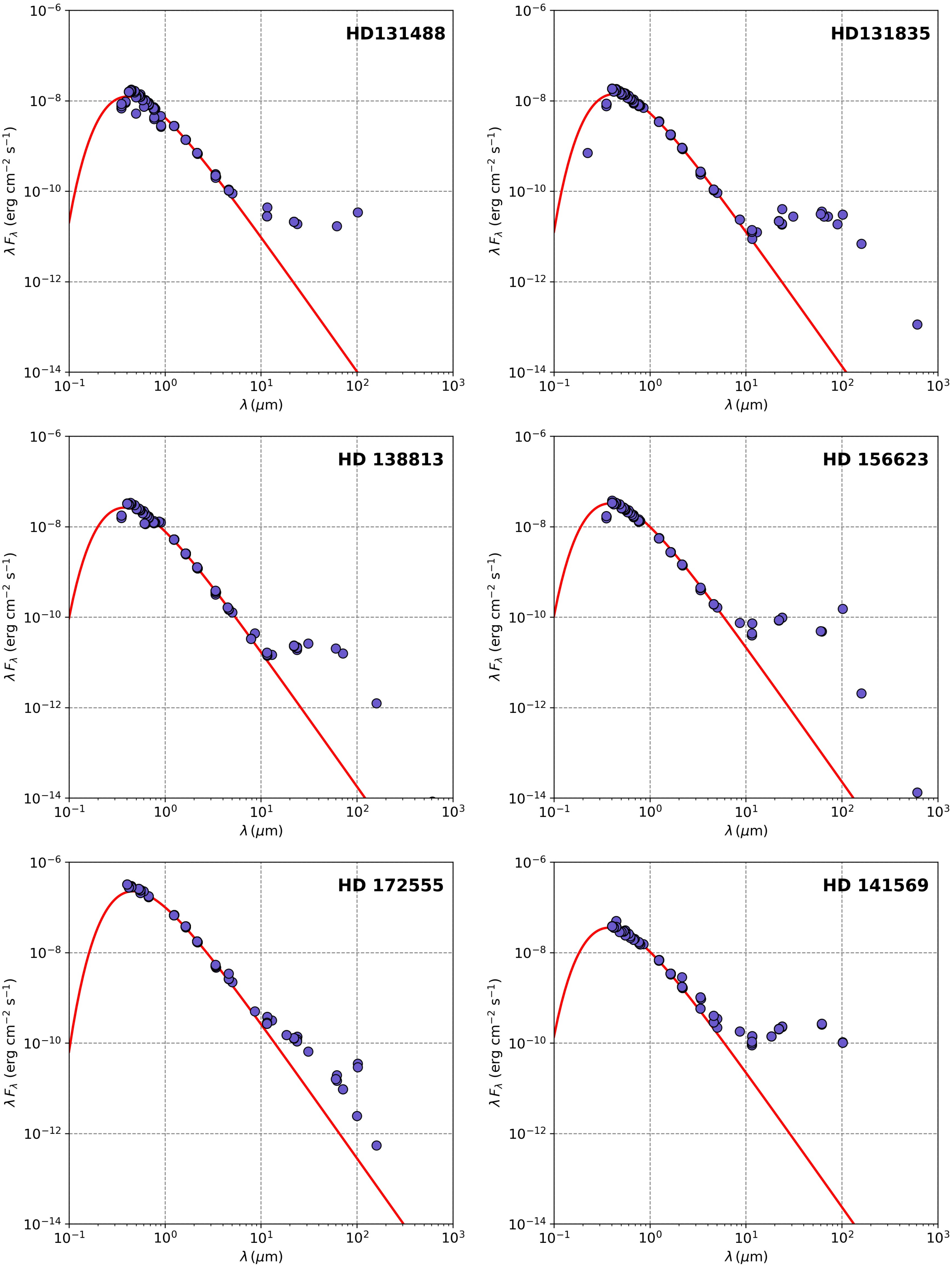

Figure 2.8: Continued.

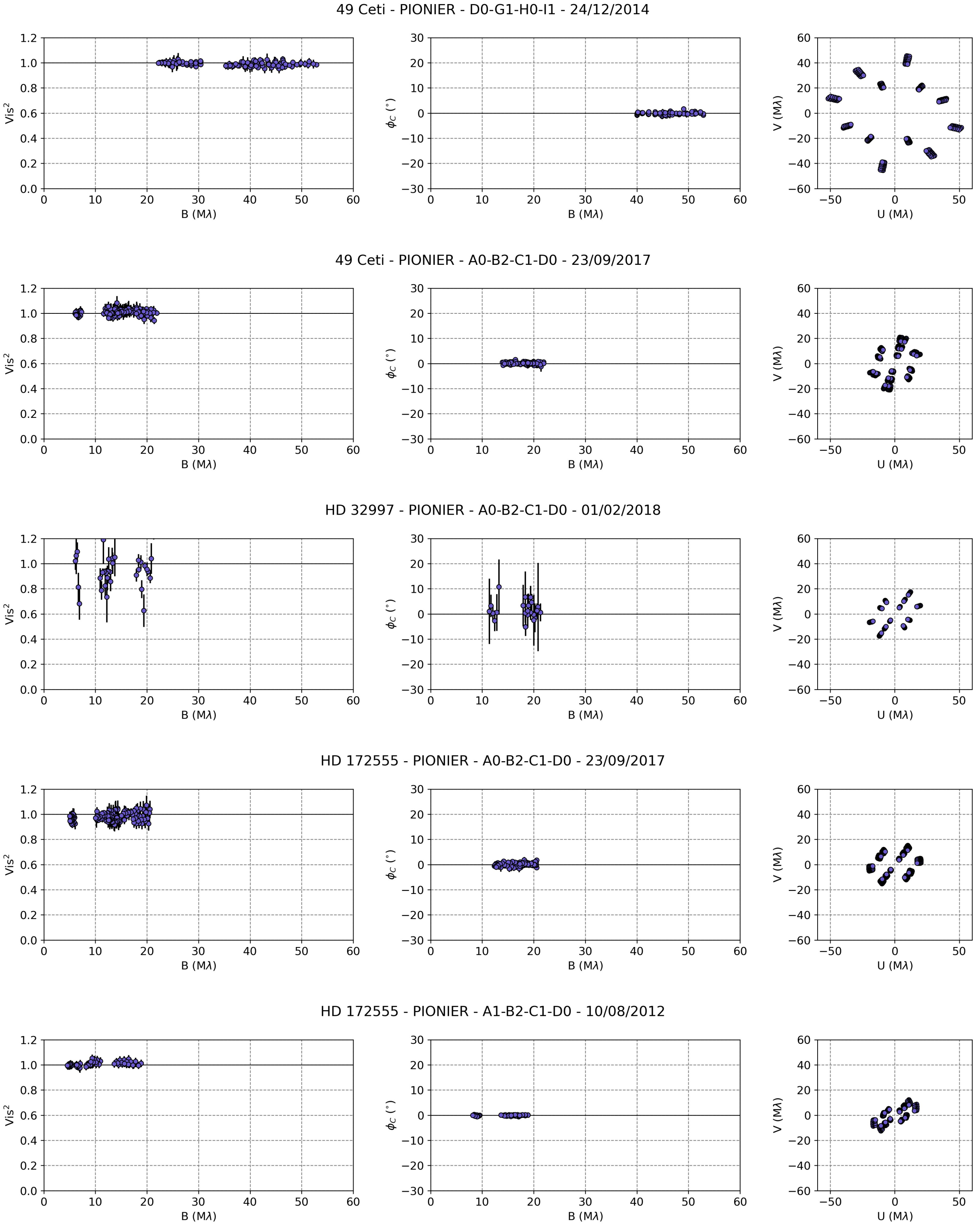

49 Ceti - PIONIER - D0-G1-H0-I1 - 24/12/2014

49 Ceti - PIONIER - A0-B2-C1-D0 - 23/09/2017

HD 32997 - PIONIER - A0-B2-C1-D0 - 01/02/2018

HD 172555 - PIONIER - A0-B2-C1-D0 - 23/09/2017

HD 172555 - PIONIER - A1-B2-C1-D0 - 10/08/2012

Figure 2.9: PIONIER calibrated data of 49 Ceti, HD 32997, and HD 172555. Left panels: squared visibilities; central panels: closure phases; right panels: (u, v)-plane coverage. Archival data from the JMMC Optical interferometry DataBase (`http://oidb.jmmc.fr/index.html`).

Chapter 3

HD 98922's Time-Variable Inner Region

In this chapter I present a study on HD 98922. The work here presented is an unrefined draft of an open-access article that was accepted for publication by the A&A journal.

3.1 Science Case Overview

Since the start of PIONIER and GRAVITY operations, a substantial number of YSOs has been observed in their near-IR emission of their innermost regions. The high-quality data, compared to the ones retrieved with past instruments like the Keck interferometer, and the homogeneous sample covering from T Tauri to the most massive Herbig stars, allowed to carry out meaningful statistical studies. Important results were found for both the H- and K-band emissions. The radius-luminosity relation ($L \propto R^{1/2}$), firstly found by Monnier et al. (2005), was confirmed and extended to higher luminosity stars ($\sim 10^4\,L_\odot$), but with a significant scatter for the luminosity range between $10^2 - 10^4\,L_\odot$ (Gravity Collaboration et al. 2019; Lazareff et al. 2017). A hint of departure from the relationship was seen for low luminosity stars ($0.4 - 10\,L_\odot$), for which the K-band circumstellar environment size is larger than expected (GRAVITY Collaboration et al. 2021c). Smooth, wide, and asymmetric rings models best fitted the interferometric data for both bands (GRAVITY Collaboration et al. 2021c; Gravity Collaboration et al. 2019; Lazareff et al. 2017). While inclination effects were able to explain closure phase signals up to 25°, they cannot explain stronger ones, and other scenario must be invoked to explain the origin of the asymmetries (Gravity Collaboration et al. 2019). Through image reconstruction, Kluska et al. (2020) found that most of the objects of their sample show a centrally peaked continuous H-band emission, while the most resolved objects images show complex asymmetric brightness distributions, hardly reproduced by geometrical parametric models.

For this reason, even though statistical studies are of high relevance, some objects require a more in-depth study. Moreover, as suggested by Kluska et al. (2020), interferometric observations of regions inside a few au could be sensitive to the temporal evolution of the system observed, that may have time-scales down to a few weeks, if the observations are taken in a time interval comparable to the latter. A strong assumption made in the previously mentioned works is the temporal non-variability of the objects. Interferometric data taken months or years apart are combined in order to improve the signal-to-noise ratio and the (u, v)-plane coverage, risking the disruption of the image reconstruction process and spurious geometrical model fitting results. Additionally, the ring half-flux radius of the Lazareff et al. (2017) model, which is used to refer to the circumstellar environment size and on which are based the statistical geometrical model fitting studies above mentioned, can be misleading about the real size and geometrical shape of a system. To better illustrate this, I refer to Fig. 3.1. In the four plots, 4 different models are depicted; they have the same half-flux radius (a) and inclination (i), and differ only on the $\mathrm{k_r}$ parameter, the ratio between the ellipsoidal kernel radius and the wireframe radius (the latter is depicted by the red lines). The wireframe is convolved with the kernel to produce a spatially thick ring, or, if the kernel radius is much larger than the wireframe one, an ellipsoidal environment. As we note, models with equal half-flux radius can be compact, extended, gapped, or centrally peaked. On the base of these two remarks, a more careful approach is needed.

HD 98922 is a well studied Herbig star with a spectral type between B9Ve and A2III (Caratti o Garatti et al. 2015; Hales et al. 2014) and classified as Meuus Group II (Garufi et al. 2022). Its innermost regions show H- and K-band emission with half-flux radii of 1.2 au and 1.5 au, respectively (Gravity Collaboration et al. 2019; Lazareff et al. 2017). The H-band estimate was derived by combining data taken between December 2012 and February 2013, which well cover the $(u, v)-$plane. The K-band estimate was derived by combining data taken between February and March 2017. The latter data were taken only through the astrometric configuration. The lack of small baseline configuration data can be problematic since they are needed to constrain the star-halo-ring flux contribution ratio (Setterholm et al. 2018), and therefore the size of the circumstellar environment. The image reconstruction done by Kluska et al. (2020), using the same data set of Lazareff et al. (2017), shows an asymmetric centrally depressed environment brightness distribution, that extends inside the dust sublimation radius of the system. Since the publication of these works, the object has been observed multiple times and with different (u, v)-plane coverage. A total of 20 PIONIER observations between 2011 and 2016, and 13 GRAVITY observations between 2017 and 2022 were taken, spaced in time by days, weeks, months, and years, giving us a unique opportunity to monitor possible time-variability over a rather extended period. Additionally, the high-quality spectroscopic capabilities of GRAVITY allows us to study in detail the Brγ-line emitting gas phase and its spatial morphology, for a first time ever interferometric time-variability study of the Brγ-line in a YSO.

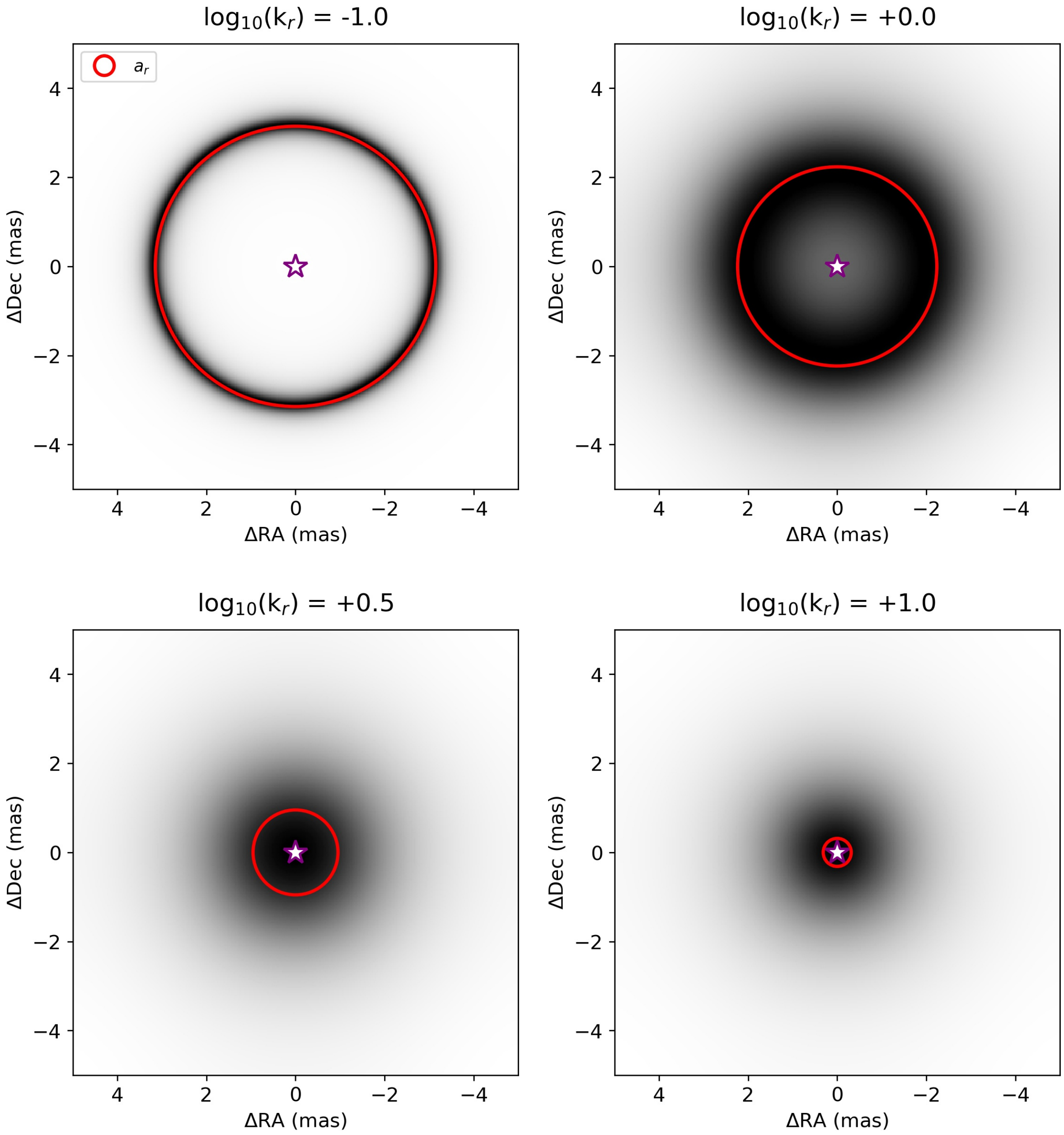

Figure 3.1: Symmetric ring model of Lazareff et al. (2017) for $\log_{10}(a) = 0.5$, $i = 0°$, and different values of $\log_{10}(\mathrm{k_r})$. The red circle represent the ring wireframe radius. The star marker is for illustration purpose.

3.2 Goals of the Study

The goal of this work is to depict the morphology of the innermost circumstellar environment of HD 98922, already known to be asymmetric and to be the main contributor of the H- and K-band system's emission. The Brγ-line emission is also analysed, and evaluated for a possible connection with the dust emission. Particular attention is invested on the potential time-variability of both dust and gas components, suggested by PIONIER and GRAVITY data taken in different epochs with similar (u, v)-plane coverage.

3.3 Approach, Steps, and Manuscript

The study is based mainly on GRAVITY and PIONIER data. The GRAVITY data were taken within the framework of the GTO YSO program, while the PIONIER ones are archival data. They came in my possession already reduced and calibrated, processes done with the GRAVITY data reduction software (Lapeyrere et al. 2014) for the GRAVITY data, and the `pndrs` package, described in Le Bouquin et al. (2011), for the PIONIER ones. As first author of a large cooperation article, here I list the actions done from my side:

(i) In depth literature study on HD 98922 and YSOs variability, which allowed me to write the Introduction Section of the manuscript.

(ii) Took part as observer in the GTO YSO program observation run in January 2020 under program ID: 0104.C-0567(A), which led to the acquisition of the 27/01/2020 epoch GRAVITY data set of HD 98922, used in this work.

(iii) Preliminary data analysis and calibration: 1) cleaning of the FT and SC data of outliers; 2) application of a wavelength calibration on the SC data, based on the atmospheric telluric lines position, radial velocity of the star, and the local standard of rest velocity; 3) calculation of the star Brγ-line photospheric absorption feature; 4) visual and quantitative examination of the SC and FT data to inspect for hints of interferometric variability. Observations taken at different epochs with similar (u, v)-plane coverage show negligible variation in the squared visibilities, suggesting no symmetrical variations (star-disk-halo flux contribution ratio variations) in the system. Significant variations in the closure phases instead suggest asymmetric time-dependent variations in both H- and K-band continuum components. From the work based on this step, the Data Set Description Section of the manuscript was written.

(iv) Fit of the FT data for each epoch with `emcee` (Foreman-Mackey et al. 2013), through parametric geometrical models described in Lazareff et al. (2017), in order to get information on the flux contribution of the circumstellar environment, its brightness distribution, and its time-variability. The results from this step led to the idea that independent fits of each epoch may lead to spurious variability of the fitted parameters that may not reflect a physical temporal variability of the system.

(v) Based on the results of step (iv), I tested my geometrical continuum model for variability, by fitting an image of a synthetic non-variable system, observed with different baseline configurations. The image was provided by Dr. Labadie. The test confirmed the spurious variability idea of step (iv).

(vi) Therefore, a Python code was written to fit all the FT epochs simultaneously but independently: all the parameters of the model are set to be constant in time, except for one (more details in the Methodology Section of the manuscript). Different models were tested: time-variable flux ratio, time-variable disk inclination, time-variable disk size, and time-variable disk azimuthal modulation. The latter fitted the best the data, suggesting a time-variable crescent feature for the H- and K-band continuum, that extends inside the dust sublimation radius of the system. This global fit approach allows to avoid the spurious variability mentioned above, to bypass the poor (u, v)-plane coverage of the single epochs, and to avoid for the known star-disk flux contribution degeneracy and the degeneracy between the halo contribution and the radial shape of the disk (f_{Lor} parameter).

(vii) Inspection for degenerate fitting solutions by looking for possible local minima in the parameters' χ^2 maps.

(viii) Regarding the SC data, the squared visibilities were fitted with parametric geometrical models in order to get an estimate of the emitting gas region size. The pure-line differential phases, as well as the pure-line photocenters shifts, were calculated from the total observed differential phases. I present more details of steps (v), (vi), (vii), and (viii) in the Methodology Section of the manuscript. The Brγ-line data analysis suggests a time-variable gas region in its location with respect to the star. The region seems to follow at first order the period of the crescent dusty feature.

(ix) HD 98922 SED modeling using the RT code MCMAx (Min et al. 2009), to get information on the dust properties. Specifically, I wanted to test the scenario of gravitational instability as origin of the crescent feature suggested by the modeling of the continuum GRAVITY and PIONIER data, by estimating the surface density distribution of HD 98922 circumstellar environment. Different models were tested to account for the emission detected by PIONIER and GRAVITY: pure silicate grains, carbonaceous silicate grains, and quantum heated particles. All the above models fit well the photometric data, and all of them are characterised by a low surface density, disfavoring the gravitational instability scenario. A comment on the SED fit and the models used is done in Section 3.4.

(x) A Python code was written to fit the time-variable azimuthal modulation position angle of the dusty disk, derived in step (vi), with a cosine function, to estimate at first order its orbital period around the star. The fit suggests a period of ~ 1 yr.

(xi) A Python code was written to calculate the equivalent width of the Brγ-line, its luminosity, and the accretion luminosity of the system, to examine possible line time variability and evaluate different origin mechanisms. The normalized peak flux varies between 1.17 and 1.25, and the equivalent width of the line increases by 30 % in ~ 4 yrs.

(xii) In combination of a literature study on topics relevant to the results obtained, the work done in the steps above allowed me to write the Results and the Discussion Section of the manuscript, as well as the Abstract and the Summary.

(xiii) All the images and Tables were produced by myself with Python and the `matplotlib` package (Hunter 2007), except for the images in Fig. 2 of the manuscript, which were produced by Dr. Labadie.

The approach, tools, equations, models, and additional data used to carry out the work are properly referenced in the manuscript.

Astronomy & Astrophysics manuscript no. output
March 20, 2023

©ESO 2023

The GRAVITY young stellar object survey

X. Mapping the time-variable inner region of HD 98922's protoplanetary disk

GRAVITY Collaboration*: V. Ganci[1, 2], L. Labadie[1], K. Perraut[3], A. Wojtczak[1], J. Kaufhold[1], M. Benisty[3, 4], A. Caratti o Garatti[5, 6, 7, 8], and C. Dougados[3]

(Affiliations can be found after the references)

Received xx, xxxx; accepted xx, xxxx

ABSTRACT

Context. While temporal variability of proto-planetary disks in their photometric properties is common in young stellar object, changes in their morphology was only hinted for a handful of sources, probably due to the lack of high cadence observations. The disk's evolution is directly linked to the formation and evolution of planetary systems, and therefore more insight on the processes taking place in proto-planetary disks are key to have a complete understanding of such systems.

Aims. The goal of this work was to depict the morphology of the innermost circumstellar environment of HD 98922 and to test its potential brightness distribution time-variability.

Methods. Monthly multi-epochs observations of HD 98922 on milliarcsecond scales taken with GRAVITY/VLTI in the near-infrared (IR) at low (R ~ 20) and high (R ~ 4000) spectral resolution were coupled with PIONIER/VLTI archive data (R ~ 40), for a total observational period of 11 years. The interferometric visibilities and spectral energy distribution were interpreted with geometrical models and through radiative transfer techniques using the code MCMax. High spectral resolution quantities (visibilities and differential phases) were investigated to obtain information on the properties of the Brackett-γ (Brγ) line emitting region.

Results. HD 98922 is resolved by both instruments and in all epochs. Comparing observations taken with similar *(u,v)* plane coverage, the squared visibilities do not vary significantly, suggesting no symmetrical variations in the system. The significant closure phases variations instead suggest asymmetric time-dependent variations in both H- and K-band continuum components. Data modeling suggest a crescent-like asymmetric dust feature located at ~ 1 au that accounts for ≈ 70 % of the total near-IR emission. The closure phases variability can be explained mainly by the change in location of the feature with respect to the star through the epochs, resembling a revolution movement. The MCMax modeling suggests that this emission could originate from a small amount of carbon-rich (25%) silicates. The model goes in contrast with a disk fragmentation scenario due to its low disk surface density. The high spectral resolution differential phases in the Brγ line suggest that the location of the gas peak emission varies through the epochs, following at first order the revolution motion of the feature. While a magnetospheric accretion scenario is ruled out as the main origin mechanism, a disk wind or a massive (~ 10 M_J) accreting embedded companion could explain the Brγ line luminosity, its variability, and the changing position of the gas location as measured by GRAVITY but further modeling is needed.

Conclusions. With a unique observational data set on HD 98922, we have shown time-dependent morphology changes in its innermost circumstellar dust and gas components that resemble a revolution period around the star. This property is probably common in protoplanetary disks, but not commonly observed due to the lack of long period monthly observations. It is important therefore to push in this direction to unlock the secrets of disk evolution and planet formation in intermediate-mass pre-main sequence stars.

Key words. stars: pre-main sequence – protoplanetary disks – stars: variables: Herbig Ae/Be – stars: individual: HD 98922 – techniques: high angular resolution – techniques: interferometric

1. Introduction

The processes of planet formation and evolution is still a matter of debate but it is acknowledged that protoplanetary disks play a major role in them, leading to a major theoretical and observational effort in the science community in studying these environments. In the last decade our knowledge on protoplanetary disks around young stars has grown considerably thanks to the drastic improvement of the observing facilities. It is nowadays established that such disks show across the optical to sub-millimeter wavelength range different substructures such as rings, gaps, spiral arms, vortices, warps and shadows in tens of au scale (Beuther et al. 2014, and references therein). Thanks to long-baseline infrared interferometry, the complex morphology of inner disks at sub-au scales has been revealed (Lazareff et al. 2017; Gravity Collaboration et al. 2019; Kluska et al. 2020). Temporal photometric variability is a common property of YSOs (e.g., Guarcello et al. 2019; Robinson & Espaillat 2019; Wolk et al. 2018; Rice et al. 2015; Kóspál et al. 2012) and may originate, for instance, from the variation of the stellar properties resulting from the presence of cool or hot spots on the stellar surface, as well as variable accretion. Alternatively, changes in the structure and morphology of the inner circumstellar environment leading to partial occultation of the central star may also cause variable dimming of the system as in the case of "dippers" or UX-Ori type objects. The question of the time-variable morphology of the inner disk has been tackled for a handful of sources (e.g., Kluska et al. 2016; Kobus et al. 2020; GRAVITY Collaboration et al. 2021). The scarcity of such studies is mainly due to the fact that long-period high-cadence observations of the same object are needed, which

---

[*] GRAVITY is developed in a collaboration by the Max Planck Institute for Extraterrestrial Physics, LESIA of Paris Observatory and IPAG of Université Grenoble Alpes / CNRS, the Max Planck Institute for Astronomy, the University of Cologne, the Centro de Astrofísica e Gravitação and the European Southern Observatory.

are not always available. In this context, observations with a large temporal baseline using the PIONIER (Le Bouquin et al. 2011) and GRAVITY instruments (GRAVITY Collaboration et al. 2017) at the VLTI can give us a unique opportunity to probe the origin of the variability in the brightness distribution of the innermost regions of YSOs.

HD 98922 is a B9Ve/A2III (Caratti o Garatti et al. 2015; Hales et al. 2014) Herbig star (Herbig 1960) characterized by a spectral energy distribution (SED) with a high near-infrared (near-IR) excess and a low far-infrared (far-IR) excess ($F_{\rm NIR}/F_\star \approx 20\,\%$, $F_{\rm FIR}/F_\star \approx 2\,\%$, Garufi et al. 2022), and therefore falling in the Group II ensemble (Meeus et al. 2001), in which systems are portrayed as having a sub-au scale disk inner rim directly exposed to the stellar radiation, translating in a puffed up region that casts a shadow on the flat outer disk. The most up-to-date estimates for some of the stellar parameters are listed in Table 1. The classification of the star and the estimates of its parameters in the years have been ambiguous. Especially the distance estimates have been drastically divergent with values going from ≈ 450 pc (Caratti o Garatti et al. 2015) to ≈ 1150 pc (van Leeuwen 2007) affecting the derivation of parameters like the star luminosity, mass, and age. Throughout the paper we will use the latest Gaia EDR3 measurement of 650.9 ± 8.8 au (Gaia Collaboration et al. 2021). Lee et al. (2016) even suggested that the star is already in the post-main sequence phase, likely a luminosity class II bright giant, based on its position on the Hertzsprung-Russell-Diagramm, coupled with the fact that the object is fairly isolated (the closest star-forming region being the Carina Nebula about 7° apart; Dame et al. 2001). Nevertheless, dust and gas excess characteristic of pre-main sequence objects has been observed at different wavelengths and spatial scales, along with relatively high accretion rates ($\dot{M}_{acc} \approx 10^{-7} - 10^{-5}\,M_\odot\,yr^{-1}$, Garcia Lopez et al. 2006; Caratti o Garatti et al. 2015; Fairlamb et al. 2015; Guzmán-Díaz et al. 2021). Thanks to a VLT/SPHERE H-band scattered-light image, Garufi et al. (2022) put a lower-limit on the physical extent of the dust disk of at least 200 au in radius. A comparison with an ALMA moderate-resolution image suggests however an even larger radius of ⪋ 500 au (Garufi et al. 2022). At scales smaller than 10 au, through VLT/MIDI interferometric observations, Menu et al. (2015) constrained the N-band emitting dust disk radius to be ≈ 7.2 au. The disk K-band counterpart was constrained thanks to VLT/GRAVITY to be inside ≈ 1.5 au (Gravity Collaboration et al. 2019), and the H-band one thanks to VLT/PIONIER inside ≈ 1.2 au (Lazareff et al. 2017).

Regarding the gas content, the presence of several emission lines suggests an active circumstellar environment. The system shows a CO-rich circumstellar disk. Hales et al. (2014) suggested, through SED and CO disk radiative transfer (RT) modeling, that the CO disk is geometrically flat with an inner radius of ≈ 1 au and an extent of ≈ 200 au. Other authors instead suggested a system with a flared CO disk, having an inner radius of ≈ 5 au, and a flattened dust disk (van der Plas et al. 2015). This transitional disk scenario was suggested due to the relatively strong polycyclic aromatic hydrocarbons (PAH) emission of HD 98922 and its similarities with two other objects, HD 101412 and HD 95881, for which such disk phase was already proposed in the past (van der Plas et al. 2015; Fedele et al. 2008; Verhoeff et al. 2010). Going towards smaller spatial scales, a rotating gaseous disk inside the dust-sublimation radius was suggested to explain the [OI] emission line profiles (Acke et al. 2005), and a strong wind/outflow was suggested to explain the P Cygni profiles in the Hα, Si II, and He I lines (Grady et al. 1996; Oudmaijer et al. 2011). Finally, the Brγ emission line was suggested to arise from a compact (≈ 0.65 au) region and possibly tracing magnetospheric accretion (Kraus et al. 2008), or a disk wind (Caratti o Garatti et al. 2015).

Table 1. HD 98922 stellar parameters

Parameter	Unit	Value	Reference
Distance	pc	650.9 ± 8.8	1
Age	Myrs	[0.2, 0.7]	2
$M_\star$	$M_\odot$	[5.0, 7.0]	2,3
$R_\star$	$R_\odot$	11.45 ± 0.36	3
$\log L_\star$	$L_\odot$	3.16 ± 0.02	3
$T_{\rm eff}$	K	10500 ± 125	3
$\log g$	$cm\,s^{-2}$	3.5 ± 0.2	4
[Fe/H]		−0.5 ± 0.2	4
$v \sin i$	km/s	39.0 ± 5.3	5
$\log \dot{M}_{acc}$	$M_\odot\,yr^{-1}$	[−7.0, −5.0]	6,3

Notes. $M_\star$ is the stellar mass, $L_\star$ the luminosity, $T_{\rm eff}$ the effective temperature, $\log g$ the surface gravity logarithm, [Fe/H] the metallicity, $v \sin i$ the projected linear velocity, and $\dot{M}_{acc}$ the accretion rate. References: (1) Gaia Collaboration et al. (2021); (2) Garufi et al. (2022); (3) Guzmán-Díaz et al. (2021); (4) Caratti o Garatti et al. (2015); (5) Aarnio et al. (2017); (6) Fairlamb et al. (2015).

With this work we aim at studying the morphological properties of the innermost circumstellar environment of HD 98922 through modeling of multi-epoch GRAVITY/VLTI and PIONIER/VLTI observations. We test the hypothesis of the time-variability of the brightness distribution and discuss it the context of disk evolution scenarios. In addition, we explore the spatial distribution of hot hydrogen via the interpretation of the interferometric differential phase signal in the Brγ-line emission line at 2.16 μm. In Section 2 we present the observations and and describe the interferometric data; in Section 3 the methodology used to analyze the data is explained; Section 4 presents our results from the analysis of the continuum and line data; finally, in Section 5 we discuss in details possible interpretations of our results.

2. Dataset description

2.1. Observations

HD 98922 was observed with VLTI/PIONIER (Le Bouquin et al. 2011) using the four 1.8 m Auxiliary Telescopes (ATs) in 21 different epochs between 2011 and 2016. Data were obtained using the small, medium, and large baseline configurations for different epochs. The data consist in low spectral resolution ($R \approx 40$) interferometric observables across the H band (at 1.55–1.80 μm; Le Bouquin et al. 2011). The observations span a spatial frequency range between about 5 Mλ to 90 Mλ with a maximal angular resolution of $\lambda/2B \sim 1.25$ mas for the longest baseline of 138.7 m, which corresponds to 0.81 au at 650.9 pc. In total, 45 files were acquired and 4 files were discarded due to bad weather conditions, leaving us with 41 files in total. The description of the data per epoch, as well as the observations logs (dates, array configurations, weather conditions, calibrators) can be found in Table A.1.

Regarding the GRAVITY observations, HD 98922 was observed at 13 different epochs between 2017 and 2022 with the astrometric, large, medium, and small baseline configurations. The data consist in high spectral resolution (R ≈ 4000) observables recorded by the science channel (SC) detector across the K band with individual integration times of 30 s, as well as in low spectral resolution (R ≈ 20) observables recorded by the fringe tracker (FT) detector (Lacour et al. 2019). The spatial frequency ranges between about 5 Mλ to 65 Mλ with a maximal angular resolution of $\lambda/2B \sim 1.72$ mas for the longest baseline of 129 m, which corresponds to 1.12 au at the object's distance. Each observation block corresponds to 5 minutes of observing time on the object. In total, 97 files were acquired. Detailed information on the GRAVITY observations is given Table A.2. All together, the PIONIER and GRAVITY dataset spans a 11-year period from 2011 to 2022.

2.2. Data reduction

The PIONIER data are archival data retrieved already reduced and calibrated from the JMMC Optical interferometry DataBase[1]. The reduced data for each single epoch can be found in Fig. A.1. The plots show the calibrated squared visibilities, the calibrated closure phases, and the *(u,v)* plane coverage (left, central, and right panel, respectively). The adopted errors bars are derived from the reduction and calibration pipeline. These range from 0.25° to 10.1° for the closure phases and from 0.001 to 0.18 for the squared visibilities, depending on the atmospheric conditions.

The GRAVITY data were reduced and calibrated using the GRAVITY data reduction software (Lapeyrere et al. 2014). For the low-resolution FT data, we discarded the first spectral channel, which might be affected by the metrology laser operating at 1.908 μm. The FT calibrated squared visibilities, closure phases, and the *(u,v)* plane coverage for each single epoch can be found in Fig. A.2 (left, central, and right panel, respectively). Following Gravity Collaboration et al. (2019) and Gravity Collaboration et al. (2021), we applied a floor value on the error bars of 2% for the squared visibilities and 1° on the closure phases as the error bars computed by the pipeline might be underestimated or correlated.

Fig. A.3 shows the high spectral resolution GRAVITY data after zooming in the wavelength region of the Brγ line between 2.164 and 2.168 μm. No high-resolution data was acquired on the 15 June 2018. For each of the remaining 12 epochs, the data set contain the spectrum, the calibrated squared visibilities, and the calibrated differential phases (top, left, and right panels, respectively). The observables for one epoch result from the averaging of N individual block files as listed in the fourth column of Table A.2. Each averaged file is wavelength-calibrated using the position of the telluric absorption lines bracketing the Brγ emission line and then correcting for the star motion with respect to the LSR. The wavelength calibration is discussed in more details in Appendix D. The error bars used are the ones derived from the reduction and calibration process and propagated through the averaging process. These range from 0.3 to 1% for the spectrum, from 0.001 to 0.01 for the squared visibilities, and from 0.5 to 2° for the differential phases, depending on the observation epoch.

2.3. Continuum data overview

PIONIER spatially resolves the emission of HD 98922 at all baselines and epochs, and fully resolves it with the longest baselines. The squared visibilities range between 0 and 0.8 going from the large to the small configurations. Clear closure phases signals are detected for all epochs and configurations. They range between −20° and 20° for the medium and large configurations, and between −4° and 4° for the small one. The data therefore clearly suggest an asymmetric brightness distribution in the H band continuum.

HD 98922 is also resolved for all baselines and fully resolved at the longest baselines by GRAVITY with squared visibilities ranging between 0 and 0.7 going from the large to the small configurations. The largest configurations detect closure phases signals ranging between −40° and 40°, the medium ones between −15° and 15°, and the small ones between −4° and 3°. As for the H-band continuum emission, the K-band counterpart is also expected to shows spatial asymmetries.

2.4. Brγ-line data overview

HD 98922 shows a slightly blue-shifted (≈ −23.5 km/s) single peaked Brγ emission line Fin all epochs. Considering the 3 Å error on the GRAVITY spectral channel wavelength, we can consider the peak's position of the continuum-normalized line ($21659.7^{+0.8}_{-1.3}$ Å) to be constant through the epochs at our spectral resolution. The normalized peak flux varies between 1.17 and 1.25 depending on the epoch, while the line width measured at the peak's 10% flux level ranges from 14 to 15 Å. The total squared visibilities vary between ≈ 0 and ≈ 0.4 depending on the epoch and baseline configurations (medium or large), while they reach ≈ 0.7 for the small configuration. We note that for all the epochs and baselines the total squared visibilities in the Brγ line is higher than in the continuum, suggesting on the first order that the line-emitting gas region is more compact than the continuum. Finally, the differential phase signals vary between −15° and 25° and have significantly different shapes (flat, single-peaked, double-peaked, or *S*-shape) for the different epochs and baselines.

2.5. Source variability and UV coverage

As mentioned in Section 2.1, our data set on HD 98922 spans a 11-year time period for the continuum component and a 6-year period for the Brγ-line one, which gives us a unique opportunity to monitor the variability over a rather extended period. The time intervals between consecutive observations range from 10 to 20 months for the PIONIER data set, and from 5 to 15 months for the GRAVITY one. We remind however that the modeling of interferometric data is sensitive to differences in the *(u,v)* plane coverage. Hence, beside relying on extended temporal coverage and frequent epoch sampling, time-variability studies using interferometric data also require observations with array configurations having similar *(u,v)* plane coverage.

In the top row of Fig. 1, we report for PIONIER (P) and GRAVITY (G) the length and position angle of the longest baseline for a given configuration. The nomenclature can be followed in Table A.1 and A.2. This provides a visual estimate of comparable (u, v) coverage planes, although a more accurate assessment requires to compare the full configurations in Fig. A.1 and Fig. A.2. Following this approach, we note that a compa-

---

[1] available at `http://oidb.jmmc.fr/index.html`

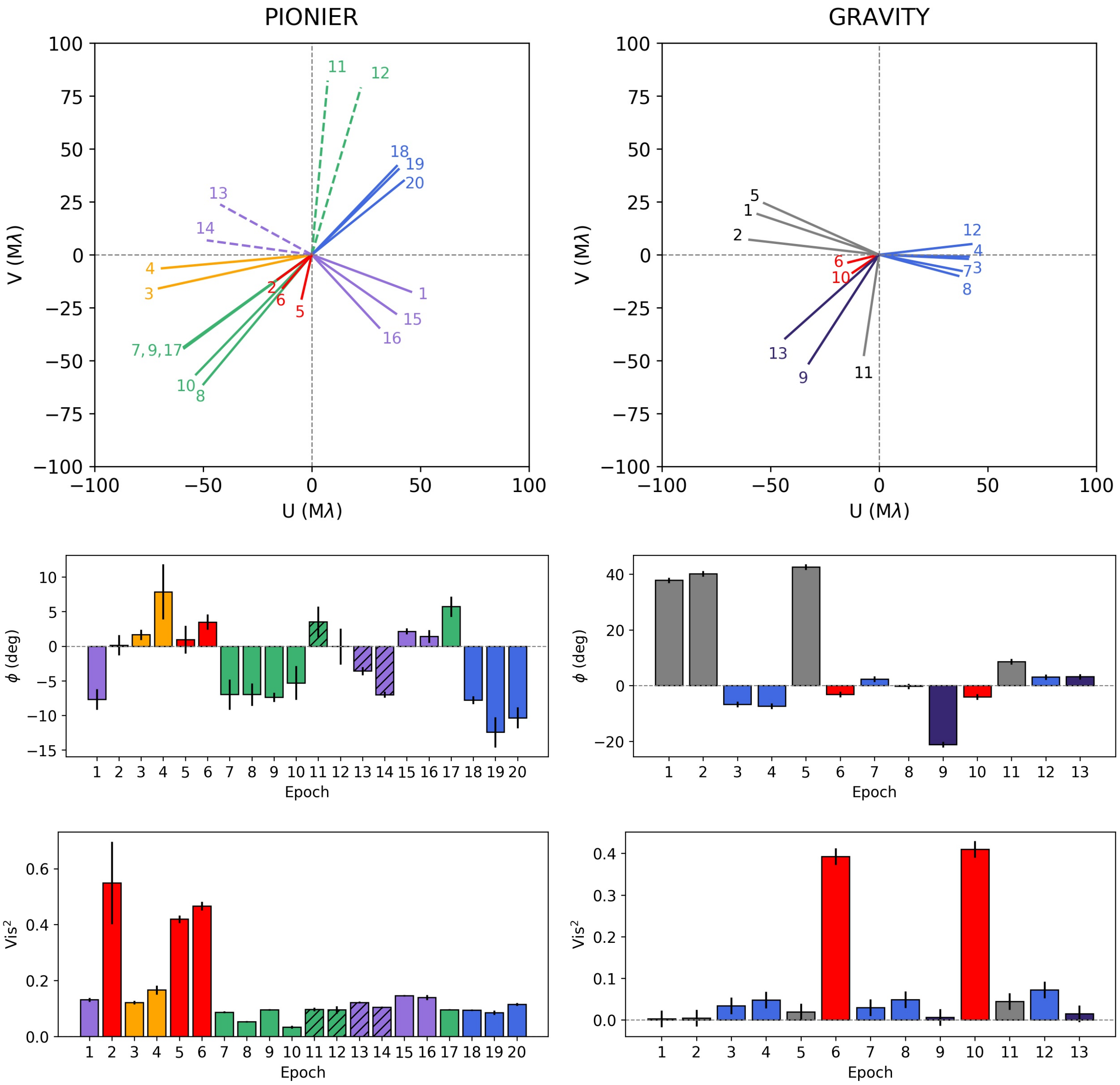

Fig. 1. HD 98922 continuum data overview. Top row: longest baselines position angle for each epoch and instrument. Medium row: closure phase signal for each epoch and instrument; the spatial frequency chosen is the one for which a strong variation in the CP signal between epochs with a comparable *(u,v)* plane coverage is observed. Bottom row: Vis^2 signal for each epoch and instrument (same spatial frequency as the CP signals shown in the above plot). Colors refer to the different baselines configurations. For a given instrument, two epochs have same color and line-style if they have a comparable *(u,v)* plane coverage. The gray color refer to epochs where the *(u,v)* plane coverage is significantly different from the ones of any other epoch. Numbers are used to identify each epoch used in this paper as listed in Table A.1 and A.2.

rable (u, v) plane coverage is found for the following groups: (P1,15), (P2,6), (P3,4), (P7,8,9,10,17), (P11,12), (P13,14), and (P18,19,20). Depending on the group, the difference in position angle of the longest baseline varies between ~5° and 20°. The small configuration epoch P5 has a significantly different position angle of ~30-40° with respect to P2 and P6, while the medium configuration epoch P16 also differs from P1 and P15. In the case of GRAVITY, the configurations with similar (u, v) plane coverage are (G3,4,7,8,12), (G6,10), and (G9,13). The configurations of the remaining epochs differ more strongly. The central and bottom rows of Fig. 1 are constructed as follows. First, we visually identify for a group of similar configurations the common spatial frequency for which a strong variation in the closure phase (CP) signal is observed and report the CP value (Fig. 1, central panels). For this same spatial frequency, we report in the bottom panels the value of the squared visibility.

For those configurations with a similar *(u,v)* coverage, we are able to detect significant variations in the CP values across the epochs. For instance, a clear difference in the CP signal of $\Delta\phi_{\max} \approx 25°$ is observed for G9 and G13, as well as in the medium configuration epochs G3, G4, G7, G8, G12 were the

CP signals vary between $\phi_{\max} \approx -7°$ to $\approx 3°$. Even though the error bars are larger, the CP variability in the PIONIER data set is also clearly observed. The epochs P1 and P15 show a significantly closure phase variation ($\Delta\phi_{\max} \approx 10°$), as well as P17 with respect to P7, P8, P9, and P10 ($\Delta\phi_{\max} \approx 13°$). On the contrary, when comparing observations taken with similar *(u,v)* plan coverage, we note that the variability of the corresponding squared visibilities is modest, typically below $V^2 \sim 0.05$.

This behavior suggests on first order that we do not observe a clear variability trend in the centro-symmetrical properties of the brightness distribution of HD 98922 (i.e., characteristic size or star/scattered light/disk thermal emission). Instead, the more marked closure phases variability observed by PIONIER and GRAVITY suggests time-varying asymmetric features in both H and K bands. We explore in further details the nature and cause of this phenomenon.

3. Methodology

3.1. Continuum: Low spectral resolution data

Following the work of Lazareff et al. (2017), we used chromatic geometric models that consist of a point-like central star, a scattered light component (called halo), and a circumstellar environment in order to fit the observed visibilities. The star is assumed to be unresolved at all baselines, and the halo is assumed to be a fully resolved emission component with a visibility of zero. The total complex visibility of the system at spatial frequencies (u, v) and at wavelength λ is therefore described by a linear combination of the three components as:

$$V(u, v, \lambda) = \frac{F_{\rm s}\,(\lambda/\lambda_0)^{k_{\rm s}} + F_{\rm c}\,(\lambda/\lambda_0)^{k_{\rm c}}\,V_{\rm c}(u, v)}{(F_{\rm s} + F_{\rm h})\,(\lambda/\lambda_0)^{k_{\rm s}} + F_{\rm c}\,(\lambda/\lambda_0)^{k_{\rm c}}}, \quad (1)$$

where $V_{\rm c}$ is the complex visibility of the circumstellar environment, $F_{\rm s}$, $F_{\rm h}$ and $F_{\rm c}$ are the specific fractional flux contributions of the star, of the halo, and of the circumstellar environment, respectively, at $\lambda_0 = \lambda_{K,0} = 2.15\,\mu$m, the wavelength of the central spectral channel of the GRAVITY FT, or at $\lambda_0 = \lambda_{H,0} = 1.68\,\mu$m for PIONIER. The parameter $k_{\rm s} = d\log F_{\lambda,s}/d\log\lambda$ is the spectral index of the star assuming it radiates as a black body at $T_{\rm eff}$=10500 K. This translates into a spectral index of $k_{\rm s} = -3.645$ at $\lambda_{K,0}$ and -3.523 at $\lambda_{H,0}$. $k_{\rm c} = d\log F_{\lambda,c}/d\log\lambda$ is the spectral index of the circumstellar environment.

The circumstellar emission is modeled through an azimuthally-modulated wireframe convolved by an ellipsoid kernel that regulates the width of the ring-like emission, and which visibility is given by Eq. 9 of Lazareff et al. (2017). Hence, the model can describe from infinitesimally thin rings to very wide rings tending to ellipsoids. It is described by ten parameters: the star flux contribution F$_s$; the halo flux contribution F$_h$; the spectral index of the circumstellar disk k$_c$; the radius of the wireframe a$_r$ and of the Kernel a$_k$, the inclination i; the position angle PA; the weighted contribution of a Gaussian or Lorentzian distribution fLor; the azimuthal modulation parameters c_1 and s_1. More details on the relation between the geometrical, physical and fitted parameters is provided in Sect. 3.6 of Lazareff et al. (2017). We recall here an important convention of the azimuthal modulation relevant for the correct interpretation of our results. The azimuthal modulation, which is parametrized with the variables c1 and s1, has a position angle of the peak emission given by the argument of the complex number $c1 + {\rm j}.s1$. The origin of this angular position is along the position angle of the disk measured from North to East, with East to the left. As an example, an azimuthal modulation described by c1=1 and s1=1 in a disk with a PA = 45° will show a visual rendering where the azimuthal modulation peak emission appears at 90° towards East.

The model fitting consists in a first minimization procedure with `scipy.optimize.minimize` using a Sequential Least Squares Programming method to get an initial guess of the free parameters, followed by a procedure based on a Markov chain Monte Carlo (MCMC, Foreman-Mackey et al. 2013) numerical approach, which is robust against trapping in local minima. The errors on the reduced chi-squared χ^2_r are calculated considering the χ^2_r as a stochastic variable following Gravity Collaboration et al. (2021).

3.2. Gas: High spectral resolution data

To estimate the Brγ gas region size, kinematics, and displacement with respect to the continuum emission from the GRAVITY SC visibilites and differential phases, we extrapolated the pure-line contribution (marked with subscript L) from the interferometric observables. Following Weigelt et al. (2011), the pure-line interferometric quantitites characterizing the gas emitting region, the visibility $V_{\rm L}$ and differential phase $\phi_{\rm L}$, are related through:

$$F^2_{\rm L}V^2_{\rm L} = F^2_{\rm tot}V^2_{\rm tot} + F^2_{\rm cont}V^2_{\rm cont} - 2F_{\rm tot}V_{\rm tot}F_{\rm cont}V_{\rm cont}\cdot\cos\phi_{\rm tot}, \quad (2)$$

$$\sin\phi_{\rm L} = \sin\phi_{\rm tot}\frac{\rm F_{tot}V_{tot}}{\rm F_L V_L}, \quad (3)$$

The quantities reported in Eq. 2 and 3 refers to values inside the Brγ-line spectral region. Since the continuum quantities $F_{\rm cont}$ and $V_{\rm cont}$ *in the line* are not directly measurable, they are estimated from the nearby continuum aside the line region. However, hot Herbig stars exhibit a strong Brγ photospheric absorption feature, which needs to be accounted for in order to retrieve the correct pure-line quantities. In the case where photospheric absorption is present, the knowledge of a model for the continuum emission is required. One can show that:

$$V_{\rm L} = \left(\frac{(V_{\rm tot}\,F'_{\rm L/C})^2 + \left(\frac{F'_{\rm s}}{F'_{\rm cont}}(\alpha-1) + V'_{\rm cont}\right)^2}{\left(F'_{\rm L/C} - \frac{\alpha+\beta+\gamma}{1+\beta+\gamma}\right)^2} \right. \\ \left. \frac{-2\,(V_{\rm tot}\,F'_{\rm L/C})\left(\frac{F'_{\rm s}}{F'_{\rm cont}}(\alpha-1) + V'_{\rm cont}\right)\cos(\phi_{\rm tot})}{\left(F'_{\rm L/C} - \frac{\alpha+\beta+\gamma}{1+\beta+\gamma}\right)^2} \right)^{1/2}. \quad (4)$$

The superscript (′) in Eq. 4 indicates that the quantities $V'_{\rm cont}$ and $F'_{\rm cont}$ are estimated outside the emission line spectral region, as opposed to Eq. 2. The line-to-continuum ratio $F'_{\rm L/C}$ is also normalized to the nearby continuum value. The parameters β and γ are the disk-to-star (β=$F_{\rm c}/F_{\rm s}$) and halo-to-star (γ=$F_{\rm h}/F_{\rm s}$) flux ratios.

The parameter α describes the star photospheric absorption, with $0<\alpha\leqslant1$. It is equal to 1 in the absence of any photospheric absorption (see Appendix D for a description of the photospheric absorption model), so that:

$$F_{\rm L} = F_{\rm tot} - F'_{\rm cont} + F_{\rm s}\,(1-\alpha), \quad (5)$$

where α is a parameter that describes the star photospheric absorption, equal to 1 when there is no absorption, and equal to

Table 2. Results of the fit of the `Aspro` synthetic data. Uncertainties are reported as 1σ errors from the 16^{th} and 84^{th} percentile of the MCMC marginal distributions. The column 'All' refers to the simultaneous fit of the three data sets combined. F_c is not a free parameter, but obtained according to $F_c = 1 - F_h - F_s$.

	All	Small	Medium	Large
Parameter	Value	Value	Value	Value
F_s [%]	$22.8^{+0.1}_{-0.1}$	$42.3^{+1.3}_{-2.4}$	$29.9^{+0.9}_{-1.9}$	$16.7^{+0.4}_{-0.4}$
F_h [%]	$0.3^{+0.1}_{-0.1}$	$0.9^{+0.2}_{-0.3}$	$0.3^{+0.7}_{-0.2}$	$33.6^{+3.7}_{-4.2}$
F_c [%]	$76.9^{+0.2}_{-0.2}$	$56.8^{+1.5}_{-2.7}$	$69.8^{+1.6}_{-2.1}$	$49.7^{+4.1}_{-4.6}$
a_r [mas]	$3.46^{+0.01}_{-0.01}$	$4.52^{+0.20}_{-0.15}$	$3.76^{+0.30}_{-0.29}$	$3.52^{+0.06}_{-0.06}$
a_k [mas]	$1.75^{+0.01}_{-0.01}$	$0.25^{+0.40}_{-0.08}$	$1.05^{+0.23}_{-0.19}$	$1.59^{+0.07}_{-0.07}$
i [deg]	$10.7^{+1.0}_{-1.1}$	$11.8^{+10.8}_{-8.1}$	$8.5^{+5.2}_{-4.1}$	$15.1^{+3.2}_{-4.4}$
PA [deg]	$0.9^{+1.6}_{-0.7}$	$37.0^{+48.9}_{-33.8}$	$1.8^{+7.6}_{-1.5}$	$2.5^{+4.5}_{-1.8}$
fLor	$0.01^{+0.01}_{-0.01}$	$0.11^{+0.24}_{-0.10}$	$0.49^{+0.16}_{-0.33}$	$0.08^{+0.11}_{-0.06}$
c_1	$0.61^{+0.01}_{-0.01}$	$0.50^{+0.17}_{-0.17}$	$0.52^{+0.10}_{-0.12}$	$0.52^{+0.04}_{-0.04}$
s_1	$0.03^{+0.02}_{-0.01}$	$0.08^{+0.19}_{-0.10}$	$0.04^{+0.16}_{-0.06}$	$0.01^{+0.05}_{-0.02}$
χ^2_r	3.0 ± 0.1	2.3 ± 0.1	4.6 ± 0.4	2.6 ± 0.2

zero when 100% of the star flux is absorbed (see Appendix D for a description of the photospheric absorption model).
Similarly, Eq. 3 is written in terms of known quantities as:

$$\sin \phi_{\mathrm{L}} = \sin \phi_{\mathrm{tot}} \frac{V_{\mathrm{tot}}}{V_{\mathrm{L}}} \frac{1}{\left(1 - \frac{\alpha+\beta+\gamma}{1+\beta+\gamma} \frac{1}{F'_{\mathrm{L/C}}}\right)} \tag{6}$$

Following Lachaume (2003), we can derive wavelength-dependent photocenter displacements along each baseline from the pure-line differential phases by

$$: \mathbf{p} = \frac{-\phi_{\mathrm{L}}}{2\pi} \cdot \frac{\lambda}{\mathbf{B}}, \tag{7}$$

where $\mathbf{p}$ is the projection on the baseline $\mathbf{B}$ of the 2D photocenter vector with origin on the continuum photocenter of the system. The results of the GRAVITY SC data analysis are shown in Section 4.5 and discussed in Section 5.4.

4. Results

4.1. Fit dependence on the (u,v) plane coverage

Since we have multiple observations taken with different baseline configurations and *(u,v)* coverage, we first verified with synthetic data whether the fit of different data sets related to a same non-variable system but obtained with different baseline configurations would lead to a same or different modelling solution. For this purpose, we generated with `Aspro`[2] three synthetic data sets of a non-variable system formed by a star and an azimuthally modulated ring that is observed with, respectively, the same small, medium, and large configurations of the 4th February 2020, 11th July 2019, and 14th February 2022 epochs. We then analysed the fit results of the synthetic data sets corresponding to our non-variable system observed with different baseline configurations having a different *(u,v)* coverage. The input model from which synthetic data are generated corresponds to an azimuthally modulated donut around a central star contributing 15% of the system total flux, and with no spatially resolved halo contribution (Fig. 2). The synthetic interferometric visibilities and closure phases generated with `Aspro` are shown in Fig. B.1. The same error bars as for the real data are adopted. The fit of the synthetic data implements the nine *free* parameters given in Table 2. The spectral indices of the star and the disk were not implemented and set to zero. Four cases are explored, corresponding to the individual small, medium, and large configurations, plus the case where all the three configurations are combined.
From the results in Table 2, we find that the flux parameters (F_s, F_h, F_c) are the most affected by some spurious variability due to a changing *(u,v)* coverage, with differences up to ~30 %. In addition, the stellar contribution is slightly (large configuration) to significantly (small configuration) overestimated with respect to the input model. The geometrical parameters (a_r, a_k) describing the characteristic size are found to be more in agreement (though not necessarily within the error bars), except for the small configuration that only loosely constrains the solution. The inclination value is consistent within the error bars between the four cases, although modestly constrained by the small and medium configurations. Also, the results are find to be generally consistent with a low-inclination disk. The same conclusion applies to the PA, with the small configuration expectedly failing to constrain this parameter. Finally, for the parameters c_1 and s_1 describing the azimuthal modulation, the fit converges towards very similar values for all four cases.

Simply accounting for the error bars on the fitted parameters, the modeling of the small-, medium- and large-configuration data sets results in a consistent value for the ring inclination, the PA, c_1 and s_1, but clearly these parameters are more stringently constrained when going from the small to the large configuration. In Fig. 2, we compare the input model image to the parametric models resulting from the fit of the different configurations. Besides the differences found in the relative flux contributions (see Table 2), we can visually observe that the size properties are not in good agreement – in particular for the small configuration – when fitting separately the data of the different configurations, although the general strucutre is retrieved. In contrast, the azimuthal position of the disk asymmetry appears to be well constrained. This simple test reminds us that the intrinsic sparsity of infrared interferometric data implies that different spatial frequencies are probed with different configurations, which may result in a spurious variability of the fitted parameters that may not reflect a physical temporal variability of the system.
Leaning on this observation, we adopted here a different strategy to test more robustly the potential time-variability of the different parameters describing our model: we fitted the full PIONIER, respectively GRAVITY, continuum data set by forcing all the free parameters to be *constant* across the different epochs, except the parameter for which we wish to test the variability hypothesis. Throughout the paper we refer to this approach as the *x global fit*, where *x* is the selected time-variable parameter, which is motivated by the fact that a rich *(u,v)* coverage remains mostly desirable. This is further used in Section 4.2.

4.2. Time variability of the system parameters

Here, we report the results of the global fit approach on the continuum data. We first explore which among seven model parameters (star flux contribution, ring inclination, position angle, characteristic size, and azimuthal modulation) is most prone to describe the temporal variability of the data suggested in Fig. 1. The global fit (see Section 4.1) was applied separately

---

[2] Available at `http://www.jmmc.fr/aspro`

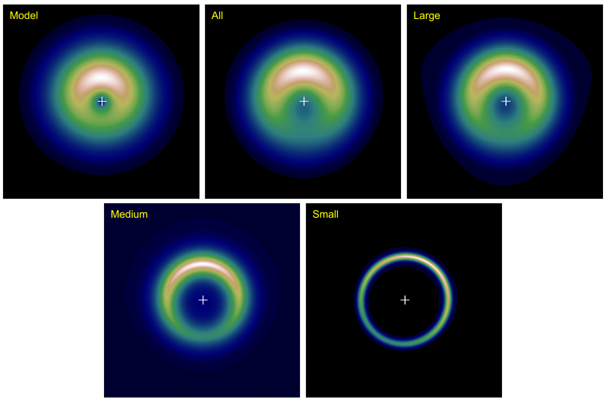

Fig. 2. `Aspro` synthetic data test images. The top-left model has been used to generate the synthetic visibilities and closure phases with `Aspro`. The resulting fitted models are shown for the respective configurations. The intensity scale is linear and ranges from 0 to the peak pixel value of the asymmetry. The central star has been removed and its position marked with the white cross. The images have a size of 20×20 mas. It is visible from this figure and Table 2 that the small configuration properly constrains the absence of halo contribution in the system, but not the disk morphology, as opposed to the large configuration.

Table 3. Results of the global fit for different parameters tested for variability. 1σ errors are reported for the χ^2_r.

#	Model	Var. par.	Nfp	χ^2_r (P)	χ^2_r (G)
1	SHRM1	F_s	9+Ne	13.5 ± 0.7	11.1 ± 0.4
2	SHRM1	a_r, a_k	8+2Ne	12.0 ± 0.6	7.7 ± 0.3
3	SHRM1	i	9+Ne	14.9 ± 0.7	14.7 ± 0.5
4	SHRM1	PA	9+Ne	12.4 ± 0.6	12.0 ± 0.5
5	SHRM1	c_1, s_1	8+2Ne	11.5 ± 0.6	5.3 ± 0.3
6	SHRM2	$c_{1,2}$, $s_{1,2}$	8+4Ne	9.5 ± 0.5	4.3 ± 0.2

Notes. The model nomenclature gives S = star, H = halo, RM1 = 1st order azimuthal modulated ring, and RM2 = 2nd order azimuthal modulated ring; Nfp gives the number of free parameters. Ne is the number of epochs, namely 20 for PIONIER (P) and 13 for GRAVITY (G)).

to each parameter (or pair of parameters) reported in Table 3. For the GRAVITY data set, we observe from the χ^2_r analysis that the time-variable azimuthal modulation models (#5 and #6) lead to the smallest χ^2_r values in comparison to other system parameters. This is less marked for the PIONIER data set for which even though the time-variable azimuthal modulation model shows the smallest χ^2_r, the other models show comparable χ^2_r values when accounting for 3σ errors. However, the trend in terms of decreasing χ^2_r suggests an analog behavior for both the PIONIER and GRAVITY data sets. A second order azimuthal modulation model was also tested with the parameters $c_{1,2}$ and $s_{1,2}$ (model #6). As one may expect, the addition of new free parameters improves the fit, but not significantly within the 3σ error bars. We therefore conclude that the current data do not require a more complex model in order to be interpreted.

This analysis confirms what is qualitatively observed in Fig. 1, in particular for the closure phases, pointing at the azimuthal modulation as the probable dominant effect in the variability of the system. Since the system described by a time-variable azimuthal modulation gives the best fitting solution for both data sets, this will remain the baseline model to pursue our analysis in the following text.

4.3. Variable brightness distribution in the inner disk

The results of the global fit with a time-variable azimuthal modulation (model #5 in Table 3) are presented in Table 4 for all the non-variable parameters. Two values are reported for the retrieved uncertainty: the error σ_{MCMC} is the confidence interval derived from the parameter marginal posterior distribution resulting from the MCMC minimization[3]; the error σ_{χ^2} corresponds to an upper limit derived from the 1D χ^2_r maps associated to each fitted parameter (Fig. C.1), which indicates how well constrained the given parameter can be. Consequently, the later is generally more conservative, and therefore larger.

Fractional flux – In the H band, we find for the different flux contributions comparable ratios to Lazareff et al. (2017), who exploited a dense *(u,v)* coverage. In the K band, we measure a stellar flux contribution of 23 ± 4 %, comparable to the contribution in the H band. Different values for the K band fractional stellar contribution based on photometry and SED analysis are reported in the literature, from ∼15 % (Kraus et al. 2008; Hales et al. 2014; Gravity Collaboration et al. 2019) to ∼23 % (Caratti o Garatti et al. 2015). Despite the model based solely on the stellar temporal variability was not favored in Table 3, we cannot fully exclude that such an effect is present to some degree. Interestingly, we also find a stronger halo contribution than Gravity Collaboration et al. (2019), which can be explained by the fact that these authors have constrained the circumstellar emission of HD 98922 in the K band only with the astrometric configuration, whereas the short baselines of the small configuration are usually needed to better constrain the halo.
To possibly strengthen our finding, we also tested a two-parameter global fit model by adding the fractional stellar contribution as an additional free and time-variable parameter. In terms of χ^2_r, this led for both PIONIER and GRAVITY data sets to a solution comparable to the one-parameter time-variable model, without significant improvement. We conclude that, while possibly present in the system, additional stellar variability is no added value in our model to describe our data and that a time-variable azimuthal modulation of the brightness distribution is the most plausible dominant effect.

Characteristic size: The radius of the ring disk emission in K band is found to be a_r=2.02±0.1 mas (or 1.31±0.07 au), in good agreement with the estimate of Kraus et al. (2008) and Caratti o Garatti et al. (2015), with 2.2 mas and 1.6 mas, respectively. Our result is only slighlty larger than the estimate of Gravity Collaboration et al. (2019) with a_r=1.8 mas, with only two snapshots with the astrometric configuration used by the later authors. In the H band, we find the circumstellar emission to be more compact than in K, with a characteristic radius of a_r=0.93±0.1 mas (or 0.60±0.07 au) in line with the estimate of 0.87 mas by (Lazareff et al. 2017). Kluska et al. (2020) reports a larger half-flux radius of 2.1 mas based on image reconstruction, which evidences the impact of different modeling approaches. The K-to-H size ratio is further discussed in Sect. 5. The ratio a_k/a_r being close or larger than unity suggests a wide, smooth, ring emission as opposed to a sharp edge. The disk has a low-inclination configuration, which is therefore harder to accurately constrain in the small-angle range. This applies to the position angle as well (Fig. C.1).

---

[3] Markov Chain Monte Carlo

Table 4. Azimuthal modulation global fit continuum models non-variable parameters

		PIONIER			GRAVITY		
Parameter	Unit	Value	$3\sigma_{\chi^2}$	$3\sigma_{MCMC}$	Value	$3\sigma_{\chi^2}$	$3\sigma_{MCMC}$
F_s	%	23.09	1.00	0.39	22.69	3.00	0.42
F_h	%	3.92	4.00	0.78	10.36	4.00	0.57
F_c	%	72.99	5.00	1.17	66.95	7.00	0.99
k_c		3.47	3.00	0.18	-0.39	5.00	0.33
a_r	mas	0.93	0.06	0.06	2.02	0.08	0.06
a_k	mas	1.60	0.10	0.03	1.73	0.16	0.06
i	deg	0.67	25.0	2.01	34.15	10.0	1.08
PA	deg	106.9	30.0	1.80	122.9	6.00	1.50
fLor		1.00	0.30	0.03	1.00	0.25	0.03
χ^2_r		11.52	1.86		5.26	0.87	

Notes. F_c is not a free parameter, but obtained according to $F_c = 1 - F_h - F_s$. The σ_{MCMC} error estimates, derived through the MCMC fitting procedure, are given by the 16^{th} and 84^{th} percentiles of the samples in the MCMC marginalized distributions. The $\sigma_{\chi^2_r}$ error estimates are derived from the χ^2_r curves in Fig. C.1.

Disk azimuthal asymmetry: Most notably, our modelling reproduces a crescent-like asymmetric dust feature resulting from the azimuthal modulation that varies in position angle through the epochs and revolves around the central star. In Fig. 3 and Fig. 4, we present the continuum images corresponding to our fitted models and from which the geometry, extent, and location of the asymmetry can be followed as a function of time. We generally observe that the continuum emission appears azimuthally more compact in the H band than in the K band. The fit of the variable azimuthal modulation appears quite robust in Fig. C.2 with one single global minimum identified in the c_1,s_1 diagram. Furthermore, for epochs only separated by a few days at most and taken with the same array configuration, the azimuthal locations of the asymmetric feature are consistent in most cases within the error bars (e.g., P7-P8-P9-P10-P11 and P19-P20 with PIONIER, or G7-G8 with GRAVITY). Fig. 3 and 4 display the azimuthal uncertainties in the form of a white-line cone as derived from the MCMC 3σ error bars on c_1 and s_1. The azimuthal uncertainty is generally smaller (up to ~10-20°, depending on the configuration) in the K band than in the H band. In addition, the azimuthal position is constrained at worst with the small configuration (e.g. P2-P5-P6 with PIONIER) since the closure phase signal is marginal for the shortest baselines.

The brightness contrast between the crescent-like feature and the centro-symmetric location in the disk is estimated from Fig. 3 and 4. The contrast is found to be ~4 in the K band (ranging from ~1.6 to 10 across the epochs, with σ~2.8) and ~2.4 in the H band (ranging from ~1.3 to 3.3, with σ ~0.7). No characteristic trend is found in the temporal evolution of the contrast.

The dynamical properties of the inner disk feature revealed by our observations are further discussed in Section 5.1.

We note that, thanks to the global fit approach, the typical degeneracy between the flux ratio and the disk size is broken. This happens also for the degeneracy between the halo flux contribution and the radial brightness profile of the dust emission determined by fLor, as shown by the χ^2_r curve of this parameter. As an additional check, we fitted the data using the azimuthal modulation global fit with the parameter fLor fixed to zero (which then corresponds to a fully Gaussian radial profile). This worsens the fit in terms of χ^2_r in comparison to the case fLor=1 (i.e., a Loretzian radial profile) for both PIONIER ($\chi^2_r = 20.6 \pm 1.02$) and GRAVITY ($\chi^2_r = 6.2 \pm 0.3$).

4.4. Dust magnitude variability

Here we estimate the relative brightness of the azimuthal disc feature revealed by PIONIER and GRAVITY, as well as its temporal variability. While the total flux of the disk F_c remains constant over time in our global fit (see Table 4), the azimuthal feature might appear more or less contrasted depending on how shallow or steep the brightness distribution is. For each epoch, we define a contour line at a given fraction of the feature peak value and calculate the relative encircled flux. An illustration is shown in Fig. 5. We calculate the apparent magnitude of the feature m_{az} following:

$$m_{\rm az} = -2.5\log\left(\frac{\rm F_{az}\,F_c\,F_0 \times 10^{-\frac{m_{tot}}{2.5}}}{\rm F_0}\right), \qquad (8)$$

where m_{tot} is the total apparent magnitude of the system in H and K, respectively, with H=5.23 and K=4.28 (Cutri et al. 2003). $F_{0,\lambda}$ is the reference flux density equal to 1024.0 Jy in H and 666.8 Jy in K (Rodrigo & Solano 2020). F_c is the total disk flux ratio as estimated in Table 4), and $F_{\rm az}$ is the encircled flux fraction for a given contour as shown in Fig. 5.

The results are presented in Fig. 6 for the two H and K bands and for different contour values. Here we did not include epochs corresponding to the small baseline configuration. By construction, at a given epoch, higher fractional peak value contours correspond to larger magnitudes due to the reduced encircled flux. The H-band magnitude of the feature is higher than its K-band magnitude when considering the same peak-value contour, as expected for a disk-related infrared excess. Regarding the feature magnitude time-variability we note that for most of the epochs the magnitude is fairly constant. Only the 1 February 2013 and the 14 December 2022 epochs shows a decrease of ≈ 0.25 mag with respect to the average value. The decrease in magnitude does not mean that the feature gets brighter, but it means that the disk gets less asymmetric with the feature getting smoother.

4.5. Brγ-line emitting region time variability

We exploit the high-spectral resolution data of GRAVITY in the Brγ-line region to constrain the spatial scale and the kinematics of the hot gas component, following the formalism presented in Sect. 3.2. From the pure-line visibilities we estimated the char-

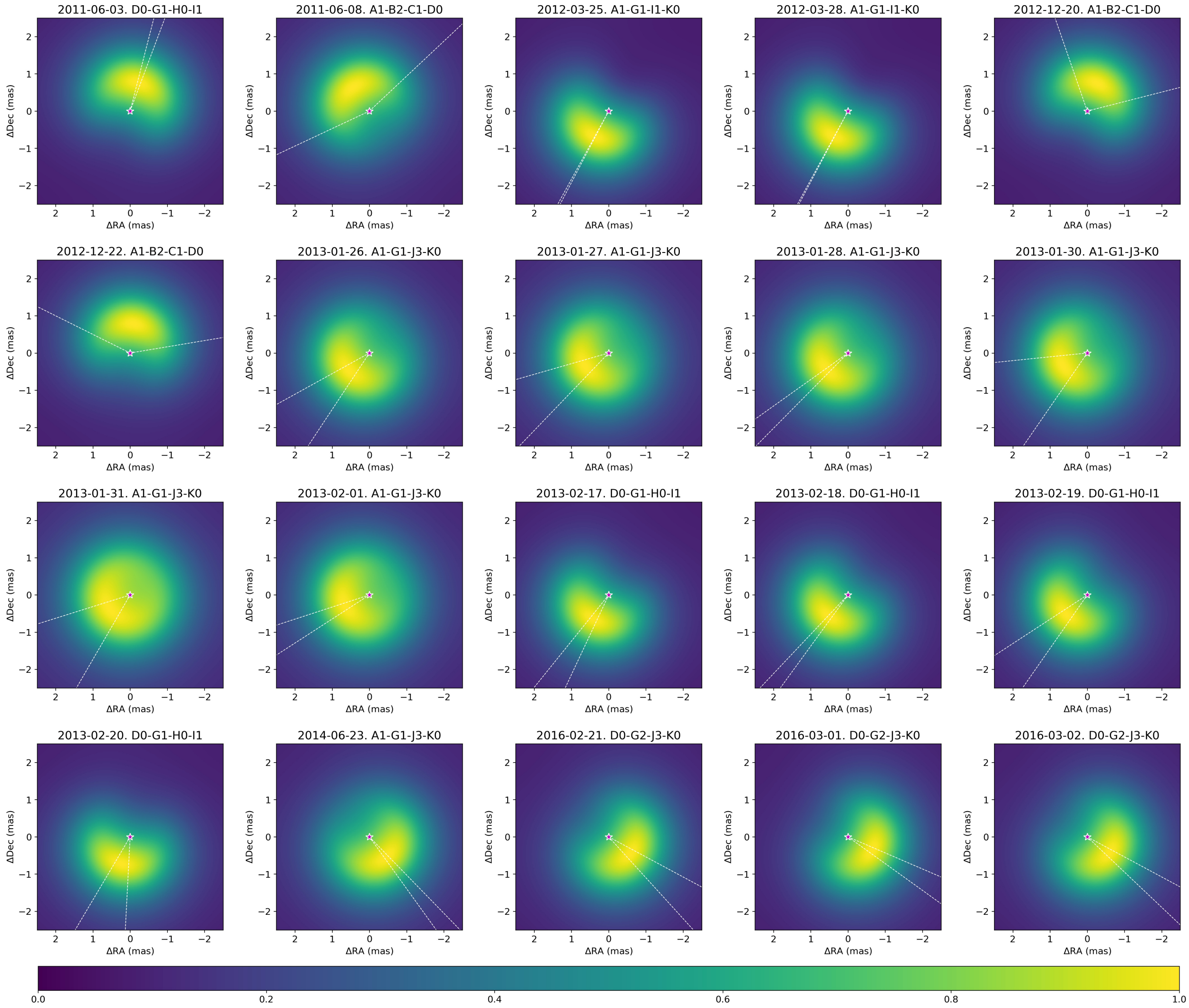

2011-06-03. D0-G1-H0-I1
2011-06-08. A1-B2-C1-D0
2012-03-25. A1-G1-I1-K0
2012-03-28. A1-G1-I1-K0
2012-12-20. A1-B2-C1-D0
2012-12-22. A1-B2-C1-D0
2013-01-26. A1-G1-J3-K0
2013-01-27. A1-G1-J3-K0
2013-01-28. A1-G1-J3-K0
2013-01-30. A1-G1-J3-K0
2013-01-31. A1-G1-J3-K0
2013-02-01. A1-G1-J3-K0
2013-02-17. D0-G1-H0-I1
2013-02-18. D0-G1-H0-I1
2013-02-19. D0-G1-H0-I1
2013-02-20. D0-G1-H0-I1
2014-06-23. A1-G1-J3-K0
2016-02-21. D0-G2-J3-K0
2016-03-01. D0-G2-J3-K0
2016-03-02. D0-G2-J3-K0

Fig. 3. Peak-normalized PIONIER continuum model images. The dashed white lines represent the ±3σ MCMC uncertainties on the position angle of the azimuthal modulation. A description of the model is given in Section 3.1, Section 4, and Table 4. The central object has been removed to enhance the circumstellar emission.

acteristic size of the gas-emitting region at the peak wavelength of 2.1662 μm using a simple Gaussian disk model, as well as a ring model with 20% radial thickness for comparison. We obtain a Gaussian HWHM radius of 0.47 mas with a temporal standard deviation of 0.04 mas. Similarly, we obtain for the thick ring a radius of 0.5±0.05 mas. In both cases, the gas-emitting component model is found to be consistent with a face-on orientation as we find an inclination of 5°±5°. These values translate into a physical radius of ~0.3 au at a distance of 651 pc, in agreement with the results of Caratti o Garatti et al. (2015).

As the estimation of the characteristic size of the hot gas region has been studied in previous works, we focus on the determination of the location of the compact hot gas component relatively to the star, and further explore whether there is a correlation between the location of the gas and of the dust feature observed in the continuum. This can be investigated through the analysis of the interferometric differential phase, which provides precise information on the spatial location of the photocenter of the gas emission component on angular scales that surpass the nominal resolution of the interferometer.

The detection of a differential phase signal as reported in Fig. A.3 indicates that the photocenter positions of the continuum and gas emission components are not coincident. From the continuum-corrected (or pure-line) differential phases (Eq. 6), we calculated the deprojected photocenter shifts in the R.A./DEC space of the hot gas component with respect to the continuum photocenter for few spectral channels around the 0 km/s velocity (Eq. 7). The location of the continuum photocenter may differ from the position of the central star if the dust emission is non-centrosymmetric. This is indeed the case for HD 98922 since our modelling of the continuum in Sect. 4.2 shows a strongly asymmetric time-variable brightness distribution of the inner circumstellar disk. Therefore, the location of the continuum photocenter is the parameter that affects the most the position of the Brγ-line photocenter with

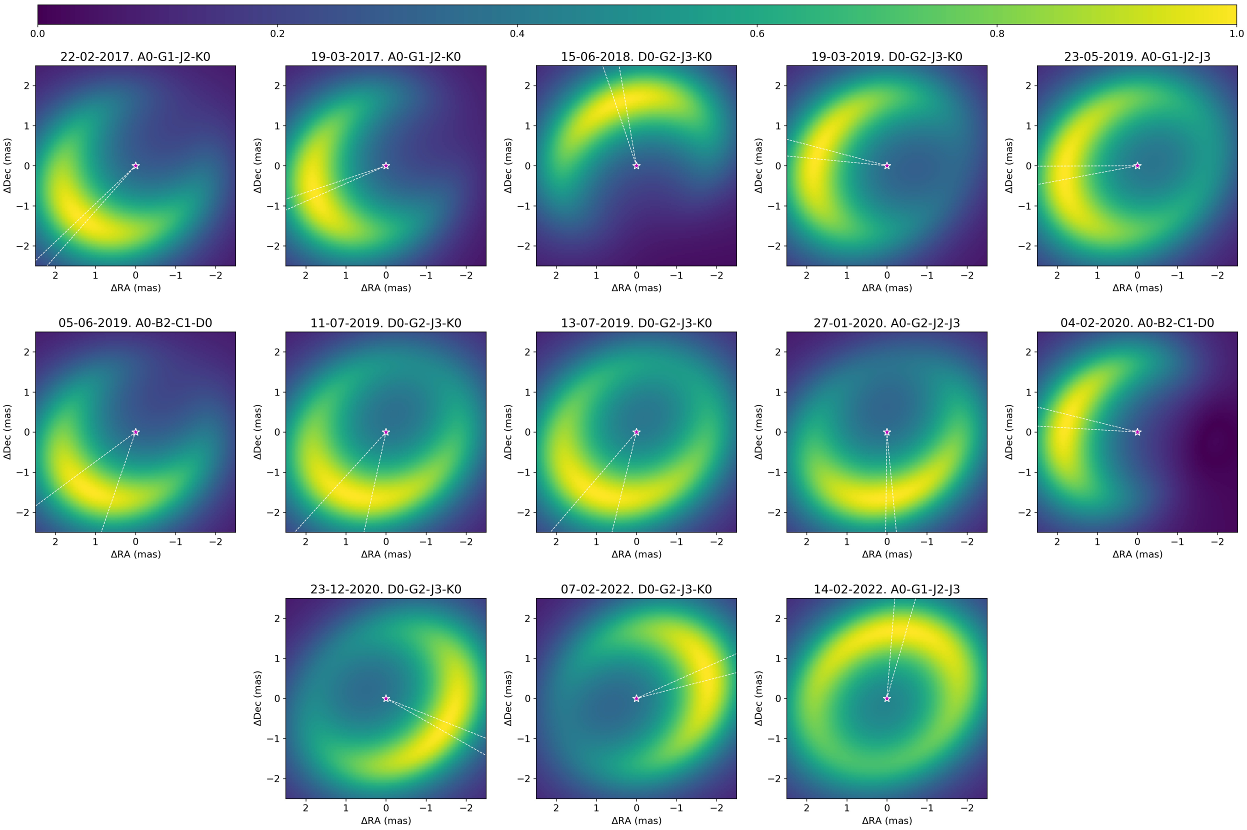

22-02-2017. A0-G1-J2-K0

19-03-2017. A0-G1-J2-K0

15-06-2018. D0-G2-J3-K0

19-03-2019. D0-G2-J3-K0

23-05-2019. A0-G1-J2-J3

05-06-2019. A0-B2-C1-D0

11-07-2019. D0-G2-J3-K0

13-07-2019. D0-G2-J3-K0

27-01-2020. A0-G2-J2-J3

04-02-2020. A0-B2-C1-D0

23-12-2020. D0-G2-J3-K0

07-02-2022. D0-G2-J3-K0

14-02-2022. A0-G1-J2-J3

Fig. 4. Same as Fig. 3 but for the GRAVITY data set.

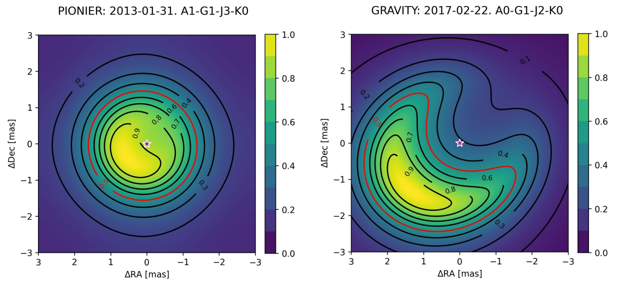

PIONIER: 2013-01-31. A1-G1-J3-K0

GRAVITY: 2017-02-22. A0-G1-J2-K0

Fig. 5. Example of contours for differental fractional peak values of the disk azimuthal modulation for two epochs of PIONIER and GRAVITY. The red line corresponds to the 50% contour.

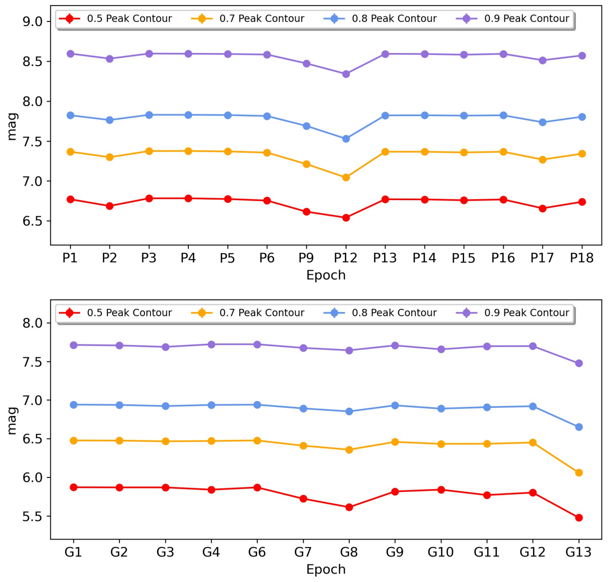

Fig. 6. Azimuthal modulation apparent magnitude time variability. Top plot refer to the H-band component, bottom plot to the K-band one. The different colors refer to different peak's value contour.

respect to the central star. Fig. 7 shows the spatial location of the gas emission photocenter with respect to the continuum photocenter, and therefore with respect to the central star. For most of the epochs, the bulk of the Brγ emission appears offset – considering the retrieved characteristic size of the gas emission component – with respect to the stellar position by up to 0.5 mas. We also observe that the location of the compact gaseous component varies with time and that it is, on first order, consistently found in an area between the central star and the peak of the dusty feature, following its orbital motion. Except for the epoch of May, 23$^{\mathrm{rd}}$, 2019 for which the continuum model closure phases did not fit our data very well (see Fig. A.2), the modeling of the continuum data delivers reliable estimates of the location of the continuum photocenter, especially since the flux contribution ratio, the dust ring size, and the azimuthal modulation parameters are well constrained.

5. Discussion

5.1. Revolution motion of the crescent-like feature

The revealed azimuthal asymmetry in the inner disk of HD 98922 shows orbital motion around the central star. Assuming this is the same asymmetric feature that is monitored with the VLTI over the 11-year period in both the H and K band, we attempt to investigate the orbital properties of the emission feature. We show in Fig. 8 the distribution of the time-variable position angle of the emission feature, after removal of the small-configuration epochs P2, P5, P6, G6 and G10 due to the rather large error bars on the PA that do not constrain properly the azimuthal position of the feature. Time zero corresponds to the first PIONIER observation of June 2011. The gray line is a cosine function corresponding to a uniform circular motion, fitted to the data in order to derive a period estimate, which suggests an orbital period of about 12 months. For the best cosine fit reported here, the χ_r^2 value is large (111±51), which can be explained by the group of points at ~60 months that clearly deviate from the best fit. When arbitrarily discarding these points, the fit is improved with a χ_r^2 value of 38±17 while the estimated period does not vary significantly (see Table 5).

The Kepler's law estimate of the central mass in the same table is reported considering a separation of the azimuthal asymmetry ranging from 0.6 to 1.3 au based on the fitted ring annular radius a$_r$, as well as for a range from 1.2 to 1.7 au based on the half-light radius a, where $a = (a_r^2 + a_k^2)^{1/2}$ following to Lazareff et al. (2017). The orbital period derived from our measurements of the azimuthal position of the asymmetric feature would imply a significantly underestimated central of ~1–3 M$_\odot$ – depending on the fearure separation – when compared to the literature value of ~6 M$_\odot$. A crude estimate of the period of the feature in a Keplerian orbit around a 6 M$_\odot$ would be about 9 months, hence shorter than what suggested by our measurement. Interestingly, our cosine fit also shows a local minimum for a period around 270 days (~9 months) but with a worse χ_r^2 value of 350 ± 193. The time intervals between consecutive observations range from 10 to 20 months for the PIONIER data set, and from 5 to 15 months for the GRAVITY one. As one can see from Fig. 8, the coverage of the orbital motion is relatively sparse and a finer temporal sampling would allow to estimate the period with greater confidence. Finally, it should be noted that we have implemented here the simplest case of a circular orbit. Therefore, accounting for some degree of eccentricity of the feature's orbit may impact the derived orbital period, which is not explored in this work.

Other scenarios can be invoked to explain this discrepancy. For instance, we assume here that PIONIER and GRAVITY are probing the lifetime of the same feature, which might not be the case. In the vortex scenario, hydro-dynamical simulations have suggested that the lifetime of a gaseous vertical structure can reach over a hundred rotation periods, and the former shortens when dust particles are taken into account due to their back-reaction on the gas, ultimately disrupting the vortex (Inaba & Barge 2006; Surville & Barge 2015; Barge et al. 2017). In our case, from our shortest and longest period estimates and the ~ 130 months total observation period, we are observing between ~ 10 and ~ 130 rotations. This could explain why the GRAVITY data points in Fig. 8 are better fitted than the PIONIER ones; we may be witnessing two time-unrelated features with different rotation periods.

Table 5. Dust revolution period estimates

Period [months]	χ_r^2	M$_\star$ [M$_\odot$]	Method
12.7 ± 0.1	111 ± 51	–	(1)
12.6 ± 0.1	38 ± 17	0.9±0.5	(2)
12.6 ± 0.1	38 ± 17	3.0±0.8	(3)
9.2 ± 0.4	–	6.0 ± 1.0	(4)

Notes: (1) period estimated from the fit of the time variable position angle of the azimuthal feature; (2) same as (1) but with the group of epochs at 60 months removed. The mass of the central star is derived by assuming that the feature has a separation ranging from 0.6 to 1.3 au as given by the ring radius a$_r$; (3) same as (1) but with the mass of the central star derived by assuming that the feature has a separation ranging from 1.2 to 1.7 au as given by the half-light radius a; (4) revolution period for a circular orbit that assumes the literature value for the central star mass and a separation of 1.5 au for the azimuthal feature.

5.2. Physical properties

5.2.1. Modelling

In an earlier work, Hales et al. (2014) have proposed a model for the disk of HD 98922 accounting for a distance of 507 pc and exploiting photometry data up to 160 μm. These authors proposed a disk model with an inner radius located at 1.5 au. We revise this model in the light of our new interferometric data and including the ALMA photometry point at 1.3 mm obtained from archival data (ID: 2015.1.01600.S / PI Panic).

Disk mass – Using the flux density F_ν measured at 1.3 mm for the unresolved HD 98922 source, we estimate the dust disk mass M_d following Beckwith et al. (1990). Assuming optically thin emission, we use the relation:

$$F_\nu \approx \kappa_\nu \frac{2k\overline{T}\nu^2}{c^2 d^2} M_\mathrm{d}, \tag{9}$$

where $\overline{T}$ is the dust mean temperature, κ_ν the dust absorption coefficient at 1.3 mm, d the distance. For comparison, we consider an alternative formulation of Eq. 9 assuming a geometrically flat disk for which the temperature and the surface density are parameterized by power-laws following:

$$T(r) = T_0(r/r_0)^{-q} \tag{10}$$

$$\Sigma(r) = \Sigma_0(r/r_0)^{-p}, \tag{11}$$

which after integration with respect to r gives:

$$F_\nu \approx \kappa_\nu \frac{2k\nu^2}{c^2 d^2} \frac{2-p}{2-p-q} T_0 r_0^q \frac{r_\mathrm{out}^{2-p-q} - r_\mathrm{in}^{2-p-q}}{r_\mathrm{out}^{2-p} - r_\mathrm{in}^{2-p}} M_\mathrm{d}. \tag{12}$$

The terms r_in and r_out are the inner and outer disk radius, respectively, T_0 is the disk temperature at a reference distance r_0=1 AU.

In Eq. 9, a large uncertainty is on the dust opacity value κ_ν and mean temperature. Therefore the mass value is only a crude approximation for first-order estimates. If we consider

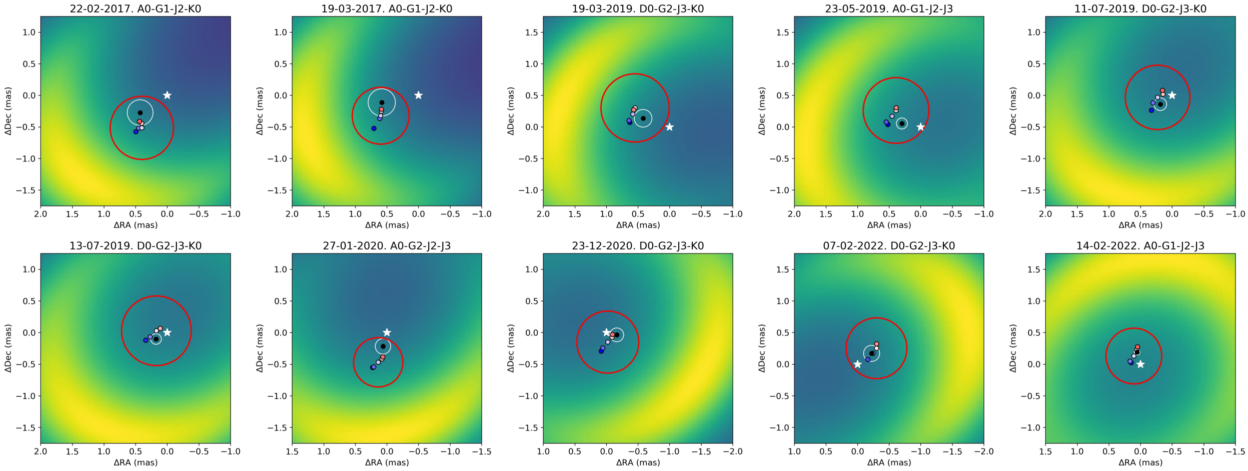

Fig. 7. GRAVITY continuum model images and Brγ-line emitting gas region. The black marker represents the continuum (star + halo + disk) photocenter. The white circle around the black marker represents the error on the continuum photocenter. The red circle represents the gas region size estimated at the peak emission. The colored markers represent the gas photoncenters. Each color refer to a spectral channel, as in Fig. A.3.

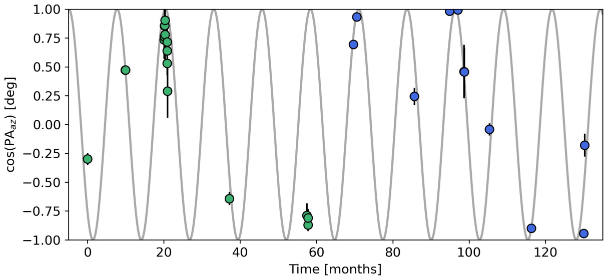

Fig. 8. Cosine of the azimuthal modulation position angles as a function of time. The markers represent the cosine of the variable dusty feature position angles depicted in Fig. 3 and 4, green for the PIONIER data and blue for the GRAVITY one. The gray line represents the best-fit (12.8 ± 0.4 months) of the uniform circular motion position angle expressed as a cosine function.

standard values of $\overline{T}$ =50 K and $\kappa_\nu(1.3\,\mathrm{mm}) = 0.02\,\mathrm{cm}^2/\mathrm{g}$ (Beckwith et al. 1990), we obtain a disk dust mass $M_d \sim 0.013\,M_\odot$ for a flux density of F_ν=10.4 mJy. However, Woitke et al. (2016) underline the strong dependence of κ_ν on the fraction of amorphous carbon and grain size distribution, and report values as high as $\kappa_\nu(1.3\,\mathrm{mm}) \sim$ 5-10 cm^2/g. The later value results consequently in a lower mass of $M_d \sim 5 \times 10^{-5}$ M$_\odot$. For a same value of κ_ν, we compare this mass estimate to the value obtained with Eq. 12. We take r_{in}=0.6 au from our PIONIER measurement and $r_{\mathrm{out}} \sim 200$ au from Garufi et al. (2022), a temperature $T_0 = 1500$ K at $r_0 = 1$ AU, and typical values $p = 1.5$ and $q = 0.75$ for a flat, group II disk. This leads to a dust mass estimate of $M_d\,0.004 M_\odot$ and $M_d\,1.3{\times}10^{-5}\,M_\odot$, for $\kappa_\nu(1.3\,\mathrm{mm})$=0.02 cm^2/g and 5 cm^2/g, respectively.

We see that the dust mass estimate is uncertain, which can be discussed in the context of the works by Hales et al. (2014) and Guzmán-Díaz et al. (2021). In the former paper, the authors report an estimated disk dust mass of $M_d = 2 \times 10^{-5}$ M$_\odot$ for a distance of 507 pc and relying on photometry up to 160 μm, which agrees with the case of a higher value for κ_ν. On the other hand, Guzmán-Díaz et al. (2021) reports a much higher total disk mass of 1.3 $M_\odot$, which compares better to our estimate using Eq. 9 and κ_ν=0.02 cm^2/g, assuming a gas-to-dust mass ratio of 100. The value reported by Guzmán-Díaz et al. (2021) is a minimum accretion-based disk mass for which the authors underline that their approach may overestimate the total disk mass (see their Fig. 2). To refine our knowledge on the disk mass and its surface density, which is relevant for the interpretation of our interferometric results, we revisit the modeling of the disk including radiative transfer simulations.

Radiative transfer in the dust – We used the radiative transfer code MCMax (Min et al. 2009) to constrain the disk density and temperature structure based on archival broadband photometry and on the spatial structure evidenced by our interferometric measurements. We started from a one-component model based on Hales et al. (2014). The inner disk radius is 1.5 au, the outer radius is 320 au, the flaring index γ=1 and the scale-height is 15 au at a radius of 100 au. We implement a grain population based on DIANA standard dust grains (Woitke et al. 2016) composed of 75% amorphous silicates (e.g., Mg$_{0.7}$Fe$_{0.3}$SiO$_3$), 25% porosity, by volume, and initially no amorphous carbon. The grain size a ranges from 1 μm to 2200 μm with a distribution $\mathrm{d}n(a) \propto a^{-3.5}$, as large grains appear to dominate in this source (Bouwman et al. 2001; van Boekel et al. 2003). The surface density profile is based on a modified version from Li & Lunine (2003) with a power-law exponent of $p_\Sigma = -1.5$, a gas-to-dust ratio of 100, and a dust disk mass of 2×10^{-5} M$_\odot$. The extinction is $A_V = 0.5$. The parameters of the central star are taken from Table 1.

With the revised stellar parameters, the stellar luminosity increases by a factor ∼3 in comparison to Hales et al. (2014) and the photospheric emission contribution results in slightly overestimating the K band near-IR flux in the spectral energy distribution by a factor ∼1.2. On the other hand, our GRAVITY and PIONIER observations show that dust is present at shorter separations. Since the SED fitting process is a degenerated problem, we attempt to better constrain the inner disk structure based on the consideration that a dust component at $\lesssim$1 au, producing ∼75%-80% near-IR excess and resolved with the VLTI has to be accounted for. Simply moving the inner radius to ∼0.6 au in the one-component model is not possible since this would lead to further overestimate the near-IR flux. We therefore revise our disk model and propose a two-component disk model in which the inner component has a lower surface density in comparison to the outer component and an inner radius at 0.6 au. We conducted a grid search for the inner disk dust mass $M_{d,in}$ and for the transition radius between the low and high surface density disk R_t to fit the SED as well as the near-IR excess (F_c+F_h) estimated by interferometry in the K band. The other disk parameters were kept identical for the inner and outer components. In parallel, we considered two approaches for the disk composition: in the first case we included a 25% fraction of carbon grains (model CS) to quench the strength of the silicate emission feature (van Boekel et al. 2003); in the second case we consider a more extreme case of an inner component only composed of quantum-heated particles (model Q) strongly coupled to the gas (e.g., Kluska et al. (2018); Gravity Collaboration et al. (2021)). Our results show that both populations of particles result in a good fit of the SED in the proposed two-component disk configuration. For the model CS, a transition radius R_t at ~ 5.5 au and an inner disk dust mass of ~ $6{\times}10^{-9}\,M_\odot$ are derived. These two best models, given in Table 6 and discussed in Sect. 5.2.2, may still contain some level of degeneracy since other parameters such as the scale height, the index of the surface density power-law, or the flaring index may influence the near-IR excess. However, we limited ourselves to the inner disk properties that can be directly constrained by the near-IR flux ratios and spatial confinement of the emission derived from our interferometric measurements.

We note that the proposed disk model, inherited from Hales et al. (2014), supports the lower-end disk mass estimate from the ALMA flux density in conjunction with a higher value of the absorption coefficient κ_ν at 1.3 mm. An increase of the total dust disk mass of the outer component in Table 6 overestimates the measured photometry in the far-infrared and sub-millimeter range.

Table 6. HD 98922 RT models. The stellar parameters are from Guzmán-Díaz et al. (2021).

Star			
Param.	Unit	Value	
$T_\star$	K	10500	
$R_\star$	$R_\odot$	11.45	
$M_\star$	$M_\odot$	7.0	
d	pc	650.9	
A_V	mag	0.5	
Disk Inner Component			
Param.	Unit	Model CS	Model Q
R_{in}	au	0.6	0.6
R_t	au	5.5	3.5
$M_{d,in}$	$M_\odot$	$6{\times}10^{-9}$	2×10^{-12}
$H_{100\,au}$	au	10.0	10.0
γ		1.0	1.0
a_{min}	μm	1.0	0.006
a_{max}	μm	2200	0.006
p_Σ		-1.5	-1.5
Carbon	%	25	0
Disk Outer Component			
Param.	Unit	Value	
R_t	au	5.5	
R_{out}	au	320	
$M_{d,out}$	$M_\odot$	$2{\times}10^{-5}$	
$H_{100\,au}$	au	10.0	
γ	-	1.0	
a_{min}	μm	1.0	
a_{max}	μm	2200	
p_Σ	-	-1.5	
Carbon	%	25	

Table 7. RT results for Model CS. The sign $^{(*)}$ indicates that the relative flux contributions of the disk and halo components are added. LDC and HDC stand for low-density and high-density component, respectively.

R_t, $M_{d,in}$	5.5 au, $6{\times}10^{-9}$ $M_\odot$				3.5 au, $3{\times}10^{-9}$ $M_\odot$			
Flux	SED		Interf.		SED		Interf.	
(%)	H	K	H	K	H	K	H	K
Star	30	16	22	23	28	14	22	23
LDC	70	75	$78^{(*)}$	$77^{(*)}$	41	44	$78^{(*)}$	$77^{(*)}$
HDC	0	9	–	–	31	42	–	–

5.2.2. Disk structure

Transition radius – For the adopted two-component disk model for HD 98922, the low- to high-density transition radius R_t is found to be located at ~5.5 au, with a lower-limit at 2.5 au below which the near-IR excess is systematically overestimated in the spectral energy distribution. Despite the degeneracy between R_t and $M_{d,in}$ for the determination of the near-IR excess flux from the fit of the SED, our interferometric measurements can set constrains on the inner radius, relative flux contribution, and compact spatial extent of the low-density component that dominates the near-infrared excess. Table 7 illustrates this point by comparing the relative flux contributions of the low- and high-density components inferred from radiative transfer to the estimates from the interferometric measurements, and this for two values of R_t giving both a good fit of the SED. For smaller values of R_t, the near-IR flux contribution of the outer high-density component increases, while the one of the inner low-density component decreases. Qualitatively, this would translate for our geometrical models into wider rings, or into a higher contribution of the halo component that we only find to be less than 10% in both bands. For instance, in the case R_t=3.5 au, the innermost low-density component probed by GRAVITY and PIONIER contributes only up to ~40%. It should be however noted that the proposed argument suffers from some degree of uncertainty: since the modeling of our interferometric observables relies on single-ring geometrical models rather than on radiative transfer images, the accuracy on the determination of R_t remains limited. As the detailed interferometric modeling of radiative transfer images goes beyond the scope of this paper, we limit ourselves to propose that the structured disk of HD 98922 shows a dust density transition located not closer than ~4-6 au from the central star. Estimating an upper value for R_t is not feasible using only the presented data since the near-IR excess (set on the first order by R_t, $M_{d,in}$ and $M_{d,out}$) is a degenerated quantity for excessively large values of R_t.

Surface density profile – The surface density profile we have implemented has a sharp break discontinuity at R_t, which does not correspond to a realistic case since a continuous transition profile would be more physically meaningful. Such sharp transitions are nonetheless proposed to differentiate between volatile-rich and volatile-free regions, as for instance in the case of the water snow line (Hayashi 1981; Lecar et al. 2006). More recent works have reported structured inner disks with regions of differentiated surface density (Tatulli et al. 2011; Matter et al.

2016). We derive a low- to high-density transition of two orders of magnitude at about 5 au (Fig. 9), with a dust surface density $\Sigma_d \sim 0.001$ g cm^{-2} in the low density region. We emphasize that we cannot exclude that a gap is present in the disk of HD 98922 beyond ~5 au, but mid-infrared interferometric data are necessary to explore this hypothesis. However, we also note that HD 98922 is classified as a group II source in the classification of Meeus et al. (2001) and based on the N-to-K size ratio (Gravity Collaboration et al. 2019), suggesting a preferentially flat, gap-free disk.

Location and temperature of the dust – The dust emission in the H and K bands are expected to originate from about the same region, close to the disk inner rim. In our case, the bulk of the emission is located at different radii for the two bands. We find the K band characteristic size is larger than the H band one by a factor ~1.4 to 2 when considering either the ring annular radius a_r or the half-light radius a parameters. This trend is seen in previous works when comparing the results of Lazareff et al. (2017) and Gravity Collaboration et al. (2019): out of 21 common sources, 17 show a larger K band size by a factor ranging from 1.1 to ~3. At first, the difference in resolution between GRAVITY (1.75 mas) and PIONIER (1.22 mas) by a factor 1.4 could explain that PIONIER resolves a more compact emission, similarly to what observed for HD 163296 (GRAVITY Collaboration et al. 2021). A more physical, albeit simplistic, argument can be formulated based on the Wien's temperature of the dust in a temperature-gradient disk (i.e., $T(r) = T_0\,(r/r_0)^{-q}$) emitting as a blackbody. For a typical value of $q = 0.75$ for a flat group II disk, we derive a size ratio $r_K/r_H \sim (1350/1750)^{1/0.75}$, or 1.41, in agreement with our findings.

One challenge posed by our results is the presence of H band emitting dust as close as ~0.6 au to the star. In the scenario of a passively irradiated disk with an optically thin inner cavity (Muzerolle et al. 2004; Monnier et al. 2005), the dust temperature at this location, assuming blackbody grain emitters (ϵ=1), is $T_g \sim 2200$ K, above the sublimation temperature of standard silicates. This is also seen in Fig. 9 for the temperature structure of our carbon-rich disk model. The problem of very hot dust grain inside the theoretical sublimation radius has been observed in other sources such as Z CMa, V1685 Cyg, MWC 297, and HD 190073 (Monnier et al. 2005; Hone et al. 2017; Setterholm et al. 2018), invoking the presence of refractory dust (e.g., Corundum or Iron), which sublimation temperature critically depends on the disk density (Kama et al. 2009). Alternatively, the possibility that a small fraction of highly refractory graphite grains with high sublimation temperature (T_s>2000 K) contributes to the near-infrared excess very close to the star has been proposed for HD 163296 (Benisty et al. 2010), and might apply in the case of HD 98922 as well. Clearly, further radiative transfer modeling is required to tackle this question by considering other values of $a_{\min}$, p_Σ and grain composition. We note that adding amorphous carbon to our initial pure-silicate model was essential to decrease the dust temperature at 0.6 au from T >3000 K to $T \sim 2300$ K. Alternatively, for Herbig stars with similar or larger masses than HD 98922, the undersized inner disk is explained by the presence of optically thick gas in the inner cavity, which is found to be favored in systems with accretion rates $M_{\rm acc} \gtrsim 10^{-8}\,M_\odot\,{\rm yr}^{-1}$ (Muzerolle et al. 2004).

Another possible explanation for the detection of excess emission very close to the star is the presence in the inner region of a fraction of quantum heated particles (QHPs), which can be stochastically heated by the strong UV radiation field from the central star, hence reaching temperatures higher than the equilibrium temperature and producing near-IR continuum emission. This scenario has been advanced for the sources HD 100453, HD 179218, and HD 141569 (Klarmann et al. 2017; Kluska et al. 2018; Gravity Collaboration et al. 2021). PAHs, as an example of QHPs, are detected in HD 98922 (Geers et al. 2007; Acke et al. 2010). Interestingly, the 6.2-to-11.3 μm feature ratio is estimated from Seok & Li (2017)[4] to be $I_{6.2}/I_{11.3} \sim 3$–4, with ratios larger than unity pointing at predominantly unshielded ionized PAH species in the disk inner regions that are directly exposed to the intense UV radiation field of the star (Maaskant et al. 2014). We tested a PAH-based inner component radiative transfer model (Model Q, Table 6), which allows a good fit of the SED with a very small mass of QHP grains (2×10^{-12} $M_\odot$) and a transition radius of 3.5 au. This value of R_t is estimated as the balance between the increasing contribution of the outer high-density component (HDC) to the near-IR SED (for R_t<3.5 au) and the increasing contribution of the inner low-density component (LDC) to the SED at $\lambda \sim 1.5\,\mu$m (for R_t>3.5 au and due to the blue spectral index of the QHP emission). In the case of Model Q, the flux fractional contribution of the LDC is estimated to be about ~ 5% in the K band and 10% in the H band.

Ultimately a mixture of refractory grains and QHPs could explain the presence of continuum emission as close as 0.6 au and detected in the H band. The presence of predominantly ionized PAH species close to the star is therefore not to be discarded.

5.3. The origin of the time-variable inner disk asymmetry

Our analysis suggests a crescent-like asymmetric dust feature in the inner au-region HD 98922 and for which orbital motion is detected. We explore here few hypothesis of dynamical evolution of the disk.

Azimuthal asymmetries in the disk brightness distribution can be explained by inclination projection effects like in the case of FS CMa (Hofmann et al. 2022; Kluska et al. 2020), which are then found to be orthogonal to the position angle of the semi-major axis of the inclined disk. It is based on this argument that Varga et al. (2021) discarded the hypothesis of a projection effect to explain the brightness asymmetry in HD 163296, later identified as a variable feature by GRAVITY Collaboration et al. (2021). Recently, Gravity Collaboration et al. (2019) suggested that projection effects due to inclination of up to 45° induce closure phase signals not larger than 25°. In the case of HD 98922, our continuum model and previous works (Hales et al. 2014; Lazareff et al. 2017; Gravity Collaboration et al. 2019; Kluska et al. 2020) suggest a moderately inclined disk with an inclination not significantly larger than ~ 30°. At the same time, GRAVITY detects closure phase signals as high as 40°, which with the detection of the time-variable azimuthal asymmetry, does not favor inclination effects of the system.

Another cause of the asymmetry could be the presence of a stellar companion. HD 98922 was suggested to be a spectro-astrometric binary system with a companion located at 0.5 mas (Baines et al. 2006). The binarity is not supported though by the latest Gaia measurements (Gaia Collaboration et al. 2021), which report a RUWE parameter of 0.94, meaning that a single-

---

[4] The ratio is uncertain due to incomplete wavelength coverage

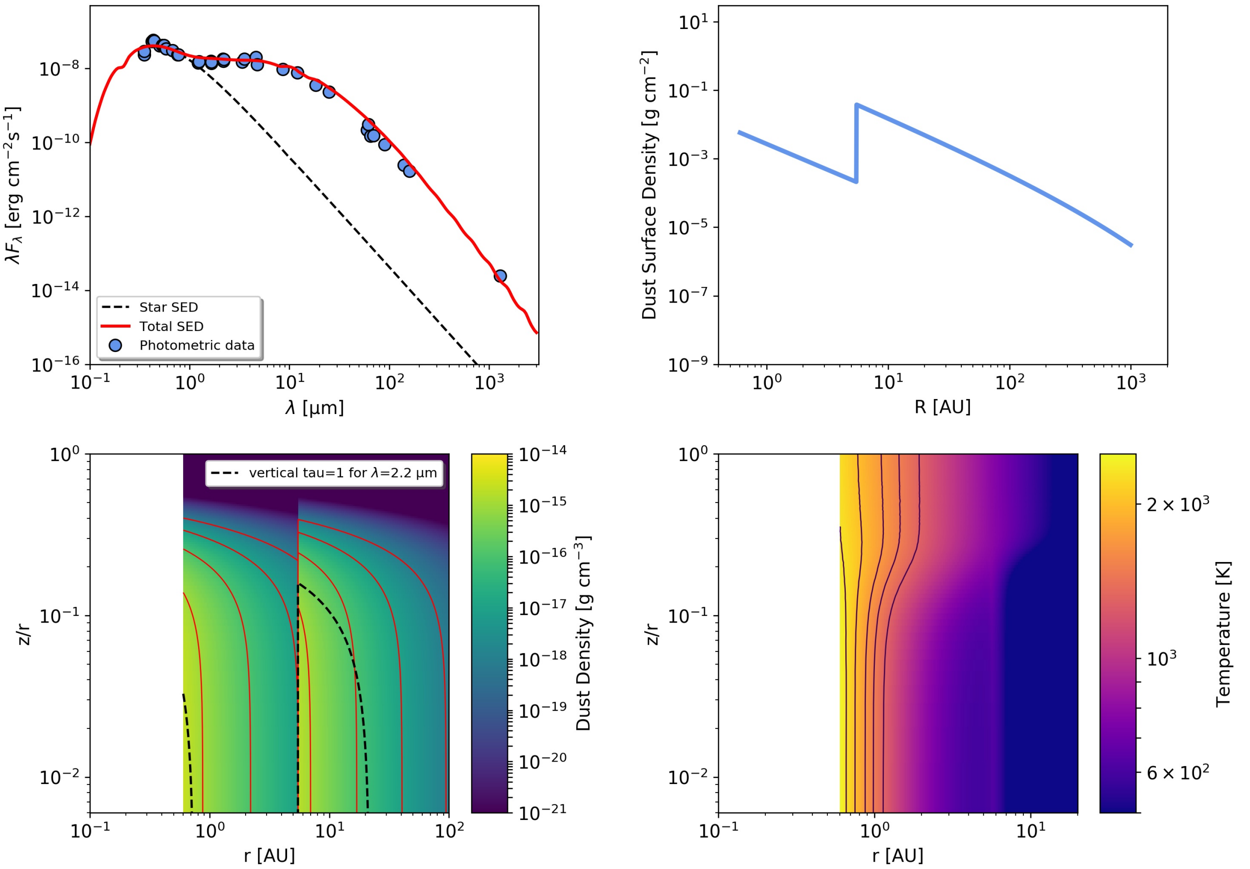

Fig. 9. RT CS model presented in Table 6. The top left panel shows the SED, where the black-dashed line represent the star black-body function, the red one the total (star+disk) SED model, and the blue markers represent the photometric data. The top right panel shows the dust surface density as a function of the distance from the star. The bottom left plot shows the dust density structure, where the black dashed line represent the vertical $\tau = 1$ surface at 2.2 μm, and the red lines represent, from left to right and for both components, the density contours at 10^{-15}, 10^{-16}, 10^{-17}, and 10^{-18} g cm^{-3}, respectively. The bottom right plot shows the dust temperature structure, where the black lines represent, from left to right, temperature contours at 2300, 2000, 1700, 1500, and 1300 K, respectively. In these last two plots the y-axis shows the height divided by the distance from the star.

star model provides a good fit to the astrometric observations. According to Gaia EDR3, HD 98922 B located at 300 pc is a foreground object and therefore not related to ours. To test stellar companion scenario through our data, we fitted each epoch of the PIONIER and GRAVITY data set independently with a simple binary plus halo model, however the model fits badly both the visibility and the closure phase signals. Therefore, we tested a more complex model that accounts for two unresolved point sources representing the primary star and the companion, a halo, and a centrosymmetric ring. The fitting procedure is a global fit, with all the free parameters constrained to be constant through the epochs except for the location of the companion. The model fits nicely the GRAVITY data set ($\chi^2_r = 4.66 \pm 0.27$) but poorly the PIONIER one ($\chi^2_r = 15.38 \pm 0.69$). Moreover, the models suggest that the companion changes drastically its location with respect to the star through the epochs from a minimum of 0.001 mas to a maximum of 1.4 mas, which would require a highly eccentric orbit. Finally, the flux contribution of the companion ($\approx 5-7\%$) suggested by the models translates in a apparent magnitude of $m_H \approx 8.1$ mag in the H-band, and $m_K \approx 7.5$ mag in the K-band. This values are not consistent with the lowest possible magnitude for a substellar object ($m_H = 18.15$ mag, $m_K = 17.63$ mag) when accounting for a mass of 10 M$_J$, an age of 1 Myr, an effective temperature of 2315.5 K, and a radius of 2.44 R$_J$ (Fortney et al. 2008). Based on this analysis, our data sets do not favour the companion scenario.

Hydrodynamic instabilities could also lead to time-variable asymmetry in disks (e.g., Meheut et al. 2010; Flock et al. 2017). Vortexes originating from pressure bumps through Rossby wave instability (e.g., Li et al. 2001) is one of those. Such a scenario was suggested by Varga et al. (2021), combined with grain collisions in the vortex region so that the creation of small grains increases its surface brightness, in order to explain the disk asymmetry in HD 163296. A hydrodynamical simulation that accounts for both the gas and the dust component could help in testing the validity of this scenario but it is out of the scope of this paper.

Finally, gravitational instabilities that lead to the fragmentation of the disk into one or more gravitationally bound objects, are another possible mechanism originating the features seen in protoplanetary disks (e.g., Lodato & Rice 2004; Pohl et al. 2015). The onset of these instabilities requires disk regions with appropriate physical properties for which the gravitational potential energy overcomes the pressure and rotational kinetic support. This can be achieved easily the more the disk is compact and massive. We note from our RT analysis of HD 98922 that in the region of our interest, that corresponds to the inner component, the dust surface density is of the order of $\Sigma_D \lesssim 0.1\,\mathrm{g\,cm^{-2}}$, i.e. $\lesssim 10\,\mathrm{g\,cm^{-2}}$ for the total disk surface density. From this value we can assess analytically if the requirements for gravitational instabilities are met through the Toomre criterion, for which a disk is unstable if the Toomre parameter (Toomre 1964) is of order unity:

$$Q_T = \frac{H_p M_\star}{\pi r^3 G \Sigma_g} \lesssim 1, \tag{13}$$

where H_p is the pressure scale-height at a given radius r, $M_\star$ the mass of the star, Σ_g the gas surface density at r, and G the gravitational constant. Our $\Sigma_G \approx 10\,\mathrm{g\,cm^{-2}}$ value translates in a Toomre parameter of $Q_T \gtrsim 40000$ at $r = 0.6$ au. The latter is well above unity, needed for gravitational instabilities to be significant, going in contrast with the disk fragmentation scenario.

5.4. The Brγ-line emitting gas region

As mentioned in the Introduction, the origin of the Brγ-line emitting gas region is unclear with previous works suggesting various scenarios like the stellar wind, X-wind, magnetospheric accretion one (Kraus et al. 2008), the latter favoured by the authors, or the disk-wind one (Caratti o Garatti et al. 2015).

The magnetospheric accretion scenario is related to the measured magnetic field of HD 98922. Hubrig et al. (2013) report for the mean longitudinal magnetic field $\langle B_z \rangle$ a value of -131 ± 34 G, but they do not show data and do not calculate the false alarm probability (FAP). Järvinen et al. (2019) republished these data reporting a value of -33 ± 4 G (FAP $< 10^{-5}$), and gives a new measurement $\langle B_z \rangle = 28 \pm 7$ G (FAP $< 10^{-6}$). Other authors have instead reported a non-detection (Wade et al. 2007; Alecian et al. 2013). Interestingly, Mendigutía (2020), following Johns-Krull et al. (1999), calculated a 49 G lower limit (with no error bar) for the magnetic field required to drive magnetospheric accretion in HD 98922, accounting for an accretion rate of $2.75 \times 10^{-6}\,\mathrm{M_\odot\,yr^{-1}}$. Comparing this estimate with the measurements listed above, only the value reported by Hubrig et al. (2013) would be consistent for magnetospheric accretion. Taking in consideration that most of the measurements are lower than 49 G, and that the work of Järvinen et al. (2019) goes in contrast with the results of Hubrig et al. (2013), we disfavour the magnetospheric accretion scenario as the main cause of HD 98922 Brγ-line emission. The disfavorment is also backed-up by the fact that the Brγ-line emitting region is spatially extended while the system co-rotation radius (Shu et al. 1994; Muzerolle et al. 2004) is $\approx 2.6\,\mathrm{R_\star}$ or ≈ 0.14 au, much more compact than the location of Brγ-line gas, meaning that emission from a more extended region is required to interpret the observations. Finally, the system does not show any inverse P Cygni profile nor variability on the red side of the Na I D and Balmer lines (Aarnio et al. 2017), which are expected if magnetospheric accretion is taking place (Aarnio et al. 2017), despite the authors fully sampled the stellar rotation period.

Strong variability is instead seen in the blue-shifted absorption components of the above mentioned lines, with few days time-scale (Aarnio et al. 2017), that probe regions between the co-rotation radius and fractions of an au. The blue-shifted absorption components are easily reproduced via a disk wind extending from 0.17 au to 0.42 − 0.85 au and a wind mass loss rate of $10^{-7}\,\mathrm{M_\odot\,yr^{-1}}$ (Aarnio et al. 2017). A disk wind model, coupled with an asymmetric continuum disk, was also able to explain HD 98922 AMBER/VLTI high spectral resolution Brγ-line interferometric data (one epoch 28 February 2013). In this case, the wind extends from ≈ 0.1 au to ≈ 1 au, with a wind mass loss rate of $2 \times 10^{-7}\,\mathrm{M_\odot\,yr^{-1}}$. To inquiry the validity of the disk-wind model with respect to the new results presented in this paper, one should check if the time-variable pure-line photocenters shifts shown in Fig. 4 can be reproduced by such model, accounting for a time-variable asymmetric continuum disk and a time-variable disk wind. The former is left for a future work.

It is interesting to note that not only the location of the Brγ-line gas changes through the epochs, but also the intensity of its emission. From the equivalent widths (EWs) and the 2MASS K-band magnitude of the object, we derived the line luminosity for each epoch beside the first two, where the line EW is strongly affected by the continuum normalization process and therefore not reliable, as follows. We derived firstly the flux of the line, $\mathrm{F_{Br\gamma}}$, by multiplying the $\mathrm{EW_{Br\gamma}}$ with the continuum flux at the center of the line, given by:

$$\mathrm{F_{cont}} = \mathrm{F_{0,K}} 10^{-0.4(\mathrm{m_K} - 0.1\mathrm{A_V})}, \tag{14}$$

where $\mathrm{F_{0,K}}$ is the flux in the K-band of a $\mathrm{m_K} = 0$ star (4.28×10^{-11} erg/s/cm^2/Å, Rodrigo & Solano 2020). The fluxes were then converted into the line luminosity, $\mathrm{L_{Br\gamma}}$, using the distance of our object. Finally, following Fairlamb et al. (2017), we derived the accretion luminosities:

$$\log_{10}\left(\frac{\mathrm{L_{acc}}}{\mathrm{L_\odot}}\right) = (1.30 \pm 0.09) \log_{10}\left(\frac{\mathrm{L_{Br\gamma}}}{\mathrm{L_\odot}}\right) + (4.46 \pm 0.23). \tag{15}$$

From Table 8 we see that in the 4 months period going from March 2019 (G4) to July 2019 (G8) the Brγ-line luminosity is relatively constant at $\approx 1.87 \times 10^{-2}\,\mathrm{L_\odot}$, but after 6 months (G9) the luminosity increases by 15 % and doesn't significantly vary for 11 months (G11), after which it increases again in 14 months by 8 % (G12), and by 8 % in the following week (G13), for a total increase of 30 %. In the scenario of a planet embedded in the circumstellar disk, emission lines and luminosity variability of these lines are expected, due to the revolution motion of the planet that affects the accretion rate onto the circumplanetary disk (Szulágyi & Ercolano 2020). Using the empirical relation from Szulágyi & Ercolano (2020) that correlates the Brγ-line luminosity to the mass of the accreting planet:

$$\log_{10}(\mathrm{L_{Br\gamma}}) = (2.29 \pm 0.55) \cdot \mathrm{M_{planet}} - 25.16, \tag{16}$$

we derive a mass of $\mathrm{M_{planet}} = 10.3 \pm 2.5\,\mathrm{M}_J$, where the error bar is mainly due to the error on the first coefficient. The Brγ-line luminosity that stems from the accreted material into the planet can be estimated with the empirical relation from Szulágyi & Ercolano (2020):

$$\log_{10}(\mathrm{L_{Br\gamma}}) = (17.59 \pm 6.08) \cdot \log_{10}(\mathrm{L_{acc}}) + 38.37, \tag{17}$$

from which we derive $\mathrm{L_{acc}} = 1.22 \pm 0.72 \times 10^2\,\mathrm{L_\odot}$, where the error bar is again mainly due to the error on the first coefficient. These values should be considered loose estimates, since the simulation done by Szulágyi & Ercolano (2020) accounts for a model with a central star of $1\,\mathrm{M_\odot}$ ($5\,\mathrm{M_\odot}$ in our case), a circumstellar disk ranging between 2 and 12.4 au (0.6 – 320 au in our case), and a planet placed at 5.2 au. Nonetheless, an embedded $\sim 10\,\mathrm{M}_J$ companion could play a role in the origin of the Brγ-line luminosity, its variability, and the changing position of the gas location as measured by GRAVITY, but further modeling is needed.

Table 8. Brγ-line properties

Epoch	$\mathrm{EW}_{\mathrm{Br}\gamma}$ [Å]	$\mathrm{L}_{\mathrm{Br}\gamma}$ [$10^{-2}\,\mathrm{L}_\odot$]	$\mathrm{L}_{\mathrm{acc}}$ [$10^{2}\,\mathrm{L}_\odot$]
G4	-1.69 ± 0.06	1.95 ± 0.09	1.72 ± 0.38
G5	-1.56 ± 0.15	1.80 ± 0.18	1.55 ± 0.43
G6	-1.63 ± 0.13	1.88 ± 0.16	1.64 ± 0.43
G7	-1.59 ± 0.24	1.83 ± 0.28	1.59 ± 0.55
G8	-1.59 ± 0.07	1.83 ± 0.09	1.59 ± 0.35
G9	-1.93 ± 0.11	2.22 ± 0.14	2.04 ± 0.51
G10	-1.96 ± 0.15	2.26 ± 0.18	2.09 ± 0.57
G11	-1.97 ± 0.14	2.27 ± 0.17	2.10 ± 0.56
G12	-2.14 ± 0.10	2.47 ± 0.13	2.34 ± 0.58
G13	-2.32 ± 0.10	2.67 ± 0.13	2.60 ± 0.66

6. Summary

We have presented new GRAVITY/VLTI observations of HD 98922 which, coupled with PIONIER/VLTI archive data, form a 11 year observational period data set of the system, accounting for a total of 33 different epochs between 2011 and 2022. The data set allowed a unique interferometric study to test the potential time-variability of the innermost circumstellar environment morphology. Here we summarize the main conclusions of our work:

- The system was resolved by both instruments in all epochs with squared visibilities that do not vary significantly through the epochs when comparing observations taken with similar *(u-v)* coverage. This suggests no significant variation in time of the star-disk flux contribution ratio.
- Significant change in time is observed in the non-null closure phase signals even for observations taken with similar *(u-v)* coverage, suggesting asymmetric time-dependent variations in both the H- and K-band continuum components.
- Geometrical modeling of the interferometric data suggests indeed an crescent-like asymmetric dust feature in the circumstellar environment of HD 98922, extending between $\sim$ 0.5 and $\sim$ 2 au dominating the near-IR flux emission ($\approx 70\%$).
- The dusty feature peak emission, constant in time in its magnitude, changes its location through the epochs with respect to the star in a seemingly revolution motion. The revolution period is not well constrained due to the low cadence of the observations. A first loose estimate is of the order of 1 year.
- MCMax SED RT modeling suggests that this innermost dusty component could be made of carbon-rich (25 %) silicates grains. The total surface density at $\sim$ 1 au is $\lesssim 10\,\mathrm{g\,cm}^{-2}$, translating in a Toomre parameter much higher than unity. Therefore, the model does not favour a gravitational instability scenario as the origin of the time-variable dusty feature.
- The GRAVITY SC data show a single-peaked Brγ-line with an increasing EW in time. The derived Brγ-line luminosity increases for a total of 30 % in 3 years.
- The Brγ-line emitting gas varies significantly in its location through the epochs with respect to the star position. For most of the epochs the gas is located in a region between the dusty feature and the star and it follows at first order the revolution motion of the feature.
- While a magnetospheric accretion scenario is not favoured, a time-variable disk wind or an embedded $\sim 10\,\mathrm{M}_J$ companion could explain the Brγ-line luminosity, its variability, and the changing position of the gas location as measured by GRAVITY, but further modeling is needed.

The study strongly support a time-variable morphology in the innermost circumstellar environment of HD 98922. Especially surprising is the Brγ-line gas emission variability, linked to the dusty feature one. These results prove the need in high cadence observations of YSOs to understand the phenomena occurring in these systems, their origin and their evolution.

Acknowledgements

V.G. was supported for this research through a stipend from the International Max Planck Research School (IMPRS) for Astronomy and Astrophysics at the Universities of Bonn and Cologne, and from the Bonn-Cologne Graduate School of Physics and Astronomy (BCGS). This work is based on observations made with ESO Telescopes at the La Silla Paranal Observatory under program IDs listed in Table A.1 and Table A.2. This work has made use of data from the European Space Agency (ESA) mission *Gaia* (`https://www.cosmos.esa.int/gaia`), processed by the *Gaia* Data Processing and Analysis Consortium (DPAC, `https://www.cosmos.esa.int/web/gaia/dpac/consortium`). Funding for the DPAC has been provided by national institutions, in particular the institutions in the *Gaia* Multilateral Agreement. We acknowledge the Gemini Observatory for the use of the IR spectrum model of the atmospheric transmission above Cerro Pachon. This research has made use of the model atmosphere grid NeMo, provided by the Department of Astronomy of the University of Vienna, Austria (`http://www.univie.ac.at/nemo/`). NeMo was funded by the Austrian Science Fonds. This research has made use of the Jean-Marie Mariotti Center `Aspro`. This research has made use of the Spanish Virtual Observatory (`https://svo.cab.inta-csic.es`) project funded by MCIN/AEI/10.13039/501100011033/ through grant PID2020-112949GB-I00. This paper makes use of the following ALMA data: ADS/JAO.ALMA#2015.1.01600.S. ALMA is a partnership of ESO (representing its member states), NSF (USA) and NINS (Japan), together with NRC (Canada), MOST and ASIAA (Taiwan), and KASI (Republic of Korea), in cooperation with the Republic of Chile. The Joint ALMA Observatory is operated by ESO, AUI/NRAO and NAOJ.

References

Aarnio, A. N., Monnier, J. D., Harries, T. J., et al. 2017, ApJ, 848, 18

Acke, B., Bouwman, J., Juhász, A., et al. 2010, ApJ, 718, 558

Acke, B., van den Ancker, M. E., & Dullemond, C. P. 2005, A&A, 436, 209

Alecian, E., Wade, G. A., Catala, C., et al. 2013, MNRAS, 429, 1001

Baines, D., Oudmaijer, R. D., Porter, J. M., & Pozzo, M. 2006, MNRAS, 367, 737

Barge, P., Ricci, L., Carilli, C. L., & Previn-Ratnasingam, R. 2017, A&A, 605, A122

Beckwith, S. V. W., Sargent, A. I., Chini, R. S., & Guesten, R. 1990, AJ, 99, 924

Beichman, C. A., Neugebauer, G., Habing, H. J., Clegg, P. E., & Chester, T. J. 1988, Infrared Astronomical Satellite (IRAS) Catalogs and Atlases.Volume 1: Explanatory Supplement., Vol. 1

Benisty, M., Natta, A., Isella, A., et al. 2010, A&A, 511, A74

Beuther, H., Klessen, R. S., Dullemond, C. P., & Henning, T. 2014, Protostars and Planets VI, University of Arizona Press, Tucson

Bouwman, J., Meeus, G., de Koter, A., et al. 2001, A&A, 375, 950

Caratti o Garatti, A., Tambovtseva, L. V., Garcia Lopez, R., et al. 2015, A&A, 582, A44

Cutri, R. M. & et al. 2012, VizieR Online Data Catalog, II/311

Cutri, R. M., Skrutskie, M. F., van Dyk, S., et al. 2003, VizieR Online Data Catalog, II/246

Dame, T. M., Hartmann, D., & Thaddeus, P. 2001, ApJ, 547, 792

Esa, . 1997, VizieR Online Data Catalog, I/239
Fairlamb, J. R., Oudmaijer, R. D., Mendigutía, I., Ilee, J. D., & van den Ancker, M. E. 2015, MNRAS, 453, 976
Fairlamb, J. R., Oudmaijer, R. D., Mendigutia, I., Ilee, J. D., & van den Ancker, M. E. 2017, MNRAS, 464, 4721
Fedele, D., van den Ancker, M. E., Acke, B., et al. 2008, A&A, 491, 809
Flock, M., Fromang, S., Turner, N. J., & Benisty, M. 2017, ApJ, 835, 230
Foreman-Mackey, D., Hogg, D. W., Lang, D., & Goodman, J. 2013, PASP, 125, 306
Fortney, J. J., Marley, M. S., Saumon, D., & Lodders, K. 2008, ApJ, 683, 1104
Gaia Collaboration. 2020, VizieR Online Data Catalog, I/350
Gaia Collaboration, Brown, A. G. A., Vallenari, A., et al. 2018, A&A, 616, A1
Gaia Collaboration, Brown, A. G. A., Vallenari, A., et al. 2021, A&A, 649, A1
Garcia Lopez, R., Natta, A., Testi, L., & Habart, E. 2006, A&A, 459, 837
Garufi, A., Dominik, C., Ginski, C., et al. 2022, A&A, 658, A137
Geers, V. C., van Dishoeck, E. F., Visser, R., et al. 2007, A&A, 476, 279
Grady, C. A., Perez, M. R., Talavera, A., et al. 1996, A&AS, 120, 157
GRAVITY Collaboration, Abuter, R., Accardo, M., et al. 2017, A&A, 602, A94
Gravity Collaboration, Ganci, V., Labadie, L., et al. 2021, A&A, 655, A112
Gravity Collaboration, Perraut, K., Labadie, L., et al. 2019, A&A, 632, A53
GRAVITY Collaboration, Sanchez-Bermudez, J., Caratti O Garatti, A., et al. 2021, A&A, 654, A97
Gravity Collaboration, Wojtczak, J. A., Labadie, L., et al. 2023, A&A, 669, A59
Gray, R. O. & Corbally, C. J. 1994, AJ, 107, 742
Guarcello, M. G., Flaccomio, E., Micela, G., et al. 2019, A&A, 628, A74
Guzmán-Díaz, J., Mendigutía, I., Montesinos, B., et al. 2021, A&A, 650, A182
Hales, A. S., De Gregorio-Monsalvo, I., Montesinos, B., et al. 2014, AJ, 148, 47
Hauck, B. & Mermilliod, M. 1998, A&AS, 129, 431
Hayashi, C. 1981, Progress of Theoretical Physics Supplement, 70, 35
Heiter, U., Kupka, F., van't Veer-Menneret, C., et al. 2002, A&A, 392, 619
Helou, G. & Walker, D. W. 1988, Infrared Astronomical Satellite (IRAS) Catalogs and Atlases: The Small Scale Structure Catalog, Vol. 7
Herbig, G. H. 1960, ApJS, 4, 337
Hofmann, K. H., Bensberg, A., Schertl, D., et al. 2022, A&A, 658, A81
Høg, E., Fabricius, C., Makarov, V. V., et al. 2000, A&A, 355, L27
Hone, E., Kraus, S., Kreplin, A., et al. 2017, A&A, 607, A17
Hubrig, S., Ilyin, I., Schöller, M., & Lo Curto, G. 2013, Astronomische Nachrichten, 334, 1093
Inaba, S. & Barge, P. 2006, ApJ, 649, 415
Ishihara, D., Onaka, T., Kataza, H., et al. 2010, A&A, 514, A1
Järvinen, S. P., Carroll, T. A., Hubrig, S., Ilyin, I., & Schöller, M. 2019, MNRAS, 489, 886
Johns-Krull, C. M., Valenti, J. A., & Koresko, C. 1999, ApJ, 516, 900
Kama, M., Min, M., & Dominik, C. 2009, A&A, 506, 1199
Klarmann, L., Benisty, M., Min, M., et al. 2017, A&A, 599, A80
Kluska, J., Benisty, M., Soulez, F., et al. 2016, A&A, 591, A82
Kluska, J., Berger, J. P., Malbet, F., et al. 2020, A&A, 636, A116
Kluska, J., Kraus, S., Davies, C. L., et al. 2018, ApJ, 855, 44
Kobus, J., Wolf, S., Ratzka, T., & Brunngräber, R. 2020, A&A, 642, A104
Kóspál, Á., Ábrahám, P., Acosta-Pulido, J. A., et al. 2012, ApJS, 201, 11
Kraus, S., Hofmann, K. H., Benisty, M., et al. 2008, A&A, 489, 1157
Lachaume, R. 2003, A&A, 400, 795
Lacour, S., Dembet, R., Abuter, R., et al. 2019, A&A, 624, A99
Lapeyrere, V., Kervella, P., Lacour, S., et al. 2014, in Society of Photo-Optical Instrumentation Engineers (SPIE) Conference Series, Vol. 9146, Proc. SPIE, 91462D
Lazareff, B., Berger, J. P., Kluska, J., et al. 2017, A&A, 599, A85
Le Bouquin, J.-B., Berger, J.-P., Lazareff, B., et al. 2011, A&A, 535, A67
Lecar, M., Podolak, M., Sasselov, D., & Chiang, E. 2006, ApJ, 640, 1115
Lee, C.-D., Chen, W.-P., & Liu, S.-Y. 2016, A&A, 592, A130
Li, A. & Lunine, J. I. 2003, ApJ, 594, 987
Li, H., Colgate, S. A., Wendroff, B., & Liska, R. 2001, ApJ, 551, 874
Lodato, G. & Rice, W. K. M. 2004, MNRAS, 351, 630
Lord, S. D. 1992, A new software tool for computing Earth's atmospheric transmission of near- and far-infrared radiation, NASA Technical Memorandum 103957
Maaskant, K. M., Min, M., Waters, L. B. F. M., & Tielens, A. G. G. M. 2014, A&A, 563, A78
Malfait, K., Waelkens, C., Waters, L. B. F. M., et al. 1998, A&A, 332, L25
Matter, A., Labadie, L., Augereau, J. C., et al. 2016, A&A, 586, A11
Meeus, G., Waters, L. B. F. M., Bouwman, J., et al. 2001, A&A, 365, 476
Meheut, H., Casse, F., Varniere, P., & Tagger, M. 2010, A&A, 516, A31
Mendigutía, I. 2020, Galaxies, 8, 39
Menu, J., van Boekel, R., Henning, T., et al. 2015, A&A, 581, A107
Min, M., Dullemond, C. P., Dominik, C., de Koter, A., & Hovenier, J. W. 2009, A&A, 497, 155
Monnier, J. D., Millan-Gabet, R., Billmeier, R., et al. 2005, ApJ, 624, 832
Muzerolle, J., D'Alessio, P., Calvet, N., & Hartmann, L. 2004, ApJ, 617, 406
Myers, J. R., Sande, C. B., Miller, A. C., Warren, W. H., J., & Tracewell, D. A. 2015, VizieR Online Data Catalog, V/145
Oudmaijer, R. D., van den Ancker, M. E., Baines, D., et al. 2011, Astronomische Nachrichten, 332, 238
Pohl, A., Pinilla, P., Benisty, M., et al. 2015, MNRAS, 453, 1768
Rice, T. S., Reipurth, B., Wolk, S. J., Vaz, L. P., & Cross, N. J. G. 2015, AJ, 150, 132
Robinson, C. E. & Espaillat, C. C. 2019, ApJ, 874, 129
Rodrigo, C. & Solano, E. 2020, in XIV.0 Scientific Meeting (virtual) of the Spanish Astronomical Society, 182
Seok, J. Y. & Li, A. 2017, ApJ, 835, 291
Setterholm, B. R., Monnier, J. D., Davies, C. L., et al. 2018, ApJ, 869, 164
Shu, F., Najita, J., Ostriker, E., et al. 1994, ApJ, 429, 781
Surville, C. & Barge, P. 2015, A&A, 579, A100
Szulágyi, J. & Ercolano, B. 2020, ApJ, 902, 126
Tatulli, E., Benisty, M., Ménard, F., et al. 2011, A&A, 531, A1
Toomre, A. 1964, ApJ, 139, 1217
van Boekel, R., Waters, L. B. F. M., Dominik, C., et al. 2003, A&A, 400, L21
van der Plas, G., van den Ancker, M. E., Waters, L. B. F. M., & Dominik, C. 2015, A&A, 574, A75
van Leeuwen, F. 2007, A&A, 474, 653
Varga, J., Hogerheijde, M., van Boekel, R., et al. 2021, A&A, 647, A56
Verhoeff, A. P., Min, M., Acke, B., et al. 2010, A&A, 516, A48
Wade, G. A., Bagnulo, S., Drouin, D., Landstreet, J. D., & Monin, D. 2007, MNRAS, 376, 1145
Weigelt, M., Baur, O., Reubelt, T., Sneeuw, N., & Roth, M. 2011, in ESA Special Publication, Vol. 696, 4th International GOCE User Workshop, 36
Woitke, P., Min, M., Pinte, C., et al. 2016, A&A, 586, A103
Wolk, S. J., Günther, H. M., Poppenhaeger, K., et al. 2018, AJ, 155, 99
Yamamura, I., Makiuti, S., Ikeda, N., et al. 2010, VizieR Online Data Catalog, II/298

---

[1] I. Physikalisches Institut, Universität zu Köln, Zülpicher Str. 77, 50937, Köln, Germany
e-mail: `ganci@ph1.uni-koeln.de`
[2] Max-Planck-Institute for Radio Astronomy, Auf dem Hügel 69, 53121 Bonn, Germany
[3] Univ. Grenoble Alpes, CNRS, IPAG, 38000 Grenoble, France
[4] Unidad Mixta Internacional Franco-Chilena de Astronomía (CNRS, UMI 3386), Departamento de Astronomía, Universidad de Chile, Camino El Observatorio 1515, Las Condes, Santiago, Chile
[5] Max Planck Institute for Astronomy, Königstuhl 17, 69117 Heidelberg, Germany
[6] Dublin Institute for Advanced Studies, 31 Fitzwilliam Place, D02 XF86 Dublin, Ireland
[7] School of Physics, University College Dublin, Belfield, Dublin 4, Ireland
[8] INAF – Osservatorio Astronomico di Capodimonte, via Moiariello 16, 80131 Napoli, Italy

Appendix A: Observations

Appendix B: `Aspro` synthetic data tests

Appendix C: Azimuthal modulation global fit parameters χ^2_r maps

Appendix D: Spectrum wavelength calibration and star photospheric absorption model

The continuum-normalization of the GRAVITY science object spectrum of each epoch (average of all the observations blocks files that come from the 4 different ATs for that epoch) was done by fitting the slope of the raw spectrum and dividing the latter by the resulting fit. The first step of the wavelength calibration was done by comparing the observed wavelength positions of the telluric lines in the HD 98922 spectrum for each epoch with respect to the positions of the telluric lines present in the IR spectrum of the atmospheric transmission above Cerro Pachon, generated using the ATRAN modeling software (Lord 1992) accounting for 4.3 mm water vapor column and 1.5 mm airmass column, available on the Gemini Observatory website. The atmospheric transmission spectrum was convolved by a Gaussian with FHWM of 6 Å to have the same resolution as GRAVITY. The correction results in a blue-shift between 0 and 5 Å depending on the epoch. The HD 98922 spectrum was then corrected for the star radial velocity (−4.9 km/s) and its proper motion with respect to the local standard of rest, with a value that depends on the epoch of observations (between ≈ -35 and ≈ 2 km/s). The same corrections (telluric lines calibration, radial velocity correction, and local standard of rest correction), were also applied on the SC visibilities and differential phases for each epoch. The stellar atmospheric Brγ absorption was taken into account through a model selected from the Vienna New Model Grid of Stellar Atmospheres (Heiter et al. 2002)[5] that best represents the star (see Table 1). The model accounts for a star effective temperature of 10500 K, a surface gravity logarithm of 3.4, a metallicity of [Fe/H] = −0.5, and a microturbulence of 2.0 km/s, common value for a Herbig star. Finally, we included in the model the rotation broadening effect due to the rotation of the star ($v \, sin \, i = 39.0$ km/s) and we convolved the final model by a Gaussian with FHWM of 6 Å to have the same resolution as GRAVITY using SPECTRUM (Gray & Corbally 1994).

Recently, a systematic spectral shift of the line features has been found in the GRAVITY SC data. The shift is seen when comparing data from an individual telescope with respect to the other telescopes, but also globally with regard to the known wavelength positions of the telluric lines in the K-band. It is thought that the shift is caused by the old grism of the science spectrometer which was upgraded in October 2019. GRAVITY data taken after this month should therefore no longer be affected. To check if our results are affected by the shift, we corrected the shift in the 19 March 2019 data following Gravity Collaboration et al. (2023), and compared the results with the ones obtained without the correction. For a description of the correction we refer to Section 3.2 of Gravity Collaboration et al. (2023). Figure D.1 shows the pure-line photocenters shift obtained with the original data (top panel) and with the corrected ones (bottom panel). We note a slight change in the shift when comparing photocenters of the same spectral channel. However, in this work we are not primarily interested in the relative position of the photocenters for each spectral channel, but rather in the overall location of the gas with respect to the star and the dusty feature. This choice is also based on the fact that our data were obtained with the ATs, meaning that we have only 4 or 5 spectral channels across the line. Data obtained with the UTs have instead around 12 spectral channels across the line, making these data more suitable for high-precision spectral analysis. With this point of view, the differences between the results obtained with the corrected and the non-corrected ATs data is negligible. Therefore, we decided to not apply this high-precision spectral calibration to our data.

Appendix E: Photometric data

---

[5] available on the NeMo webpage (Ch. Stütz and E. Paunzen, `http://www.univie.ac.at/nemo/`)

Table A.1. Observation logs of the VLTI/PIONIER HD 98922 observations

ID	Date	UT	Configuration	N	Calibrator	Seeing [$''$]	Airmass	τ_0 [ms]	ID$_{obs}$
P1	03-06-2011	00:21	D0-G1-H0-I1	4	NDA	0.5-0.9	1.17-1.26	1.6-2.9	087.C-0458(C)
P2	08-06-2011	23:28	A1-B2-C1-D0	2	NDA	0.8-1.3	1.15-1.16	2.0-2.7	087.C-0458(B)
P3	25-03-2012	04:50	A1-G1-I1-K0	2	NDA	0.5-0.9	1.16-1.38	2.6-4.8	088.D-0828(B)
P4	28-03-2012	05:22	A1-G1-I1-K0	2	NDA	1.4-1.6	1.22-1.28	1.3-1.4	088.D-0185(A)
P5	20-12-2012	06:47	A1-B2-C1-D0	2	NDA	0.5-0.6	1.38-1.47	8.1-8.5	190.C-0963(C)
P6	22-12-2012	09:13	A1-B2-C1-D0	1	NDA	0.8-0.9	1.15-1.16	8.1-9.5	190.C-0963(C)
P7	26-01-2013	08:48	A1-G1-J3-K0	1	NDA	1.2-1.5	1.16-1.51	1.1-1.2	190.C-0963(A)
P8	27-01-2013	07:11	A1-G1-J3-K0	2	NDA	0.9-1.0	1.14-1.15	2.7-2.8	190.C-0963(A)
P9	28-01-2013	08:39	A1-G1-J3-K0	3	NDA	0.8-1.5	1.17-1.28	1.5-3.3	190.C-0963(A)
P10	30-01-2013	07:25	A1-G1-J3-K0	1	NDA	1.6-1.3	1.30-1.80	1.5-1.6	190.C-0963(C)
P11	31-01-2013	03:39	A1-G1-J3-K0	2	NDA	0.9-1.1	1.15-1.16	1.8-2.3	190.C-0963(A)
P12	01-02-2013	04:35	A1-G1-J3-K0	3	NDA	0.8-1.1	1.18-1.34	2.0-3.4	190.C-0963(A)
P13	17-02-2013	01:47	D0-G1-H0-I1	3	NDA	0.7-0.8	1.19-1.22	3.7-4.4	190.C-0963(B)
P14	18-02-2013	03:27	D0-G1-H0-I1	4	NDA	0.5-0.9	1.14-1.52	3.2-5.4	190.C-0963(B)
P15	19-02-2013	08:20	D0-G1-H0-I1	1	NDA	0.7-0.9	1.26-1.27	3.1-3.9	190.C-0963(B)
P16	20-02-2013	02:36	D0-G1-H0-I1	2	NDA	0.7-1.0	1.41-1.49	3.8-5.2	190.C-0963(B)
P17	23-06-2014	22:57	A1-G1-J3-K0	2	HD 98895	0.5-0.8	1.17-1.19	1.9-2.6	093.C-0559(D)
P18	21-02-2016	06:08	D0-G2-J3-K0	1	HD 98895	1.4-1.9	1.13-1.14	0.9-1.4	096.C-0867(C)
P19	01-03-2016	05:44	D0-G2-J3-K0	2	HD 98895	1.0-1.7	1.14-1.16	1.7-2.9	096.C-0867(D)
P20	02-03-2016	06:18	D0-G2-J3-K0	2	HD 98895	0.8-1.0	1.16-1.20	1.9-2.3	096.C-0867(E)

Notes. The date format is day-month-year. N denotes the number files that have been recorded on the target. NDA: no data available; These archival data were retrieved already calibrated from the JMMC Optical interferometry DataBase (`http://oidb.jmmc.fr/index.html`).

Table A.2. Observation logs of the VLTI/GRAVITY HD 98922 observations

ID	Date	UT	Configuration	N	Calibrator	Seeing [$''$]	Airmass	τ_0 [ms]	ID$_{obs}$
G1	22-02-2017	07:13	A0-G1-J2-K0	14	HD 103125	0.7-1.7	1.18-1.70	NDA	098.C-0765(C)
G2	19-03-2017	04:36	A0-G1-J2-K0	5	HD 100825	0.7-0.9	1.14-1.17	NDA	098.D-0488(A)
G3	15-06-2018	00:09	D0-G2-J3-K0	4	HD 100825	0.8-1.2	1.21-1.30	2.3-3.2	0101.C-0311(A)
G4	19-03-2019	05:45	D0-G2-J3-K0	6	HD 100825	0.5-0.6	1.20-1.27	3.5-5.9	0102.C-0408(D)
G5	24-05-2019	01:45	A0-G1-J2-J3	6	HD 103125	0.6-0.9	1.22-1.29	1.8-3.2	0103.C-0347(C)
G6	04-06-2019	23:21	A0-B2-C1-D0	7	HD 103125	0.8-1.1	1.14-1.16	2.8-4.1	0103.C-0347(B)
G7	11-07-2019	23:22	D0-G2-J3-K0	5	HD 103125	0.8-1.1	1.33-1.42	2.0-3.0	0103.C-0347(A)
G8	13-07-2019	22:56	D0-G2-J3-K0	7	HD 103125	0.3-0.5	1.29-1.41	1.3-1.4	0103.C-0347(A)
G9	27-01-2020	05:56	A0-G2-J2-J3	5	HD 103125	0.7-1.0	1.16-1.21	3.6-5.9	0104.C-0567(A)
G10	04-02-2020	05:35	A0-B2-C1-D0	11	HD 103125	0.7-1.1	1.14-1.20	2.1-4.9	0104.C-0567(C)
G11	23-12-2020	06:31	D0-G2-J3-K0	13	HD 99311	0.7-1.9	1.20-1.47	2.1-4.6	106.212G.002
G12	07-02-2022	07:43	D0-G2-J3-K0	8	HD 103125	0.5-1.2	1.16-1.24	4.4-12.6	108.228Z.002
G13	14-02-2022	06:11	A0-G1-J2-J3	6	HD 103125	NDA	1.14-1.15	NDA	108.228Z.001

Notes. Same as A.1

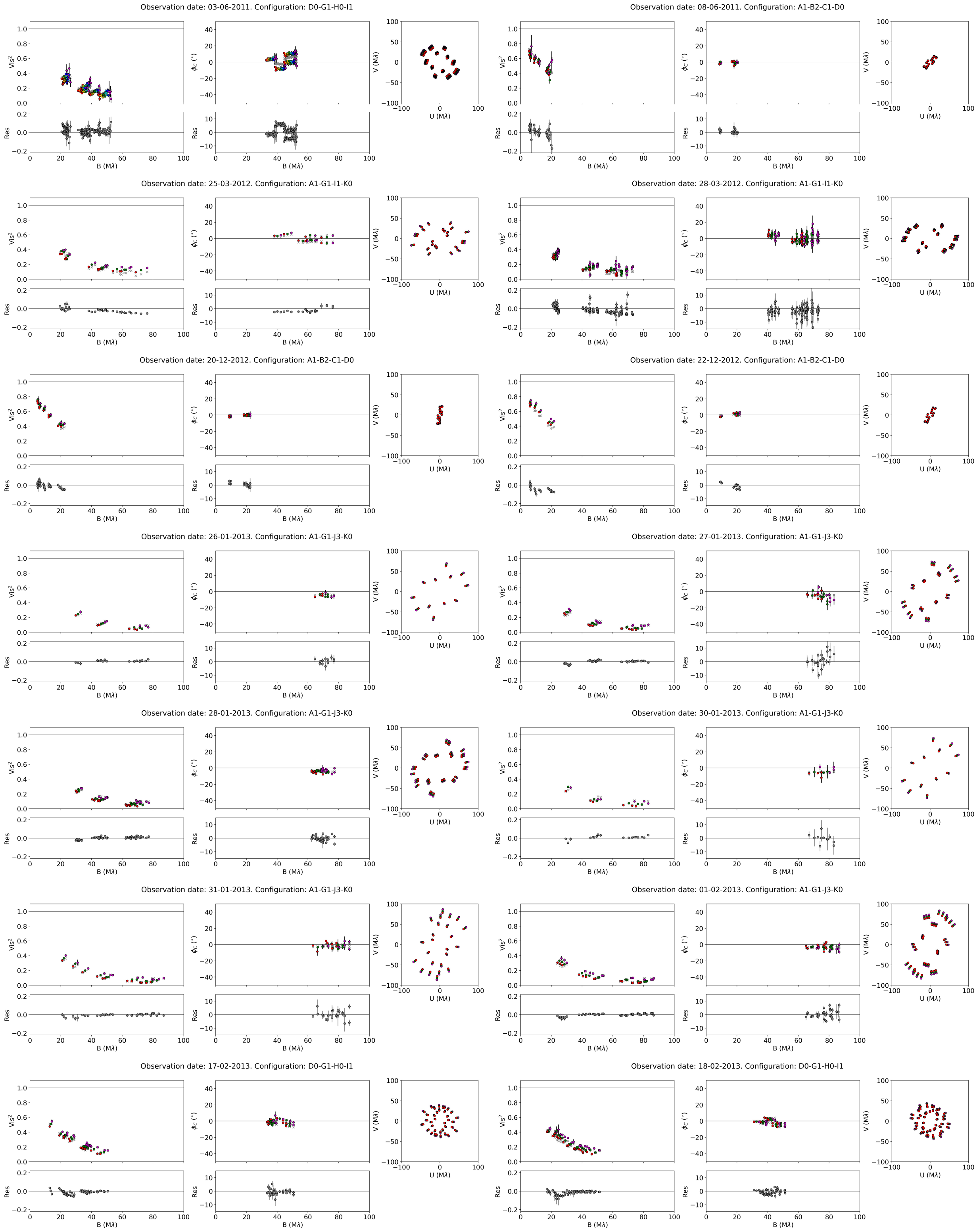
Observation date: 03-06-2011. Configuration: D0-G1-H0-I1

Observation date: 08-06-2011. Configuration: A1-B2-C1-D0

Observation date: 25-03-2012. Configuration: A1-G1-I1-K0

Observation date: 28-03-2012. Configuration: A1-G1-I1-K0

Observation date: 20-12-2012. Configuration: A1-B2-C1-D0

Observation date: 22-12-2012. Configuration: A1-B2-C1-D0

Observation date: 26-01-2013. Configuration: A1-G1-J3-K0

Observation date: 27-01-2013. Configuration: A1-G1-J3-K0

Observation date: 28-01-2013. Configuration: A1-G1-J3-K0

Observation date: 30-01-2013. Configuration: A1-G1-J3-K0

Observation date: 31-01-2013. Configuration: A1-G1-J3-K0

Observation date: 01-02-2013. Configuration: A1-G1-J3-K0

Observation date: 17-02-2013. Configuration: D0-G1-H0-I1

Observation date: 18-02-2013. Configuration: D0-G1-H0-I1

Fig. A.1. HD 98922 PIONIER data, squared visibilities, closure phases, and *(u,v)* plan coverage for each epoch. Colors referees to the different PIONIER spectral channels. Gray crosses represent the model described in Section 3.1 and Table 4. Gray circles in the bottom plots show the residuals.

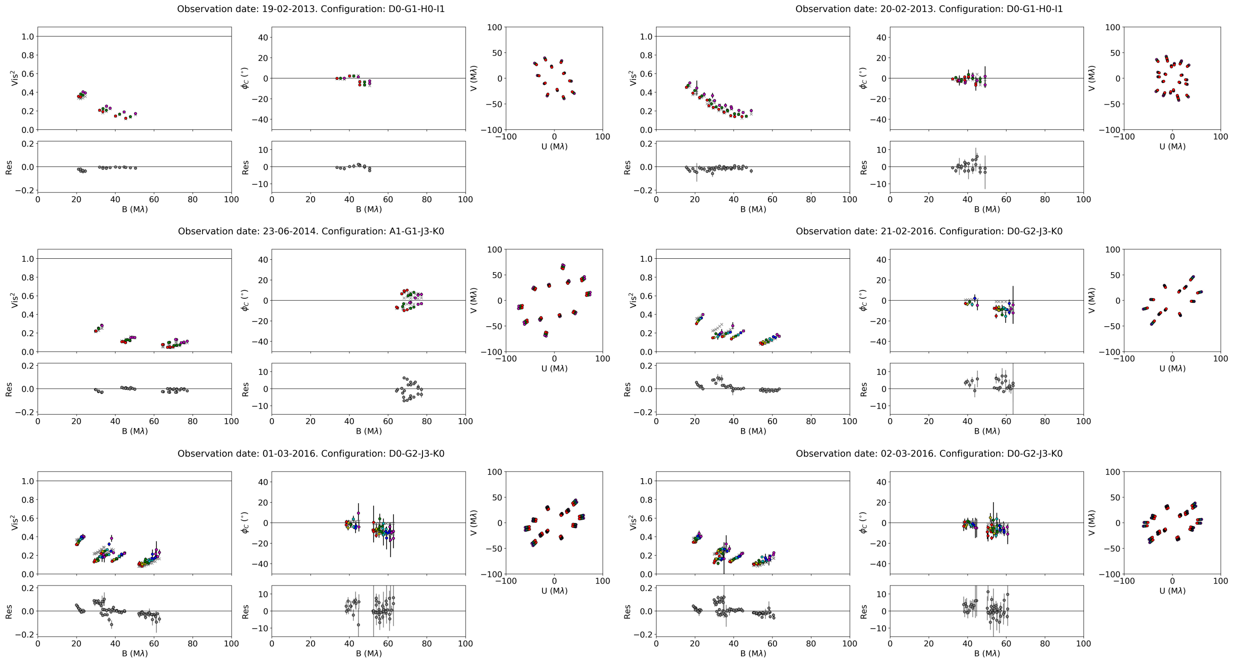

Fig. A.1. Continued.

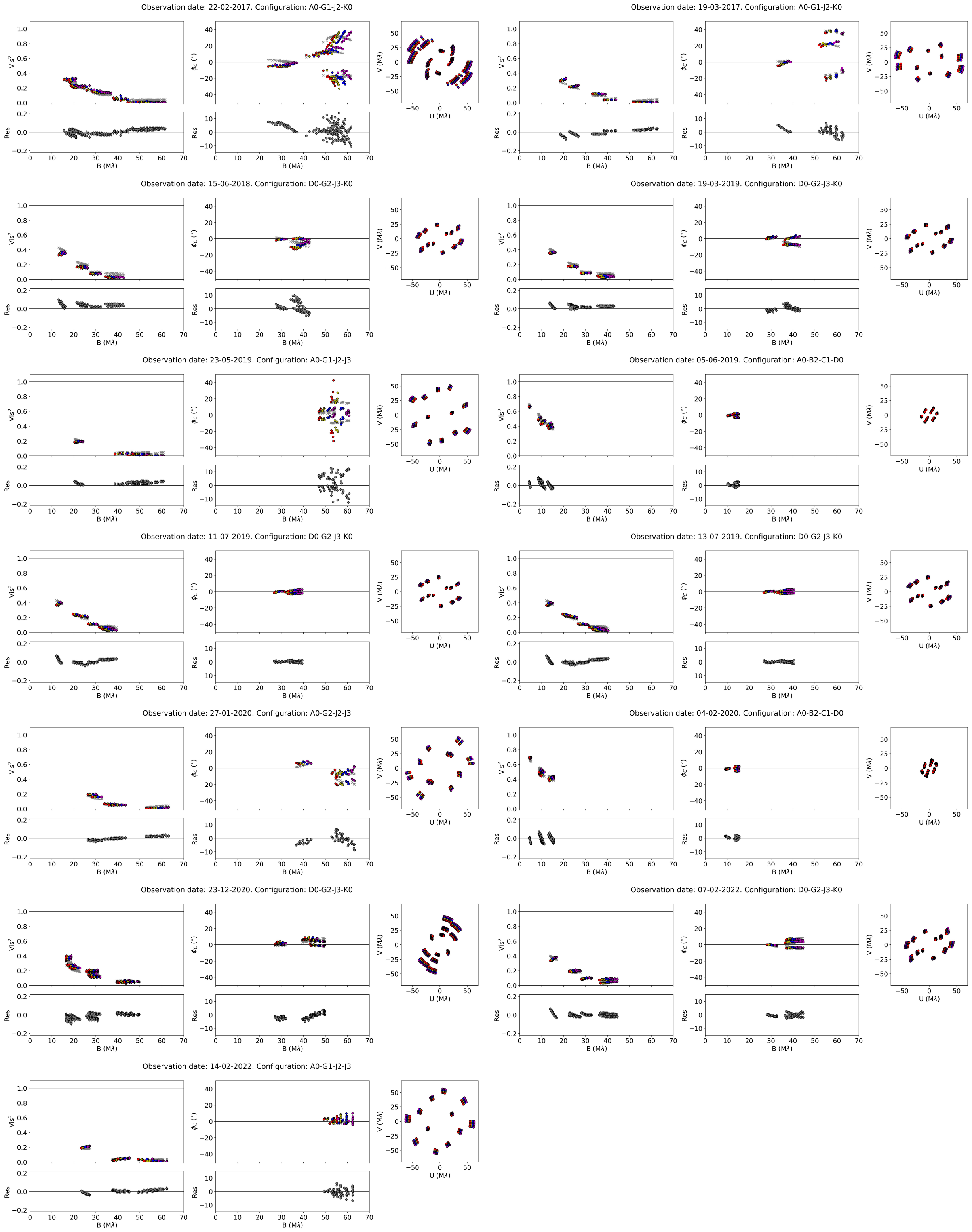

Fig. A.2. HD 98922 GRAVITY FT data, squared visibilities, closure phases, and *(u,v)* plan coverage for each epoch. Colors referees to the different GRAVITY spectral channels. Gray crosses represent the model described in Section 3.1, and Table 4. Gray circles in the bottom plots show the residuals.

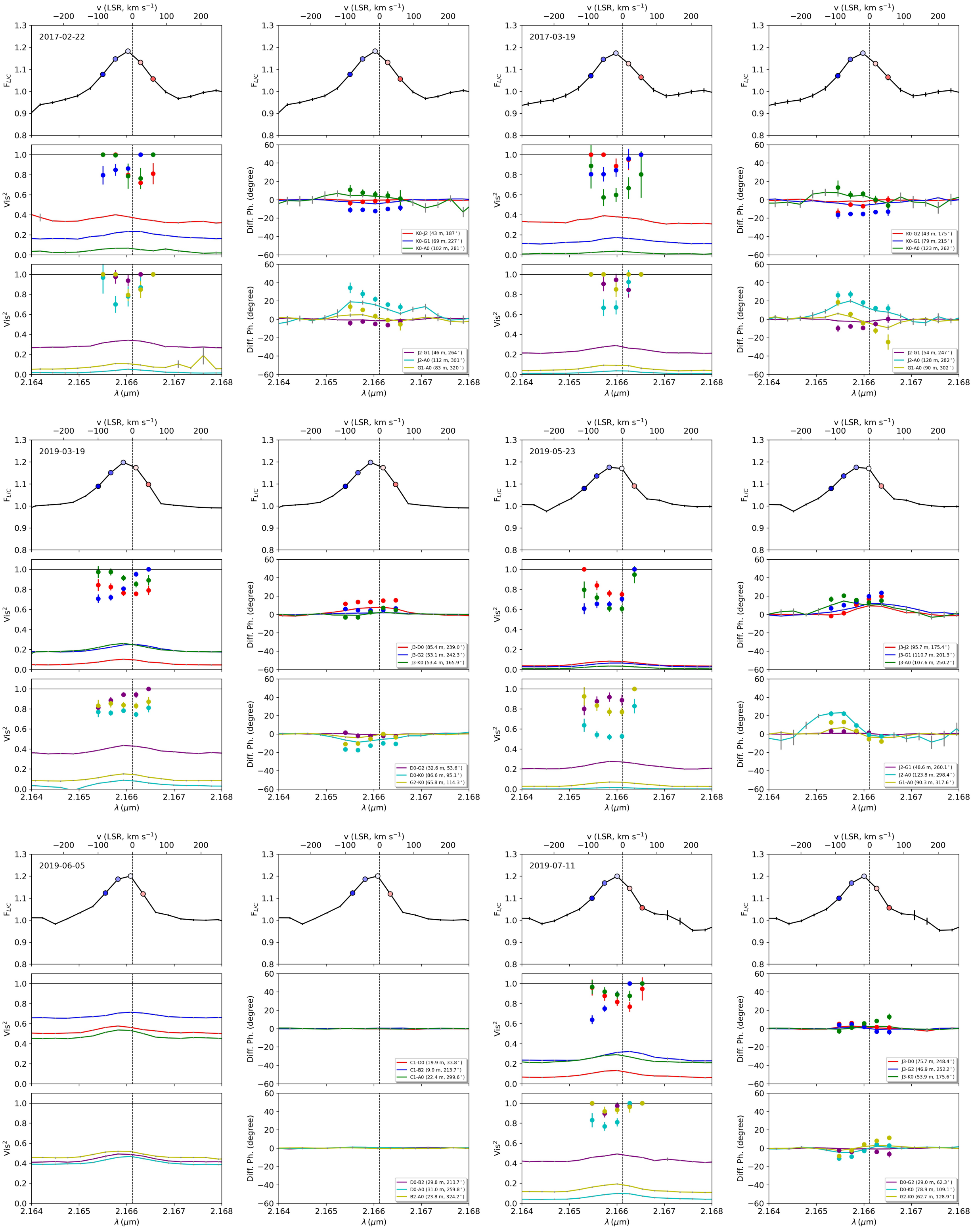

Fig. A.3. HD 98922 GRAVITY SC data for the different epochs. For each epoch, top plots show the wavelength-calibrated and continuum-normalized spectrum, left plots show the total squared visibilities, and right plots show the total differential phases. Circles represent the pure-line quantities. Colors refers to the different baselines.

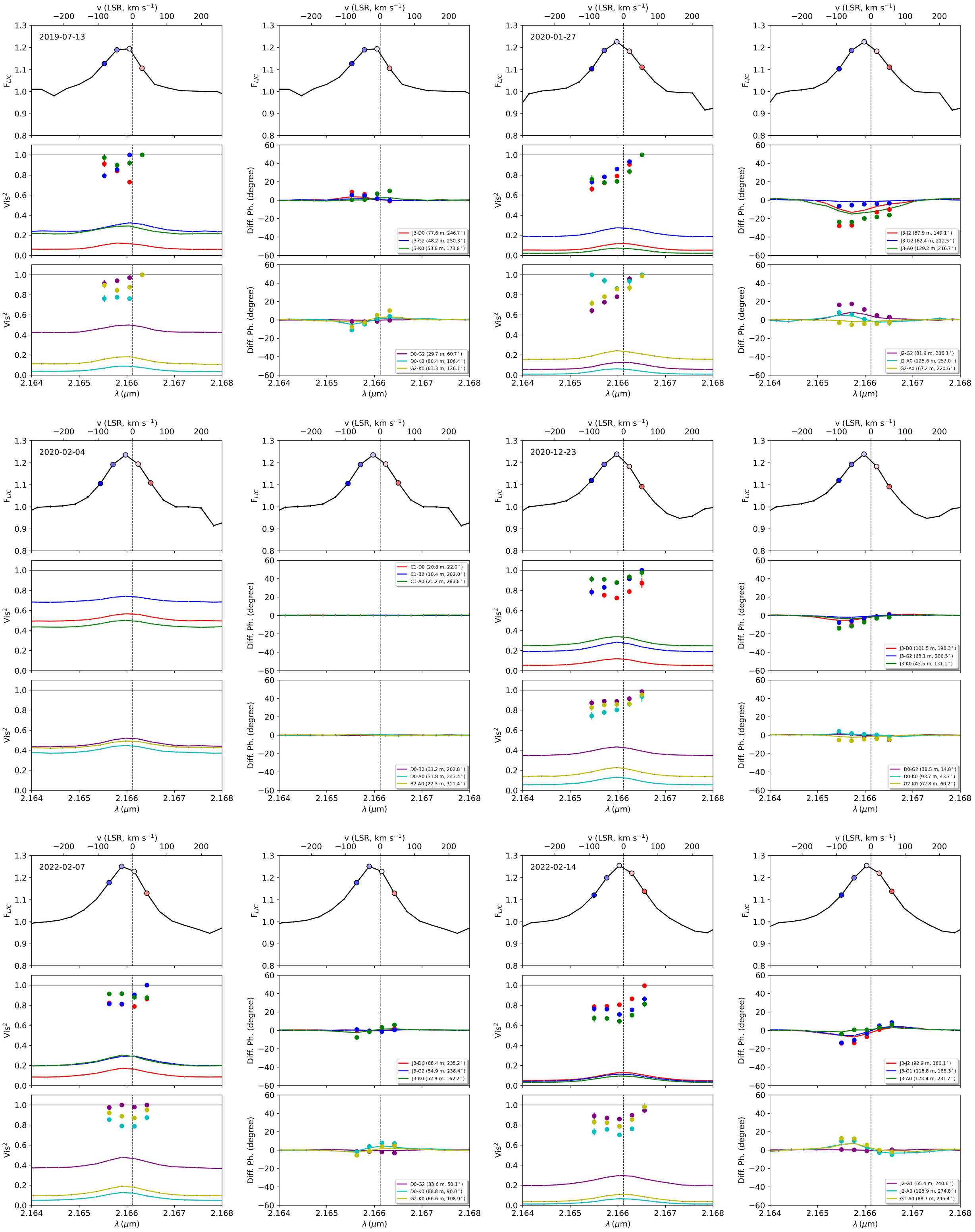

Fig. A.3. Continued.

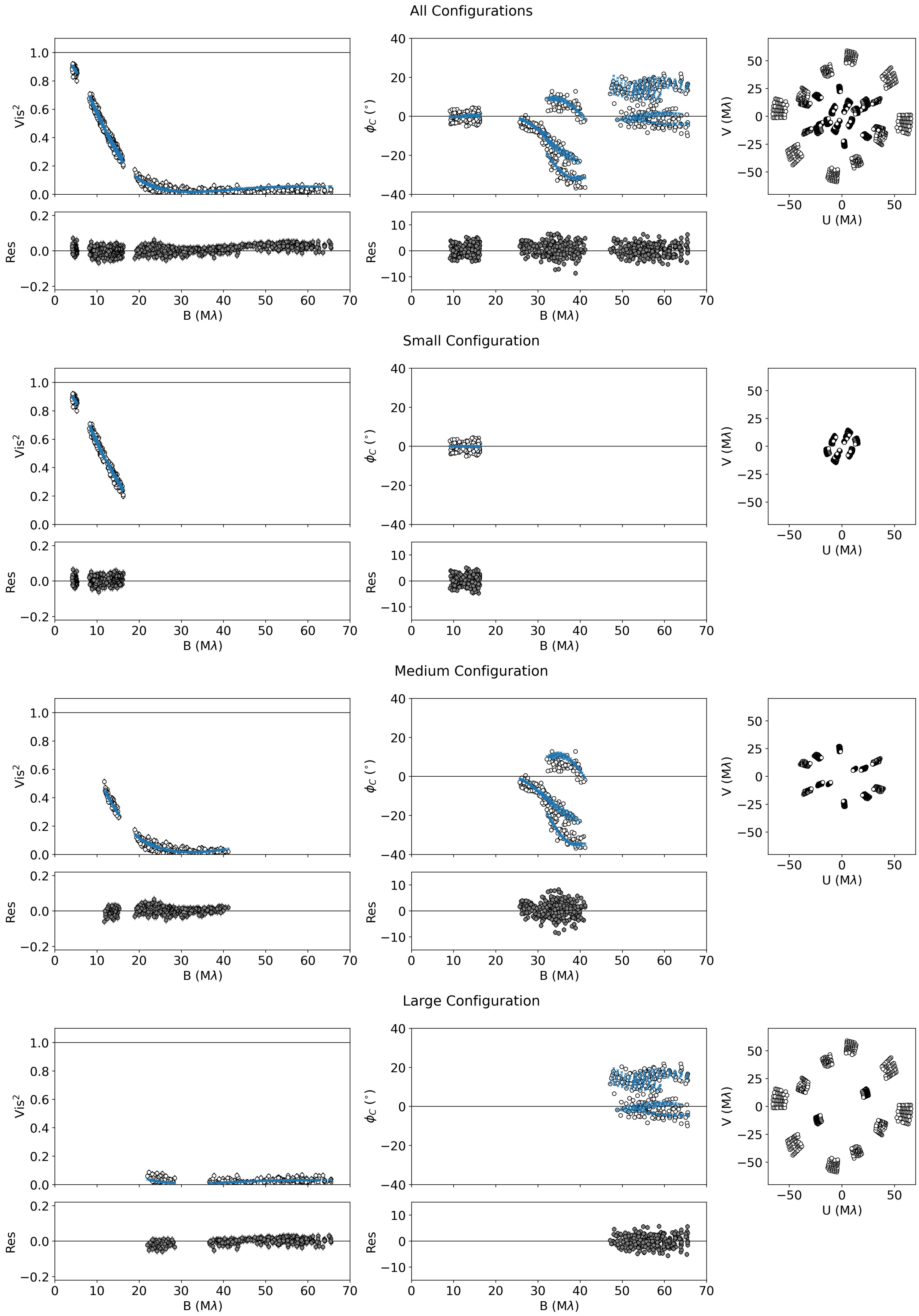

Fig. B.1. `Aspro` synthetic data (white markers), Vis^2, closure phases, and *(u,v)* plane (left, center, and right panel, respectively) for the different baseline configurations. Blue markers represent the model described in Section 4.1. Bottom panels show the residuals of the fitting process.

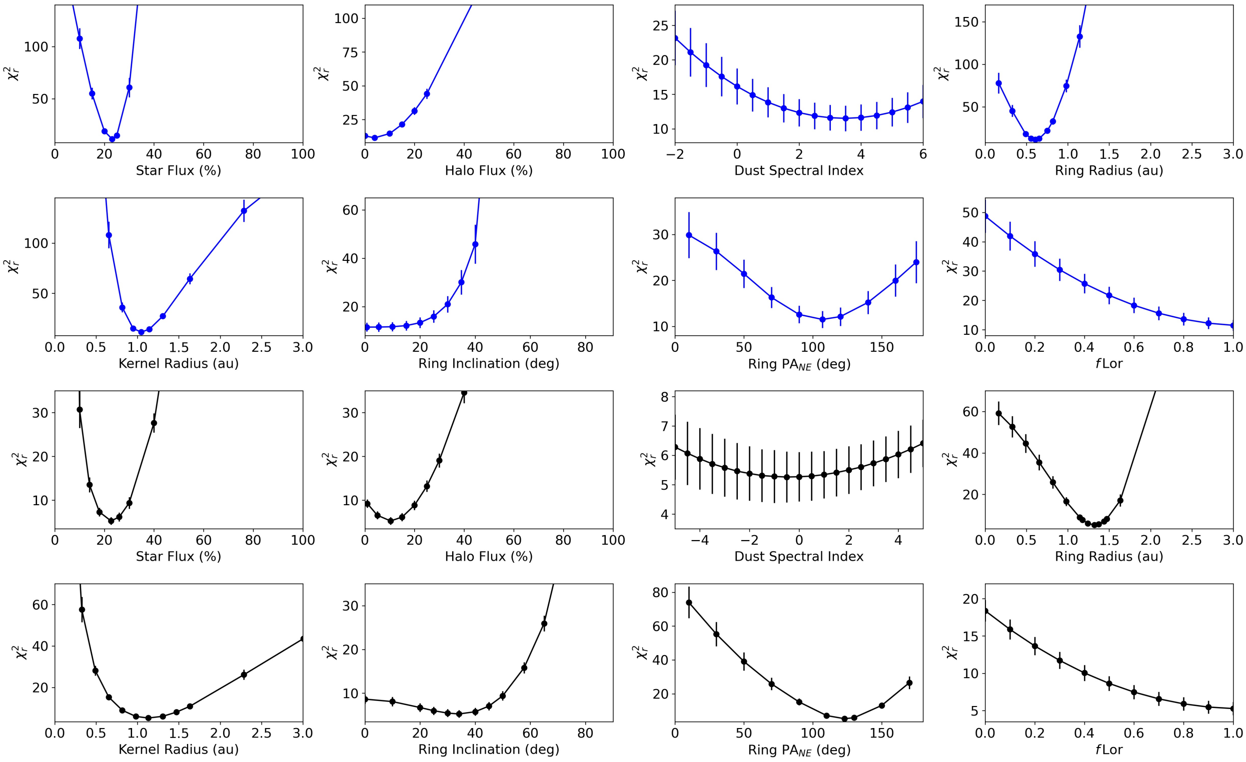

Fig. C.1. Reduced chi-squared χ_r^2 curves of each non-time-variable parameter from the azimuthal modulation global fit model. The first two rows, where the curves are blue, refer to the PIONIER data model, while the last two rows, where the curves are black, refer to the GRAVITY data model.

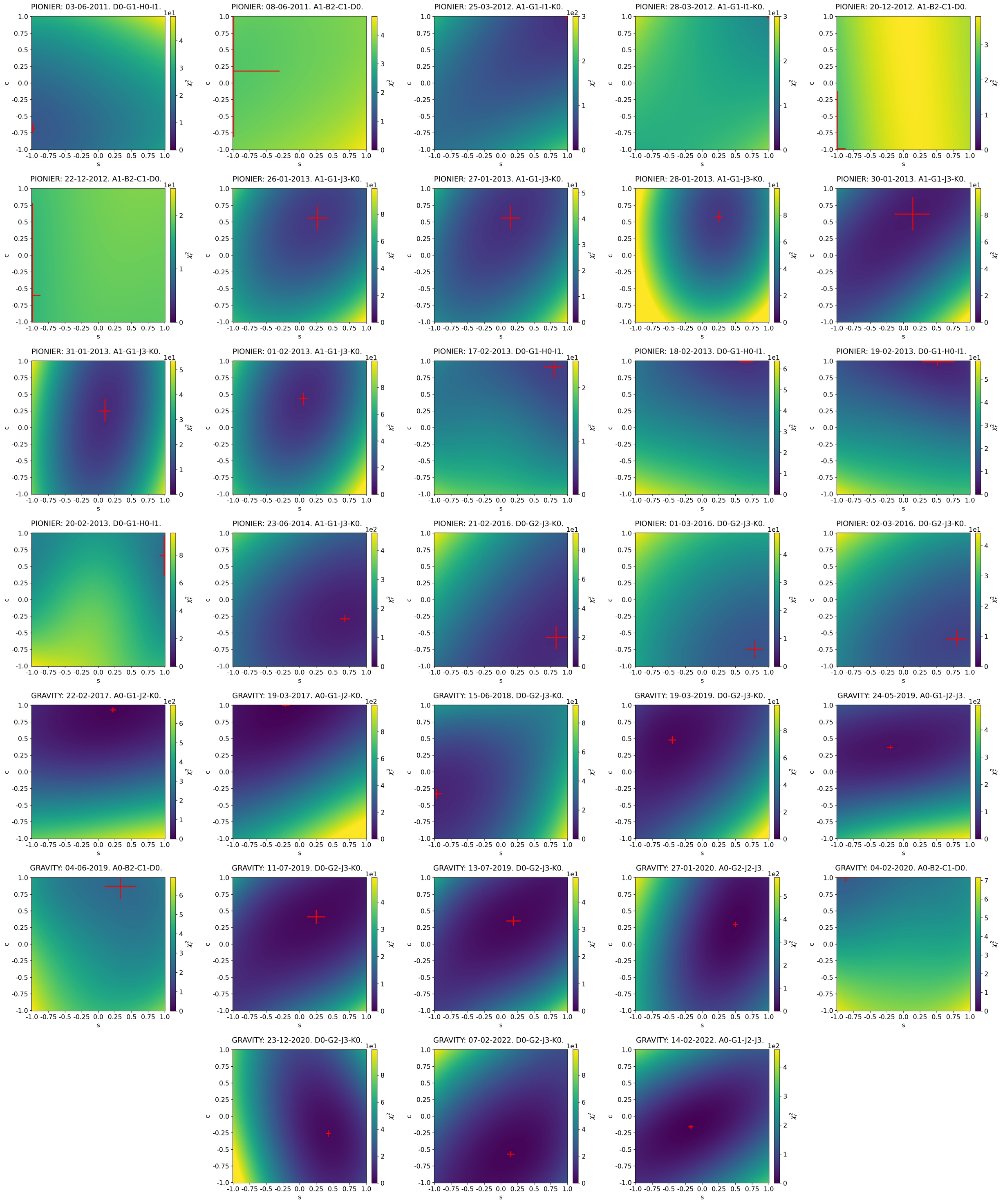

Fig. C.2. Global fit azimuthal modulation parameters χ^2_r maps. The red lines represent the $3\,\sigma$ error bars of the parameters derived through the MCMC fitting procedure. Their intersections give the smallest χ^2_r for a given epoch.

Table E.1. HD 98922 photometry data

λ (μm)	F_λ (erg cm^{-2} s^{-1} Å)	ΔF_λ (erg cm^{-2} s^{-1} Å)	Reference
0.35	6.73×10^{-12}	6.73×10^{-13}	Malfait et al. (1998)
0.35	8.30×10^{-12}	1.44×10^{-13}	Myers et al. (2015)
0.42	1.27×10^{-11}	6.79×10^{-14}	Esa (1997)
0.50	8.05×10^{-12}	2.35×10^{-14}	Gaia Collaboration et al. (2018)
0.43	1.33×10^{-11}	1.33×10^{-12}	Malfait et al. (1998)
0.44	1.25×10^{-11}	1.25×10^{-12}	Høg et al. (2000)
0.53	7.82×10^{-12}	7.42×10^{-14}	Esa (1997)
0.55	7.17×10^{-12}	3.30×10^{-13}	Malfait et al. (1998)
0.55	7.39×10^{-12}	7.39×10^{-13}	Høg et al. (2000)
0.55	7.54×10^{-12}	7.54×10^{-13}	Hauck & Mermilliod (1998)
0.58	5.80×10^{-12}	1.77×10^{-14}	Gaia Collaboration (2020)
0.67	4.56×10^{-12}	1.99×10^{-14}	Gaia Collaboration et al. (2018)
0.76	3.04×10^{-12}	1.55×10^{-14}	Gaia Collaboration (2020)
0.77	3.01×10^{-12}	1.51×10^{-14}	Gaia Collaboration et al. (2018)
1.22	1.15×10^{-12}	1.15×10^{-13}	Malfait et al. (1998)
1.24	1.24×10^{-12}	2.29×10^{-14}	Cutri et al. (2003)
1.63	9.53×10^{-13}	2.60×10^{-14}	Cutri et al. (2003)
1.65	8.26×10^{-13}	8.26×10^{-14}	Malfait et al. (1998)
1.66	9.03×10^{-13}	2.41×10^{-14}	Cutri et al. (2003)
2.16	8.32×10^{-13}	2.76×10^{-14}	Cutri et al. (2003)
2.18	7.12×10^{-13}	7.12×10^{-14}	Malfait et al. (1998)
2.19	7.94×10^{-13}	2.50×10^{-14}	Cutri et al. (2003)
3.35	4.41×10^{-13}	6.41×10^{-14}	Cutri & et al. (2012)
3.55	4.99×10^{-13}	4.99×10^{-14}	Malfait et al. (1998)
4.60	4.35×10^{-13}	5.67×10^{-15}	Cutri & et al. (2012)
4.77	2.68×10^{-13}	2.68×10^{-14}	Malfait et al. (1998)
8.61	1.08×10^{-13}	4.04×10^{-16}	Ishihara et al. (2010)
12.0	6.34×10^{-14}	6.34×10^{-15}	Beichman et al. (1988)
18.4	1.91×10^{-14}	8.86×10^{-17}	Ishihara et al. (2010)
25.0	9.25×10^{-15}	9.25×10^{-16}	Beichman et al. (1988)
60.0	3.56×10^{-16}	3.56×10^{-17}	Beichman et al. (1988)
61.9	4.85×10^{-16}	4.39×10^{-17}	Helou & Walker (1988)
65.0	2.30×10^{-16}	1.70×10^{-17}	Yamamura et al. (2010)
70.0	2.19×10^{-16}	1.10×10^{-17}	Hales et al. (2014)
90.0	9.60×10^{-17}	5.29×10^{-18}	Yamamura et al. (2010)
140.0	1.73×10^{-17}	7.98×10^{-18}	Yamamura et al. (2010)
160.0	1.03×10^{-17}	5.14×10^{-19}	Hales et al. (2014)
1290.0	1.88×10^{-21}	1.88×10^{-22}	ALMA Archive data

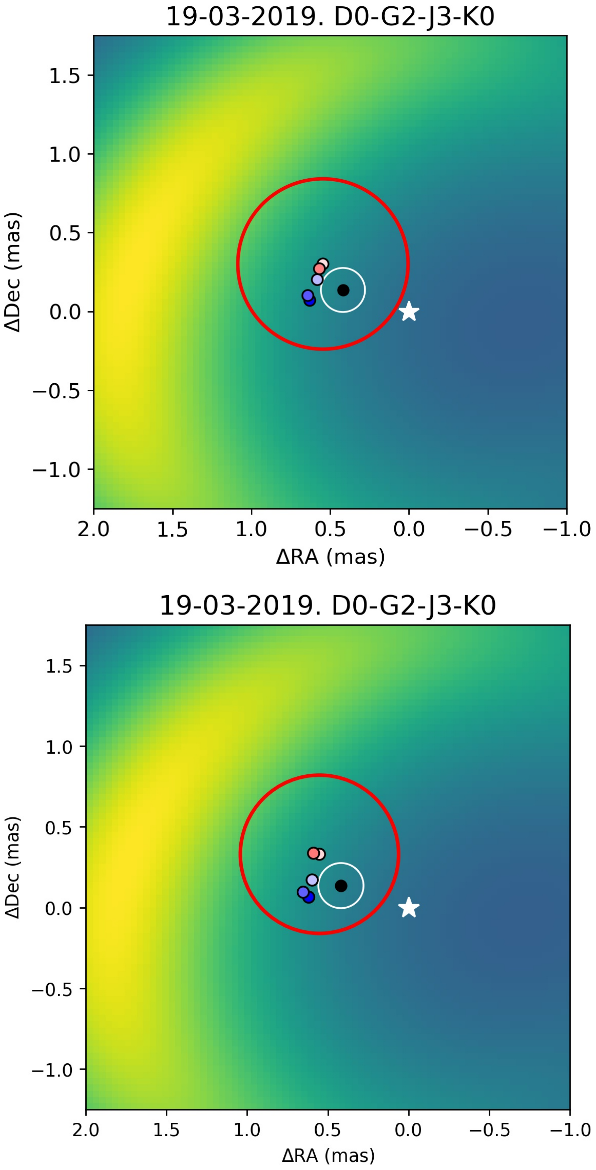

Fig. D.1. Difference between pure-line photocenters shift obtained with data corrected with the GRAVITY data reduction software (Lapeyrere et al. 2014, top panel), and with the high-precision spectral calibration of Gravity Collaboration et al. (2023). Same markers as in Fig. 7.

3.4 Comments

The study on HD 98922 here presented, covers many aspects of the astrophysical properties of YSOs, many of which are still not well understood. Relaxed assumptions were proved inadequate, supposedly discrepancy were afresh highlighted, and new questions also arose.

3.4.1 On the Repercussions of Different Modeling Approaches

A first comment goes on the impact of different interferometric modeling approaches. It is now clear that assuming temporal non-variability for a given object is inappropriate, if done without a careful analysis of data taken at different epochs. An example of the latter would be comparing interferometric observables retrieved through similar (u, v)-plane coverage at epochs spaced in time by days, weeks, and months. Another approach would be the one proposed by Kobus et al. (2020), which is based on comparing visibility curves of a given system taken at different epochs and also through different (u, v)-plane coverage. However, the latter approach does not take into account the closure phases, which retain the most information on the spatial distribution of the continuum emission and its possible time-variability, and therefore it should be further developed.

One would be tempted to use data sets taken at different epochs and with different baseline configurations independently. As shown by Section 4.1 of the manuscript however, this approach can lead to spurious results. As an example, in Fig. 3.2 I show some parameters estimates obtained from fitting each epoch of the HD 98922 GRAVITY data set independently. We note the wide ranges for the star flux contribution (~ 20-60 %), for the halo one (~ 0-40 %), for the ring inclination (~ 20°-50°), and for the ring wireframe radius (~ 1-5 mas). I also emphasize the fairly large error bars, in contrast with the ones derived by the global fit approach presented in the manuscript. Finally, as already known and previously mentioned, the accounting of small baseline configuration data impact significantly the fitting results. The star flux K-band contribution found by Gravity Collaboration et al. (2019), based solely on the fit of the February and March 2017 epochs astrometric configuration data sets, is 6 % smaller than the one found in this new work. Moreover, their halo contribution estimate is null, substantially different from the new 10 % value.

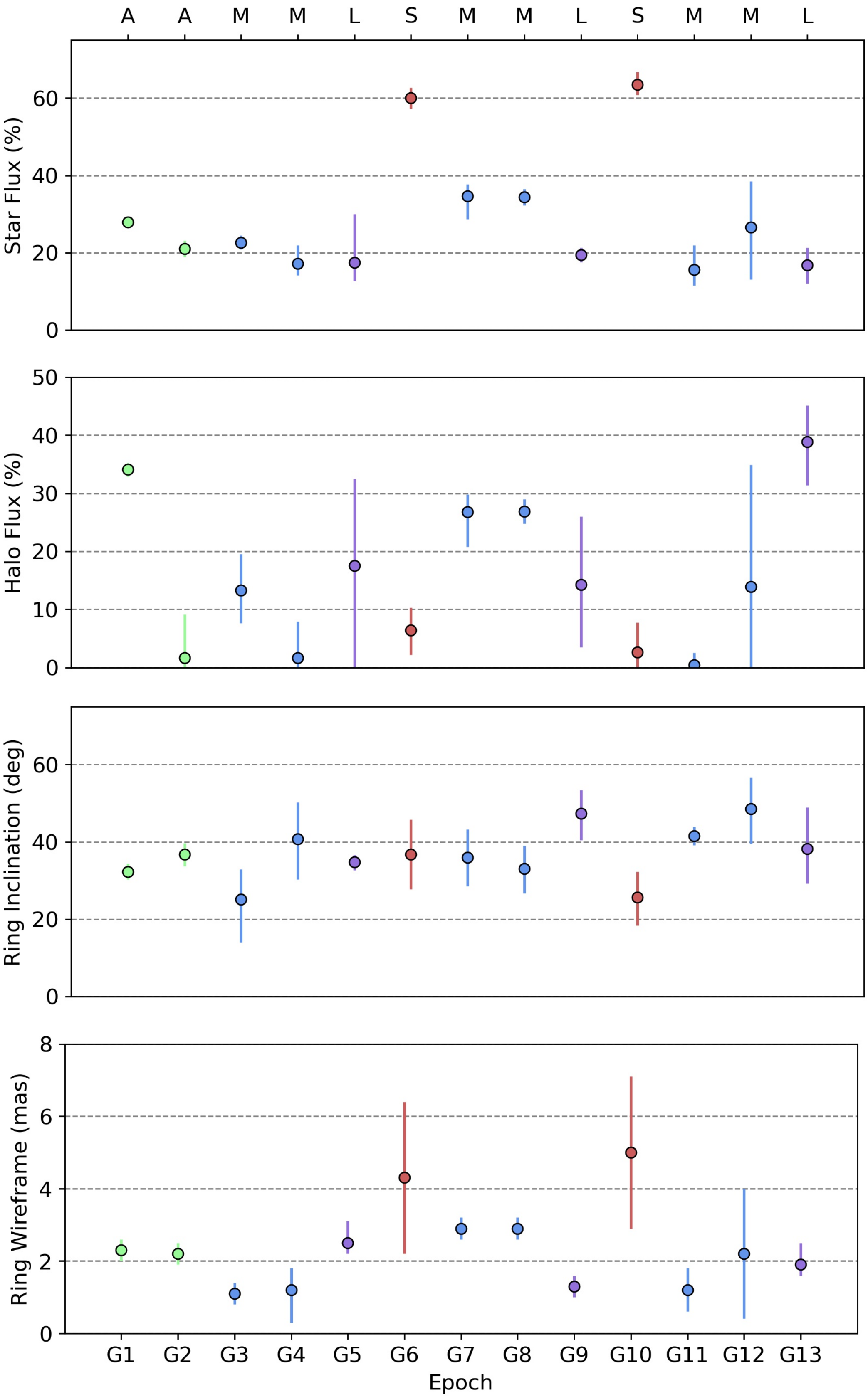

Figure 3.2: HD 98922 GRAVITY data set single epoch fits results for the different parameters. Colors refer to the different baseline configurations: A - Astrometric, M - Medium, L - Large, S - Small. Epochs are listed in Table A.2 of the manuscript.

3.4.2 On the H- and K-Band Emission Excess Spatial Extent

A second comment goes on the different sizes of the H- and K-band continuum emissions retrieved in this work for HD 98922. For the former, the model suggests a wireframe radius of 0.93 mas, and a half-flux radius of 1.85 mas. For the latter, a wireframe radius of 2.02 mas, and a half-flux radius of 2.66 mas. This is better illustrated in Fig. 3.3. In the top plots are depicted the HD 98922 models for the K-band (left) and the H-band (right) continuum emissions, with an azimuthal modulation position angle explicitly set at 90° NE. In the bottom plot, the radial profiles along the x-axis of both emissions is shown. The intensity of the two emissions in the plot are not scaled, as we know from literature data that the system total magnitude in the H-band is higher than the one in the K-band (see Section 4.4 of the manuscript). The goal of the plot is to show just the relative position of the two emissions' peaks. We note indeed a clear separation between the two.

The H- and K-band continuum excess emissions stem from re-radiation of the stellar emission at $\sim 1.65\,\mu$m and $\sim 2.15\,\mu$m, respectively. Assuming black-body radiation, from the Wien's displacement law, the H-band emitting dust has a temperature of $T_H \sim 1750\,$K, and the K-band emitting one has a temperature of $T_K \sim 1350\,$K. Assuming that the disk is classically parameterized by a temperature power law $T(r) = T_0\,(r/r_0)^{-q}$, where T_0 is the temperature at $r_0 = 1\,$au, and $q = 0.75$, typical value for a flat, group II disk, then, from the ratio $T_K/T_H = (r_K/r_H)^{-q}$, the K- and H-band sizes ratio would be $(r_K/r_H) \sim 1.41$. Considering the half-flux radius, the ratio estimated for HD 98922 ($r_K/r_H \approx 1.44$) is consistent with the former value. The separation between the two components however was not seen in our RT model, which images were produced with *RADMC-3D* (Dullemond et al. 2012). It was instead reproduced by the RT modeling of HD 98922 done by Hales et al. (2014) with *MCFOST* (Pinte et al. 2006), leading to a value of $(r_K/r_H) \sim 1.5$ (F. Ménard, private communication 2022). We cannot exclude that other phenomena afflicting the two components in different way may be at play.

This allegedly discrepancy was already seen in previous works for a few sources. In Table 3.1, the H- and K-band continuum emissions sizes derived through PIONIER and GRAVITY data modeling by Lazareff et al. (2017) and Gravity Collaboration et al. (2019) are listed. The first thing we note, is that different models can lead to significantly different results. The estimates derived with the ellipsoid model are often larger then the ones derived with the ring model. Secondly, and more relevant to the topic discussed in this paragraph, we note that for a few sources the ratio between the two sizes depart considerably from my simple estimate of 1.4. Surprisingly, some sources show a ratio substantially smaller than unity, like HD 45677, HD 142666, and HD 179218, which would translate in a K-band component located closer to the star with respect to the H-band one. The resulting inconsistency with the temperatures (the K-band component would be hotter than the H-band one) is enigmatic. GRAVITY Collabora-

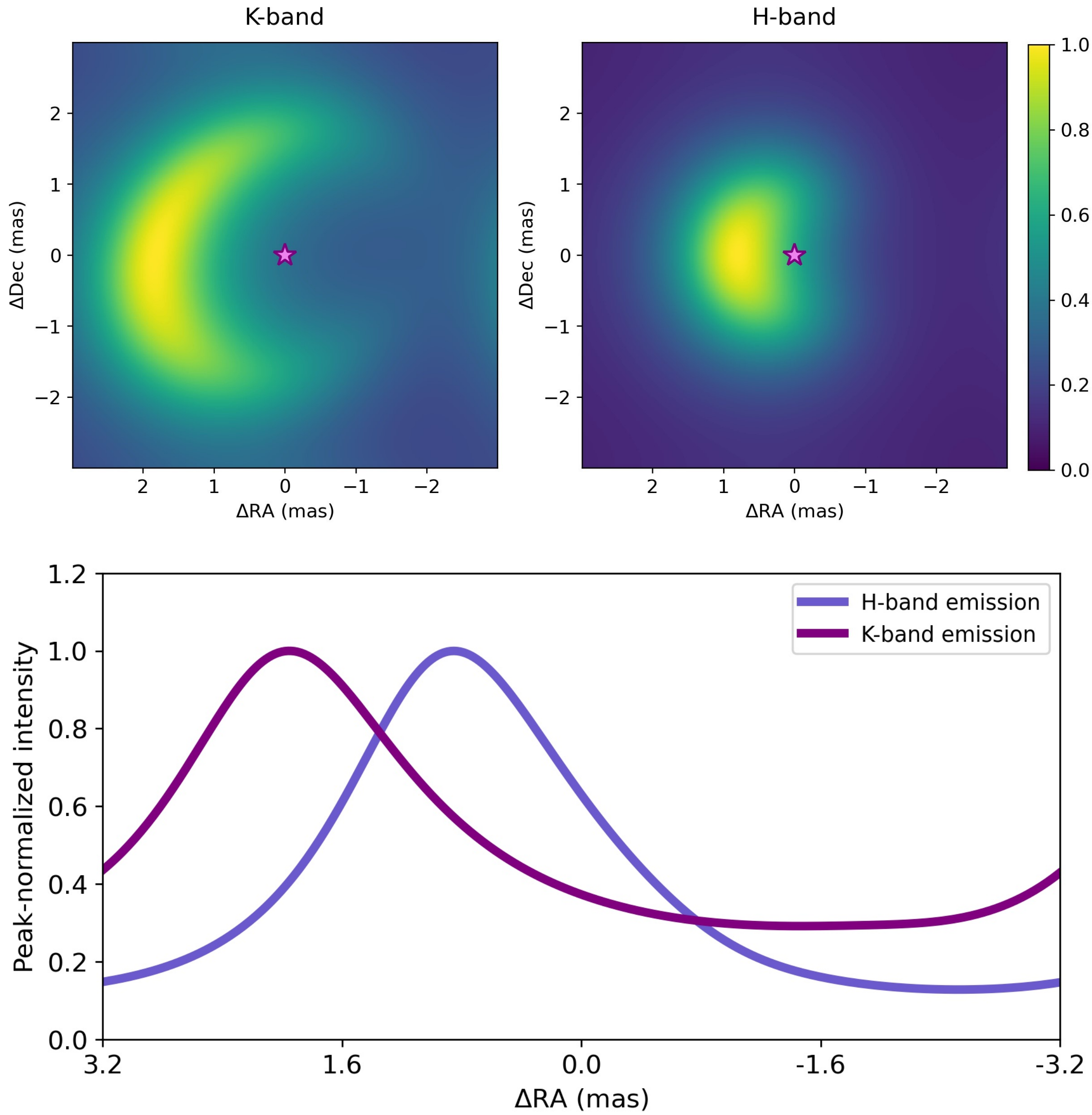

Figure 3.3: Top. HD 98922 K-band (left) and H-band (right) continuum model. The star has been removed to enhance the circumstellar emission. Bottom. Radial profile of the peak-normalized emissions shown above along the x-axis. Intensities not on scale.

tion et al. (2021b) suggested that the separation found between the two bands components for HD 163296, with the K-band apparent size being larger by a factor of two than the H-band one, is due to the different effective resolutions of PIONIER and GRAVITY; the extended emission of the source is filtered out more efficiently, the larger the interferometer baselines, leading to an observed more compact object. In the case of HD 98922 observations analysed in the manuscript, the maximum angular resolution obtained by PIONIER is 1.25 mas, and the one obtained by GRAVITY is 1.72 mas, backing-up the interpretation of GRAVITY Collaboration et al. (2021b). This is also consistent with the fact that the fit of HD 98922 PIONIER data led to a 4 % halo flux contribution, in contrast to the 10 % value found by the GRAVITY data fit.

Table 3.1: H-band and K-band continuum emitting regions size

Object	Ellipsoid Model HWHM (mas)			Ring Model Wireframe Radius (mas)		
	H-band	K-band	r_K/r_H	H-band	K-band	r_K/r_H
HD37806	1.45 ± 0.03	1.59 ± 0.04	1.10 ± 0.06	1.38 ± 0.11	1.48 ± 0.16	1.07 ± 0.21
HD45677	9.77 ± 0.23	3.09 ± 0.25	0.32 ± 0.03	8.37 ± 0.28	6.42 ± 0.47	0.77 ± 0.08
HD58647	1.55 ± 0.04	2.09 ± 0.05	1.35 ± 0.07	1.59 ± 0.30	1.78 ± 0.06	1.12 ± 0.43
HD85567	0.54 ± 0.03	0.54 ± 0.02	1.00 ± 0.10	0.38 ± 0.19	0.56 ± 0.04	1.48 ± 1.47
HD95881	1.00 ± 0.05	1.52 ± 0.07	1.52 ± 0.16	0.65 ± 0.13	0.29 ± 0.80	0.44 ± 1.25
HD97048	1.07 ± 0.13	1.07 ± 0.06	1.00 ± 0.25	0.73 ± 0.46	1.22 ± 0.15	1.68 ± 2.14
HD98922	1.78 ± 0.00	2.95 ± 0.07	1.66 ± 0.04	0.87 ± 0.06	1.31 ± 0.14	1.50 ± 0.27
HD100546	2.34 ± 0.06	2.46 ± 0.06	1.05 ± 0.05	2.25 ± 0.17	2.23 ± 0.07	0.99 ± 0.16
HD139614	1.29 ± 0.09	3.98 ± 0.10	3.09 ± 0.45	0.79 ± 0.51	2.36 ± 2.89	3.01 ± 5.37
HD142527	1.15 ± 0.03	1.32 ± 0.03	1.15 ± 0.06	0.33 ± 0.12	0.90 ± 0.07	2.70 ± 1.99
HD142666	1.07 ± 0.05	0.89 ± 0.06	0.83 ± 0.10	0.64 ± 0.36	0.10 ± 1.44	0.16 ± 2.26
HD144432	1.23 ± 0.06	1.45 ± 0.04	1.17 ± 0.11	0.53 ± 0.12	1.12 ± 0.08	2.12 ± 0.99
HD144668	1.86 ± 0.04	2.09 ± 0.05	1.12 ± 0.06	1.06 ± 0.08	1.42 ± 0.16	1.33 ± 0.25
HD150193	1.62 ± 0.04	2.82 ± 0.07	1.74 ± 0.09	–	–	–
HD158643	1.07 ± 0.28	2.95 ± 0.07	2.75 ± 1.42	0.28 ± 0.29	0.75 ± 2.99	2.69 ± 12.1
HD163296	2.19 ± 0.05	3.16 ± 0.08	1.44 ± 0.08	–	–	–
HD169142	0.98 ± 0.17	3.05 ± 0.40	3.12 ± 1.17	0.28 ± 0.45	1.07 ± 3.04	3.84 ± 16.7
HD179218	24.0 ± 2.93	6.75 ± 1.95	0.28 ± 0.11	–	–	–
HD190073	1.55 ± 0.04	1.91 ± 0.05	1.23 ± 0.06	1.63 ± 0.15	2.02 ± 0.05	1.24 ± 0.23
HD259431	0.46 ± 0.02	0.51 ± 0.02	1.12 ± 0.11	–	–	–
R CrA	4.27 ± 0.10	4.80 ± 0.10	1.13 ± 0.06	–	–	–

Notes: The values listed are taken from Lazareff et al. (2017) and Gravity Collaboration et al. (2019) for the H- and K-band, respectively.

3.4.3 On the SED RT Modeling

In this Section I am going to discuss in more details the SED RT modeling of HD 98922 presented in the manuscript, and the already known degeneracy solutions problem, encountered also in this work. The goal of the modeling was to derive an estimate of the disk surface density in order to test the gravitational instability scenario through the Toomre parameter. The degeneracy solutions issue was reduced by using the results obtained through the PIONIER and GRAVITY data analysis. For example, even though the one component model of Hales et al. (2014) does not fit well the photometric data once I account for the most update stellar parameters (top left panel of Fig. 3.4), the model can again fit the data if I change the disk inner radius from 1.5 to 2.5 au, and account for 25 % of carbon in the dust composition (Fig. 3.4, top right plot). This model nonetheless is not consistent with the PIONIER emission detection as close as 0.6 au, and it was eventually discarded.

Consequentially, the idea of a two components model was tested. However, by adding an inner component, the number of possible solutions increases. Good fits can be obtained by tweaking the masses of the two components and the transition location from the inner to the outer

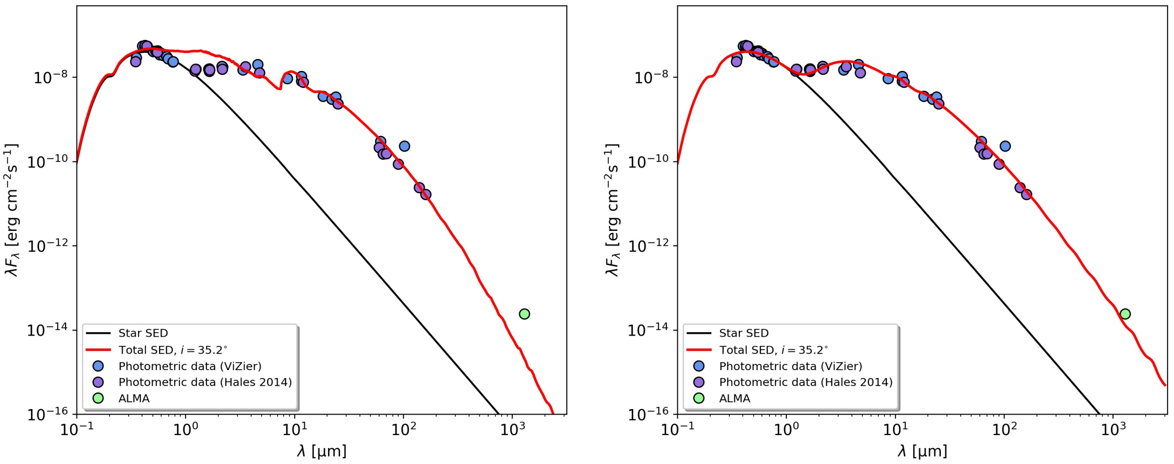

(a) Hales et al. (2014) model with new star parameters.

(b) One component CS model with $R_{\text{inner}} = 2.5$ au.

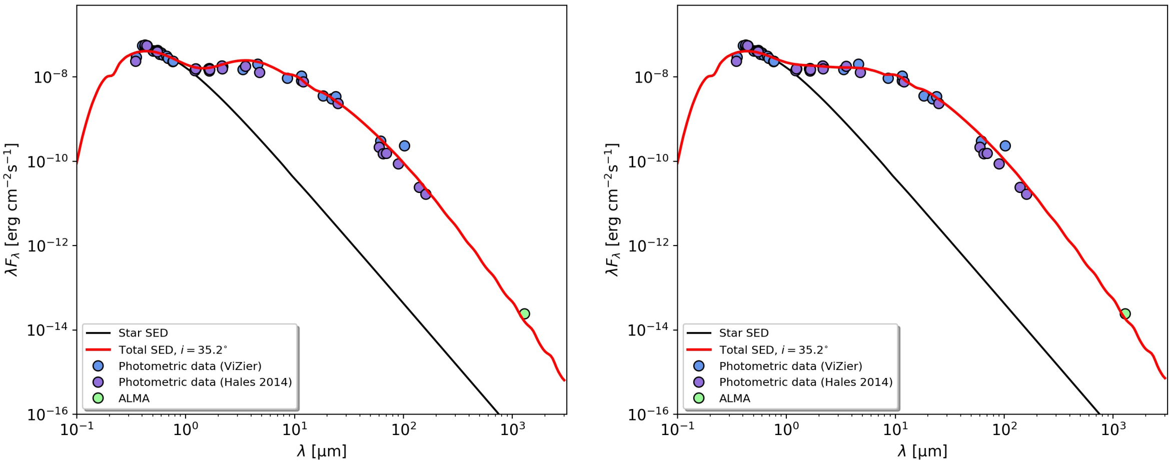

(c) Two components CS model with $R_{\text{trans}} = 3.5$ au.

(d) Two components CS model with $R_{\text{trans}} = 5.5$ au.

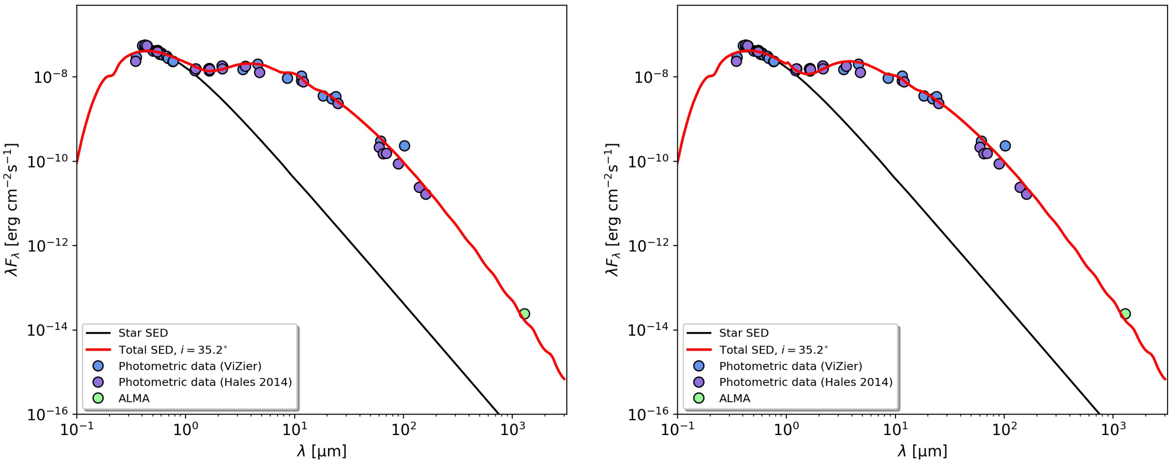

(e) Two components model with silicate inner one.

(f) Two components model with QHPs inner one.

Figure 3.4: HD 98922 RT models. The black line represent the star black-body, the red line the total (star+disk) model, the circle markers the literature photometric data. CS = carbon+silicate. For a description of the models see Section 3.4.3.

component, i.e. by varying the outer radius of the inner component and the inner radius of the outer component, which I both set to overlap. Examples are the models shown in the center left and center right plots of Fig. 3.4. The former accounts for a transition radius of 3.5 au, an inner component mass of $3 \times 10^{-9}\,\mathrm{M}_\odot$, and an outer component mass of $10^{-5}\,\mathrm{M}_\odot$. The latter accounts for a transition radius of 5.5 au, an inner component mass of $6 \times 10^{-9}\,\mathrm{M}_\odot$, and the same outer component mass. Both lead to visually good fit of the photometric data.

Additionally, equally good solutions can be found with models accounting for different inner component dust chemical composition. Carbon plus silicates models (Fig. 3.4, center plots), pure silicates models (bottom left plot), and QHPs models (bottom right plot) were tested, all with satisfactory fit. In order to discriminate between the models, I relied once again on the PIONIER and GRAVITY data analysis results. Specifically on the PIONIER and GRAVITY flux contribution estimates of the circumstellar environment. These values allowed to relatively constrain the disk inner component mass and the transition radius. The best model, presented in the manuscript and shown again in the center right plot of Fig. 3.4, accounts for an inner component that is the most consistent in its flux contribution with both the PIONIER and GRAVITY data analysis estimates.

3.4.4 On the Near-IR Excess Crescent-Like Feature

The HD 98922 PIONIER and GRAVITY data analysis suggested a crescent feature in orbital motion around the central star, with a sub-Keplerian best fit orbital period of about 1 year. By construction, the model fitted to the data results in a uniform circular motion, as it does not take in consideration possible eccentricity of the orbit. To account for the latter, two additional parameters should be added in the visibility continuum model, (α,β), the angular coordinates in the sky of the ring/ellipsoid center with respect to the star, as an exponential term:

$$\mathrm{V}(u, v, \lambda) = \frac{\mathrm{F_s} + \mathrm{F_c}\,\mathrm{V_c}\exp[2\pi \mathrm{i}\,(u\,\alpha + v\beta)]}{\mathrm{F_s} + \mathrm{F_h} + \mathrm{F_c}}. \tag{3.1}$$

The parameters would reflect the eccentricity of the feature orbit if they do not correspond with the central star position, fixed at (0,0). In this case we are assuming that the eccentricity is constant in time, otherwise the number of additional parameters would be 2 multiplied by the number of epochs of each data set (20 for PIONIER and 13 for GRAVITY). The eccentricity of the crescent feature is not only interesting to assess so that a more accurate estimate of the orbital period can be obtained, but also to obtain hints on the possible origin mechanism producing the feature itself. Indeed, Ragusa et al. (2017) have shown through gas and dust numerical hydrodynamic simulations of a disk surrounding a binary system, that the interactions between the binary and the disk can cause the development of an eccentric inner cavity in the disk itself. Consequently, a crescent-like feature arise at the edge of the cavity in the gas density and in the

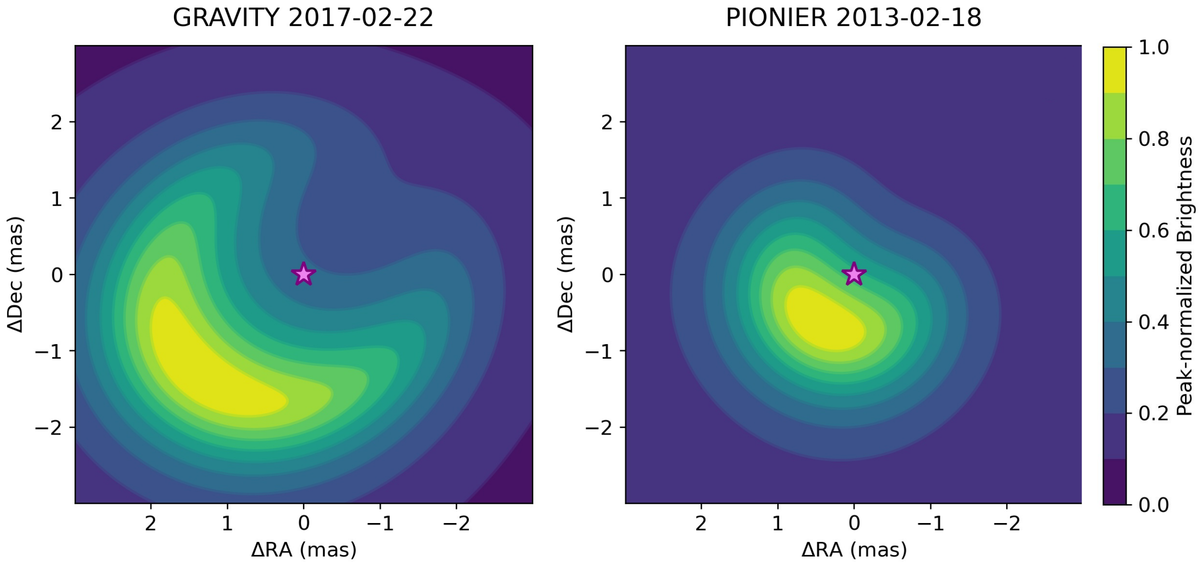

Figure 3.5: HD 98922 K-band (left) and H-band (right) continuum model contrast depiction.

mm dust grain population, which orbits with velocities close to the local Keplerian ones. The authors, therefore, suggest the scenario as a possible origin mechanism for asymmetric structures in transition disks. The asymmetric structures contrast ($C_{\mathrm{max,min}}$), the ratio between the disk maximum and minimum brightness, is found to be proportional to the binary mass ratio q, with a typical value of $C_{\mathrm{max,min}} \approx 5$ when $q = 0.1$.

For the case of HD 98922, the PIONIER and GRAVITY data analysis suggest a feature with a contrast between 1 and 3 for the H-band and between 2 and 10 for the K-band continuum (see Fig. 3.5), values comparable with the results obtained by Ragusa et al. (2017). However, three aspects seem to go in contrast to this scenario for the case of HD 98922. Firstly, the PIONIER data analysis does not suggest the presence of an inner disk cavity, but rather a centrally depressed continuum emission, as we can see in Fig 3.3. One explanation could be that the cavity is smaller than the angular resolution of the observations, and therefore not possible to constrain with the data available. The second contrasting point is the fact that the binary mass ratio of $q \approx 0.1$ would translate, knowing the HD 98922 primary star mass being $5 - 7\,\mathrm{M}_{\odot}$, in a companion mass of $0.5 - 0.7\,\mathrm{M}_{\odot}$. Nevertheless, no clear sign of a companion is detected by PIONIER and GRAVITY, and a binary+disk model did not give good fitting results (see Section 5.3 of the manuscript). Lastly, the PIONIER and GRAVITY data analysis suggest a feature with a sub-Keplerian orbital motion. If the orbit would follow the local Keplerian velocity, as predicted by the Ragusa et al. (2017) model, the period would be ~ 9 months, in contrast with the 12 months period found.

Interestingly, a similar horseshoe-like feature was detected for HD 98922 by SINFONI in the K-band (Caratti o Garatti et al. 2015), emission attributed by the authors to the disk scattered

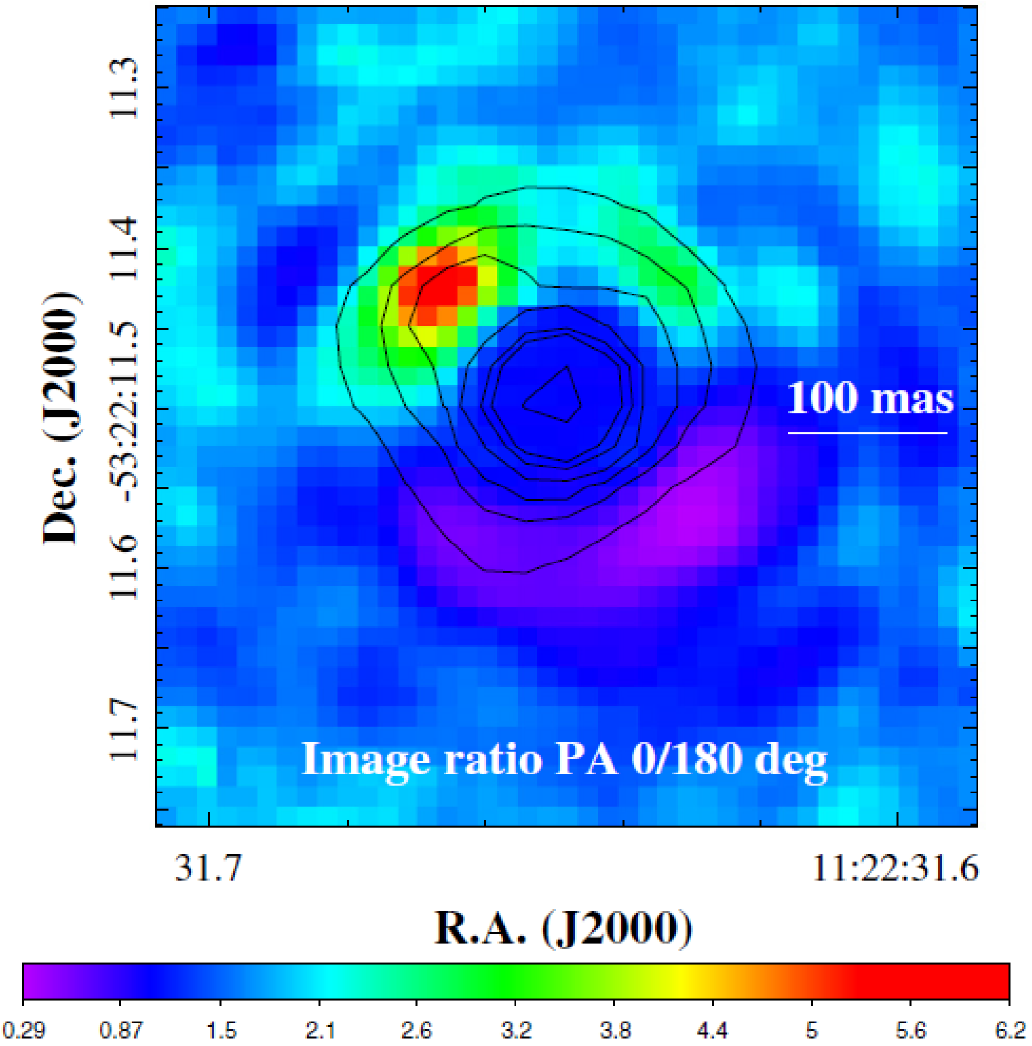

Figure 3.6: Intensity ratio image of two SINFONI K-band continuum images. The two images were taken at a PA of 0° and 180°. Image from Caratti o Garatti et al. (2015).

light. This circumstellar structure, shown in Fig. 3.6, is located at ~ 90 mas from the star (or ~ 60 au for d = 650.9 pc), and has a contrast of $C_{\mathrm{max,min}} = 3$. I support therefore the suggestion of Caratti o Garatti et al. (2015) that the disk might have a similar morphology from ~ 0.6 to ~ 60 au. Additionally, SINFONI did not detected any companion between 40 and 520 au, and it is intriguing the fact that the authors set a mass upper limit for the possible undetected companion of ~ 0.5 $M_{\odot}$. The asymmetric continuum was taken in consideration by the authors to create a model in order to fit HD 98922 AMBER/VLTI interferometric Brγ-line data. A magneto-centrifugally driven disk-wind model coupled with the asymmetric disk continuum was able to reproduce all the interferometric observations. The wind would extend from ~ 0.1 to ~ 1 au, with an opening angle of 30°, which produce a mass loss rate of ~ $2 \times 10^{-7}\,M_{\odot}\,\mathrm{yr}^{-1}$. The model was only tested for a single epoch data set. It would be interesting to test again the model, accounting for the time-variable continuum asymmetry and the time-variable interferometric Brγ-line data presented in this Chapter.

Chapter 4

A New Companion in HD 52721

In this chapter I present a study on HD 52721. The work is not yet in its final form and only a provisional manuscript is given in this thesis. Nonetheless, the results already obtained are remarkable and worthy of a display. After additional analysis of the data and discussion, the manuscript will be submitted to the A&A journal.

4.1 Science Case Overview

Multiple gravitationally bound stars with separation $\lesssim 0.1$ pc are not unusual systems observed in the sky. At least half of all the solar mass type stars have at least one companion, while protostars and YSOs show a higher rate of multiplicity (see Offner et al. 2022, and reference therein). Statistical studies have also shown that the rate of multiplicity and the number of companions for a given system (or order of multiplicity) decrease monotonically with increasing age, and increase likewise monotonically the more massive the primary star is (see Offner et al. 2022, and reference therein). Duchêne et al. (2013) suggested that the smooth variation of the multiple stars systems' key properties with the primary star mass, stems from a similar formation mechanism across all core masses. While the formation of single stars is generally well understood, the multiple stars systems one is still a matter of debate. The formation models proposed for multiple stars systems can be classified into three groups: fragmentation of a core or filament, fragmentation of the circumstellar accretion disk, and dynamical capture. A depiction of the models with observational and numerical simulation examples is given in Fig. 4.1. Each formation scenario is expected to translate to distinctive multiple stars systems properties. For a comprehensive review of the formation processes and stellar multiplicity in general, I refer the reader to the work of Offner et al. (2022). Here I shortly summarize some information relevant to introduce the work on HD 52721.

- The core/filament fragmentation scenario is thought to originate mainly from turbulence, and consists in a gravitational instability that leads to two or more regions of the core/filament to evolve and gravitationally collapse independently. Turbulence fragmentation leads to

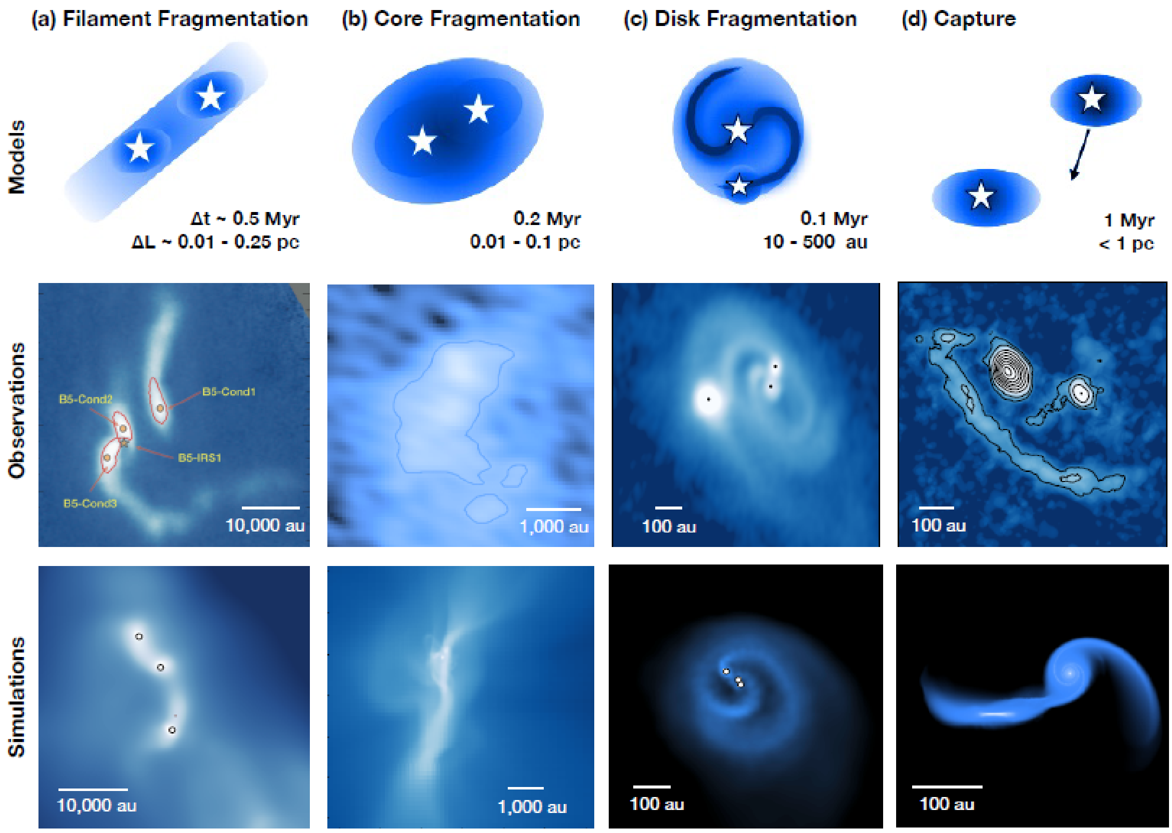

Figure 4.1: Multiple stars systems' formation scenarios. For each scenario (column), the top row depicts the model, the middle row shows an observational example, and the bottom row shows a numerical simulation example. On the top row, Δt and ΔL refer respectively to the process temporal and length scale. Image from Offner et al. (2022). References. Middle row, from left to right: (Pineda et al. 2015); (Kirk et al. 2017); (Reynolds et al. 2021); (Rodriguez et al. 2018). Bottom row, from left to right: (Guszejnov et al. 2021); (Offner et al. 2016); (Bate 2018); (Muñoz et al. 2015).

the production of multiple stars systems with companions separations between 100 au and 0.1 pc (Offner et al. 2022). Other mechanism are therefore required to explain close separation companions. Moreover, numerical simulations predict that turbulence fragmentation can produce only two or three companions per core, characterized by similar age since the process happens during the embedded phase (e.g., Lee et al. 2019; Offner et al. 2016, 2022). Higher order multiplicity systems are nonetheless observed (e.g., HD 52721, Obolentseva et al. 2021).

- The circumstellar disk fragmentation scenario is thought to originate in the same way spiral arms form in galaxies as proposed by Toomre (1964). This kind of gravitational instability is favoured to happen in the outer regions of massive disks, as expressed by the Toomre criterion for instability outbreak $Q_T \lesssim 1$, since the Toomre parameter Q_T commonly declines with radius. Moreover, numerical simulations of circumstellar disk fragmentation have shown to favor the production of equal mass binaries (e.g., Ochi et al. 2005).

- The dynamical capture scenario consists in the gravitationally bounding of two unbounded single stars, of a single star and a multiple stars system, or two multiple stars systems. Relevant in dense open clusters and globular clusters, this mechanism, as the previously two mentioned, is not able to produce very close binaries $\lesssim 1$ au (e.g., Wall et al. 2019).

The existence of very close binaries is thought to be caused by the inward migration of the companions subsequently their formation, with migration and final orbit settling taking place before the primordial cloud dissipates (see Offner et al. 2022, and reference therein). The migration is thought to be produce by gas accretion into the primary star and the consequent dynamical friction torque, that removes angular momentum on the companion, decreasing therefore the major axis of its orbit (e.g., Lee et al. 2019; Tokovinin et al. 2020). This dynamical evolution affects the cirumstellar environment in many ways. For example, the circumstellar disks around single stars are observed to be more massive and larger in radius than the one around primary stars of multiple stars systems (e.g., Akeson et al. 2019; Manara et al. 2019). Additionally, the tidal forces and truncation effects due to the companions presence and dynamical evolution, could affect the circumstellar and the circumbinary disks morphologies (e.g., Kurtovic et al. 2018).

Multi-epoch astrometric observations of multiple stars systems are therefore of prime interest, since they can give us information on their orbital properties, and therefore the separation of the companions. Moreover, the determination of the orbital parameters allows us to obtain a model-independent estimate of the dynamical mass of the system studied, where with dynamical mass one refers to the sum of each companion mass, derived through the third Kepler's Law, knowing the orbit period, the orbit semi-major axis, and the distance of the system, since the orbit semi-major axis estimate is in unit of arcsec (e.g., GRAVITY Collaboration et al. 2021a). If the orbit inclination is also known and radial velocity spectroscopic measurements are available, then the mass of each companion can be derived (e.g., Prato et al. 2018). These kind of studies are very influential on the theory of star formation and evolution. Indeed, nowadays, PMS stars masses are generally extracted from the Hertzsprung-Russell (HR) diagram, by comparing the positions of the stars in the latter with theoretical models of PMS stellar evolution (e.g., Baraffe et al. 2015). Additionally, beside the accuracy of the models, the mass estimates through the HR diagram are also affected by the precision of the required photometric measurements, and by the estimate of the interstellar medium and atmospheric extinction. Therefore, multi-epoch astrometric observations are nowadays one of the most reliable ways to estimate stellar masses.

In the light of the above remarks, I focused my last PhD project study on HD 52721. The object has been observed to be a binary-binary system, two companions orbiting around each other and at the same time orbiting at ~ 350 au around the primary close binary stars, having the latter a separation of ~ 0.1 au (Obolentseva et al. 2021; Perryman et al. 1997; Pogodin et al. 2011). Even though no IR excess has been detected in the circumstellar environment (e.g., Sissa et al. 2019), relating the stars to classical Be stars (Cauley et al. 2014), a significant amount of gas (Hα and Brγ) has been observed, from which a relevant mass accretion rate has been derived (between 10^{-7} and $10^{-5}\,M_{\odot}yr^{-1}$, Ababakr et al. 2016; Fairlamb et al. 2017; Grant et al. 2022). The stars are therefore generally considered Herbig Be stars (e.g., Vioque et al. 2018).

4.2 Goals of the Study

The goals of this work are to inquiry the multiple-stars system HD 52721 for interferometric binarity on au scales, and to gain information on the dynamic of its Brγ-line emission. As I will show, a new interferometric companion is detected. This result opens up new questions and analysis directions, that will be addressed in the future, like estimating the system orbit and its dynamical mass.

4.3 Approach, Steps, and Manuscript

The study is based on GRAVITY data, taken within the framework of the GTO YSO program. They came in my possession already reduced and calibrated, processes done with the GRAVITY data reduction software (Lapeyrere et al. 2014). As first author of a large cooperation article, here I list the actions done from my side:

(i) In depth literature study on HD 52721 and binarity in YSOs, which allowed me to write the Introduction Section of the manuscript.

(ii) Preliminary data analysis and calibration: 1) cleaning of the FT and SC data of outliers; 2) application of a wavelength calibration on the SC data, based on the atmospheric telluric lines position, radial velocity of the star, and the local standard of rest velocity; 3) visual and quantitative examination of the FT and SC data. This allowed me to write the Data Set Description Section of the manuscript.

(iii) Fit of the FT data for each epoch with `emcee` (Foreman-Mackey et al. 2013), through parametric geometrical models described in Berger et al. (2007) and Lazareff et al. (2017), in order to get information on possible circumstellar environment flux contribution, on possible companions, and their potential time-variability. While a model that accounts a single star and a ring is not able to reproduce the data, a binary model with no circumstellar environment contribution (except for the halo) fits well the data for each epoch.

(iv) Inspection for degenerate fitting solutions by looking for possible local minima in the parameters' χ^2 maps.

(v) Regarding the SC data, I fitted the squared visibilities with parametric geometrical models in order to get an estimate of the emitting gas region size. Additionally, I calculated the pure-line differential phases, and therefore, the pure-line photocenters shifts, from the total observed differential phases. I present more details of steps (iii), (iv), and (v) in the Methodology Section of the manuscript.

(vi) Calculated the equivalent width of the Brγ-line, its luminosity, the accretion luminosity of the system, and its mass accretion rate under the assumption of magnetospheric accretion, to examine possible line time-variability and evaluate different origin mechanisms.

(vii) In combination of a literature study on topics relevant to the results obtained, the work done in the steps above allowed me to write the Results and Discussion Section in the manuscript, as well as the Abstract and the Summary.

(viii) All the images and Tables were produced by myself with Python and the `matplotlib` package (Hunter 2007).

The approach, tools, equations, models, and additional data used to carry out the work are properly referenced in the manuscript.

Astronomy & Astrophysics manuscript no. output
March 19, 2023

©ESO 2023

The GRAVITY young stellar object survey

XI. A new companion in HD 52721 and its variable Brγ-line emission

GRAVITY Collaboration[⋆]: V. Ganci[1, 2], L. Labadie[1], K. Perraut[3], M. Benisty[3, 4], and A. Wojtczak[1]

(Affiliations can be found after the references)

Received xx, xxxx; accepted xx, xxxx

ABSTRACT

Context. The properties and evolution of circumstellar environments in young stellar objects are one the keys to understand the still obscure processes of planet formation. The situation is more complex in binary systems, in which the companions may dynamically influence their vicinity and the stellar processes happening in those areas.

Aims. The goal of this work was to test the variability of HD 52721 at mas spatial scales in its continuum and in its Brγ-line gas emission.

Methods. Multi-epochs observations of HD 52721 on milliarcsecond scales were taken with GRAVITY/VLTI in the near-infrared at low (R ∼ 20) and high (R ∼ 4000) spectral resolution, for a total observational period of 3 years. The interferometric visibilities were interpreted with geometrical models to gain information on the continuum brightness distribution. High spectral resolution quantities (visibilities and differential phases) were investigated to obtain information on the properties of the Brackett-γ (Brγ) line emitting region.

Results. HD 52721 is resolved by GRAVITY in all epochs except one, where the object is only marginally resolved. A simple binary model can reproduce the low spectral resolution data for all the epochs suggesting the presence of an additional companion located at ∼ 5 au from the primary. The marginally resolved data set hints that the companion follows an eccentric orbit. The gas region is spectrally resolved, but spatially unresolved. The high spectral resolution data show a strongly variable Brγ spectrum, and complex time-dependent differential phase signals.

Conclusions. Thanks to interferometric GRAVITY data, we suggest an additional companion for HD 52721, making it a five star system. The observations reinforce the already known significant time-variability of the Brγ-line emitting gas region. The complexity of the data however do not allow to unravel the origin of the emission.

Key words. binaries: close – stars: pre-main sequence – stars: variables: Herbig Ae/Be – stars: individual: HD 52721 – techniques: high angular resolution – techniques: interferometric

1. Introduction

Even though the multiplicity frequency in star systems estimated to date is affected by biases, is it certain that binary systems are not rare (Duchêne & Kraus 2013, and references therein). It is then of prime interest to understand how tidal interactions affect the circumstellar environment of young stars, the key stellar processes like time-dependent accretion phenomena, and therefore the process of planet formation, yet mysterious. Moreover, binary systems offer the unique opportunity to estimate model-independent dynamical masses through the determination of the orbital parameters (e.g., GRAVITY Collaboration et al. 2021), which would give useful information on the stellar formation and evolution processes.

In this work, we study HD 52721 (GU CMa, HIP 33868). It is generally considered a Herbig Ae/Be star (Herbig 1960; Alecian et al. 2013; Fairlamb et al. 2015; Reiter et al. 2018; Vioque et al. 2018). It is the the brightest (V = 6.58, Ducati 2002) member of the low-mass stars cluster called the "GU CMa cluster" made of relatively young stars (up to 10 Myr, Gregorio-Hetem et al. 2009). The cluster (d = 531 ± 163 pc, Fairlamb et al. 2015) is located away from the dense molecular material area of the star formation region CMa R1 (Shevchenko et al. 1999; Gregorio-Hetem et al. 2009), suggesting that star formation processes already stopped in its close environment. No evidence of an IR excess was found around HD 52721 (Hillenbrand et al. 1992; Sissa et al. 2019). Based on this fact, Cauley & Johns-Krull (2014) suggested that HD 52721 may be a classical Be star, since the system shows a very weak and broad He I λ10830 (Cauley & Johns-Krull 2014; Reiter et al. 2018). Beside He I, other gas emissions were observed. The system shows a strong single-peaked Hα emission line (Ababakr et al. 2016), and a Brγ line in absorption (EW = 0.5 ± 2.8 Å, Fairlamb et al. 2017), which was then dected as a large double-peaked profile emission line (EW = −6.2 ± 0.8 Å, Grant et al. 2022). Grant et al. (2022) suggested that the large EW variability may be due to a change in the accretion rate of the object ($10^{-7} - 10^{-5}\,M_\odot\,yr^{-1}$, Fairlamb et al. 2017, $2 \pm 2 \times 10^{-6}\,M_\odot\,yr^{-1}$, Grant et al. 2022), since continuum variability in Herbig Ae/Be stars is typically less than 0.3 mag, 0.04 mag for HD 52721 (Davies et al. 1990; Doering & Meixner 2009).

HD 52721 is known to be a quadruple star system. The first visual companion is located at ρ = 0.65 arcsec from the primary, differing in magnitude by Δ = 0.95 mag (Perryman et al. 1997). The primary was then observed to be a spectroscopic eclipsing binary at a separation of 0.19 mas with a period of 1.61 days (Pogodin et al. 2011). Additionally to the spectroscopic companion, azimuthal circumstellar inhomogeneities were found in the circumstellar envelope, which

---

[⋆] GRAVITY is developed in a collaboration by the Max Planck Institute for Extraterrestrial Physics, LESIA of Paris Observatory and IPAG of Université Grenoble Alpes / CNRS, the Max Planck Institute for Astronomy, the University of Cologne, the Centro de Astrofísica e Gravitação and the European Southern Observatory.

rotate synchronously with the orbital motion of the binary component stars (Pogodin et al. 2011; Beskrovnaya et al. 2013; Pavlovskiy et al. 2015; Pogodin et al. 2020). Finally, the visual companion was resolved through speckle interferometry and found to be two separate stars (Obolentseva et al. 2021).

We present in this work GRAVITY observations of HD 52721 taken during a period of 3 years, in order to test the variability of the system at mas spatial scales in its continuum emission as well as in its Brγ-line gas one. In Section 2 we give information on the observations and describe the interferometric data; in Section 3 a description of the methodology used to analyze the data is given; Section 4 presents our results and in Section 5 we summarize the main findings.

2. Dataset description

2.1. Observations

HD 52721 was observed with VLTI/GRAVITY (Gravity Collaboration et al. 2017) using the four 1.8 m Auxiliary Telescopes (ATs) in 4 different epochs between 2018 and 2021. Data were obtained through the large A0-G1-J2-J3 baseline configuration, and through the medium D0-G2-J3-K0 baseline configuration. The data consist in high spectral resolution (R $\approx$ 4000) observables recorded by the science channel (SC) detector across the K band with individual integration times of 30 s, as well as in low spectral resolution (R $\approx$ 20) observables recorded by the fringe tracker (FT) detector (Lacour et al. 2019). The spatial frequency ranges between about 15 Mλ to 65 Mλ with a maximal angular resolution of $\lambda/2$B, 1.68 mas for the longest baseline of 132 m, which corresponds to 0.89 au at the distance of the object. Each observation block corresponds to 5 minutes on the object. In total, 27 files were acquired. HD 52721 observations were preceded by the observation of a point-source calibration star, close to our object on the sky, and of similar spectral type and brightness in order to calibrate the atmospheric and instrumental transfer function. Further details on the executed runs and observing conditions are listed in Table 1.

2.2. Data reduction and calibration

The GRAVITY data were reduced and calibrated using the GRAVITY data reduction software (Lapeyrere et al. 2014). For the low-resolution FT data, we discarded the first spectral channel, which might be affected by the metrology laser operating at 1.908 μm. The FT calibrated squared visibilities, closure phases, and the *(u,v)* plane coverage for each single epoch can be found in Fig. A.1 (left, central, and right panel, respectively). Following Gravity Collaboration et al. (2019) and Gravity Collaboration et al. (2021), we applied a floor value on the error bars of 2% for the squared visibilities and 1° on the closure phases as the error bars computed by the pipeline might be underestimated or correlated.

In Fig. A.2 are shown the high spectral resolution GRAVITY data after zooming in the wavelength range of the Brγ line between 2.162 and 2.170 μm. For each epoch, the data set contains the spectrum, the calibrated squared visibilities, and the calibrated differential phases (top, left, and right panels, respectively). The observables for one epoch result from the averaging of N individual block files as listed in the fifth column of Table 1. The error bars used are the ones derived from the reduction and calibration process and propagated through the averaging process. These are on the order of 0.01% for the spectrum, 0.02 for the squared visibilities, and 1° for the differential phases.
The continuum-normalization of the GRAVITY science object spectrum of each epoch was done by fitting the slope of the raw spectrum and dividing the latter by the resulting fit. The first step of the wavelength calibration was done by comparing the observed wavelength positions of the telluric lines in the HD 52721 spectrum for each epoch with respect to the positions of the telluric lines present in the IR spectrum of the atmospheric transmission above Cerro Pachon, generated using the ATRAN modeling software (Lord 1992) accounting for 4.3 mm water vapor column and 1.5 mm airmass column, available on the Gemini Observatory website. The atmospheric transmission spectrum was convolved by a Gaussian with FHWM of 6 Å to have the same resolution as GRAVITY. The correction results in a blue-shift between 1 and 6 Å depending on the epoch. The HD 52721 spectrum was then corrected for the star radial velocity (21.7 km/s) and its proper motion with respect to the local standard of rest, with a value that depends on the epoch of observations (between about -18 and 12 km/s). The same corrections (telluric lines calibration, radial velocity correction, and local standard of rest correction), were also applied on the SC visibilities and differential phases for each epoch.

2.3. Continuum data overview

GRAVITY resolved HD 52721 in all epochs, except for the E2 observation where the system is only marginally resolved. Both the medium and the large condifurations fully resolve the system, with squared visibilities ranging between 0 and 1.0 depending on the spatial frequency. The visibilities observed in the E1 and E4 observations clearly show a sinusoidal shape, suggesting a binary system. More complex is the signal observed in the E3 epoch. Strong closure phases signals are detected in all epochs and for all baselines, except in the E2 observation where they are null at all spatial frequencies. They range between $-70°$ and $70°$ in the medium configuration E2 observation, and between $-100°$ and $100°$ in the large E1, and E4 ones. The data therefore clearly suggest an asymmetric brightness distribution in the K band continuum.

2.4. Brγ-line data overview

As we see from the top panels in Fig. A.2 showing the spectrum of the system for each epoch, HD 52721 shows a highly variable double-peaked Brγ emission line in its intensity and shape. The continuum-normalized blueshifted-peak flux ranges between 1.25 and 1.45 depending on the epoch, while the redshifted-peak one ranges between 1.2 and 1.4, always weaker than the blueshifted-peak except in E2. Considering the 3 Å error on the GRAVITY spectral channel wavelength, the blueshifted-peak's position can be consider constant through the epochs at our spectral resolution, while the redshifted-peak's one clearly varies going from 2.1666 to 2.1675 μm. Regarding the total squared visibilities, they range between ≈ 0.2 and ≈ 1.0 depending on the epoch and baseline configurations. We note that for some baselines in the E3 and E4 epochs the total squared visibilities increase in the Brγ wavelength range with respect to the visibility in the continuum range, meaning that the line-emitting gas region is more compact than the continuum. For the other baselines they appear to be spectrally flat with no clear signature at 2.16612 μm, or too noisy to see a clear signature (E1). Finally,

Table 1. Observation logs of the VLTI/GRAVITY HD 52721 observations

ID	Date	UT	Configuration	N	Calibrator	Seeing [″]	τ_0 [ms]	Airmass	ID$_{obs}$
E1	06-03-2018	2:45	A0-G1-J2-J3	8	HD 53244	0.66-1.60	1.8-4.1	1.16-1.42	0100.C-0278(F)
E2	18-03-2019	2:36	D0-G2-J3-K0	4	HD 67751	0.44-0.64	7.1-9.2	1.07-1.11	0102.C-0408(D)
E3	23-12-2020	4:54	D0-G2-J3-K0	4	HD 31464	0.51-1.20	3.9-7.8	1.03-1.04	106.212G.002
E4	09-02-2021	2:42	A0-G1-J2-J3	11	HD 53244	0.62-1.61	2.3-5.3	1.03-1.23	106.212G.003

Notes. The date format is day-month-year. N denotes the number files that have been recorded on the target.

the differential phases signals range between −20° and 10° and have different shapes (flat, single-peaked, or *S*-shape) for the different epochs and baselines.

3. Methodology

3.1. Continuum: Low spectral resolution data

The properties of the spatially resolved continuum emission were investigated with the help of the low spectral resolution FT data. The squared visibility curve was modeled through non-chromatic geometrical models accounting for two point-like stars depicting a binary system and a scattered light component (called halo), whose visibility following Berger & Segransan (2007) is given by:

$$V(u, v, \lambda) = \frac{F_{\star,1} + F_{\star,2}\exp[2\pi i\,(u\,\alpha_{\star,2} + v\beta_{\star,2})]}{F_{\star,1} + F_{\star,2} + F_H}, \qquad (1)$$

where $F_{\star,1}$ is the flux contribution of the primary star, $F_{\star,2}$ the secondary star one, F_H the one of the halo, $\alpha_{\star,2}$ and $\beta_{\star,2}$ the position in the sky of the secondary star. F_H is not a free parameter, but obtained according to $F_H = 1 - F_{\star,1} - F_{\star,2}$. The stars are assumed to be unresolved at all baselines (visibility constant and equal to 1), and the halo is assumed to be a fully resolved emission component with a visibility of zero. Additionally, following the work of Lazareff et al. (2017), a model accounting a point-like central star, a halo, and an azimuthally-modulated ring representing the circumstellar environment was used, whose visibility is given by:

$$V(u, v, \lambda) = \frac{F_\star + F_R\,V_R}{F_\star + F_H + F_R}, \qquad (2)$$

where F_R is the flux contribution of the ring, and V_R is its visibility given by equation 9 of Lazareff et al. (2017). We refer to the former work for more details on the azimuthally-modulated ring model.

The model fitting consists in a first minimization procedure with `scipy.optimize.minimize` using a Sequential Least Squares Programming method to get an initial guess of the free parameters, followed by a procedure based on a Markov chain Monte Carlo (MCMC, Foreman-Mackey et al. 2013) numerical approach, which is robust against trapping in local minima. The errors on the reduced chi-squared χ^2_r are calculated considering the χ^2_r as a stochastic variable following Gravity Collaboration et al. (2021). The results of the GRAVITY FT data analysis are shown in Section 4.1.

3.2. Gas: High spectral resolution data

To estimate the Brγ gas region size, kinematics, and displacement with respect to the continuum emission from the GRAVITY SC visibilites (V) and differential phases (ϕ), we extrapolated the pure-line contribution (subscript *L*) from the observed total quantities (line+continuum, subscript *tot*, where the continuum accounts for the star, the disk, and the halo contributions), following Weigelt et al. (2011) and Mendigutía et al. (2015):

$$F_L^2 V_L^2 = F_{tot}^2 V_{tot}^2 + F_{cont}^2 V_{cont}^2 - 2F_{tot}V_{tot}F_{cont}V_{cont}\cdot\cos\phi_{tot}, \qquad (3)$$

$$\sin\phi_L = \sin\phi_{tot}\frac{F_{tot}V_{tot}}{F_L V_L}, \qquad (4)$$

where the F parameters refer to the flux contributions of each component. The values for F_{cont} and V_{cont} are the averaged ones at both sides of Brγ line (since the spectrum is continuum-normalized $F_{cont} = 1$). Finally, we derived the wavelength-dependent photocenter displacements along each baseline from the pure-line differential phases following Lachaume (2003):

$$\mathbf{p} = \frac{-\phi_L}{2\pi}\cdot\frac{\lambda}{\mathbf{B}}, \qquad (5)$$

where **p** is the projection on the baseline **B** of the 2D photocenter vector with origin on the continuum photocenter of the system. The results of the GRAVITY SC data analysis are shown in Section 4.2.

4. Results and Discussion

4.1. A new binary companion

Of the two models discussed in Sect. 3.1, the fit of the FT data to the binary model gave the best results in term of χ^2, in which both squared visibilities and closure phases are well fitted for all epochs, suggesting a new companion in the HD 52721 system. The single-star plus azimuthally-modulated ring model was only able to reproduce the data observed in the E2 epoch, but not the ones observed in the other three epochs, resulting in $\chi^2_r > 100$. To have a better fit of the data and obtain information on the stars' temperatures we tried a chromatic binary model that accounts for two additional free parameters, the spectral indeces of both stars. The additional parameters did not improve the fit of the data in terms of χ^2 for E1, E2, and E3. A small improvement was obtained for E4, however the spectral indeces estimates have non-physical values (< -8). We therefore conclude that the current data do not allow to estimate this parameters.

We performed a wide scan range of the fitted parameters to find convergence toward a global solution. The results of the minimization are presented in Table 2, Fig. A.1, and Fig. B.1 for the best binary model. GRAVITY was not able to resolve the spectroscopic eclipsing binary observed by Pogodin et al. (2011). Therefore, for the rest of the paper we will treat the spectroscopic binary as a single star-like object (referred as *primary star*). We note that the primary star and the newly detected companion show a relatively small variability in their photospheric near-IR flux contribution through the epochs, with the primary star having a contribution of ~60 − 70%, and the

Table 2. Binary model FT data best-fit solution

Epoch	$F_{\star,1}$ [%]	$F_{\star,2}$ [%]	F_H [%]	$\alpha_{\star,2}$ [mas]	$\beta_{\star,2}$ [mas]	χ^2_r
E1	59.2 ± 0.1	29.5 ± 0.1	11.3 ± 0.2	-9.712 ± 0.002	-2.438 ± 0.002	13.9 ± 1.3
E2	$31.2^{+37.8}_{-21.2}$	$67.8^{+21.2}_{-37.8}$	0.1 ± 0.1	$-0.393^{+0.067}_{-0.184}$	$-0.042^{+0.052}_{-0.057}$	0.6 ± 0.1
E3	69.2 ± 0.1	30.5 ± 0.1	0.3 ± 0.1	-5.806 ± 0.006	-5.454 ± 0.010	17.4 ± 5.4
E4	67.4 ± 0.1	28.1 ± 0.1	4.5 ± 0.1	-6.224 ± 0.003	-5.599 ± 0.002	4.8 ± 0.3

Notes. $F_{\star,1}$ is the flux contribution of the primary star, $F_{\star,2}$ the secondary star one, F_H the one of the halo, $\alpha_{\star,2}$ and $\beta_{\star,2}$ the position in the sky of the secondary star. F_H is not a free parameter, but obtained according to $F_H = 1 - F_{\star,1} - F_{\star,2}$. The error estimates, derived through the MCMC fitting procedure, are given by the 16th and 84th percentiles of the samples in the MCMC marginalized distributions shown in Fig. B.1.

secondary having a contribution of $\sim 28 - 31\%$ depending on the epoch. The contribution of the scattered light is estimated to be small, close to null for the medium E2 and E3 data sets, $\sim 10\%$ for the E1 one, and $\sim 5\%$ for the E4 one. We have to remember however that these values are estimated through data taken with medium and large baseline configurations, and that for a reliable estimate of this parameter one requires small baselines configurations (Setterholm et al. 2018), which are not yet available for this object. Moreover, Gravity Collaboration et al. (2023, in prep.) have shown that estimates of the scattered light contribution made solely through large baseline configuration data sets are not reliable. If the E1 epoch is not considered, the variability of the primary star flux contribution is significantly smaller, of the order of 2%. Nonetheless, the visibility sinusoidal shape and the strong closure phases signals observed at all baselines, coupled with the good fitting results through a binary model, make a strong evidence for a newly detected companion.

In Fig. 1 we can see visually how the position of the secondary star varies through the epochs with respect to the primary one. The positions are well constrained as shown in Fig. B.1 and Fig. B.2, where the absolute minima in the secondary star position χ^2-maps are well defined for each epoch. We note the very close position of the two stars in E2. This is a direct consequence of the interferometric quantities observed in this epoch, i.e. squared visibilities close to 1 and null closure phases signals, where the interferometer was not able to distinguish the two stars. The secondary star position in E2 suggests a significantly eccentric orbit. Two additional observations of the object were taken after the beginning of this work with GRAVITY, in February 7 2022 and February 14 2022, with the medium and large baseline configuration, respectively. The implementation of these epochs in the paper is planned before its submission to the A&A journal. This will increase the number of the secondary star positions with respect to the primary through the epochs, with the goal of better constraining the parameters of the system orbit through a fit of the data.

One could argue that the secondary star is a background star not related to the primary. However, as we can see in Fig. 1, the relative position of the primary star after 1 year of proper motion with respect to the secondary one would translate in interferometric quantities different than the ones observed by GRAVITY. It's clear that if the two stars would not be related, the interferometer would be able to resolve the system in E2, which is not the case.

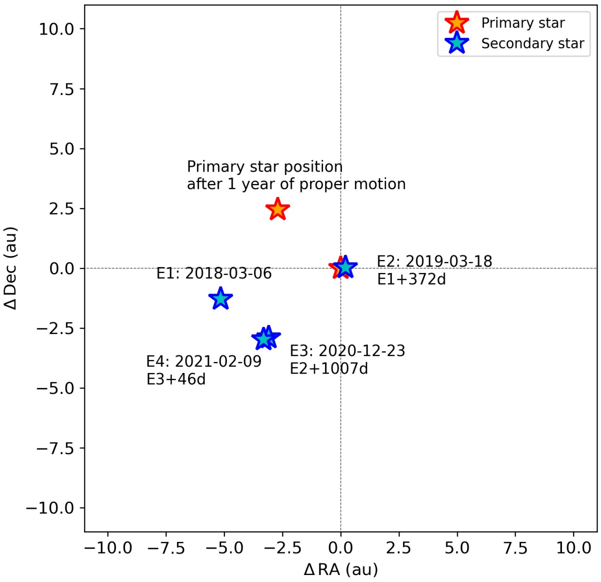

Fig. 1. Secondary star position with respect to the primary one through the epochs, according to the model described in Sec. 4.1 and in Table 2.

4.2. The Brγ-line gas emission in HD 52721

We exploited the high-spectral resolution data of GRAVITY in the Brγ region to constrain the spatial scale of the hot gas emitting component, following the formalism in Sect. 4.2. Unfortunately, the resulting pure-line visibilities plotted in the left plots of Fig.A.2 are of the order of unity for all the baselines for the E2, E3, and E4 epochs. Considering the error bars in E1 we can say that the gas region is spatially unresolved in all epochs. Further information on the spatial and kinematics properties of the gas component were obtained through the differential phase signal. Typically, the differential phases provide information on photocenter displacements along the baselines on angular scales that can surpass the nominal resolution of the interferometer. Figure A.2 shows the GRAVITY pure-line differential phases. After removal of the continuum contribution, the signatures show an amplitude in the differential phase ranging between −50° and +50°. The resulting deprojected photocenter shifts per spectral channel, with reference frame fixed to the continuum photocenter location, are shown in Fig. 2. The binarity hinted by the FT data analysis makes the interpretation of the pure-line photocenters not trivial. This is due to the fact that both the primary and secondary stars could have Brγ-line emitting gas, and the gas photocenters would give the barycenter of the two

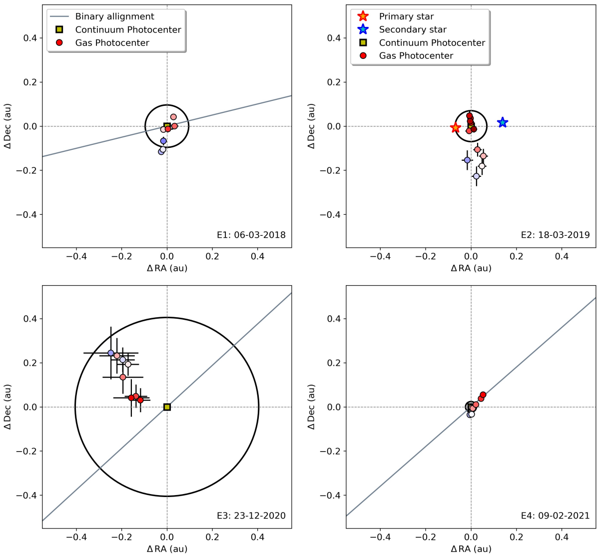

Fig. 2. Brγ pure-line photocenters shifts (colored circles) with respect to the continuum photocenter (yellow square). The different colors of the circles refer to the different gas velocities as in Fig. A.2. The black circle around the continuum photocenter gives its error. The gray line gives the direction connecting the two binary stars.

emissions. To understand better the situation we refer to Fig. 3, where three different scenarios are depicted. Each scenario differs on the relative gas emission intensity of the two stars. The gas photocenter, with reference frame fixed to the continuum photocenter location, is closer to the star where the Brγ-line emission is more intense, and it is clear that the photocenter does not give the real spatial location of the gas. The case of HD 52721 seen through GRAVITY is even more complex, since as we see in Fig. 2, the gas photocenters are not alligned with the direction connecting the two stars, but they show an almost 90° offset in their position angle in the E1, E2, and E3 data set. The offset is null in the E4 data set.

Finally, it is our interest to quantify the variability shown through the epochs by the Brγ-line spectrum. The line is a common accretion tracer of circumstellar environment material into the star (Grant et al. 2022, and references therein). It can also give information on the kinematics of the gas closest to the star, like infall accretion or outward wind (e.g., Muzerolle et al. 2001). In Fig. 4 are shown the HD 52721 wavelength-calibrated and continuum-normalized GRAVITY Brγ-line spectra from our 4 observations. From the equivalent widths (EWs), listed in Table 3, and the 2MASS K-band magnitude of the object ($m_K = 6.038$ mag, Cutri et al. 2003), we derived the line luminosity for each epoch as follows. The EWs listed are the ones corrected for both the underlying photospheric absorption, and the presence of any excess continuum emission. The correction was calculated by Grant et al. (2022) for HD 52721 to be ∼ 1 Å. Therefore, we derived the flux of the line, $F_{\mathrm{Br}\gamma}$, by multiplying $\mathrm{EW}^{\mathrm{corr}}_{\mathrm{Br}\gamma}$ with the continuum flux at the center of the line given by:

$$F_{\mathrm{cont}} = F_{0,\mathrm{K}} 10^{-0.4(m_{\mathrm{K}} - 0.1 A_{\mathrm{V}})}, \tag{6}$$

where $F_{0,\mathrm{K}}$ is the flux in the K-band of a $m_{\mathrm{K}} = 0$ star (4.28×10^{-11} erg/s/cm^2/Å, Rodrigo & Solano 2020), and $A_{\mathrm{V}} = 0.8$ (Grant et al. 2022). The fluxes were then converted into the line luminosity, $L_{\mathrm{Br}\gamma}$, using the distance of our object ($d = 531 \pm 163$, Fairlamb et al. 2015). Finally, following Fairlamb et al. (2017), we derived the accretion luminosities:

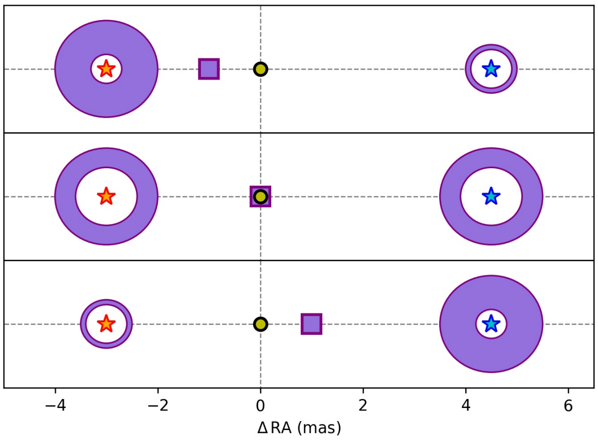

Fig. 3. Effect of different gas emission ratios in a binary system on the gas photocenter position (purple square) with respect to the continuum photocenter (yellow circle). The primary star (orange) has a higher continuum flux contribution than the secondary (cyan). The purple circles around the stars refer to their gas regions, larger for stronger emission.

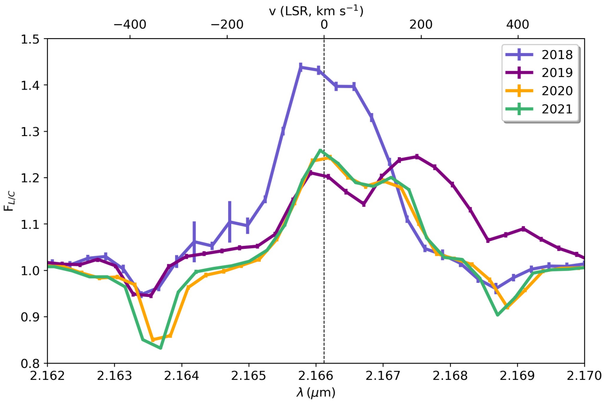

Fig. 4. HD 52721 wavelength-calibrated and continuum-normalized Brγ-line GRAVITY spectra for the different epochs.

$$\log_{10}\left(\frac{L_{\mathrm{acc}}}{L_\odot}\right) = (1.30 \pm 0.09) \log_{10}\left(\frac{L_{\mathrm{Br}\gamma}}{L_\odot}\right) + (4.46 \pm 0.23), \tag{7}$$

which were converted to the mass accretion rates:

$$\dot{M}_{\mathrm{acc}} = \frac{R_\star L_{\mathrm{acc}}}{M_\star G}, \tag{8}$$

with $R_\star = 5.7 \pm 1.7\,R_\odot$ radius of the star, and $M_\star = 9.5 \pm 6.8\,M_\odot$ mass of the star, both from Fairlamb et al. (2015). Unfortunately, the uncertainties on the quantities are large, due to the large uncertainties on the distance, on the mass, and on the radius of the object, and only speculations on the origin of the emission can be made. It is clear however the variability in EW and shape of the Brγ-line, going from a strong almost single-peaked line in E1, to a clear and strong double-peaked line in November 19 2018 (Grant et al. 2022), to a weaker double-peaked line in E2, in which the read peak gets broader and stronger than the blue

Table 3. Brγ-line properties

Epoch	$\mathrm{EW}^{\mathrm{corr}}_{\mathrm{Br}\gamma}$ [Å]	$\mathrm{L}_{\mathrm{Br}\gamma}$ [$10^{-2}\,\mathrm{L}_{\odot}$]	$\mathrm{L}_{\mathrm{acc}}$ [$\mathrm{L}_{\odot}$]	$\dot{\mathrm{M}}_{\mathrm{acc}}$ [$10^{-8}\,\mathrm{M}_{\odot}$/yr]
E1	-8.10 ± 0.57	1.3 ± 0.8	98 ± 79	1.9 ± 1.9
E2	-6.08 ± 0.41	0.9 ± 0.6	68 ± 54	1.3 ± 1.3
E3	-4.48 ± 0.27	0.7 ± 0.4	45 ± 37	0.9 ± 0.9
E4	-4.59 ± 0.14	0.7 ± 0.4	47 ± 38	0.9 ± 0.9

Notes. With $\mathrm{EW}^{\mathrm{corr}}_{\mathrm{Br}\gamma}$ we refer to the observed EW corrected for the star photospheric absorption and the excess continuum emission. This results in a $\mathrm{EW}^{\mathrm{corr}}_{\mathrm{Br}\gamma}$ which is larger than 1 Å in absolute value (Grant et al. 2022) with respect to the observed EW.

one, and finally into a line shape which seems to go close to a single peak profile in E3 and E4, with the red peak being again weaker than the blue one. The additional GRAVITY observations mentioned earlier, and possible future observations, could help us to check if the change in line shape is cyclical and related to the orbit of the newly detected interferometric binary.

5. Summary

In this work, we report a study of the multi-objects system HD 52721, using new near-infrared interferometric data obtained with VLTI/GRAVITY. Here we summarize our results:

- GRAVITY resolved the system in all epochs except E2, where it is only marginally resolved with no CP signals detected. The Vis^2 show a clear sinusoidal shape, characteristic of a binary system.
- A simple geometrical binary model can reproduce well the data, suggesting a fifth companion in HD 52721 located at $\sim$ 5 au. The position of the companion in E2 suggests an eccentric orbit.
- The Brγ-line is strongly variable in EW and line-shape, going from single-peaked to double-peaked. The two peaks also vary in intensity; notably, the red peak gets broader and stronger than the blue one in E2.
- The gas photocenters, derived from the pure-line differential phases, are located close to the continuum photocenter, and their interpretation is not trivial. Their positions vary through the epochs, and show a $\sim 90°$ offset with the direction connecting the two companions. The offset is null in E4.

The implementation of the new GRAVITY observations, and possible future ones, will allow us to better estimate the orbit of the system by increasing the number of the companion positions through time. Moreover, it will be interesting to check if the Brγ-line shape variability is related with the position of the newly detected companion.

Acknowledgements

V.G. was supported for this research through a stipend from the International Max Planck Research School (IMPRS) for Astronomy and Astrophysics at the Universities of Bonn and Cologne, and from the Bonn-Cologne Graduate School of Physics and Astronomy (BCGS). This work is based on observations made with ESO Telescopes at the La Silla Paranal Observatory under program IDs listed in Table 1. We acknowledge the Gemini Observatory for the use of the IR spectrum model of the atmospheric transmission above Cerro Pachon. This research has made use of the Spanish Virtual Observatory (https://svo.cab.inta-csic.es) project funded by MCIN/AEI/10.13039/501100011033/ through grant PID2020-112949GB-I00.

References

Ababakr, K. M., Oudmaijer, R. D., & Vink, J. S. 2016, MNRAS, 461, 3089
Alecian, E., Wade, G. A., Catala, C., et al. 2013, MNRAS, 429, 1001
Berger, J. P. & Segransan, D. 2007, New A Rev., 51, 576
Beskrovnaya, N. G., Pogodin, M. A., Valyavin, G. G., et al. 2013, Astrophysics, 56, 42
Cauley, P. W. & Johns-Krull, C. M. 2014, ApJ, 797, 112
Cutri, R. M., Skrutskie, M. F., van Dyk, S., et al. 2003, VizieR Online Data Catalog, II/246
Davies, J. K., Evans, A., Bode, M. F., & Whittet, D. C. B. 1990, MNRAS, 247, 517
Doering, R. L. & Meixner, M. 2009, AJ, 138, 780
Ducati, J. R. 2002, VizieR Online Data Catalog
Duchêne, G. & Kraus, A. 2013, ARA&A, 51, 269
Fairlamb, J. R., Oudmaijer, R. D., Mendigutía, I., Ilee, J. D., & van den Ancker, M. E. 2015, MNRAS, 453, 976
Fairlamb, J. R., Oudmaijer, R. D., Mendigutia, I., Ilee, J. D., & van den Ancker, M. E. 2017, MNRAS, 464, 4721
Foreman-Mackey, D., Hogg, D. W., Lang, D., & Goodman, J. 2013, PASP, 125, 306
Grant, S. L., Espaillat, C. C., Brittain, S., Scott-Joseph, C., & Calvet, N. 2022, ApJ, 926, 229
Gravity Collaboration, Abuter, R., Accardo, M., et al. 2017, A&A, 602, A94
GRAVITY Collaboration, Eupen, F., Labadie, L., et al. 2021, A&A, 648, A37
Gravity Collaboration, Ganci, V., Labadie, L., et al. 2021, A&A, 655, A112
Gravity Collaboration, Perraut, K., Labadie, L., et al. 2019, A&A, 632, A53
Gregorio-Hetem, J., Montmerle, T., Rodrigues, C. V., et al. 2009, A&A, 506, 711
Herbig, G. H. 1960, ApJS, 4, 337
Hillenbrand, L. A., Strom, S. E., Vrba, F. J., & Keene, J. 1992, ApJ, 397, 613
Lachaume, R. 2003, A&A, 400, 795
Lacour, S., Dembet, R., Abuter, R., et al. 2019, A&A, 624, A99
Lapeyrere, V., Kervella, P., Lacour, S., et al. 2014, in Society of Photo-Optical Instrumentation Engineers (SPIE) Conference Series, Vol. 9146, Proc. SPIE, 91462D
Lazareff, B., Berger, J. P., Kluska, J., et al. 2017, A&A, 599, A85
Lord, S. D. 1992, A new software tool for computing Earth's atmospheric transmission of near- and far-infrared radiation, NASA Technical Memorandum 103957
Mendigutía, I., de Wit, W. J., Oudmaijer, R. D., et al. 2015, MNRAS, 453, 2126
Muzerolle, J., Calvet, N., & Hartmann, L. 2001, ApJ, 550, 944
Obolentseva, M. A., Dyachenko, V. V., Pogodin, M. A., et al. 2021, Astrophysical Bulletin, 76, 292
Pavlovskiy, S. E., Pogodin, M. A., Kupriyanov, V. V., & Gorshanov, D. L. 2015, Astronomy Letters, 41, 289
Perryman, M. A. C., Lindegren, L., Kovalevsky, J., et al. 1997, A&A, 323, L49
Pogodin, M. A., Beskrovnaya, N. G., Guseva, I. S., Pavlovskiy, S. E., & Rusomarov, N. 2011, Astrophysics, 54, 214
Pogodin, M. A., Beskrovnaya, N. G., Pavlovskiy, S. E., et al. 2020, Azerbaijani Astronomical Journal, 15, 143
Reiter, M., Calvet, N., Thanathibodee, T., et al. 2018, ApJ, 852, 5
Rodrigo, C. & Solano, E. 2020, in XIV.0 Scientific Meeting (virtual) of the Spanish Astronomical Society, 182
Setterholm, B. R., Monnier, J. D., Davies, C. L., et al. 2018, ApJ, 869, 164
Shevchenko, V. S., Ezhkova, O. V., Ibrahimov, M. A., van den Ancker, M. E., & Tjin A Djie, H. R. E. 1999, MNRAS, 310, 210
Sissa, E., Gratton, R., Alcalà, J. M., et al. 2019, A&A, 630, A132
Vioque, M., Oudmaijer, R. D., Baines, D., Mendigutía, I., & Pérez-Martínez, R. 2018, A&A, 620, A128
Weigelt, M., Baur, O., Reubelt, T., Sneeuw, N., & Roth, M. 2011, in ESA Special Publication, Vol. 696, 4th International GOCE User Workshop, 36

---

[1] I. Physikalisches Institut, Universität zu Köln, Zülpicher Str. 77, 50937, Köln, Germany
e-mail: `ganci@ph1.uni-koeln.de`
[2] Max-Planck-Institute for Radio Astronomy, Auf dem Hügel 69, 53121 Bonn, Germany
[3] Univ. Grenoble Alpes, CNRS, IPAG, 38000 Grenoble, France
[4] Unidad Mixta Internacional Franco-Chilena de Astronomía (CNRS, UMI 3386), Departamento de Astronomía, Universidad de Chile, Camino El Observatorio 1515, Las Condes, Santiago, Chile

Appendix A: GRAVITY Data

In this Section are shown the GRAVITY FT data (Fig. A.1) and SC data (Fig. A.2). The residual of the binary model fit to the FT data are also shown in Fig. A.1. In Fig. A.2 the pure-line visibilities and differential phases are likewise presented.

Appendix B: FT data binary model fit corner plots and χ^2-maps

In this Section are shown the MCMC marginal posterior distributions for the FT data binary model fit and the secondary star position parameters' χ^2-maps.

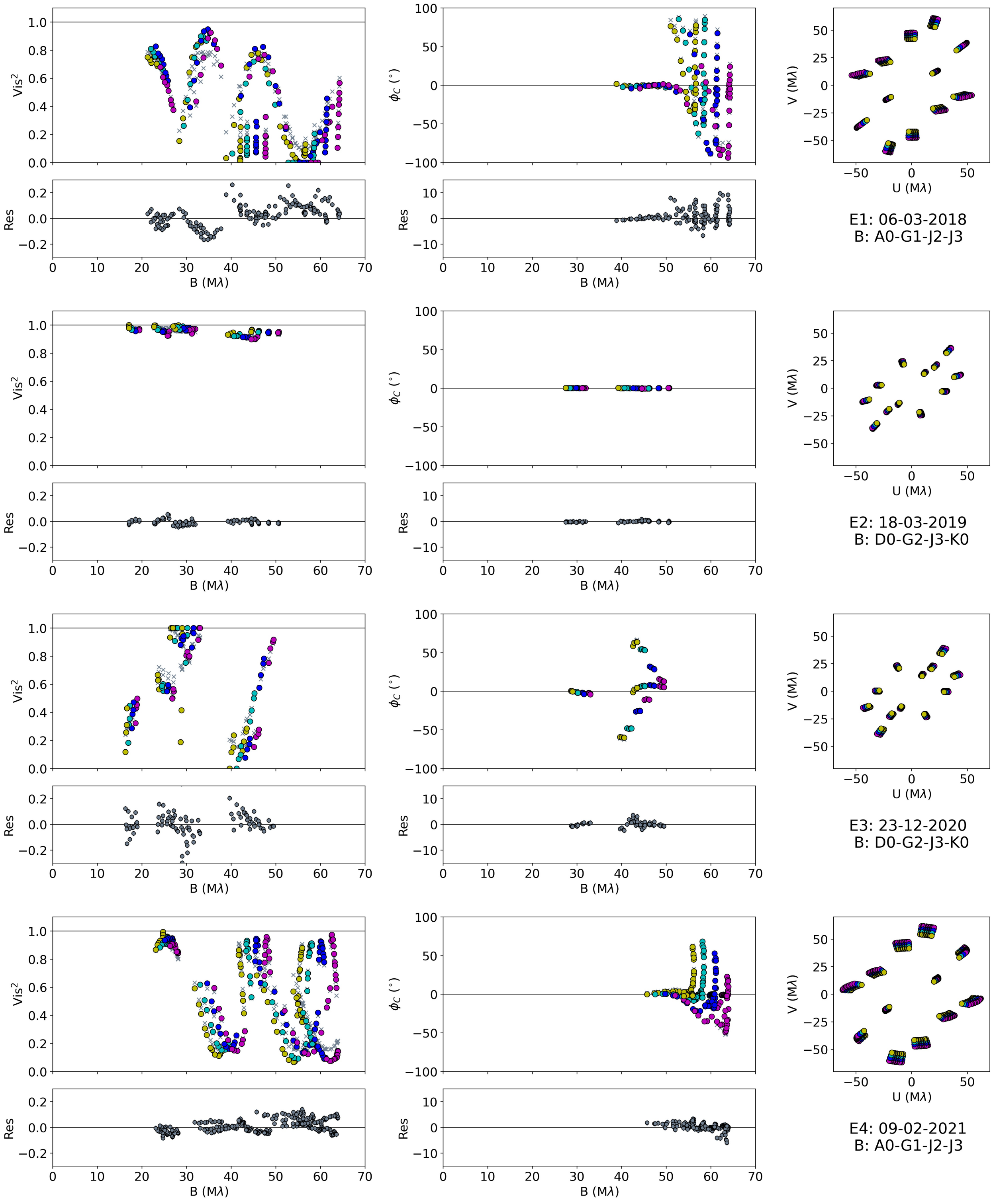

Fig. A.1. HD 52721 GRAVITY FT data, squared visibilities, closure phases, and *(u,v)* plan coverage for each epoch. Colors referees to the different GRAVITY spectral channels. Gray crosses represent the model described in Section 3.1, and Table 2. Gray circles in the bottom plots show the residuals of the binary model fit described in Section 3.1.

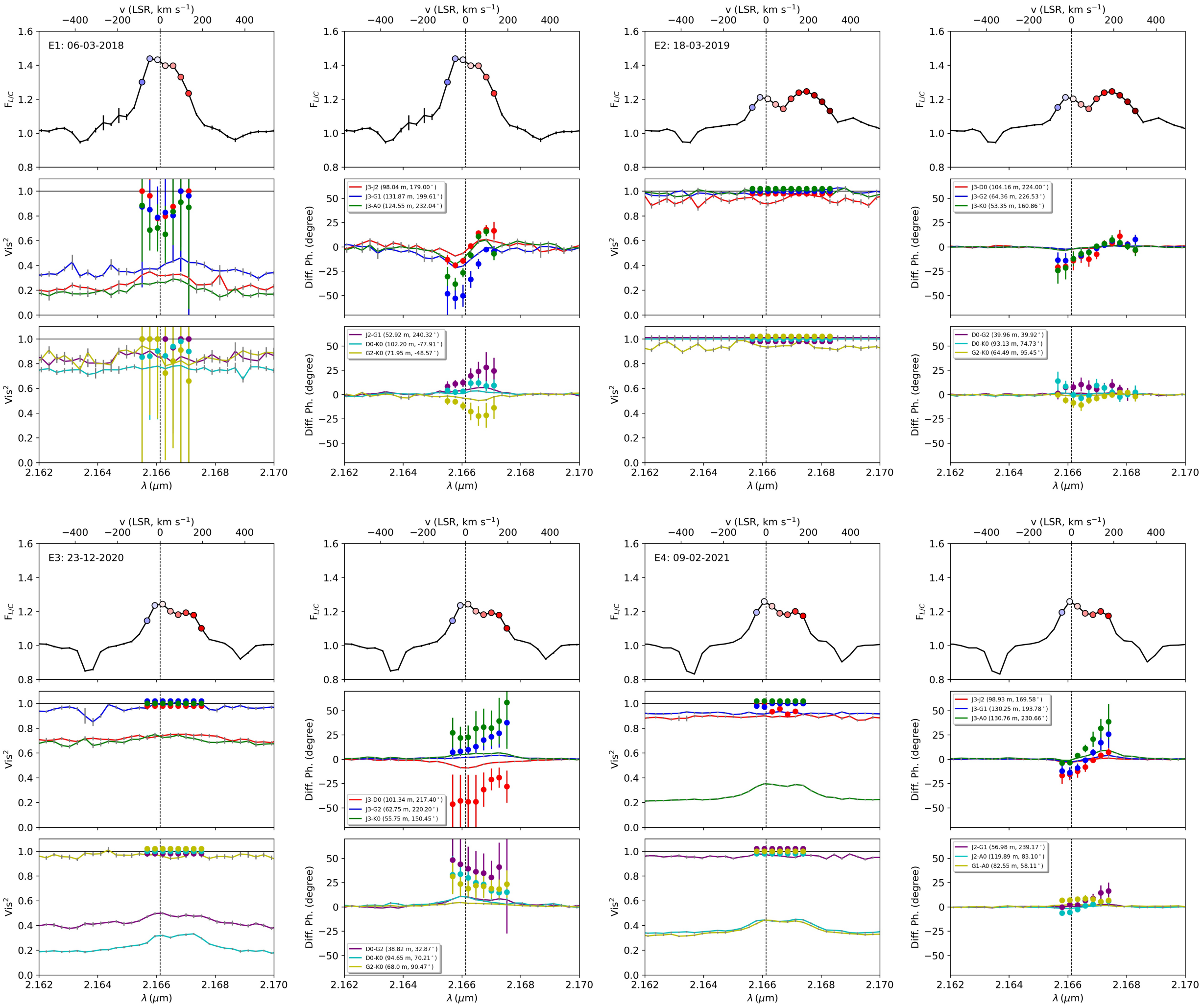

Fig. A.2. HD 52721 GRAVITY SC data for the different epochs. For each epoch, top plots show the wavelength-calibrated and continuum-normalized spectrum, left plots show the total squared visibilities, and right plots show the total differential phases. Circles represent the pure-line quantities. Colors refers to the different baselines.

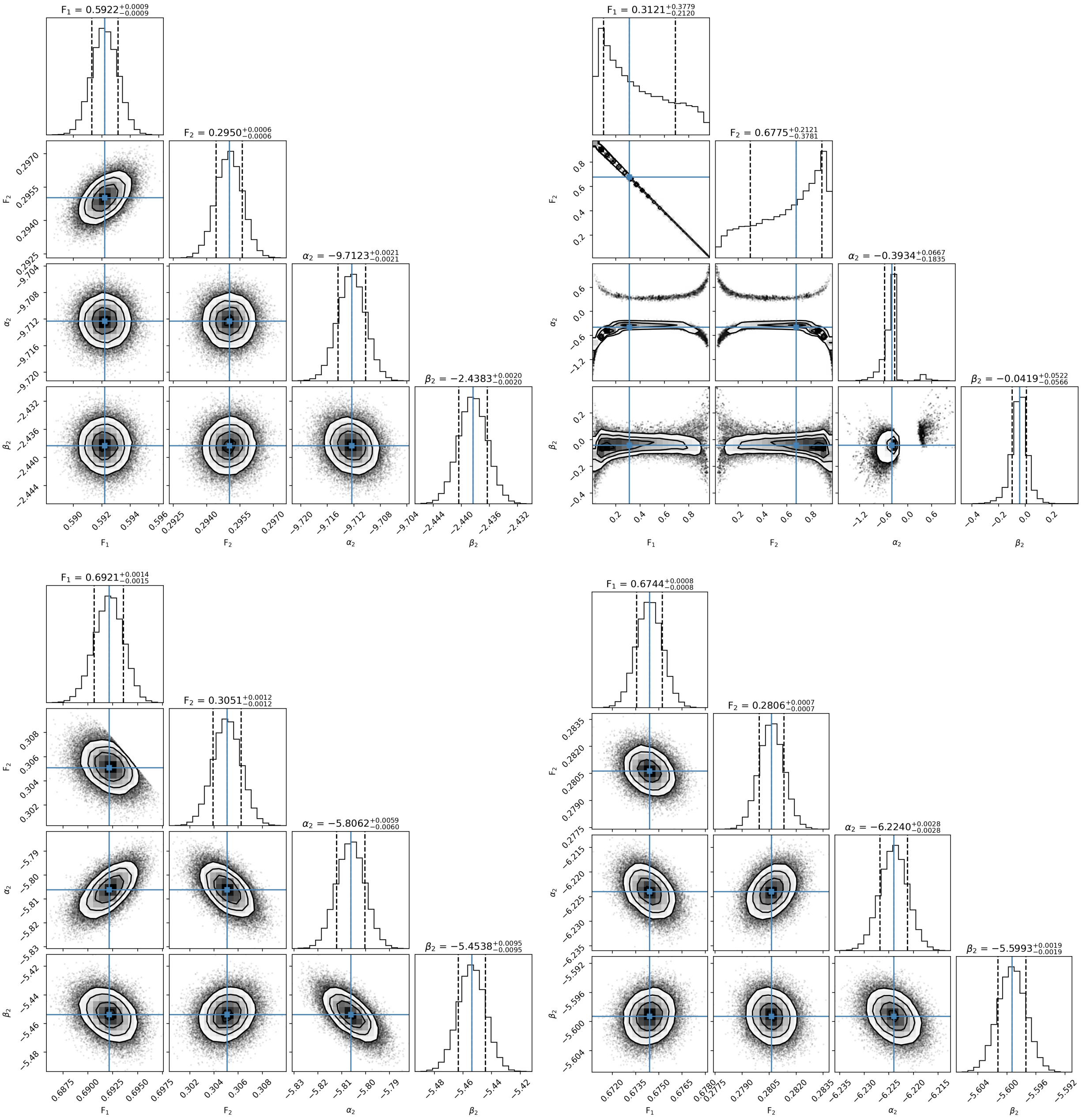

Fig. B.1. MCMC marginal posterior distributions for the FT data binary model fit for each of the four epochs (from top to bottom and from left to right: E1, E2, E3, E4). The blue lines give the 50th percentile of the samples in the MCMC marginalized distributions, while the dashed black lines give the 16th and 84th percentiles.

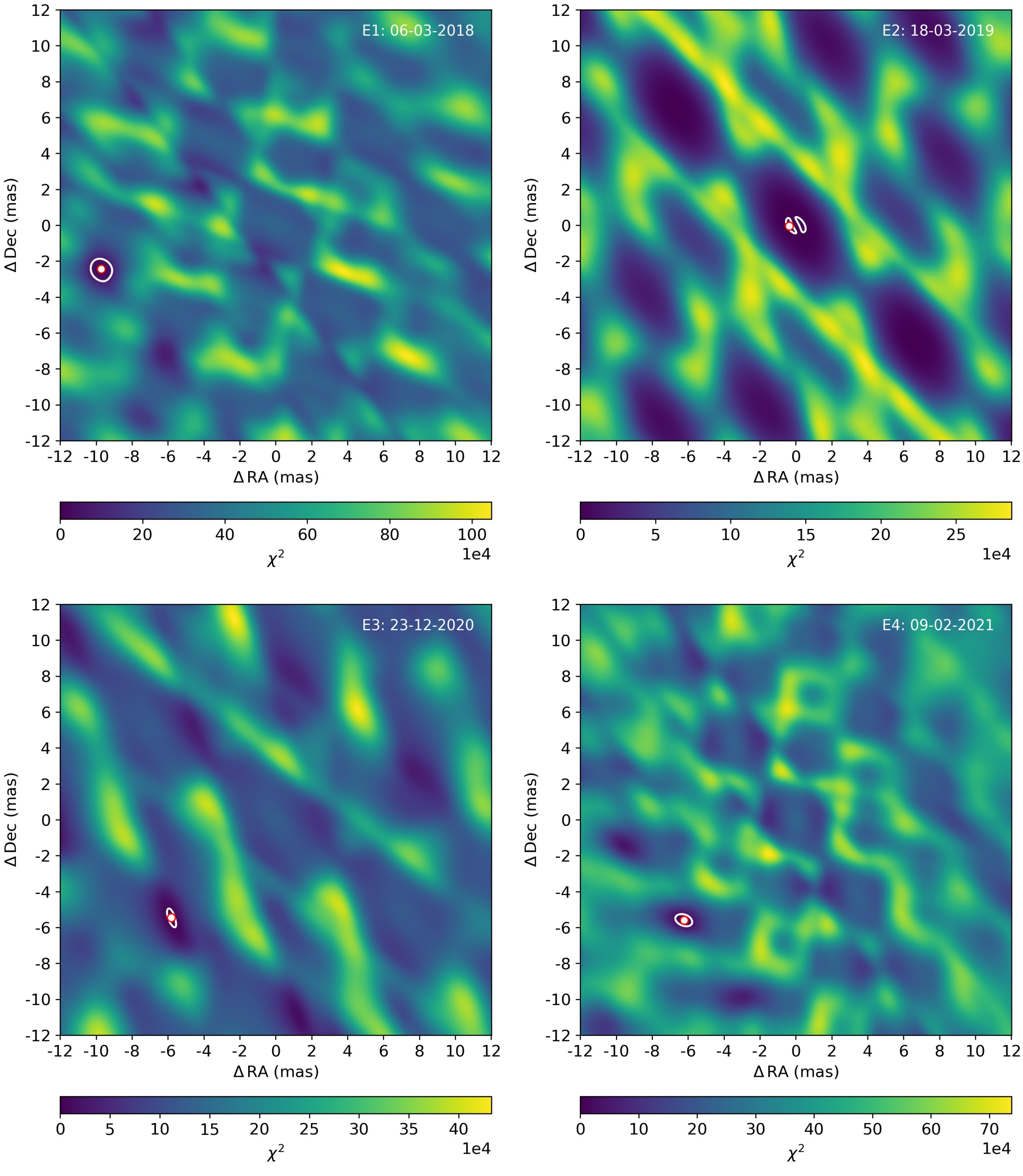

Fig. B.2. Secondary star position parameters' χ^2-maps of each epoch for the best value of flux ratios (see Table 2). The white circle marker represents the smallest χ^2. The grey line refer to the χ^2 error calculated following Gravity Collaboration et al. (2021), and represent the absolute minima error.

4.4 Comments

4.4.1 On the Stellar Photospheric Absorption Correction

The HD 52721 SC visibilities and differential phases analysis presented in the manuscript, does not take into account the stellar photospheric absorption feature. As mentioned in the manuscript, the photospheric absorption correction for HD 52721 was estimated by Grant et al. (2022), and led to an increase of the $\mathrm{EW}_{\mathrm{Br}\gamma}$ by ~ 1 Å. The correction would likely affect also the estimate of the pure-line visibilities and differential phases. However the case of HD 52721 is not simple as the ones of HD 141569 and HD 98922, both of them being single star systems. Since HD 52721 is a multiple stars one, each companion could have a distinctive Brγ-line emitting gas region. Moreover, it is not certain that the companions have the same stellar properties, and therefore they could have stellar photospheric absorption features which differ in intensity and shape. Thus, the above ~ 1 Å correction, estimated under the simplification of a single star system, could be underestimated.

In order to assess the impact of the stellar photospheric absorption feature correction on the estimates of the pure-line visibilities and differential phases, in Fig. 4.2 I compare these quantities derived in three different scenarios, for the 19 March 2019 epoch of the HD 98922 GRAVITY data set. The scenario “A” is the case shown in the HD 98922 manuscript, in which the photospheric absorption profile at the line wavelength rest position is $\alpha = 0.84$. In scenario “B”, the photospheric absorption profile is constant (no wavelength dependence) and equal to $\alpha = 0.4$. Finally, in scenario “C”, no photospheric absorption correction is accounted ($\alpha = 1$). In this last case, I remark that the pure-line visibilities and differential phases derivation does not depend on the flux contribution of the environment, as one can see from Eq. 4 of the HD 98922 manuscript (the β and γ parameters get simplified out). From this test, it results that the stronger the stellar photospheric absorption (lower values of α), the more close to unity are the pure-line squared visibilities, resulting in a more compact gas region size. The gas region radius estimate goes from 0.59 mas when $\alpha = 1$, to 0.54 mas when $\alpha = 0.84$, and finally to 0.46 mas when $\alpha = 0.4$. Additionally, when α decreases, the pure-line differential phases get smaller, translating in gas photocenters shifts (left plots of Fig. 4.2) less distant to the continuum photocenters. Taking in consideration the spectral channel closest to 2.16612 μm, the separation goes from 0.26 mas when $\alpha = 1$, to 0.21 mas when $\alpha = 0.84$, and to 0.14 mas when $\alpha = 0.4$. I note that the position angle estimates of the gas photocenters shifts are not affected by the photospheric absorption correction, since the correction is equally applied to each baseline. To conclude, the correction is necessary to take into account when a precise measurement of the gas photocenters shifts is required, and/or when the stellar photospheric absorption is significantly strong. For the case of HD 52721, I regard the correction as not vital, since a change of $\lesssim 0.1$ mas in the gas region size estimate and in the gas photocenters shifts separations does not change the system’s gas picture depicted in the manuscript.

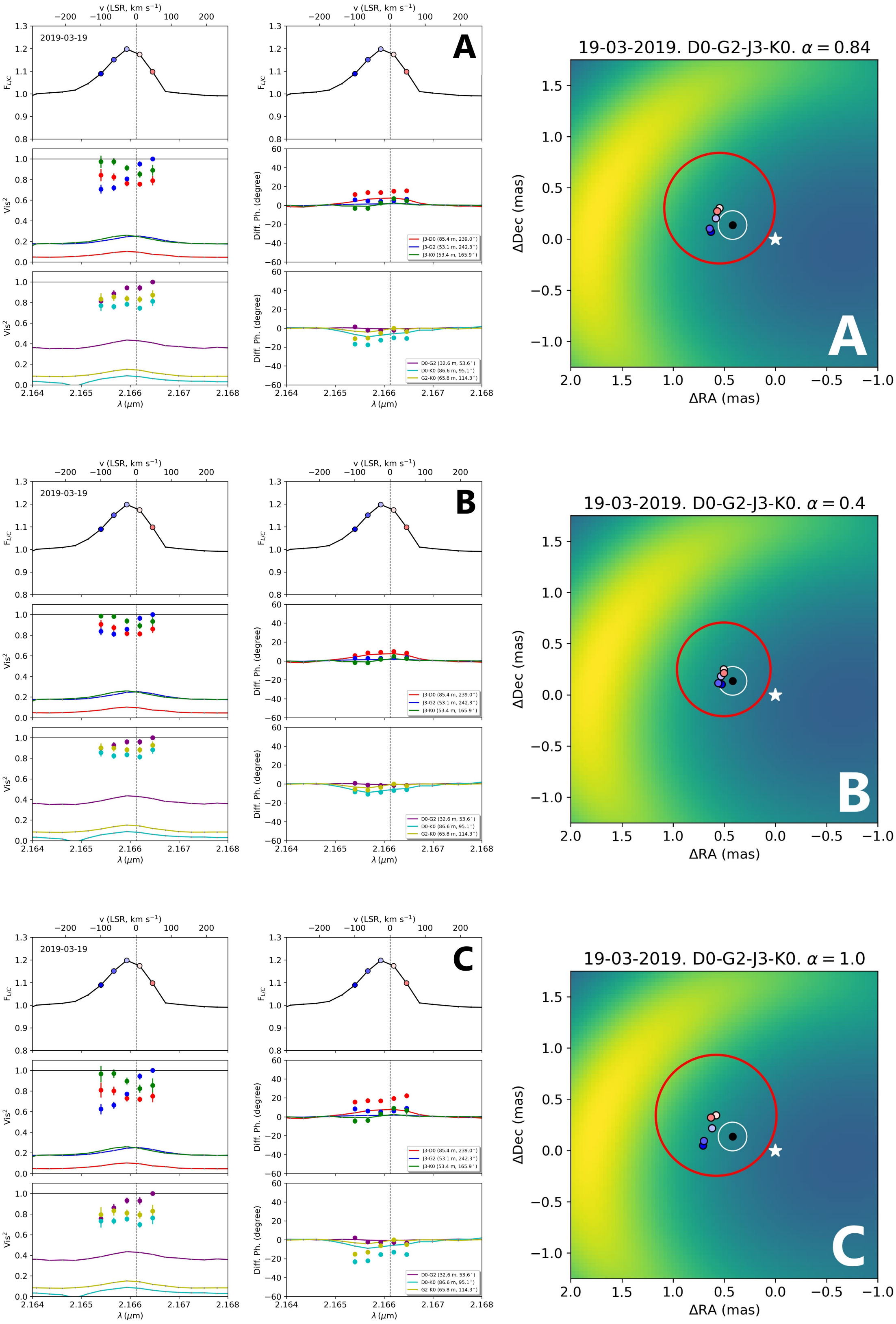

Figure 4.2: HD 98922 19 March 2019 epoch data set and pure-line quantities (left: visibilities and differential phases; right: photocenters shifts) for three different stellar photospheric absorption feature. These are identified by the letters: “A” where $\alpha = 0.84$; “B” where $\alpha = 0.4$; and “C” where $\alpha = 1.0$ (no absorption feature).

4.4.2 On the Impact of Distance Estimates

The distance from Earth of the celestial objects we observe and study, is a key parameter for data analysis and for creating theoretical models of their formation and evolution. Reliable distance measurements of a large sample of stars were available only after the first space astrometry mission named "*Hipparcos*", launched by ESA in 1989 (Perryman et al. 1997). The satellite allowed to observe the entire celestial sphere and to avoid the atmosphere perturbing effects, reaching a precision of ~ 1 mas for a total of $\sim 120\,000$ stars. With the advent of the new generation mission "*Gaia*", launched by ESA in 2013, distance measurements of 1.468 billion sources were obtained (Gaia Collaboration et al. 2021). The new satellite observed objects ~ 100 times further than the furthest source observed by *Hipparcos* with a precision of ~ 0.01 mas, setting a new standard for such measurements.

The first aspect related to distance and relevant for this thesis, is the relation between the angular sizes and the linear ones, relation given by the simple trigonometry equation:

$$\theta \approx \sin\theta \approx \tan\theta = l/d, \tag{4.1}$$

where θ is the angular size of the object observed, l is its linear size, d is its distance from the observer, and where the approximations translate in a relative error of $\lesssim 1\,\%$ when $\theta \lesssim 10°$. Since in astronomy the angular size of objects is often only a few arcsec (a few mas for the innermost regions of YSOs), the approximation is appropriate. The linear size is therefore directly proportional to the distance of the object. Thus, reliable distance measurements are of significant importance for an accurate depiction of the systems observed. An example pertinent to this thesis, is the fact that different distance values can lead to spatially locate the detection of near-IR excess emission inside or outside the sublimation radius of the system observed, with consequences on the chemical properties of the emitting dust and/or on the optical properties of the innermost gaseous component (see Section 1.2.5). With regard to the gas, different distance values can hint at different gas emission mechanisms. Indeed, for example, it is known from magnetospheric accretion theory that the truncation of the accreting disk within the co-rotation radius, where the gas angular velocity is equal to the one of the star (Bouvier 2013), is a necessary condition for the formation of stable accreting funnels (Romanova et al. 2016). Detecting emission lines arising from gas located inside or outside the co-rotation radius would respectively favor or disfavor the magnetospheric accretion scenario as origin of the emission. Such a case was encountered in the work by Gravity Collaboration et al. (2023) for AS 353, with literature distance estimates going from 150 pc to 450 pc, leading to different interpretations of the system.

Lastly, but not for importance, by estimating the distance of a star, one can derive also an estimate of its evolutionary stage. The latter estimate is done by comparing the position in the

HR-diagram of the observed object with theoretical isochrones and evolutionary tracks (e.g., Bressan et al. 2012; Guzmán-Diaz et al. 2021). Different values may therefore lead to spurious stellar classifications, with mischievous implications on statistical studies and stellar evolution theory. One such case is HD 98922 itself. With literature distance estimates ranging from ~ 450 pc (Caratti o Garatti et al. 2015) to ~ 1150 pc (van Leeuwen 2007), the estimates of HD 98922 parameters in the years have been ambiguous. Based on the *Hypparcos* measurement (~ 1150 pc) and on the work of Hales et al. (2014), in conjunction with the fact that the object is fairly isolated, being the closest star-forming region, the Carina Nebula, about 7° apart (Dame et al. 2001), Lee et al. (2016) suggested that the star may be already in the post-main sequence phase, likely a luminosity class II bright giant. The latest *Gaia* EDR3 measurement of 650.9 ± 8.8 pc, used in Chapter 3, is instead consistent with the general view of HD 98922 as Herbig star (e.g., Guzmán-Diaz et al. 2021). Regarding HD 52721, no *Gaia* measurement is available. Also for this object, the literature distance estimates greatly range, between the latest value of 531 ± 163 pc (Fairlamb et al. 2015), used in this Chapter and that was derived by the authors through X-shooter and optical data analysis, and 1050 ± 150 pc (Shevchenko et al. 1999), derived by the authors through HR-diagram evolutionary tracks fitting to the apparent stellar luminosity of the system, obtained from its spectral classification. While the former value is consistent with the view of HD 52721 as Herbig star, the latter authors, based on the latter distance estimate, suggested that HD 52721 may be a classical Be star. A more reliable distance estimate would be therefore needed.

Chapter 5

Summary and Conclusions

With this monograph, I presented my almost 4 years-long work as PhD student at the University of Köln, Germany. The goal of the project was firstly to acquire the competence and mindset to be a proper science researcher, and the up-to-date knowledge on the subject studied; secondly, to advance the state-of-the-art with regard to YSOs and their innermost circumstellar environment. Three different Herbig stars, each one of them being a benchmark for various open-ended questions on YSOs, were investigated through near-IR interferometry. The latter is nowadays the only technique to achieve the mas resolution needed to obtain information about the first astronomical units around the central star on sub-au scales, considering that the distance of such objects range from ~ 100 to $\gtrsim 500\,\mathrm{pc}$.

Through the analysis of HD 141569 GRAVITY data, we showed that stars having a transitional disk can still bear near-IR emitting hot dust as close as 1 au. This was generally considered not the case, mainly based on results obtained through SED analysis and model fitting. For this reason, the circumstellar disks evolution theory regards transitional disks as an evolutionary stage in which the disk is depleted of its material from inside out, evolutionary stage between the young proto-planetary disk and the old debris disk one (see Section 2.1). The detection of hot dust in the supposedly vacant inner gap, raises new questions which here lack explanations. Specifically, on the origin of this second generation dust and/or the survival of primordial material, despite the relatively old age of the system ($\sim 7\,\mathrm{Myr}$ for HD 141569).

The same question can be posed on the detected Brγ-line emitting gas. Although we tested, with good results, the stellar radiation heating mechanism of a gaseous disk in Keplerian rotation as the origin of the HD 141569 Brγ-line emission, the gas presence is not yet rationalized. Additionally, while the magneto-spheric accretion mechanism is ruled out as the major contributor for the Brγ-line emission, due to the fact that the magnetic field in HD 141569 was never detected, and even though the star radiated Keplerian gaseous disk can explain the observations, a star/disk wind scenario cannot be ruled out. Indeed, the latter can produce also a double-peaked line profile (e.g., Tambovtseva et al. 2016). Testing a wind model would be required to check the validity of this scenario in HD 141569. The fact that the magneto-spheric accretion scenario is not suitable for Herbig stars was also hinted by the study of HD 98922. Indeed, we showed that in this system the Brγ-line emitting gas region spatially extends farther than the system co-rotation radius, the opposite being a condition for magneto-spheric accretion to happen (Romanova et al. 2016).

For the first time, we observed a Brγ-line emitting gas which strongly varies its peak emission spatial location with respect to the star, following at first order the orbital motion of a crescent feature in the H- and K-band continuum. While asymmetric features were already been observed at all scales in YSOs disks, from their innermost to their outermost regions, their variability has never been studied with such details and with such long time coverage as we did in Chapter 3. From this study, numerous questions arose, with some of them already posed in the past and some of them being new. The cause of the asymmetric features, which hint to dust traps, is still a matter of debate. While we tested the gravitational instability scenario, with inconsistent results for the case of HD 98922, it's difficult to discriminate between the competing scenarios suggested. The vortex scenario is one of them being worthy of attention. It was tested, for example, with good results to explain the asymmetric L-band continuum emission of HD 163296 as seen by VLTI/MATISSE (Varga et al. 2021). Multi-band observations could help in this sense, similarly to the case of Oph IRS 48, for which mm and μm observations were analysed in combination, leading to the first observation of a dust trap in a vortex (van der Marel et al. 2013).

Related to the asymmetric continuum, is the question on why the crescent feature observed in HD 98922 orbits at sub-Keplerian velocity. A scenario suggested to explain sub-Keplerian orbiting features is the so-called "traffic-jam" scenario (Ataiee et al. 2013; Ragusa et al. 2020). In the latter, the presence of a companion makes the disk eccentric, with the eccentricity decreasing going farther from the central star, so that it causes orbits clustering. An over-density located at the apocenter of the gas elliptical orbit is created, which slowly precess at the same rate as the pericenter longitude of the gas orbits. However this scenario produces features that do not orbit, but are rather still (moving on time scales of hundreds of binary orbits). It would be interesting to test a vortex model in combination with the presence of a companion, which could supposedly slow down the vortex to sub-Keplerian velocities.

Once again, we detected hot dust inside the sublimation radius of a YSO disk. While it is true that the sublimation radius estimate is based on many assumptions, we cannot rule out that this scenario takes place. Although there are two suggested explanations, refractory dust grains and/or an optically thick gas region, both of them are not yet validated. In this regard, it would be interesting to test for HD 98922 a RT model that accounts a disk inner component made by a certain percentage of refractory dust grains. Corundum is one of such material that was shown to resist high temperatures (e.g., Kama et al. 2009).

A new interferometric companion was discovered in the quadruple Herbig stars system HD 52721. The companion is located at around 5 au, suggesting disk fragmentation as its origin, even though binary formation theory is still a matter of debate. The system belongs to the minority group of Herbig stars having close companions, group that accounts between 10 and 30 % of all Herbig stars (see Offner et al. 2022, and references therein). It is important to remind that no *Hipparcos* and *Gaia* distance measurements are available for HD 52721. An effort in this sense has to be maid in order to properly assess the YSO nature of the system, since no IR excess has been detected from its circumstellar environment. Finally, thanks to the GRAVITY multi-epoch astrometric observations it will be possible to obtain information on the orbital parameters. These will give a unique opportunity to obtain a model-independent dynamical mass estimate of the system. Therefore, radial velocity spectroscopic observations would be the next relevant step.

To conclude, I had the chance to access during my PhD the data from one of the most advanced infrared instruments available to the community to study PMS stars at the highest angular resolution. Thanks to it, I could achieve a number of relevant steps towards the comprehension of the intrinsic properties of YSOs, including for aspects related to stellar multiplicity. As expected, many aspects require further investigation, which will hopefully become possible in the near future. For instance, a short term objective would be the observation of HD 98922 with MATISSE at the VLTI in the mid-IR to further explore the change in surface density detected in the disk. In the longer term, the recently launched telescope JWST will certainly add unique new insight to the topic of PMS stars and planet formation. A new window of opportunity will come up with the Square Kilometer Array and the Next Generation Very Large Array over the next decades. I see with enthusiasm the future perspectives that will be offered in this field.

Acknowledgements

I take some space here to thank all the people that contributed, in a way or another, to my astronomy journey, knowing that I wouldn't be where I am without their encounter and support. Firstly, for credit and merit, I thank Dr. Lucas Labadie, who is not only the major contributor of the work here presented, but also the guide and mentor of my PhD years, allowing me to become what can be called a researcher. Afterwards, I thank my colleagues, Alex Wojtczak, Fabio Eupen, Rebekka Grellmann, and Jonas Kaufhold, who helped my work with constructive criticism, and lightening up the office days. I thank my, basically, co-supervisors, Dr. Karine Perraut and Dr. Myriam Benisty for their critique and guidelines. I thank my Master's and Bachelor's degrees supervisors, Dr. Paola Marziani and Dr. Paola Marigo, who initiated my astronomy adventure. I thank the secretariat, the IT, and the logistic people at the University of Köln for their essential work. And lastly, I thank my family, my parents and brothers, who are every day by my side.

Bibliography

Ababakr, K. M. et al. (2016). “Linear spectropolarimetry across the optical spectrum of Herbig Ae/Be stars”. In: *MNRAS* 461.3, pp. 3089–3110.

Ababakr, K. M. et al. (2017). “A statistical spectropolarimetric study of Herbig Ae/Be stars”. In: *MNRAS* 472.1, pp. 854–868.

Absil, O. et al. (2021). “A near-infrared interferometric survey of debris-disk stars. VII. The hot-to-warm dust connection”. In: *A&Ap* 651, A45, A45.

Acke, B. and M. E. van den Ancker (2004). “ISO spectroscopy of disks around Herbig Ae/Be stars”. In: *A&Ap* 426, pp. 151–170.

Acke, B. et al. (2009). “On the interplay between flaring and shadowing in disks around Herbig Ae/Be stars”. In: *A&Ap* 502.2, pp. L17–L20.

Akeson, Rachel L. et al. (2019). “Resolved Young Binary Systems and Their Disks”. In: *ApJ* 872.2, 158, p. 158.

Alecian, E. et al. (2013). “A high-resolution spectropolarimetric survey of Herbig Ae/Be stars - I. Observations and measurements”. In: *MNRAS* 429.2, pp. 1001–1026.

Alencar, S. H. P. et al. (2010). “Accretion dynamics and disk evolution in NGC 2264: a study based on CoRoT photometric observations”. In: *A&Ap* 519, A88, A88.

ALMA Partnership et al. (2015). “The 2014 ALMA Long Baseline Campaign: An Overview”. In: *ApJL* 808, L1, p. L1.

Andre, Philippe et al. (1993). “Submillimeter Continuum Observations of rho Ophiuchi A: The Candidate Protostar VLA 1623 and Prestellar Clumps”. In: *ApJ* 406, p. 122.

Andrews, Sean M. (2020). “Observations of Protoplanetary Disk Structures”. In: *ARA&Ap* 58, pp. 483–528.

Andrews, Sean M. et al. (2016). “Ringed Substructure and a Gap at 1 au in the Nearest Protoplanetary Disk”. In: *ApJL* 820.2, L40, p. L40.

Ansdell, M. et al. (2016). “Young “Dipper” Stars in Upper Sco and Oph Observed by K2”. In: *ApJ* 816.2, 69, p. 69.

Armitage, Philip J. (2007). “Lecture notes on the formation and early evolution of planetary systems”. In: *arXiv e-prints*, astro-ph/0701485, astro–ph/0701485.

Ataiee, S. et al. (2013). “Asymmetric transition disks: Vorticity or eccentricity?” In: *A&Ap* 553, L3, p. L3.

Avenhaus, H. et al. (2017). “Exploring Dust around HD 142527 down to 0.025” (4 au) Using SPHERE/ZIMPOL”. In: *AJ* 154.1, 33, p. 33.

Banzatti, A. et al. (2018). “Observing the linked depletion of dust and CO gas at 0.1-10 au in disks of intermediate-mass stars”. In: *A&Ap* 609, L2, p. L2.

Baraffe, Isabelle et al. (2015). “New evolutionary models for pre-main sequence and main sequence low-mass stars down to the hydrogen-burning limit”. In: *A&Ap* 577, A42, A42.

Bate, Matthew R. (2018). “On the diversity and statistical properties of protostellar discs”. In: *MNRAS* 475.4, pp. 5618–5658.

Becker, Juliette C. et al. (2021). “Migrating Planets into Ultra-short-period Orbits during Episodic Accretion Events”. In: *ApJ* 919.2, 76, p. 76.

Benisty, M. et al. (2010). “Strong near-infrared emission in the sub-AU disk of the Herbig Ae star HD 163296: evidence of refractory dust?” In: *A&Ap* 511, A74, A74.

Berger, Jean Philippe and Damien Segransan (2007). “An introduction to visibility modeling”. In: *NAR* 51.8-9, pp. 576–582.

Bertout, Claude et al. (1988). “Accretion Disks around T Tauri Stars”. In: *ApJ* 330, p. 350.

Bessolaz, N. et al. (2008). “Accretion funnels onto weakly magnetized young stars”. In: *A&Ap* 478.1, pp. 155–162.

Beust, H. et al. (1990). “The beta Pictoris circumstellar disk. X. Numerical simulations of infalling evaporating bodies.” In: *A&Ap* 236, p. 202.

Beuzit, J. -L. et al. (2019). “SPHERE: the exoplanet imager for the Very Large Telescope”. In: *arXiv e-prints*, arXiv:1902.04080.

Birnstiel, T. et al. (2010). “Gas- and dust evolution in protoplanetary disks”. In: *A&Ap* 513, A79, A79.

Bosman, Arthur D. et al. (2019). “Probing planet formation and disk substructures in the inner disk of Herbig Ae stars with CO rovibrational emission”. In: *A&Ap* 631, A133, A133.

Bouvier, J. (2013). “Observational studies of stellar rotation”. In: *EAS Publications Series*. Ed. by P. Hennebelle and C. Charbonnel. Vol. 62. EAS Publications Series, pp. 143–168.

Bouvier, J. et al. (2007a). “Magnetospheric Accretion in Classical T Tauri Stars”. In: *Protostars and Planets V*. Ed. by Bo Reipurth et al., p. 479.

Bouvier, J. et al. (2007b). “Magnetospheric accretion-ejection processes in the classical T Tauri star AA Tauri”. In: *A&Ap* 463.3, pp. 1017–1028.

Brackett, Frederick Sumner (1922). “Visible and Infra-Red Radiation of Hydrogen”. In: *ApJ* 56, pp. 154–161.

Brauer, F. et al. (2008). “Coagulation, fragmentation and radial motion of solid particles in protoplanetary disks”. In: *A&Ap* 480.3, pp. 859–877.

Bressan, Alessandro et al. (2012). “PARSEC: stellar tracks and isochrones with the PAdova and TRieste Stellar Evolution Code”. In: *MNRAS* 427.1, pp. 127–145.

Brittain, Sean D. et al. (2023). “Herbig Stars: A Quarter Century of Progress”. In: *arXiv e-prints*, arXiv:2301.01165, arXiv:2301.01165.

Capistrant, Benjamin K. et al. (2022). “A Population of Dipper Stars from the Transiting Exoplanet Survey Satellite Mission”. In: *ApJS* 263.1, 14, p. 14.

Caratti o Garatti, A. et al. (2015). “AMBER/VLTI high spectral resolution observations of the Brγ emitting region in HD 98922. A compact disc wind launched from the inner disc region”. In: *A&Ap* 582, A44, A44.

Catala, C. (1994). “The spectroscopic variability of the Herbig Ae/Be stars”. In: *The Nature and Evolutionary Status of Herbig Ae/Be Stars*. Ed. by Pik Sin The et al. Vol. 62. Astronomical Society of the Pacific Conference Series, p. 91.

Catala, C. et al. (1999). “Short-term spectroscopic variability in the pre-main sequence Herbig AE star AB Aurigae during the MUSICOS 96 campaign”. In: *A&Ap* 345, pp. 884–904.

Cauley, P. Wilson and Christopher M. Johns-Krull (2014). “Diagnosing Mass Flows around Herbig Ae/Be Stars Using the He I λ10830 Line”. In: *ApJ* 797.2, 112, p. 112.

Chen, Christine H. et al. (2014). “The Spitzer Infrared Spectrograph Debris Disk Catalog. I. Continuum Analysis of Unresolved Targets”. In: *ApJS* 211.2, 25, p. 25.

Chokshi, Arati et al. (1993). “Dust Coagulation”. In: *ApJ* 407, p. 806.

Choquet, Élodie et al. (2017). “First Scattered-light Images of the Gas-rich Debris Disk around 49 Ceti”. In: *ApJL* 834.2, L12, p. L12.

Cieza, Lucas A. et al. (2019). “The Ophiuchus DIsc Survey Employing ALMA (ODISEA) - I: project description and continuum images at 28 au resolution”. In: *MNRAS* 482.1, pp. 698–714.

Cody, Ann Marie et al. (2014). “CSI 2264: Simultaneous Optical and Infrared Light Curves of Young Disk-bearing Stars in NGC 2264 with CoRoT and Spitzer—Evidence for Multiple Origins of Variability”. In: *AJ* 147.4, 82, p. 82.

Colavita, M. M. et al. (1999). “The Palomar Testbed Interferometer”. In: *ApJ* 510.1, pp. 505–521.

Colavita, M. Mark and Peter L. Wizinowich (2003). “Keck Interferometer update”. In: *Proc. SPIE*. Ed. by Wesley A. Traub. Vol. 4838. Society of Photo-Optical Instrumentation Engineers (SPIE) Conference Series, pp. 79–88.

Costigan, G. et al. (2014). “Temperaments of young stars: rapid mass accretion rate changes in T Tauri and Herbig Ae stars”. In: *MNRAS* 440.4, pp. 3444–3461.

Curran, R. L. et al. (2011). “Multiwavelength diagnostics of accretion in an X-ray selected sample of CTTSs”. In: *A&Ap* 526, A104, A104.

Czechowski, A. and I. Mann (2007). “Collisional Vaporization of Dust and Production of Gas in the β Pictoris Dust Disk”. In: *ApJ* 660.2, pp. 1541–1555.

Dame, T. M. et al. (2001). “The Milky Way in Molecular Clouds: A New Complete CO Survey”. In: *ApJ* 547.2, pp. 792–813.

De Valon, Alois (2021). “Origin and impact of protostellar jets/outflows in ALMA & JWST era”. PhD thesis. Universite de Grenoble Alpes.

Decin, G. et al. (2003). “Age Dependence of the Vega Phenomenon: Observations”. In: *ApJ* 598.1, pp. 636–644.

Di Folco, E. et al. (2020). “An ALMA/NOEMA study of gas dissipation and dust evolution in the 5 Myr-old HD 141569A hybrid disc”. In: *A&Ap* 635, A94, A94.

Di Francesco, James et al. (2019). “The Next Generation Very Large Array”. In: *Canadian Long Range Plan for Astronomy and Astrophysics White Papers*. Vol. 2020, 32, p. 32.

Donaldson, J. K. et al. (2013). “Modeling the HD 32297 Debris Disk with Far-infrared Herschel Data”. In: *ApJ* 772.1, 17, p. 17.

Donati, J. -F. et al. (2011). “Non-stationary dynamo and magnetospheric accretion processes of the classical T Tauri star V2129 Oph”. In: *MNRAS* 412.4, pp. 2454–2468.

Dong, Ruobing (2015). “The Effects of Self-shadowing by a Puffed-up Inner Rim in Scattered Light Images of Protoplanetary Disks”. In: *ApJ* 810.1, 6, p. 6.

Duchêne, Gaspard and Adam Kraus (2013). “Stellar Multiplicity”. In: *ARA&Ap* 51.1, pp. 269–310.

Duchêne, Gaspard et al. (2020). “The Gemini Planet Imager View of the HD 32297 Debris Disk”. In: *AJ* 159.6, 251, p. 251.

Dullemond, C. P. and C. Dominik (2004a). “Flaring vs. self-shadowed disks: The SEDs of Herbig Ae/Be stars”. In: *A&Ap* 417, pp. 159–168.

Dullemond, C. P. and C. Dominik (2004b). “The effect of dust settling on the appearance of protoplanetary disks”. In: *A&Ap* 421, pp. 1075–1086.

Dullemond, C. P. et al. (2001). “Passive Irradiated Circumstellar Disks with an Inner Hole”. In: *ApJ* 560.2, pp. 957–969.

Dullemond, C. P. et al. (2003). “Explaining UX Orionis Star Variability with Self-shadowed Disks”. In: *ApJL* 594.1, pp. L47–L50.

Dullemond, C. P. et al. (2012). *RADMC-3D: A multi-purpose radiative transfer tool*. Astrophysics Source Code Library, record ascl:1202.015.

Eisner, J. A. et al. (2004). “Resolved Inner Disks around Herbig Ae/Be Stars”. In: *ApJ* 613.2, pp. 1049–1071.

Eisner, J. A. et al. (2009). “Spatially Resolved Spectroscopy of Sub-AU-Sized Regions of T Tauri and Herbig Ae/Be Disks”. In: *ApJ* 692.1, pp. 309–323.

Engler, N. et al. (2018). “Detection of scattered light from the hot dust in HD 172555”. In: *A&Ap* 618, A151, A151.

Ercolano, Barbara et al. (2017). “A photoevaporative gap in the closest planet-forming disc”. In: *MNRAS* 464.1, pp. L95–L99.

Ertel, S. et al. (2014). “A near-infrared interferometric survey of debris-disk stars. IV. An unbiased sample of 92 southern stars observed in H band with VLTI/PIONIER”. In: *A&Ap* 570, A128, A128.

Ertel, S. et al. (2016). “A near-infrared interferometric survey of debris-disc stars. V. PIONIER search for variability”. In: *A&Ap* 595, A44, A44.

Esposito, Thomas M. et al. (2020). “Debris Disk Results from the Gemini Planet Imager Exoplanet Survey’s Polarimetric Imaging Campaign”. In: *AJ* 160.1, 24, p. 24.

Fairlamb, J. R. et al. (2015). “A spectroscopic survey of Herbig Ae/Be stars with X-shooter - I. Stellar parameters and accretion rates”. In: *MNRAS* 453.1, pp. 976–1001.

Fairlamb, J. R. et al. (2017). “A spectroscopic survey of Herbig Ae/Be stars with X-Shooter - II. Accretion diagnostic lines”. In: *MNRAS* 464.4, pp. 4721–4735.

Fedele, D. et al. (2018). “ALMA continuum observations of the protoplanetary disk AS 209. Evidence of multiple gaps opened by a single planet”. In: *A&Ap* 610, A24, A24.

Feldt, M. et al. (2017). “SPHERE/SHINE reveals concentric rings in the debris disk of HIP 73145”. In: *A&Ap* 601, A7, A7.

Ferreira, J. (1997). “Magnetically-driven jets from Keplerian accretion discs.” In: *A&Ap* 319, pp. 340–359.

Ferreira, J. et al. (2006). “Which jet launching mechanism(s) in T Tauri stars?” In: *A&Ap* 453.3, pp. 785–796.

Ferrière, Katia M. (2001). “The interstellar environment of our galaxy”. In: *Reviews of Modern Physics* 73.4, pp. 1031–1066.

Flock, M. et al. (2015). “Gaps, rings, and non-axisymmetric structures in protoplanetary disks. From simulations to ALMA observations”. In: *A&Ap* 574, A68, A68.

Follette, Katherine B. et al. (2017). “Complex Spiral Structure in the HD 100546 Transitional Disk as Revealed by GPI and MagAO”. In: *AJ* 153.6, 264, p. 264.

Foreman-Mackey, Daniel et al. (2013). “emcee: The MCMC Hammer”. In: *PASP* 125.925, p. 306.

Gaia Collaboration et al. (2021). “Gaia Early Data Release 3. Summary of the contents and survey properties”. In: *A&Ap* 649, A1, A1.

Garcia Lopez, R. et al. (2015). “Probing the accretion-ejection connection with VLTI/AMBER. High spectral resolution observations of the Herbig Ae star HD 163296”. In: *A&Ap* 576, A84, A84.

Garcia Lopez, Rebeca et al. (2016). “Investigating the origin and spectroscopic variability of the near-infrared H I lines in the Herbig star VV Ser”. In: *MNRAS* 456.1, pp. 156–170.

Gargaud, Muriel et al. (2015). *Encyclopedia of Astrobiology*.

Garufi, A. et al. (2017a). “Evolution of protoplanetary disks from their taxonomy in scattered light: Group I vs. Group II”. In: *A&Ap* 603, A21, A21.

Garufi, A. et al. (2017b). “Three Years of SPHERE: The Latest View of the Morphology and Evolution of Protoplanetary Discs”. In: *The Messenger* 169, pp. 32–37.

Garufi, A. et al. (2022). “A SPHERE survey of self-shadowed planet-forming disks”. In: *A&Ap* 658, A137, A137.

Geers, V. C. et al. (2007). “Spatial separation of small and large grains in the transitional disk around the young star IRS 48”. In: *A&Ap* 469.3, pp. L35–L38.

Goldreich, P. and D. Lynden-Bell (1965). “I. Gravitational stability of uniformly rotating disks”. In: *MNRAS* 130, p. 97.

Goldreich, Peter and William R. Ward (1973). “The Formation of Planetesimals”. In: *ApJ* 183, pp. 1051–1062.

Grant, Sierra L. et al. (2022). “Tracing Accretion onto Herbig Ae/Be Stars Using the Brγ Line”. In: *ApJ* 926.2, 229, p. 229.

GRAVITY Collaboration et al. (2017). “First light for GRAVITY: Phase referencing optical interferometry for the Very Large Telescope Interferometer”. In: *A&Ap* 602, A94, A94.

GRAVITY Collaboration et al. (2021a). “The GRAVITY young stellar object survey. V. The orbit of the T Tauri binary star WW Cha”. In: *A&Ap* 648, A37, A37.

GRAVITY Collaboration et al. (2021b). “The GRAVITY young stellar object survey. VI. Mapping the variable inner disk of HD 163296 at sub-au scales”. In: *A&Ap* 654, A97, A97.

GRAVITY Collaboration et al. (2021c). “The GRAVITY young stellar object survey. VII. The inner dusty disks of T Tauri stars”. In: *A&Ap* 655, A73, A73.

Gravity Collaboration et al. (2017). “First light for GRAVITY: Phase referencing optical interferometry for the Very Large Telescope Interferometer”. In: *A&Ap* 602, A94, A94.

Gravity Collaboration et al. (2019). “The GRAVITY Young Stellar Object survey. I. Probing the disks of Herbig Ae/Be stars in terrestrial orbits”. In: *A&Ap* 632, A53, A53.

Gravity Collaboration et al. (2021). “The GRAVITY young stellar object survey. VIII. Gas and dust faint inner rings in the hybrid disk of HD141569”. In: *A&Ap* 655, A112, A112.

Gravity Collaboration et al. (2023). “The GRAVITY young stellar object survey. IX. Spatially resolved kinematics of hot hydrogen gas in the star-disk interaction region of T Tauri stars”. In: *A&Ap* 669, A59, A59.

GRAVITY+ Collaboration et al. (2022). “First light for GRAVITY Wide. Large separation fringe tracking for the Very Large Telescope Interferometer”. In: *A&Ap* 665, A75, A75.

Gregory, S. G. et al. (2012). “Can We Predict the Global Magnetic Topology of a Pre-main-sequence Star from Its Position in the Hertzsprung-Russell Diagram?” In: *ApJ* 755.2, 97, p. 97.

Gullbring, Erik et al. (1998). “Disk Accretion Rates for T Tauri Stars”. In: *ApJ* 492.1, pp. 323–341.

Güsten, R. et al. (2006). “The Atacama Pathfinder EXperiment (APEX) - a new submillimeter facility for southern skies -”. In: *A&Ap* 454.2, pp. L13–L16.

Guszejnov, Dávid et al. (2021). “STARFORGE: the effects of protostellar outflows on the IMF”. In: *MNRAS* 502.3, pp. 3646–3663.

Guzmán-Diaz, J. et al. (2021). “Homogeneous study of Herbig Ae/Be stars from spectral energy distributions and Gaia EDR3”. In: *A&Ap* 650, A182, A182.

Habe, Asao and Kanji Ohta (1992). “Gravitational Instability Induced by a Cloud-Cloud Collision: The Case of Head-on Collisions between Clouds with Different Sizes and Densities”. In: *PASJ* 44, pp. 203–226.

Hales, A. S. et al. (2014). “A CO Survey in Planet-forming Disks: Characterizing the Gas Content in the Epoch of Planet Formation”. In: *AJ* 148.3, 47, p. 47.

Hales, A. S. et al. (2019). “Modeling the Spatial Distribution and Origin of CO Gas in Debris Disks”. In: *ApJ* 878.2, 113, p. 113.

Hales, Antonio S. et al. (2017). “Atomic gas in debris discs”. In: *MNRAS* 466.3, pp. 3582–3593.

Hales, Antonio S. et al. (2022). “ALMA Observations of the HD 110058 Debris Disk”. In: *ApJ* 940.2, 161, p. 161.

Hashimoto, J. et al. (2011). “Direct Imaging of Fine Structures in Giant Planet-forming Regions of the Protoplanetary Disk Around AB Aurigae”. In: *ApJL* 729.2, L17, p. L17.

Herbig, George H. (1960). “The Spectra of Be- and Ae-Type Stars Associated with Nebulosity”. In: *ApJS* 4, p. 337.

Herbst, W. et al. (1994). “Catalogue of UBVRI Photometry of T Tauri Stars and Analysis of the Causes of Their Variability”. In: *AJ* 108, p. 1906.

Herczeg, Gregory J. and Lynne A. Hillenbrand (2008). “UV Excess Measures of Accretion onto Young Very Low Mass Stars and Brown Dwarfs”. In: *ApJ* 681.1, pp. 594–625.

Higuchi, Aya E. et al. (2020). “Physical Conditions of Gas Components in Debris Disks of 49 Ceti and HD 21997”. In: *ApJ* 905.2, 122, p. 122.

Holland, Wayne S. et al. (2017). “SONS: The JCMT legacy survey of debris discs in the submillimetre”. In: *MNRAS* 470.3, pp. 3606–3663.

Honda, M. et al. (2015). “High-resolution 25 μm Imaging of the Disks around Herbig Ae/Be Stars”. In: *ApJ* 804.2, 143, p. 143.

Huang, Jane et al. (2018). “CO and Dust Properties in the TW Hya Disk from High-resolution ALMA Observations”. In: *ApJ* 852.2, 122, p. 122.

Hughes, A. Meredith et al. (2017). “Radial Surface Density Profiles of Gas and Dust in the Debris Disk around 49 Ceti”. In: *ApJ* 839.2, 86, p. 86.

Hughes, A. Meredith et al. (2018). “Debris Disks: Structure, Composition, and Variability”. In: *ARA&Ap* 56, pp. 541–591.

Hung, Li-Wei et al. (2015). “First Scattered-light Image of the Debris Disk around HD 131835 with the Gemini Planet Imager”. In: *ApJL* 815.1, L14, p. L14.

Hunter, J. D. (2007). “Matplotlib: A 2D graphics environment”. In: *Computing in Science & Engineering* 9.3, pp. 90–95.

Ingleby, Laura et al. (2013). “Accretion Rates for T Tauri Stars Using Nearly Simultaneous Ultraviolet and Optical Spectra”. In: *ApJ* 767.2, 112, p. 112.

Isella, Andrea et al. (2010). “Investigating Planet Formation in Circumstellar Disks: CARMA Observations of Ry Tau and Dg Tau”. In: *ApJ* 714.2, pp. 1746–1761.

Järvinen, S. P. et al. (2019). “New evidence for weak magnetic fields in Herbig Ae/Be stars”. In: *MNRAS* 489.1, pp. 886–890.

Jeans, James Hopwood (1928). *Astronomy and cosmogony*.

Jiménez-Donaire, M. J. et al. (2017). “Herschel observations of the circumstellar environments of the Herbig Be stars R Mon and PDS 27”. In: *A&Ap* 605, A62, A62.

Johansen, Anders et al. (2007). “Rapid planetesimal formation in turbulent circumstellar disks”. In: *Nat* 448.7157, pp. 1022–1025.

Johns-Krull, Christopher M. (2007). “The Magnetic Fields of Classical T Tauri Stars”. In: *ApJ* 664.2, pp. 975–985.

Kama, M. et al. (2009). “The inner rim structures of protoplanetary discs”. In: *A&Ap* 506.3, pp. 1199–1213.

Kasper, Markus et al. (2015). “Discovery of an Edge-on Debris Disk with a Dust Ring and an Outer Disk Wing-tilt Asymmetry”. In: *ApJL* 812.2, L33, p. L33.

Kenyon, Scott J. and Lee Hartmann (1995). “Pre-Main-Sequence Evolution in the Taurus-Auriga Molecular Cloud”. In: *ApJS* 101, p. 117.

Kiefer, F. et al. (2014). “Exocomets in the circumstellar gas disk of HD 172555”. In: *A&Ap* 561, L10, p. L10.

Kirk, H. et al. (2017). “ALMA Observations of Starless Core Substructure in Ophiuchus”. In: *ApJ* 838.2, 114, p. 114.

Klahr, H. Hubertus and Thomas Henning (1997). “Particle-Trapping Eddies in Protoplanetary Accretion Disks”. In: *Icarus* 128.1, pp. 213–229.

Kluska, J. et al. (2020). “A family portrait of disk inner rims around Herbig Ae/Be stars. Hunting for warps, rings, self shadowing, and misalignments in the inner astronomical units”. In: *A&Ap* 636, A116, A116.

Kobus, J. et al. (2020). “Interferometric study on the temporal variability of the brightness distributions of protoplanetary disks”. In: *A&Ap* 642, A104, A104.

Koepferl, C. M. et al. (2013). “Disc clearing of young stellar objects: evidence for fast inside-out dispersal”. In: *MNRAS* 428.4, pp. 3327–3354.

Kóspál, Á. et al. (2013). “ALMA Observations of the Molecular Gas in the Debris Disk of the 30 Myr Old Star HD 21997”. In: *ApJ* 776.2, 77, p. 77.

Kothe, Stefan et al. (2010). “The Physics of Protoplanetesimal Dust Agglomerates. V. Multiple Impacts of Dusty Agglomerates at Velocities Above the Fragmentation Threshold”. In: *ApJ* 725.1, pp. 1242–1251.

Kral, Q. et al. (2016). “A self-consistent model for the evolution of the gas produced in the debris disc of β Pictoris”. In: *MNRAS* 461.1, pp. 845–858.

Kral, Quentin et al. (2017). “Predictions for the secondary CO, C and O gas content of debris discs from the destruction of volatile-rich planetesimals”. In: *MNRAS* 469.1, pp. 521–550.

Kral, Quentin et al. (2019). “Imaging [CI] around HD 131835: reinterpreting young debris discs with protoplanetary disc levels of CO gas as shielded secondary discs”. In: *MNRAS* 489.4, pp. 3670–3691.

Kral, Quentin et al. (2020). “Survey of planetesimal belts with ALMA: gas detected around the Sun-like star HD 129590”. In: *MNRAS* 497.3, pp. 2811–2830.

Kraus, S. et al. (2008). “The origin of hydrogen line emission for five Herbig Ae/Be stars spatially resolved by VLTI/AMBER spectro-interferometry”. In: *A&Ap* 489.3, pp. 1157–1173.

Kuiper, R. and T. Hosokawa (2018). “First hydrodynamics simulations of radiation forces and photoionization feedback in massive star formation”. In: *A&Ap* 616, A101, A101.

Kulkarni, A. K. and M. M. Romanova (2008). “Accretion to magnetized stars through the Rayleigh-Taylor instability: global 3D simulations”. In: *MNRAS* 386.2, pp. 673–687.

Kurtovic, Nicolás T. et al. (2018). “The Disk Substructures at High Angular Resolution Project (DSHARP). IV. Characterizing Substructures and Interactions in Disks around Multiple Star Systems”. In: *ApJL* 869.2, L44, p. L44.

Lada, Charles J. (1987). “Star formation: from OB associations to protostars.” In: *Star Forming Regions*. Ed. by Manuel Peimbert and Jun Jugaku. Vol. 115, p. 1.

Lagrange, A. M. et al. (2020). “Unveiling the β Pictoris system, coupling high contrast imaging, interferometric, and radial velocity data”. In: *A&Ap* 642, A18, A18.

Lapeyrere, V. et al. (2014). “GRAVITY data reduction software”. In: *Proc. SPIE*. Vol. 9146. Society of Photo-Optical Instrumentation Engineers (SPIE) Conference Series, 91462D, p. 91462D.

Larson, Richard B. (2003). “The physics of star formation”. In: *Reports on Progress in Physics* 66.10, pp. 1651–1697.

Lazareff, B. et al. (2017). “Structure of Herbig AeBe disks at the milliarcsecond scale . A statistical survey in the H band using PIONIER-VLTI”. In: *A&Ap* 599, A85, A85.

Le Bouquin, J.-B. et al. (2011). “PIONIER: a 4-telescope visitor instrument at VLTI”. In: *A&Ap* 535, A67, A67.

Lee, Aaron T. et al. (2019). “The Formation and Evolution of Wide-orbit Stellar Multiples In Magnetized Clouds”. In: *ApJ* 887.2, 232, p. 232.

Lee, Chien-De et al. (2016). “Evolutionary status of isolated B[e] stars”. In: *A&Ap* 592, A130, A130.

Lieman-Sifry, Jesse et al. (2016). “Debris Disks in the Scorpius-Centaurus OB Association Resolved by ALMA”. In: *ApJ* 828.1, 25, p. 25.

Liu, Qiong (2021). “A WISE view of IRAS debris disks: revising the dust properties”. In: *Research in Astronomy and Astrophysics* 21.3, 060, p. 060.

Long, Feng et al. (2018). “Gaps and Rings in an ALMA Survey of Disks in the Taurus Star-forming Region”. In: *ApJ* 869.1, 17, p. 17.

Lopez, B. et al. (2014). “An Overview of the MATISSE Instrument — Science, Concept and Current Status”. In: *The Messenger* 157, pp. 5–12.

Luhman, K. L. et al. (2010). “The Disk Population of the Taurus Star-Forming Region”. In: *ApJS* 186.1, pp. 111–174.

Lumsden, S. L. et al. (2013). “The Red MSX Source Survey: The Massive Young Stellar Population of Our Galaxy”. In: *ApJS* 208.1, 11, p. 11.

Lynden-Bell, D. and J. E. Pringle (1974). “The evolution of viscous discs and the origin of the nebular variables.” In: *MNRAS* 168, pp. 603–637.

Maaskant, K. M. et al. (2013). “Identifying gaps in flaring Herbig Ae/Be disks using spatially resolved mid-infrared imaging. Are all group I disks transitional?” In: *A&Ap* 555, A64, A64.

MacGregor, Meredith A. et al. (2018). “ALMA Detection of Extended Millimeter Halos in the HD 32297 and HD 61005 Debris Disks”. In: *ApJ* 869.1, 75, p. 75.

Manara, C. F. et al. (2019). “Observational constraints on dust disk sizes in tidally truncated protoplanetary disks in multiple systems in the Taurus region”. In: *A&Ap* 628, A95, A95.

Mathews, Geoffrey S. et al. (2012). “The Late Stages of Protoplanetary Disk Evolution: A Millimeter Survey of Upper Scorpius”. In: *ApJ* 745.1, 23, p. 23.

McGinnis, P. T. et al. (2015). “CSI 2264: Probing the inner disks of AA Tauri-like systems in NGC 2264”. In: *A&Ap* 577, A11, A11.

McMillan, Paul J. (2011). “Mass models of the Milky Way”. In: *MNRAS* 414.3, pp. 2446–2457.

Meeus, G. et al. (2001). “ISO spectroscopy of circumstellar dust in 14 Herbig Ae/Be systems: Towards an understanding of dust processing”. In: *A&Ap* 365, pp. 476–490.

Melis, Carl et al. (2013). “Copious Amounts of Hot and Cold Dust Orbiting the Main Sequence A-type Stars HD 131488 and HD 121191”. In: *ApJ* 778.1, 12, p. 12.

Mendigutia, I. et al. (2011a). “Accretion rates and accretion tracers of Herbig Ae/Be stars”. In: *A&Ap* 535, A99, A99.

Mendigutia, I. et al. (2011b). “Optical spectroscopic variability of Herbig Ae/Be stars”. In: *A&Ap* 529, A34, A34.

Mendigutia, I. et al. (2015). “High-resolution Br γ spectro-interferometry of the transitional Herbig Ae/Be star HD 100546: a Keplerian gaseous disc inside the inner rim”. In: *MNRAS* 453.2, pp. 2126–2132.

Mendigutia, I. et al. (2017). “The compact Hα emitting regions of the Herbig Ae/Be stars HD 179218 and HD 141569 from CHARA spectro-interferometry”. In: *MNRAS* 464.2, pp. 1984–1989.

Menu, J. et al. (2015). “The structure of disks around intermediate-mass young stars from mid-infrared interferometry. Evidence for a population of group II disks with gaps”. In: *A&Ap* 581, A107, A107.

Mestel, L. (1968). “Magnetic braking by a stellar wind-I”. In: *MNRAS* 138, p. 359.

Millan-Gabet, R. et al. (1999). “A NICMOS3 Camera for Fringe Detection at the IOTA Interferometer”. In: *PASP* 111.756, pp. 238–245.

Millan-Gabet, Rafael et al. (2001). “Spatially Resolved Circumstellar Structure of Herbig AE/BE Stars in the Near-Infrared”. In: *ApJ* 546.1, pp. 358–381.

Min, M. et al. (2009). “Radiative transfer in very optically thick circumstellar disks”. In: *A&Ap* 497.1, pp. 155–166.

Monnier, J. D. and R. Millan-Gabet (2002). “On the Interferometric Sizes of Young Stellar Objects”. In: *ApJ* 579.2, pp. 694–698.

Monnier, J. D. et al. (2005). “The Near-Infrared Size-Luminosity Relations for Herbig Ae/Be Disks”. In: *ApJ* 624, pp. 832–840.

Monnier, John D. (2007). “Phases in interferometry”. In: *NAR* 51.8-9, pp. 604–616.

Monnier, John D. and Ronald J. Allen (2013). “Radio and Optical Interferometry: Basic Observing Techniques and Data Analysis”. In: *Planets, Stars and Stellar Systems. Volume 2: Astronomical Techniques, Software and Data*. Ed. by Terry D. Oswalt and Howard E. Bond, p. 325.

Moór, A. et al. (2011). “Molecular Gas in Young Debris Disks”. In: *ApJL* 740.1, L7, p. L7.

Moór, A. et al. (2013). “ALMA Continuum Observations of a 30 Myr Old Gaseous Debris Disk around HD 21997”. In: *ApJL* 777.2, L25, p. L25.

Moór, A. et al. (2015). “Discovery of Molecular Gas around HD 131835 in an APEX Molecular Line Survey of Bright Debris Disks”. In: *ApJ* 814.1, 42, p. 42.

Moór, Attila et al. (2017). “Molecular Gas in Debris Disks around Young A-type Stars”. In: *ApJ* 849.2, 123, p. 123.

Moór, Attila et al. (2019). “New Millimeter CO Observations of the Gas-rich Debris Disks 49 Cet and HD 32297”. In: *ApJ* 884.2, 108, p. 108.

Moór, Attila et al. (2021). “A New Sample of Warm Extreme Debris Disks from the ALLWISE Catalog”. In: *ApJ* 910.1, 27, p. 27.

Muñoz, D. J. et al. (2015). “Stellar orbit evolution in close circumstellar disc encounters”. In: *MNRAS* 446.2, pp. 2010–2029.

Muro-Arena, G. A. et al. (2018). “Dust modeling of the combined ALMA and SPHERE datasets of HD 163296. Is HD 163296 really a Meeus group II disk?” In: *A&Ap* 614, A24, A24.

Muzerolle, James et al. (1998). “Magnetospheric Accretion Models for the Hydrogen Emission Lines of T Tauri Stars”. In: *ApJ* 492.2, pp. 743–753.

Muzerolle, James et al. (2001). “Emission-Line Diagnostics of T Tauri Magnetospheric Accretion. II. Improved Model Tests and Insights into Accretion Physics”. In: *ApJ* 550.2, pp. 944–961.

Muzerolle, James et al. (2004). “Magnetospheres and Disk Accretion in Herbig Ae/Be Stars”. In: *ApJ* 617.1, pp. 406–417.

Natta, A. et al. (2001). “A reconsideration of disk properties in Herbig Ae stars”. In: *A&Ap* 371, pp. 186–197.

Nilsson, R. et al. (2012). “VLT imaging of the β Pictoris gas disk”. In: *A&Ap* 544, A134, A134.

Obolentseva, M. A. et al. (2021). “HD 52721 as a Quadruple System”. In: *Astrophysical Bulletin* 76.3, pp. 292–296.

Ochi, Yasuhiro et al. (2005). “Evolution of a Protobinary: Accretion Rates of the Primary and Secondary”. In: *ApJ* 623.2, pp. 922–939.

Offner, Stella S. R. et al. (2016). “The Turbulent Origin of Outflow and Spin Misalignment in Multiple Star Systems”. In: *ApJL* 827.1, L11, p. L11.

Offner, Stella S. R. et al. (2022). “The Origin and Evolution of Multiple Star Systems”. In: *arXiv e-prints*, arXiv:2203.10066, arXiv:2203.10066.

Ogilvie, G. I. and S. H. Lubow (2002). “On the wake generated by a planet in a disc”. In: *MNRAS* 330.4, pp. 950–954.

Olofsson, J. et al. (2022). “The halo around HD 32297: μm-sized cometary dust”. In: *A&Ap* 664, A122, A122.

Owen, James E. (2016). “The Origin and Evolution of Transition Discs: Successes, Problems, and Open Questions”. In: *Publications of the Astronomical Society of Australia* 33, e005, e005.

Papaloizou, J. and D. N. C. Lin (1984). “On the tidal interaction between protoplanets and the primordial solar nebula. I - Linear calculation of the role of angular momentum exchange”. In: *ApJ* 285, pp. 818–834.

Pearce, Tim D. et al. (2022). “Planet populations inferred from debris discs. Insights from 178 debris systems in the ISPY, LEECH, and LIStEN planet-hunting surveys”. In: *A&Ap* 659, A135, A135.

Perryman, M. A. C. et al. (1997). “The HIPPARCOS Catalogue”. In: *A&Ap* 323, pp. L49–L52.

Pineda, Jaime E. et al. (2015). “The formation of a quadruple star system with wide separation”. In: *Nat* 518.7538, pp. 213–215.

Pinilla, P. et al. (2012). “Ring shaped dust accumulation in transition disks”. In: *A&Ap* 545, A81, A81.

Pinte, C. et al. (2006). “Monte Carlo radiative transfer in protoplanetary disks”. In: *A&Ap* 459.3, pp. 797–804.

Pinte, C. et al. (2018). “Kinematic Evidence for an Embedded Protoplanet in a Circumstellar Disk”. In: *ApJL* 860.1, L13, p. L13.

Pinte, C. et al. (2019). “Kinematic detection of a planet carving a gap in a protoplanetary disk”. In: *Nature Astronomy* 3, pp. 1109–1114.

Pogodin, M. A. et al. (2011). “HD 52721 - A close binary system among the Ae/Be Herbig stars”. In: *Astrophysics* 54.2, pp. 214–230.

Pohl, A. et al. (2017). “The Circumstellar Disk HD 169142: Gas, Dust, and Planets Acting in Concert?” In: *ApJ* 850.1, 52, p. 52.

Pollack, James B. et al. (1994). “Composition and Radiative Properties of Grains in Molecular Clouds and Accretion Disks”. In: *ApJ* 421, p. 615.

Prato, L. et al. (2018). “Orbital Solution for the Spectroscopic Binary in the GW Ori Hierarchical Triple”. In: *ApJ* 852.1, 38, p. 38.

Prialnik, Dina (2009). *An Introduction to the Theory of Stellar Structure and Evolution*.

Ragusa, Enrico et al. (2017). “On the origin of horseshoes in transitional discs”. In: *MNRAS* 464.2, pp. 1449–1455.

Ragusa, Enrico et al. (2020). “The evolution of large cavities and disc eccentricity in circumbinary discs”. In: *MNRAS* 499.3, pp. 3362–3380.

Rebollido, I. et al. (2018). “The co-existence of hot and cold gas in debris discs”. In: *A&Ap* 614, A3, A3.

Regaly, Zs. et al. (2012). “Possible planet-forming regions on submillimetre images”. In: *MNRAS* 419.2, pp. 1701–1712.

Reynolds, Nickalas K. et al. (2021). “Kinematic Analysis of a Protostellar Multiple System: Measuring the Protostar Masses and Assessing Gravitational Instability in the Disks of L1448 IRS3B and L1448 IRS3A”. In: *ApJL* 907.1, L10, p. L10.

Ricci, L. et al. (2010). “Dust properties of protoplanetary disks in the Taurus-Auriga star forming region from millimeter wavelengths”. In: *A&Ap* 512, A15, A15.

Rivière-Marichalar, P. et al. (2020). “AB Aur, a Rosetta stone for studies of planet formation. I. Chemical study of a planet-forming disk”. In: *A&Ap* 642, A32, A32.

Roberge, A. et al. (2013). “Herschel Observations of Gas and Dust in the Unusual 49 Ceti Debris Disk”. In: *ApJ* 771.1, 69, p. 69.

Rodriguez, Joseph E. et al. (2018). “Multiple Stellar Flybys Sculpting the Circumstellar Architecture in RW Aurigae”. In: *ApJ* 859.2, 150, p. 150.

Romanova, Marina M. and Stanley P. Owocki (2016). “Accretion, Outflows, and Winds of Magnetized Stars”. In: *The Strongest Magnetic Fields in the Universe: Space Sciences Series of ISSI*. Vol. 54, p. 347.

Setterholm, Benjamin R. et al. (2018). “Probing the Inner Disk Emission of the Herbig Ae Stars HD 163296 and HD 190073”. In: *ApJ* 869.2, 164, p. 164.

Shevchenko, V. S. et al. (1999). “The stellar composition of the star formation region CMa R1 - I. Results from new photometric and spectroscopic classifications”. In: *MNRAS* 310.1, pp. 210–222.

Sibthorpe, B. et al. (2010). “The Vega debris disc: A view from Herschel”. In: *A&Ap* 518, L130, p. L130.

Sibthorpe, B. et al. (2018). “Analysis of the Herschel DEBRIS Sun-like star sample”. In: *MNRAS* 475.3, pp. 3046–3064.

Sissa, E. et al. (2019). “The origin of R CrA variability. A complex triple system hosting a disk”. In: *A&Ap* 630, A132, A132.

Smith, R. et al. (2012). “Resolving the terrestrial planet forming regions of HD 113766 and HD 172555 with MIDI”. In: *MNRAS* 422.3, pp. 2560–2580.

Smith, Rowan J. et al. (2016). “On the nature of star-forming filaments - II. Subfilaments and velocities”. In: *MNRAS* 455.4, pp. 3640–3655.

Stauffer, John et al. (2014). “CSI 2264: Characterizing Accretion-burst Dominated Light Curves for Young Stars in NGC 2264”. In: *AJ* 147.4, 83, p. 83.

Strafella, F. et al. (1998). “Stellar Winds in Herbig Ae/Be Stars”. In: *ApJ* 505.1, pp. 299–314.

Sylvester, R. J. et al. (1996). “Optical, infrared and millimetre-wave properties of Vega-like systems.” In: *MNRAS* 279.3, pp. 915–939.

Tafalla, M. et al. (2017). “Anatomy of the internal bow shocks in the IRAS 04166+2706 protostellar jet”. In: *A&Ap* 597, A119, A119.

Tambovtseva, L. V. et al. (2014). “Hydrogen lines as a diagnostic tool for studying multicomponent emitting regions in hot young stars: magnetosphere, X-wind, and disk wind”. In: *A&Ap* 562, A104, A104.

Tambovtseva, L. V. et al. (2016). “Brackett γ radiation from the inner gaseous accretion disk, magnetosphere, and disk wind region of Herbig AeBe stars”. In: *A&Ap* 590, A97, A97.

Testi, L. et al. (2014). “Dust Evolution in Protoplanetary Disks”. In: *Protostars and Planets VI*. Ed. by Henrik Beuther et al., pp. 339–361.

Thamm, E. et al. (1994). “Ambiguities of parametrized dust disk models for young stellar objects.” In: *A&Ap* 287, pp. 493–502.

The, P. S. et al. (1994). “A new catalogue of members and candidate members of the Herbig Ae/Be (HAEBE) stellar group”. In: *A&Ap Supp.* 104, pp. 315–339.

Thi, W. -F. et al. (2014). “Gas lines from the 5-Myr old optically thin disk around HD 141569A . Herschel observations and modeling”. In: *A&Ap* 561, A50, A50.

Tokovinin, Andrei and Maxwell Moe (2020). “Formation of close binaries by disc fragmentation and migration, and its statistical modelling”. In: *MNRAS* 491.4, pp. 5158–5171.

Toomre, A. (1964). “On the gravitational stability of a disk of stars.” In: *ApJ* 139, pp. 1217–1238.

Valdivia, Valeska et al. (2016). “H_2 distribution during the formation of multiphase molecular clouds”. In: *A&Ap* 587, A76, A76.

van Boekel, R. et al. (2003). “Grain growth in the inner regions of Herbig Ae/Be star disks”. In: *A&Ap* 400, pp. L21–L24.

van Boekel, R. et al. (2017). “Three Radial Gaps in the Disk of TW Hydrae Imaged with SPHERE”. In: *ApJ* 837.2, 132, p. 132.

van Cittert, P. H. (1934). “Die Wahrscheinliche Schwingungsverteilung in Einer von Einer Lichtquelle Direkt Oder Mittels Einer Linse Beleuchteten Ebene”. In: *Physica* 1.1, pp. 201–210.

van der Marel, Nienke et al. (2013). “A Major Asymmetric Dust Trap in a Transition Disk”. In: *Science* 340.6137, pp. 1199–1202.

van der Marel, Nienke et al. (2021). “On the Diversity of Asymmetries in Gapped Protoplanetary Disks”. In: *AJ* 161.1, 33, p. 33.

van Leeuwen, F. (2007). “Validation of the new Hipparcos reduction”. In: *A&Ap* 474.2, pp. 653–664.

Varga, J. et al. (2021). “The asymmetric inner disk of the Herbig Ae star HD 163296 in the eyes of VLTI/MATISSE: evidence for a vortex?” In: *A&Ap* 647, A56, A56.

Vican, Laura et al. (2016). “Herschel Observations of Dusty Debris Disks”. In: *ApJ* 833.2, 263, p. 263.

Villebrun, F. et al. (2019). “Magnetic fields of intermediate-mass T Tauri stars. I. Magnetic detections and fundamental stellar parameters”. In: *A&Ap* 622, A72, A72.

Vink, Jorick S. et al. (2005). “Probing the circumstellar structures of T Tauri stars and their relationship to those of Herbig stars”. In: *MNRAS* 359.3, pp. 1049–1064.

Vioque, M. et al. (2018). “Gaia DR2 study of Herbig Ae/Be stars”. In: *A&Ap* 620, A128, A128.

Vrba, F. J. et al. (1993). “Photometric and Spectroscopic Monitoring of AA Tau, DN Tau, UX Tau A, T Tau, RY Tau, LK CA 4, and LK CA 7”. In: *AJ* 106, p. 1608.

Wade, G. A. et al. (2007). “A search for strong, ordered magnetic fields in Herbig Ae/Be stars”. In: *MNRAS* 376.3, pp. 1145–1161.

Wall, Joshua E. et al. (2019). “Collisional N-body Dynamics Coupled to Self-gravitating Magnetohydrodynamics Reveals Dynamical Binary Formation”. In: *ApJ* 887.1, 62, p. 62.

Watkins, Laura L. et al. (2019). “Evidence for an Intermediate-mass Milky Way from Gaia DR2 Halo Globular Cluster Motions”. In: *ApJ* 873.2, 118, p. 118.

Weidenschilling, S. J. (1977). “Aerodynamics of solid bodies in the solar nebula.” In: *MNRAS* 180, pp. 57–70.

Weidenschilling, S. J. and Jeffrey N. Cuzzi (1993). “Formation of Planetesimals in the Solar Nebula”. In: *Protostars and Planets III*. Ed. by Eugene H. Levy and Jonathan I. Lunine, p. 1031.

Whipple, F. L. (1972). “From plasma to planet.” In: p. 211.

Wichittanakom, C. et al. (2020). “The accretion rates and mechanisms of Herbig Ae/Be stars”. In: *MNRAS* 493.1, pp. 234–249.

Windmark, F. et al. (2012). “Planetesimal formation by sweep-up: how the bouncing barrier can be beneficial to growth”. In: *A&Ap* 540, A73, A73.

Wyatt, M. C. (2008). “Evolution of debris disks.” In: *ARA&Ap* 46, pp. 339–383.

Wyatt, M. C. et al. (2015). “Five steps in the evolution from protoplanetary to debris disk”. In: *ApSS* 357.2, 103, p. 103.

Yang, Chao-Chin et al. (2017). “Concentrating small particles in protoplanetary disks through the streaming instability”. In: *A&Ap* 606, A80, A80.

Youdin, Andrew N. and Jeremy Goodman (2005). “Streaming Instabilities in Protoplanetary Disks”. In: *ApJ* 620.1, pp. 459–469.

Youdin, Andrew N. and Frank H. Shu (2002). “Planetesimal Formation by Gravitational Instability”. In: *ApJ* 580.1, pp. 494–505.

Zernike, F. (1938). “The concept of degree of coherence and its application to optical problems”. In: *Physica* 5.8, pp. 785–795.

Zhu, Zhaohuan et al. (2012). “Dust Filtration by Planet-induced Gap Edges: Implications for Transitional Disks”. In: *ApJ* 755.1, 6, p. 6.

Zsom, A. et al. (2010). “The outcome of protoplanetary dust growth: pebbles, boulders, or planetesimals? II. Introducing the bouncing barrier”. In: *A&Ap* 513, A57, A57.